Measurements of Single Dissociative Diffraction of Protons in $\sqrt{s} = 13$ TeV Collisions with the ATLAS Experiment

James Kendrick

Thesis submitted for the degree of Doctor of Philosophy

Particle Physics Group,
School of Physics and Astronomy,
University of Birmingham.

20th September 2019

ABSTRACT

The first cross-section measurement of single dissociative diffraction in proton-proton collisions ($pp \to pX$) at $\sqrt{s} = 13$ TeV is presented. ATLAS data are used to make the measurement differentially as a function of the squared four momenta transfer (t), the fractional energy loss of the intact proton (ξ) and the observable gap in rapidity space ($\Delta\eta$). ALFA, one of the ATLAS forward spectrometers, is used to tag and reconstruct intact protons giving a direct t measurement. Components of the main ATLAS detector, primarily the Inner Detector, are used to reconstruct the dissociative X system and measure ξ and $\Delta\eta$.

The fiducial range of the measurement is $-4 \leq \log_{10}\xi \leq -2$ and $0.06\ \text{GeV}^2 \leq |t| \leq 0.9\ \text{GeV}^2$. Regge theory is applied to extract the slope parameter and the Pomeron intercept from the unfolded $|t|$ and $\log_{10}\xi$ distributions, respectively. The measured value of the slope parameter governing the exponentially falling t dependence is $B = 5.5 \pm 0.5\ \text{GeV}^{-2}$. The measured value of the Pomeron intercept is $\alpha_{\mathbb{P}}(0) = 1.15 \pm 0.13$.

Simulation work on the L1CALO upgrade of ATLAS is also presented, studying the design of the e/γ algorithm for the phase-1 upgrade.

DECLARATION OF AUTHOR'S CONTRIBUTION

The successful design, construction and operation of ATLAS and the LHC is due to the hard work and cooperation of thousands of individuals throughout the world. While based at CERN, I contributed to the continued running of ATLAS by completing trigger, runcontrol and L1CALO on-call expert shifts.

Chapters 2 and 3 are used to motivate the analysis presented in the rest of the thesis. With the exception of section 2.9, I have not contributed to what is presented in these chapters.

Section 2.9 presents an ATLAS measurement, equivalent to the main one presented in this thesis, at a lower centre-of-mass energy. This analysis was completed by a team of five ATLAS collaborators, including myself. My role was relatively small, primarily the preparation of the final figures, but crucial as the majority of the team had left academia before publication of the measurement.

The main analysis presented in this thesis is entirely my own work. Unusually for an ATLAS analysis, I have been the only one working 'hands-on' on it. All plots and diagrams shown in chapters 4 to 9 have been produced in the course of my work.

Chapter 10 presents the work of my qualification task, completed to gain ATLAS authorship. The first part of this chapter summarises work by others that motivates these studies. Section 10.4 onwards, with the exception of figure 10.10, is the result of my contribution to the L1CALO community.

ACKNOWLEDGEMENTS

When Frodo set out from Rivendell to destroy the One Ring, he went with the Fellowship of the Ring. While his quest was for him and him alone to complete, he had the support, help and guidance of his companions. Frodo's task was to cast the ring into the fires of Mount Doom, mine has been to complete my PhD. Neither of us would have achieved our aims without assistance.

There have been many physics and computing wizards who have helped me get to this point, too many to name here. Paul and Alan, most of all, have given me the advice and guidance that have made this thesis possible. Thank you both.

Frodo wouldn't have even made it out of the Shire without the help of his fellow hobbits. While I didn't have Merry and Pippin's cheerfulness and antics, I have had the chance to make friends through Carnival RAG, UoB Cycling Club and sharing an office. Andy and Briglin, in particular, deserve a special mention for their advice and amusement, respectively. Thank you to you all.

Sam never stopped believing in Frodo. He was there at the start and end of their journey and every day in between. Aileen you have been more than a companion to me. A comparison to Samwise the Brave doesn't do you justice. Thank you for everything and here's to our future together.

Thank you to the support from my family, in particular my parents. It is your encouragement that set me out on this journey. Unlike Frodo's I do not know, yet, where I will end up.

This thesis is testament to the support each and every one of you have given me. Thank you all.

One does not simply walk into Mordor.

Contents

CHAPTER 1

Introduction

The analogy of observing games of chess, without any prior understanding of the rules, was used by Feynman to explain the scientific method[1]. When observing a single game of chess one would likely see many instances of a pawn moving and so could relatively quickly infer that pawns can (usually) only move one space forwards or diagonally forwards when taking another piece. One would have to observe many more games to gain a similar understanding of less common moves, such as castling. Based on one's understanding of the rules, predictions of allowable moves could be made for a given set-up of pieces and thus the predictions could be tested by observing games in such a set-up. It is in this way, by making hypotheses and observing nature, that scientists are able to build their understanding of it.

This metaphor is particular applicable to LHC analyses involving the study of rare processes at the energy frontier, made possible due to the large instantaneous luminosities provided by the collider and the elaborate trigger systems of detectors vetoing 'uninteresting' events. Despite the rare occurrence of the production of a top

quark, bottom quark or Higgs boson, physicists are able to study their properties with increasing levels of precision. For example, in 2017 the LHCb collaboration announced the single-experiment observation of the decay $B_s^0 \to \mu^+\mu^-$ which has a branching ratio of $\sim 10^{-9}$[2].

Despite the precision with which rare particles and processes can be measured, the more common processes at the LHC are surprisingly poorly understood. Elastic and diffractive processes (in which one or both protons stay intact), and which are likely vetoed by the trigger and ignored by most analyses, occur in around 50% of collisions at LHC energies. Continuing the chess analogy, the vast majority of games are being ignored to gain an understanding of an uncommon specific move, say queen-side castling, yet we do not have an exact understanding of the rules governing pawns! Even with a basic understanding of the 'usual' moves a pawn may make, one may still be surprised, and even lose a game, due to unusual behaviour such as en-passant! For example, a recent ATLAS analysis has shown that Single Diffraction, which contributes to $\sim 10\%$ of the total pp cross-section, happens around $^2/_3$ of the time that is predicted by event generators at $\sqrt{s} = 8$ TeV[3]. The understanding of these elastic and diffractive processes are crucial for input parameters for MC event generators and are also important in their own right, probing the non-perturbative regime of QCD.

This thesis presents an inclusive measurement of the differential cross-section of Single Diffraction $pp \to pX$ in $\sqrt{s} = 13$ TeV proton-proton collisions using the ATLAS detector. It is structured as follows:

- Chapter 2 presents the theoretical motivations for understanding diffractive collisions.
- Chapter 3 describes the LHC and ATLAS, with an emphasis on the components relevant to the analysis.
- Chapter 4 explains the analysis strategy and the event selection. The fiducial region and binning of variables are also defined.

- Chapter 5 describes the measurement of, and subsequent corrections for, the efficiency of several aspects of the event selection.
- Chapter 6 describes the backgrounds contaminating the event selection and how they are modelled.
- Chapter 7 explains the unfolding procedure, used to correct the measurement for detector effects.
- Chapter 8 quantifies the contribution of different sources of systematic errors to the uncertainties.
- Chapter 9 presents the results of the measurement. Theoretical parameters are also extracted from the unfolded distributions. The Single Diffraction (SD) measurement is summarised.
- Chapter 10 is a stand-alone chapter, motivating and presenting work completed for the ATLAS trigger upgrade.

A summary is given for the diffractive measurement and the L1CALO work at the end of chapters 9 and 10, respectively.

CHAPTER 2

Diffraction and Regge theory

The analysis presented in this thesis studies Single Diffraction (SD) in proton-proton collisions $pp \to pX$. This chapter explains the importance of this process and motivates the analysis.

A brief introduction is given to the standard model, rapidity, the Mandelstam variables and the strong interaction in sections 2.1, 2.2, 2.3 and 2.4, respectively. Regge theory is then introduced in section 2.5. Next, in section 2.6, the Pomeron is explained in the context of the total proton-proton cross-section. The mathematical ideas behind single diffraction are outlined in section 2.7. In section 2.8, the Monte Carlo (MC) method is explained with further details given on the modelling of single diffraction in PYTHIA. To conclude this chapter, section 2.9 reviews the recent ATLAS result on SD at $\sqrt{s} = 8$ TeV.

2.1 The standard model

The standard model is our best understanding of fundamental matter and forces in the universe[4, 5, 6]. Constructed through a combination of the Dirac equation, quantum field theory, the local gauge principle, the Higgs mechanism and experimental results, it contains 26 parameters which represent the fermion masses, the coupling constants of the interactions, the Higgs potential and mixing angles[7]. The 3 fundamental forces are governed by the exchange of integer-spin gauge bosons: $W^{\pm}$ and Z^0 for the weak interaction, γ for the Electromagnetic (EM) interaction and gluons for the strong interaction[8, 9, 10, 11]. Gravity cannot yet be included at the quantum mechanical level. General relativity is the most complete theory explaining gravity but is not compatible with the standard model[7].

Matter consists of fermions, $\frac{1}{2}$-integer spin particles, which obey the Pauli-exclusion principle[12]. Fermions are massive and split into two families, quarks and leptons, which are further separated into three generations of two particles. Each particle also has a corresponding anti-particle with equal but opposite charge[13].

Each generation of quarks consists of two quarks: one with an EM charge of $+\frac{2}{3}$ and the other $-\frac{1}{3}$. Quarks carry the additional 'colour' charge and so can interact through the strong interaction[14]. Despite being fundamental particles in our current understanding, quarks do not exist freely in nature. The concept of colour confinement means that they form colour singlets - neutral composite particles of two or three quarks, known as mesons and baryons, respectively[6]. The strong interaction is further described in section 2.4.

Each lepton generation consists of a charged lepton and a neutrino. The 3 charged leptons are the: electron ($e^{\pm}$), muon ($\mu^{\pm}$) and tau ($\tau^{\pm}$) and their respective neutrinos: ν_e, ν_μ and ν_τ. All leptons are able to interact through the weak interaction and additionally the EM force for those that carry an EM charge. Leptons do not carry colour charge so do not interact strongly.

The standard model originally predicted the bosons to be massless but this was observed to not be the case[8, 9, 10]. The Higgs mechanism was subsequently theorized in 1964. It explains the masses of the bosons through spontaneous symmetry breaking of the Higgs field while preserving the gauge invariance of the standard model. It also generates the masses of the fermions through the Yukawa coupling[15, 16].

The standard model has some shortcomings. For example the neutrinos are described as massless by the standard model, but neutrino oscillation experiments have shown the neutrinos to have a mass[17, 18]. There is also no known mechanism to explain the matter-antimatter asymmetry observed in the universe[19]. Dark matter, introduced to explain the excess of gravitational forces measured from visible matter in astronomical measurements, is also not explained by the standard model[20].

2.2 Rapidity and pseudorapidity

The rapidity y of relativistic massive particles is a useful quantity as differences are Lorentz invariant for any boost along the beam axis, taken as the z axis. For a particle with momentum, $\vec{p}$, and energy, $E = \sqrt{\vec{p}^2 + m^2}$, it is defined as:

$$y = \frac{1}{2} \ln \left[\frac{E + p_z}{E - p_z} \right]. \tag{2.1}$$

In the highly relativistic limit ($m \to 0$ or $E \approx |p|$), this is equivalent to the pseudorapidity η. This is defined as:

$$\eta = -\ln \left[\tan \left(\frac{\theta}{2} \right) \right], \tag{2.2}$$

in terms of cylindrical polar coordinates, defining the polar angle, θ, in the $r - z$ plane with respect to the positive z axis.

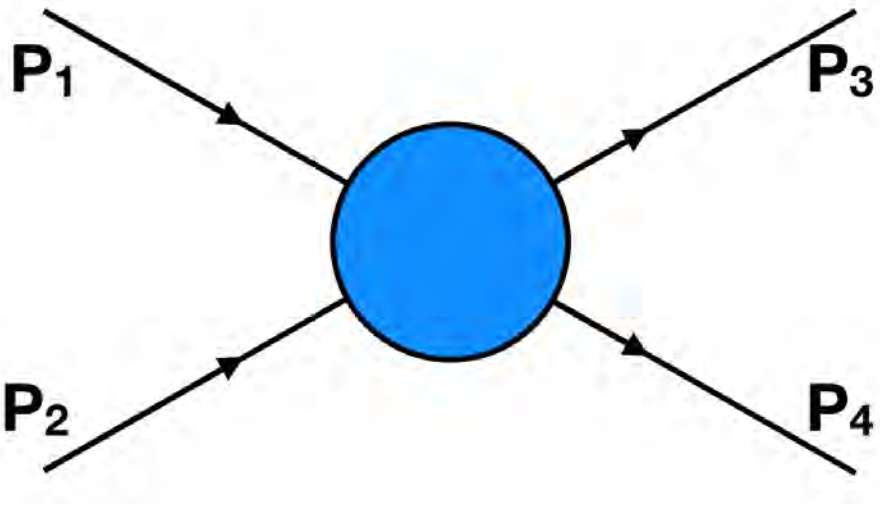

Figure 2.1: The general case of 2-body scattering of $12 \rightarrow 34$. Two initial state particles interact resulting in two final state particles.

2.3 Mandelstam variables

The momentum exchange in a general 2-body interaction can be described by a set of 3 convenient variables: the Mandelstam variables s, t and u which are Lorentz invariant observables[21]. They can describe the different possible processes shown in figure 2.1 where two initial state particles with 4-momenta $\mathbf{P_1}$ and $\mathbf{P_2}$ interact in some way resulting in two final state particles with 4-momenta $\mathbf{P_3}$ and $\mathbf{P_4}$.

The Mandelstam variable s is equivalent to the squared centre-of-mass energy for an annihilation process and t is equivalent to the squared 4-momentum exchanged in a scattering process. u is the third Mandelstam variable. They are calculated as shown in equations 2.3 – 2.5.

$$s = (\mathbf{P_1} + \mathbf{P_2})^2 = (\mathbf{P_3} + \mathbf{P_4})^2 \tag{2.3}$$

$$t = (\mathbf{P_1} - \mathbf{P_3})^2 = (\mathbf{P_2} - \mathbf{P_4})^2 \tag{2.4}$$

$$u = (\mathbf{P_1} - \mathbf{P_4})^2 = (\mathbf{P_2} - \mathbf{P_3})^2. \tag{2.5}$$

It can be shown that the sum of the Mandelstam variables is equivalent to the sum

of the squared invariant masses of the initial and final state particles, as shown in equation 2.6.

$$s + t + u = \sum_{i=1}^{4} m_i^2. \tag{2.6}$$

The Mandelstam variables are closely related to the three observables measured in this analysis: the fractional energy loss of the proton, the gap in rapidity space and the magnitude of the t-channel exchange. This will be shown below with their importance and relevance explained in subsequent sections.

2.3.1 Fractional energy loss of the proton

Consider the semi-inclusive process $p_1 + p_2 \to p_3 + X$. The incoming protons are travelling along the z-axis and have equal and opposite momentum. Each particle has four momenta $\mathbf{P_i} = (E_i, \vec{p_i})$. The X system has a total 4-momentum of $\mathbf{P_4}$ with $\vec{p'}$ being a vector sum over all particles in the system. Therefore, in the centre of mass frame each particle's four-momentum is:

$$\mathbf{P_1} = (E_1, \vec{p}) = (E_1, 0, 0, p_z), \tag{2.7}$$

$$\mathbf{P_2} = (E_2, -\vec{p}) = (E_2, 0, 0, -p_z), \tag{2.8}$$

$$\mathbf{P_3} = (E_3, \vec{p'}) = (E_3, \vec{p'_T}, p'_z), \tag{2.9}$$

$$\mathbf{P_4} = (E_4, -\vec{p'}) = (E_4, -\vec{p'_T}, -p'_z). \tag{2.10}$$

It is possible to express the energy and momentum of the interacting particles as:

$$E_{1,2,3,4} = \frac{1}{2\sqrt{s}}(s + m^2_{1,2,3,4} - m^2_{2,1,4,3}), \tag{2.11}$$

$$\vec{p^2} = p_z^2 = E_1^2 - m_1^2 = \frac{1}{4s}\Big(s - (m_1 + m_2)^2\Big)\Big(s - (m_1 - m_2)^2\Big), \tag{2.12}$$

$$\vec{p'^2} = \vec{p'^2_T} + p'^2_z = E_3^2 - m_3^2 = \frac{1}{4s}\Big(s - (m_3 + m_4)^2\Big)\Big(s - (m_3 - m_4)^2\Big). \tag{2.13}$$

These equations simplify further for the case of high energy single diffraction in pp collisions. Both incoming particles and one of the outgoing particles are protons ($m_1 = m_2 = m_3 = m_p \ll \sqrt{s}$) and the mass of the diffractive system is large ($m_4 = M_X \gg m_p$):

$$E_{1,2} = |\vec{p}| = \frac{\sqrt{s}}{2}, \tag{2.14}$$

$$\begin{aligned} E_3 &= |\vec{p'}| \\ &= \frac{1}{2\sqrt{s}}(s + m_p^2 - M_X^2) \\ &\approx \frac{s - M_X^2}{2\sqrt{s}}, \end{aligned} \tag{2.15}$$

$$\begin{aligned} E_4 &= \frac{1}{2\sqrt{s}}(s + M_X^2 - m_p^2) \\ &\approx \frac{s + M_X^2}{2\sqrt{s}}. \end{aligned} \tag{2.16}$$

We can define a useful quantity, ξ, the fractional energy loss of the intact proton as:

$$\begin{aligned} \xi &= 1 - \frac{E_3}{E_1} \\ &= \frac{E_1 - E_3}{E_1} \\ &\approx \frac{\frac{\sqrt{s}}{2} - \frac{s - M_X^2}{2\sqrt{s}}}{\frac{\sqrt{s}}{2}} \\ &\approx \frac{M_X^2}{s}. \end{aligned} \tag{2.17}$$

ξ can be reconstructed directly by measuring the energy of the intact proton E_3 or indirectly by reconstructing the invariant mass of the diffractive system. A well-used experimental approximation is the ξ_{EPz} method, where the sign of $p_{z,i}$ is determined by the direction in z of the intact proton and the index i runs over all measurable particles in the diffractive system:

$$\begin{aligned}
\xi &\approx \frac{M_X^2}{s} \\
&= \frac{1}{s}\sum_i (E_i^2 - \vec{p}_i^{\,2}) \\
&= \frac{1}{s}\sum_i \Big((E_i - p_{z,i})(E_i + p_{z,i}) - p_{T,i}^2\Big) \\
&\approx \frac{2E}{s}\sum_i (E_i - p_{z,i}) \\
\xi_{EPz} &\approx \frac{1}{\sqrt{s}}\sum_i E_i \pm p_{z,i}.
\end{aligned} \tag{2.18}$$

2.3.2 Squared four-momentum transfer

Recall the Mandelstam variable t from equation 2.4:

$$\begin{aligned}
t &= (\mathbf{P_1} - \mathbf{P_3})^2 \\
&= \mathbf{P_1}^2 + \mathbf{P_3}^2 - 2\mathbf{P_1}\cdot\mathbf{P_3} \\
&= m_1^2 + m_3^2 - 2E_1E_3 + 2\vec{p_1}\cdot\vec{p_3}.
\end{aligned} \tag{2.19}$$

In the case of single diffraction of protons, the intact proton p_3 is scattered through a small angle θ. Its transverse and longitudinal momentum will be $p'_T = |\vec{p'}|\sin\theta$ and $p'_z = |\vec{p'}|\cos\theta$ respectively. This can then be substituted into equation 2.19

along with equations 2.14, 2.15 and 2.17:

$$\begin{aligned} t &= 2m_p^2 - 2E_1E_3 + 2\cos\theta|p_1||p_3| \\ &\approx -2\frac{\sqrt{s}}{2}\frac{s-M_X^2}{2\sqrt{s}} + 2\cos\theta\frac{\sqrt{s}}{2}\frac{s-M_X^2}{2\sqrt{s}} \\ &= -\frac{s-M_X^2}{2}\Big(1-\cos\theta\Big) \\ &\approx -\Big(\frac{s-M_X^2}{2}\Big)\frac{\theta^2}{2} \\ &\approx -\Big(\frac{s-M_X^2}{2}\Big)\frac{p_T'^2}{2p'^2} \\ &\approx \frac{-p_T'^2}{1-\xi} \\ &\approx -p_T'^2. \end{aligned} \tag{2.20}$$

Hence we can see that the t-channel exchange can be measured from the transverse momentum of the intact proton for the case where the energy loss of the intact proton is small.

2.3.3 Rapidity Gap

Single diffractive collisions typically exhibit a large rapidity gap, an area in rapidity space without any particles being produced. The relationship between ξ and gap size, $\Delta\eta$, is approximately[22, 23, 24, 25]:

$$\Delta\eta \approx -\ln\xi + C. \tag{2.21}$$

To reach this result, consider the case of an elastic pp collision where both protons stay intact. With reference to hadronic momentum scale $s_0 \sim 1$ GeV^2, the rapidity span between the two outgoing protons is expected be:

$$\eta_{pp} \sim \ln\frac{s}{s_0}. \tag{2.22}$$

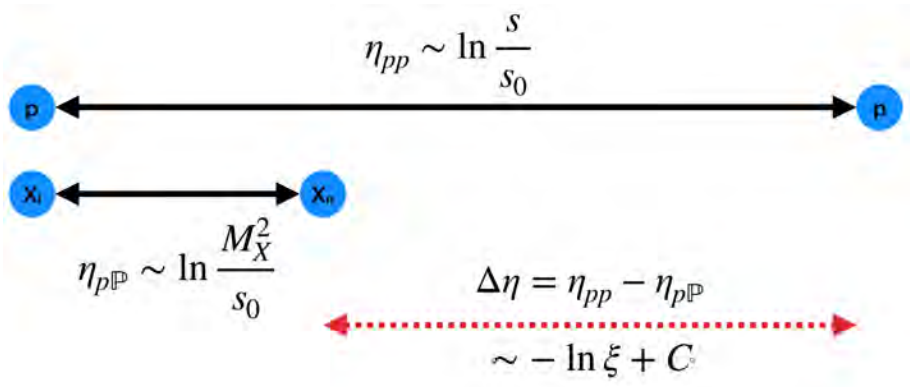

Figure 2.2: The rapidity gap formed by a pX system with η shown on the x-axis.

In the case of single diffraction, one proton dissociates and forms the 'X' system. The rapidity spanned by this system is expected to follow[1]:

$$\eta_{p\mathbb{P}} \sim \ln\left(\frac{M_X^2}{s_0}\right). \tag{2.23}$$

Therefore a rapidity gap is expected between the intact outgoing proton and the dissociative system, with the size dependent on M_X^2 or ξ.

$$\begin{aligned} \Delta\eta &= \eta_{pp} - \eta_{p\mathbb{P}} \\ &\sim \ln \frac{s}{M_X^2} + C \\ &\sim -\ln \xi + C. \end{aligned} \tag{2.24}$$

This reasoning is shown pictorially in figure 2.2.

2.4 The strong interaction

The strong interaction is described by the modern theory of Quantum Chromodynamics (QCD). It couples to the property of quarks known as colour charge and is mediated by the exchange of eight gluons[26]. The gluons are massless, independent of the singlet state and correspond to the 8-generators of the Gell-Mann matrices[27].

[1]The symbol $\mathbb{P}$ denotes the Pomeron which is introduced in section 2.6

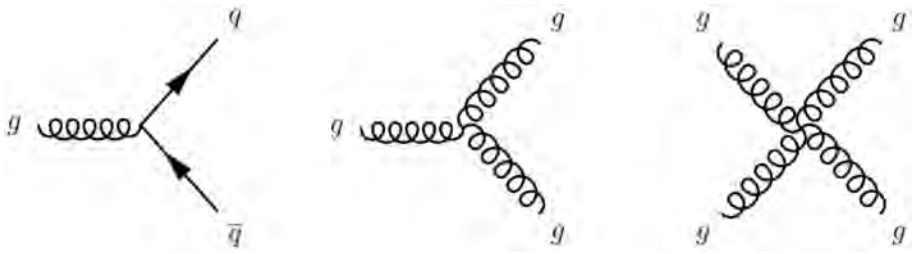

Figure 2.3: The 3 different QCD vertices. From left to right: a quark-gluon interaction vertex, a triple gluon self-coupling and quartic gluon self-coupling. Adapted from [28].

In contrast to the case of the EM interaction where there is only one charge and the photon itself carries no EM charge, there are three orthogonal colour charges in QCD (r, g and b) and the gluons carry both colour and anti-colour charge. The symmetry between the different colour charges is an exact SU(3) symmetry and therefore interactions are invariant under unitary transformations. QCD interactions conserve colour, electric charge and flavour quantum numbers. There are 3 different interaction vertices allowed, shown in figure 2.3. The concept of colour confinement applies to all particles carrying colour charge[6]. It states that quarks can only exist in combinations forming colour singlet states and was introduced to explain why quarks have not been observed existing freely in nature. Quarks have only been observed in mesons ($r\bar{r}$ / $g\bar{g}$ / $b\bar{b}$), baryons (rgb / $\bar{r}\bar{g}\bar{b}$) or, more recently, combinations of the two in tetraquarks or pentaquarks[29]. Colour confinement also applies to gluons and consequently limits their range.

The process that occurs as quarks separate is not well understood at a fundamental level, but is explained qualitatively by models, such as the Lund string model[30]. Consider the simplest case of two quarks in a meson. As they are forced apart the strong interaction forms an attractive force between them. The dominant term in the potential is proportional to the distance between them, such that:

$$V(r) \approx \kappa r. \tag{2.25}$$

where $\kappa \approx 1\text{GeV fm}^{-1} \approx 0.2\ \text{GeV}^2$[7]. As the distance between the quarks increases, the potential increases. This continues until the point where it is energetically

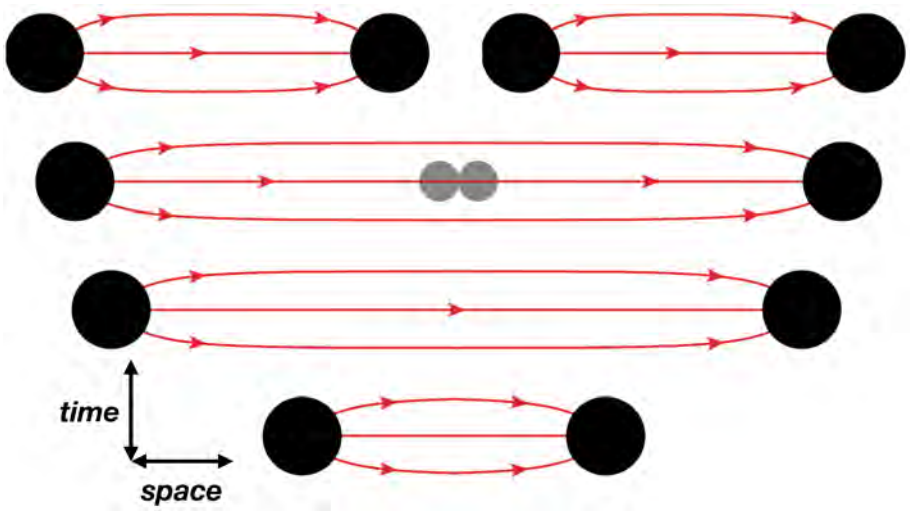

Figure 2.4: Hadronization following the Lund string model. Adapted from [32].

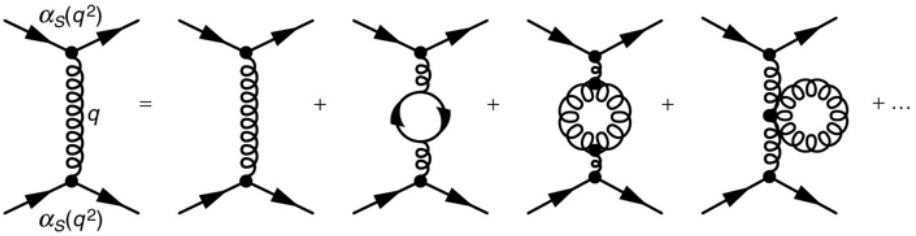

Figure 2.5: An example of loop diagrams in QCD calculations[7].

favourable to produce a new $q\bar{q}$ pair. Each of the quarks in the original meson 'pair' up with one of the newly formed quarks forming a pair of mesons. This model is illustrated in figure 2.4. This process, which explains how jets are formed in colliders, is known as hadronization. There are also other models, for example the cluster model[31].

Gluons carry colour charge and are therefore selfcoupling[33]. The leads to additional loop corrections in calculations that depend on $|Q|$, the four-momentum transfer involved. Figure 2.5 shows an example of a QCD interaction. It contains additional terms compared to the equivalent for Quantum Electrodynamics (QED). As a result, the coupling strength decreases as the magnitude of four-momentum exchange (denoted as Q) increases in contrast to the slow increase in the QED case.

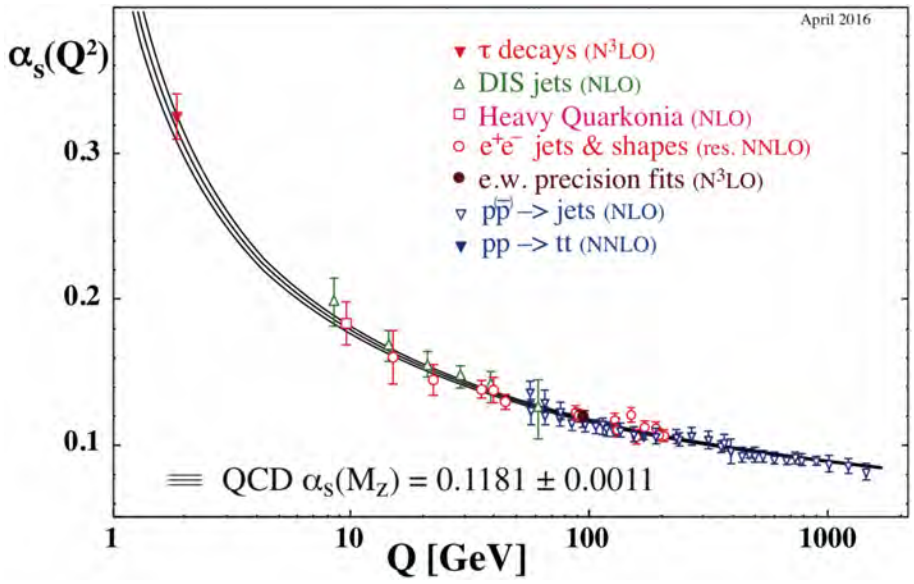

Figure 2.6: Measurements of α_S at different $|Q|$ scales[35].

This 'running coupling' is predicted to follow (for the leading order)[34, 7]:

$$\alpha_S(Q^2) = \frac{\alpha_S(\mu^2)}{1 + B\alpha_S(\mu^2)\ln\left(\frac{Q^2}{\mu^2}\right)}. \tag{2.26}$$

To ensure finite results the strength can be renormalised with respect to a characteristic energy scale μ. This is typically taken to be $\Lambda_{\text{QCD}} \approx 200$ MeV[34]. The factor B depends on the number of loops arising from both the quark and gluon contributions. For N_C colours and N_f quark flavours, (for the leading order) it is equivalent to[34, 7]:

$$B = \frac{11N_C - 2N_f}{12\pi}. \tag{2.27}$$

Experimental data on the running of α_S are shown in figure 2.6. At very high energies or very small distances, α_S decreases leading to the asymptotic freedom of quarks[36, 37]. Perturbation theory can then be used but Next-to-Leading Order (NLO) corrections, or better, are still needed for accurate results[32, 38]. At small Q^2, below a few GeV^2, perturbation theory is not reliable and other methods must be sought. The region where perturbation theory can't be applied is referred to as soft QCD. One of the more modern methods for making calculations in the non-

perturbative regime is Lattice QCD[39]. However it is computationally intensive and it can take months for results to be obtained even when using supercomputers.

2.5 Regge theory and scattering amplitudes

Historically Yukawa explained the range of the nuclear force by applying the uncertainty principle and predicting the existence of the pions as exchange particles[40]. This treatment was generalised in Regge theory to cover the short and long range components of the nuclear force, including contributions of all possible exchange particles - the lowest lying state with appropriate quantum numbers and its angular momentum excitations[41]. An example is the spin-1 ρ meson and its excitations: ρ_3, ρ_5 etc. This set of particles form a straight line, a Regge trajectory, when plotted on a Chew-Frautschi plot of M^2 (in the s-channel region) or Mandelstam t (in the t-channel region) against spin. An example plot is shown in figure 2.7. This arises from Regge theory's treatment of potential scattering. Angular momentum is treated as a continuous complex variable and observable s-channel resonances are seen where the real component ($Re[\alpha(t)]$) takes half-integer or integer values. A Regge trajectory can then be described by the linear equation:

$$\alpha_{\mathbb{R}}(t) = \alpha_{\mathbb{R}}(0) + \alpha'_{\mathbb{R}} t. \tag{2.28}$$

The parameters have been measured to be $\alpha_{\mathbb{R}}(0) \approx 0.5$ and $\alpha'_{\mathbb{R}} \approx 1$ GeV^{-2}[43]. Regge theory also predicts the elastic cross-section to follow:

$$\frac{d\sigma_{El}}{dt} \propto s^{2\alpha_{\mathbb{R}}(t)-2}, \tag{2.29}$$

where $\alpha_{\mathbb{R}}(t)$ is the highest lying trajectory that can be exchanged.

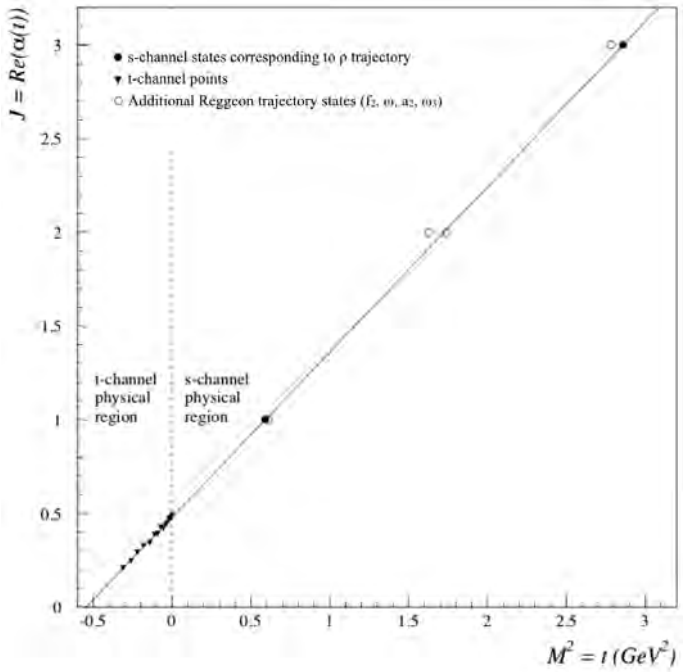

Figure 2.7: Chew-Frautschi plot adapted from [42].

2.6 Total cross-section and the Pomeron

The optical theorem predicts a relationship between the total proton-proton cross-section and the imaginary component of the forward ($\frac{t}{s} \to 0$) elastic amplitude $T_{El}^{pp\to pp}$. Applying this to the predictions of Regge theory, equation 2.29, we arrive at[42]:

$$\sigma_{Tot}^{pp}(s) \approx \frac{1}{s}\Im(T_{El}^{pp\to pp})|_{t=0} \approx s^{\alpha_{\mathbb{R}}(0)-1}. \tag{2.30}$$

Applying the experimental result for the trajectory shown in equation 2.29 of $\alpha_{\mathbb{R}} \approx 0.5$ to this theory predicts a dependence of $\sigma_{Tot}^{pp} \approx s^{-0.5}$. This prediction provides a good description for the fall in σ_{Tot}^{pp} below $\sqrt{s} \sim 30$ GeV as shown in figure 2.8. Above this point a rise in the cross-section is observed with good agreement from different sources. This suggests the Regge trajectory $\alpha_{\mathbb{R}}$ is not sufficient to describe what is happening.

To explain this increase in σ_{Tot}^{pp} an additional trajectory was introduced and named the Pomeron, after Isaac Pomeranchuk, with $\alpha_{\mathbb{P}}(0) > 0$. It is also used to explain the increase in σ_{El}^{pp} and so must have positive charge parity and carry the quantum

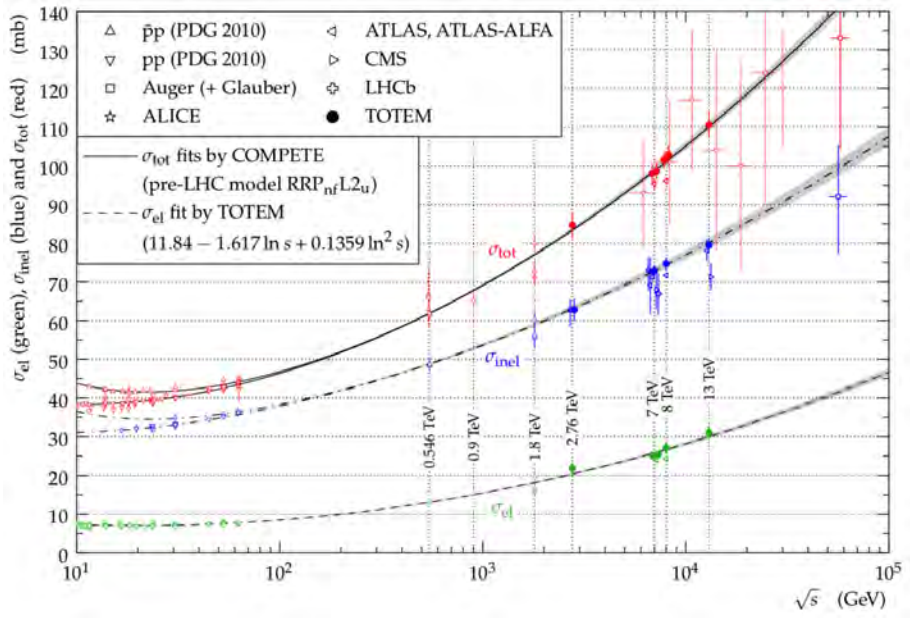

Figure 2.8: Measurements of σ_{PP}[44].

numbers of the vacuum. It must also couple to both particles and anti-particles equally to satisfy the Pomeranchuk theorem applied to pp collisions[45]:

$$\sigma_{Tot}^{pp} \xrightarrow[s\to\infty]{} \sigma_{Tot}^{p\bar{p}}. \tag{2.31}$$

The contributions of the Reggeon and Pomeron trajectories can be seen in figure 2.8. At low $\sqrt{s}$ there is a discrepancy between σ_{Tot}^{pp} and $\sigma_{Tot}^{p\bar{p}}$. This is due to the Regge trajectory $\alpha_{\mathbb{R}}$ dominating. At higher $\sqrt{s}$ the Pomeron contribution dominates and the cross-section for pp and $p\bar{p}$ increase and converge.

The intercept of the Pomeron trajectory $\alpha_{\mathbb{P}}(0)$ is often expressed as $\alpha_{\mathbb{P}}(0) = 1 + \epsilon$. A 'critical' Pomeron has $\epsilon = 0$ and, according to equation 2.30 would correspond to a constant total cross-section as a function of $\sqrt{s}$. A supercritical Pomeron has $\epsilon > 0$ and would correspond to a cross-section increasing as a function of $\sqrt{s}$.

There is evidence that the Pomeron couples to individual quarks, rather than composite hadrons[46]. Donnachie and Landshoff fitted the Pomeron trajectory to cross-

section measurements to find the t dependence[47]:

$$\alpha_{\mathbb{P}}(t) = 1.08 + 0.25t. \tag{2.32}$$

To summarise, the total cross-section has contributions from both the Pomeron and the Regge trajectories:

$$\begin{aligned} \sigma_{Tot}(s) &= A_{\mathbb{P}} s^{\alpha_{\mathbb{P}}(0)-1} + A_{\mathbb{R}} s^{\alpha_{\mathbb{R}}(0)-1} \\ &= 21.70 s^{0.0808} + 56.08 s^{-0.4545} \text{ mb}, \end{aligned} \tag{2.33}$$

where the parameters are a result of Donnachie and Landshoff's fit to data[48]. This is an impressive achievement for Regge theory considering it is not derivable from the modern picture of QCD. However something must change at even higher energy scales to prevent the cross-section from breaking the Froissart-Martin bound, which places an asymptotic upper limit on the growth of the cross-section[49]:

$$\sigma_{Tot}(s) < K \ln^2(s). \tag{2.34}$$

As a result, the growth of the cross-section can not be faster than $\ln^2(s)$ at large s.

2.6.1 Proton-proton cross-section decomposition

The total cross-section, has been measured by the 'TOTal cross section, Elastic scattering and diffraction dissociation Measurement at the LHC' (TOTEM) collaboration to be $\sigma_{Tot} = 110.6 \pm 3.4$ mb at $\sqrt{s} = 13$ TeV[44]. The total cross-section can be broken down into a number of components as shown in equation 2.35, with each component depicted in figure 2.9.

$$\sigma_{Tot} = \underbrace{\sigma_{El}}_{\text{Elastic}} + \underbrace{\underbrace{\sigma_{SD} + \sigma_{DD} + \sigma_{CD}}_{\text{Diffractive}} + \underbrace{\sigma_{ND}}_{\text{Non-diffractive}}}_{\text{Inelastic}} \tag{2.35}$$

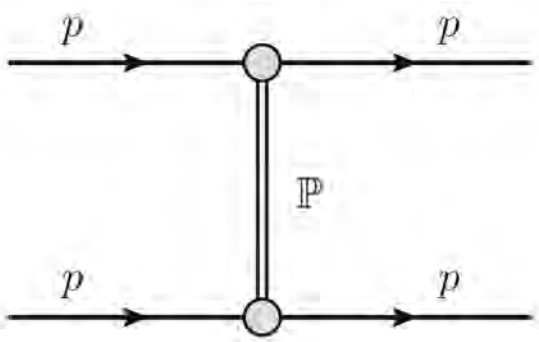

(a) Elastic

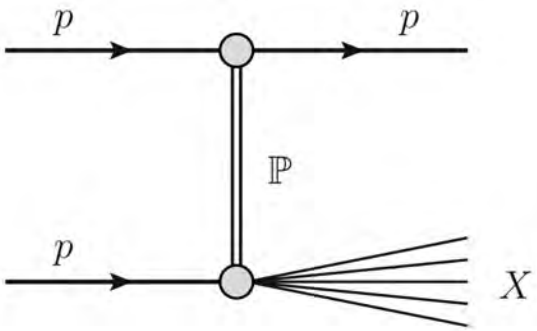

(b) Single Diffraction (SD)

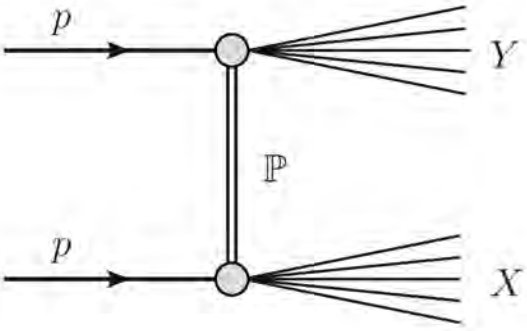

(c) Double Diffraction (DD)

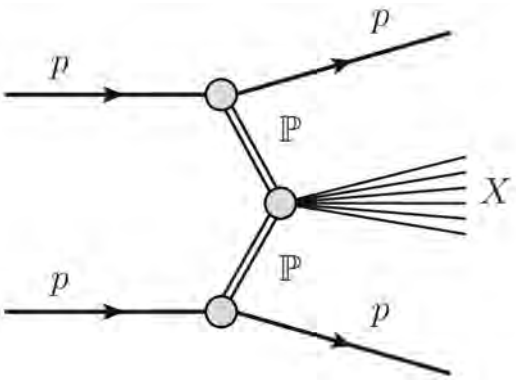

(d) Central Diffraction (CD)

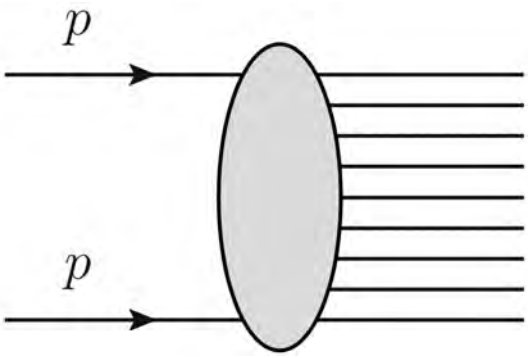

(e) Non-Diffractive (ND)

Figure 2.9: Feynman diagrams for the different processes[50].

Elastic collisions ($pp \to pp$) have two intact protons in the final state and no other particles, as shown in figure 2.9a. The elastic cross-section has also been measured by TOTEM to be $\sigma_{El} = 31.0 \pm 1.7$ mb at $\sqrt{s} = 13$ TeV[44]. Typically protons are scattered through very small angles (< 10 μrad) with a small exchange in the t channel ($|t| < 1$ GeV^2). Pomeron exchange is the dominant interaction that produces elastic collisions at the LHC for $|t| > 0.1$ GeV^2 . In the Coulomb Nuclear Interference (CNI) region, reached at very small values of t ($|t| \ll 0.01$ GeV^2), Pomeron exchange and photon exchange provide similar contributions to the elastic scattering amplitude. At even smaller values of t, photon exchange becomes dominant[51].

The remaining collisions in equation 2.35 are known as inelastic and ATLAS has measured $\sigma_{Inel} = 78.1 \pm 2.9$ mb at $\sqrt{s} = 13$ TeV[52]. The equivalent result from the TOTEM collaboration was $\sigma_{Inel} = 79.5 \pm 1.8$ mb[44]. The total inelastic cross-section consists of several diffractive processes and numerous non-diffractive processes. The diffractive processes occur when a colour singlet is exchanged in the t-channel. At LHC energy scales, this is dominated by Pomeron exchange. Three different diffractive processes are usually considered:

- Single Diffraction (SD) where one proton remains intact, and the other dissociates. This is shown in figure 2.9b.
- Double Diffraction (DD) where both protons dissociate and form 2 separate systems, shown in figure 2.9c.
- Central Diffraction (CD), also known as Double Pomeron Exchange (DPE) or central exclusive production, where both protons remain intact and a central diffractive system forms at a third vertex. This is a second order process so its cross-section is suppressed relative to the other diffraction processes. CD is shown in figure 2.9d.

Each of the diffractive processes contains at least one diffractive system formed by dissociation of a proton or fusion of two Pomerons. The quantum numbers of the proton (or Pomeron) are conserved in the diffractive systems. The rapidity space

between the final state protons or diffractive systems is typically large and devoid of particles. This is referred to as a rapidity gap and is understood to be due to the exchange particle being a colour singlet. Section 2.3 has already shown how the rapidity gap is related to the energy loss of the proton.

The cross-section of single diffraction has not yet been measured at $\sqrt{s} = 13$ TeV. At $\sqrt{s} = 8$ TeV ATLAS performed the only measurement so far of SD using proton tagging. It measured $\sigma_{SD} = (1.88 \pm 0.15)$ mb in the fiducial range of $-4.0 < \log_{10} \xi < 1.6$, showing that measured cross-section is $\sim \frac{2}{3}$ of that predicted by PYTHIA8[3]. This measurement is discussed in more detail in section 2.9.

Non-diffractive processes involve the exchange of a colour octet between the partons of the two incoming protons. The exchange of colour charge between the protons causes them to dissociate as explained in section 2.4. This generally produces a high multiplicity of particles throughout the rapidity space. Rapidity gaps do form due to statistical fluctuations but are suppressed as[22, 53]:

$$\frac{dN}{\Delta\eta} \propto e^{-\rho\Delta\eta} \tag{2.36}$$

where ρ denotes the density of particles. The definitions discussed in this section are theoretical. Looser definitions are often adopted for observables based on the reconstructed rapidity gap[54].

2.7 Single diffraction cross-section formalism

If the analytic form of the scattering amplitude ($T_{AB\to CX}$) is not affected by the exchange of the outgoing particle C with momentum p_C for an incoming anti-particle $\bar{C}$ with momentum $-p_C$, the amplitude of the physical process $AB \to CX$ is comparable to that of the unphysical hypothetical process $AB\bar{C} \to X$ after $s-t$ channel

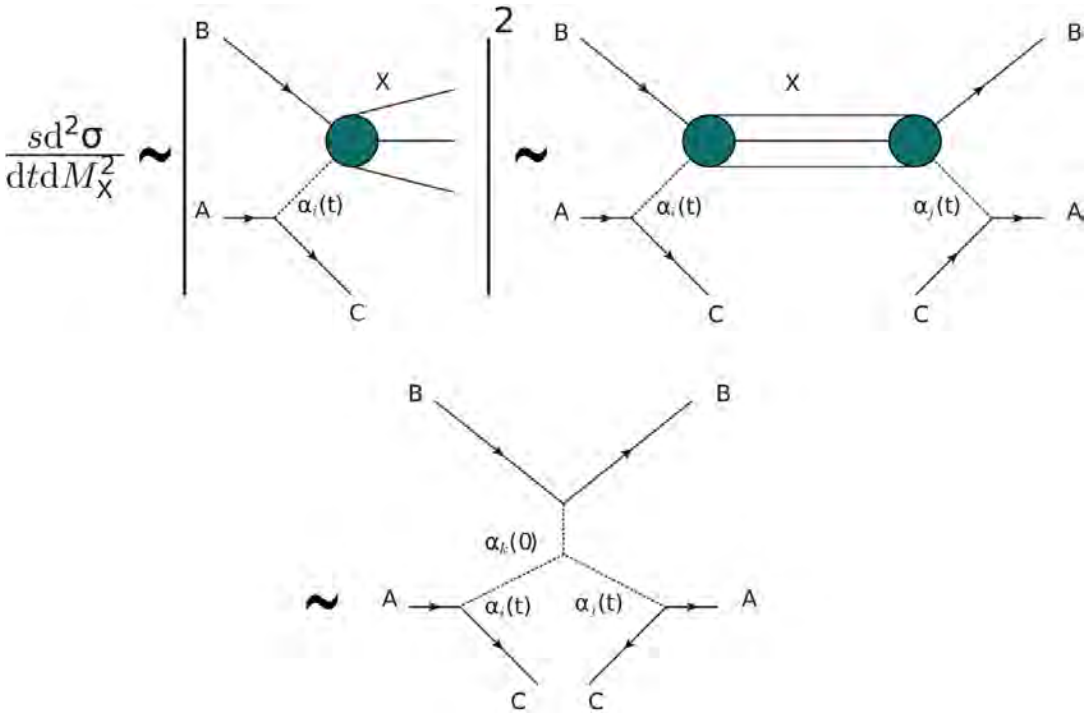

Figure 2.10: A diagram of Mueller's generalization of the optical theorem when applied to the scattering process $AB \to CX$ resulting in the triple Regge amplitude[56].

crossing. This can be written as:

$$T_{AB\to CX}(p_C, X) = T_{AB\bar{C}\to X}(-p_C, X). \tag{2.37}$$

Mueller's generalisation of the optical theorem[55], shown conceptually in figure 2.10, can then be applied to calculate the cross-section of the process:

$$\sigma_{Tot}(AB\bar{C} \to X) \approx \frac{1}{s}\Im\Big(T_{AB\bar{C}\xrightarrow{X}AB\bar{C}}\Big)_{t=0}, \tag{2.38}$$

where $\xrightarrow{X}$ denotes the sum over all possible intermediate states with total mass M_X.

It is possible to understand this scattering in terms of Regge trajectories. The triple Regge limit $t \ll M_X^2 \ll s$ and $m_p^2 \ll M_X^2$ is satisfied for soft SD at the LHC and therefore this scattering can be understood using Regge trajectories. Figure 2.10 shows a representation of the Regge amplitudes obtained using the generalised optical theorem. In the case of SD, particles A and C are both protons and therefore the $\alpha_i(t)$ and $\alpha_j(t)$ must represent Pomerons. In the Triple Regge limit the Pomeron

term of $\alpha_k(0)$ dominates and therefore so does the $\mathbb{P}_i\mathbb{P}_j\mathbb{P}_k$ contribution[2]. Therefore σ_{SD} is also referred to as the triple Pomeron cross-section. It can be expressed differentially as[57, 58]:

$$\frac{d^2\sigma_{SD}}{dtdM_X^2} = k(t)s^{2\alpha_{\mathbb{P}}(t)-2}\left(\frac{1}{M_X^2}\right)^{2\alpha_{\mathbb{P}}(t)-1}(M_X^2)^{\alpha_{\mathbb{P}}(0)-1}. \tag{2.39}$$

For a fixed centre of mass energy $\sqrt{s}$, this can be considered as two separate components. One is the total cross-section for $\mathbb{P}p \to X$, $\sigma_{Tot}^{\mathbb{P}p\to X} \propto (M_X^2)^{\alpha_{\mathbb{P}}(0)-1}$. The other is $F_{\mathbb{P}/p}$, the Pomeron flux from the proton, which includes the numerical constants and triple Pomeron coupling in the $k(t)$ term and the t dependence of the elastic scattering amplitude. The t dependence in the $k(t)$ term has been measured, and is found to be well described by an exponential function[59]. Therefore:

$$\begin{aligned} F_{\mathbb{P}/p} &= k(t)\frac{1}{M_X^2}^{2\alpha_{\mathbb{P}}(t)-1} \\ &\propto e^{B_0 t}\frac{1}{M_X^2}^{2\alpha_{\mathbb{P}}(t)-1}. \end{aligned} \tag{2.40}$$

Therefore using the definition of ξ (equation 2.17), equation 2.39 can be expressed as:

$$\begin{aligned} \frac{d^2\sigma_{SD}}{dtd\xi} &\propto \left(\frac{1}{\xi}\right)^{2\alpha_{\mathbb{P}}(t)-\alpha_{\mathbb{P}}(0)} e^{B_0 t} \\ &\propto \left(\frac{1}{\xi}\right)^{\alpha_{\mathbb{P}}(0)} e^{Bt}. \end{aligned} \tag{2.41}$$

Hence B, the slope parameter, is equivalent to:

$$B = B_0 - 2\alpha'_{\mathbb{P}} \ln \xi. \tag{2.42}$$

The very high mass case of single diffraction at $\xi \to 1$ is indistinguishable from ND collisions. The lower limit to M_X^2, the mass of the dissociative system, is the first excitation that preserves the quantum numbers of the proton $p \to p+\pi^0$. Therefore,

[2]The non-negligible contribution from $\mathbb{P}_i\mathbb{P}_j\mathbb{R}_k$ is poorly constrained.

using equation 2.17, M_X should have a lower limit:

$$1.1 \text{ GeV} \lesssim M_X, \tag{2.43}$$

or, expressed logarithmically in ξ for $\sqrt{s} = 13$ TeV:

$$-8.1 \lesssim \log_{10} \xi. \tag{2.44}$$

2.8 Monte Carlo models of diffraction

2.8.1 The Monte Carlo Method

The Monte Carlo (MC) method is a way of calculating a numerical estimate for a problem when the analytic answer can't easily be found.

An example of an MC calculation is finding an approximate value of π based on random number generation. Pairs of random numbers are generated in the range $0 \leq n \leq 1$ and are considered pairs of x, y coordinates in Euclidean space. One can then calculate the proportion of these points that would fall within a circle centred on $(0, 0)$ with radius of $r = 1$ i.e. those with $r_i < 1$ with $r_i = \sqrt{x_i^2 + y_i^2}$. The ratio of these points to the total number of points should be an estimation for $\frac{\pi}{4}$ with the accuracy of the estimate improving as more points are used for the sampling.

MC methods are widely used in High Energy Physics. Some examples include modelling backgrounds to measurements, comparing predictions to measured distributions and motivating the design of detectors[38]. For a single hard-scatter event there are several components that need to be modelled: the initial hard interaction, the decay or showering of the hard scatters into softer partons and the underlying event.

The detector response should then be simulated. These steps can then be 'factorized'

into smaller separate problems and dealt with individually. Different components can be shared in modern software. For example, PYTHIA[60] or Herwig[61] could be used to generated two samples of events but both could make use of GEANT4[62] to simulate the detector response to the resultant particles.

2.8.2 Event Generation

The creation of MC samples is done in distinct steps[38]. These steps are shown in diagram 2.11 and are explained in order below:

- Hard sub-process - the hardest sub-process is chosen by the user and only these events are simulated. This is to reduce computation time when only the rarer processes are of interest. Parton Distribution Functions (PDFs) and matrix elements are used to calculate cross-sections and produce accurate distributions. It is possible to apply selection cuts at this stage to ensure events are suitable for use, for example ensuring the products of the hard scatter are within an η range of interest.

- Parton shower - This step takes the particles emerging from the high-energy hard scatters and transforms them to the low-energy regime where non-perturbative QCD and confinement apply by successive emission of QCD radiation. All simulated partons (whether scattered, annihilated or created) are capable of emitting radiation.

- Hadronization - Hadronization can not be calculated from first principles. Instead different models are used to confine systems of partons into hadrons. For example PYTHIA8 uses the Lund String Model for hadronization while Herwig uses a cluster model[60, 64, 65].

- Particle decay - The decay of τ's and 'unstable' hadrons are simulated. A close relationship exists between the hadronization and decay stage, the hadronization model should be re-tuned when decay models are changed.

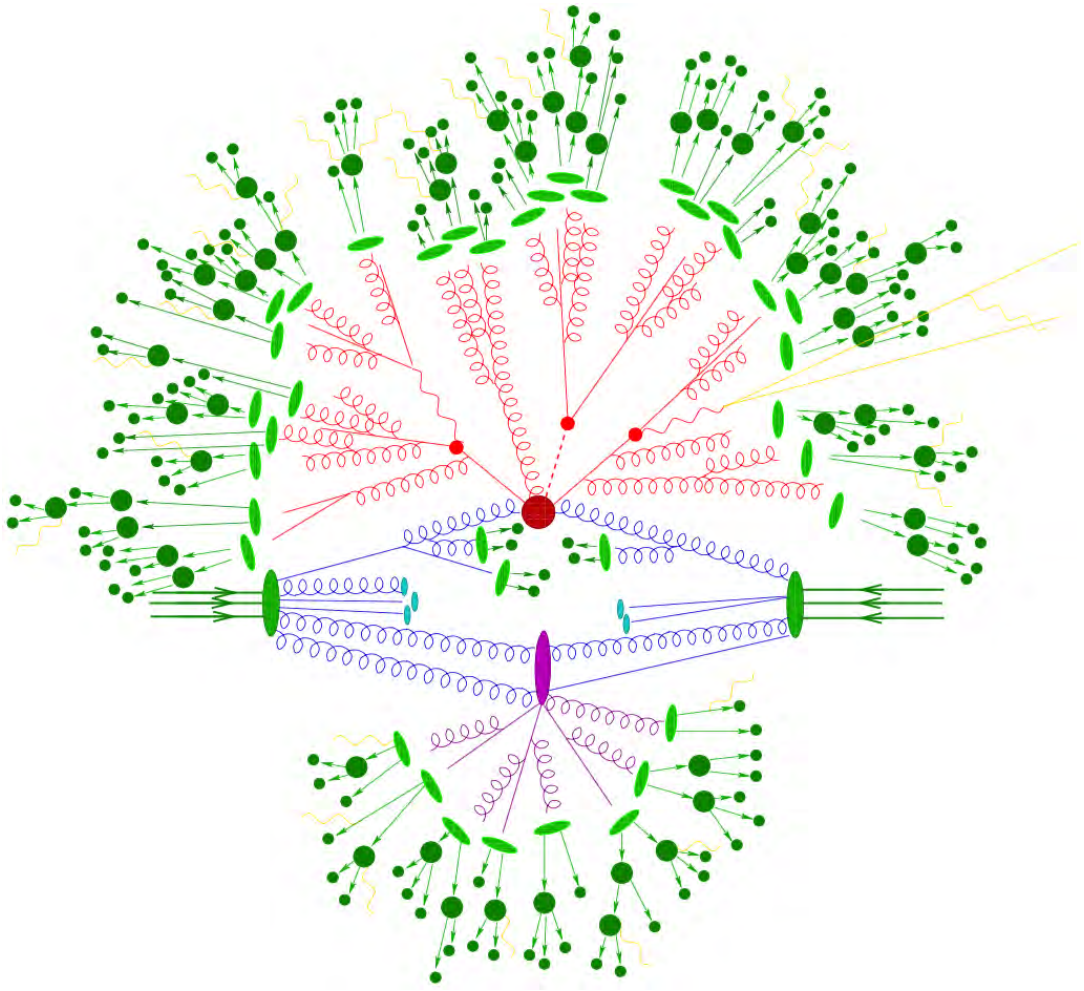

Figure 2.11: The stages of event generation using a $t\bar{t}H$ event as an example. The hard scatter (large red circle) is followed by the decay of the top quarks and Higgs boson (smaller red circles). Hadronization occurs at a later stage (light green ovals) before the hadronic decays are modelled (dark green circles). Other features visible include a secondary partonic interaction (purple oval) and leptonic decays and EM radiation (both yellow)[63].

- Underlying event - The simulation of the underlying event, which includes contributes from both hard and soft processes between the remaining partons of the scattering particles[66].

Following these steps a 'truth' sample can be created which is equivalent to a record of the particles entering the sensitive material of the detector. Usually one wishes to know how these particles would be interpreted if they were real data. Therefore one has to carry out additional steps. A short summary of these are[67]:

- Simulation of the response of the detector to the particles to produce 'HITS' files. This uses a detailed digital model of the detector, including the materials each component is constructed from, to calculate the probability of each particle interacting with it. GEANT4 is the standard software of choice for this step[62].

- Digitisation converts the simulated response of the detector into the same format of data that is read-out from the detector in real-life. In ATLAS, this is known as a 'RDO' file. In real collisions the detector readout would include pile-up[3] effects and to simulate this it is possible to overlay minimum bias events on MC in this step[68].

- Reconstruction of the 'RDO' file into the physics objects used in analyses. Simulated data should be reconstructed identically to real data and therefore the methods detailed in section 3.2.9.2 are followed.

2.8.3 PYTHIA

PYTHIA is a multi-purpose event generator. The main MC samples used by the analysis presented in this thesis are generated using the current version of it,

[3]Pile-up is the term used to describe hard scatters that occur in addition to the main one of interest. In-time and out-of-time pile-up refers to collisions from either the same or previous bunch crossings respectively.

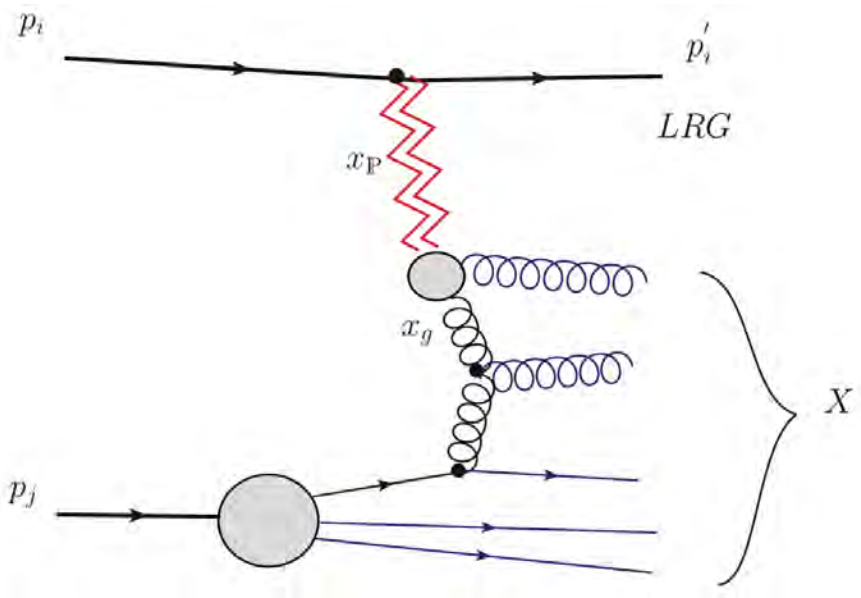

Figure 2.12: A Feynman diagram showing the method that PYTHIA follows for modelling SD in its high mass region. The proton p_i emits a Pomeron with momentum $x_{\mathbb{P}} = \xi$. The Pomeron interacts with proton p_j, modelled using PYTHIA's perturbative framework[69].

PYTHIA8[60]. Therefore its description of SD will be briefly detailed here with more details available elsewhere[69, 70, 71].

The total cross-section follows the Donnachie and Landshoff fits summarised in equation 2.33[48]. By default the diffractive and elastic components of the cross-section follow the Schuler and Sjöstrand model[72, 73]. The non-diffractive component is subsequently inferred as:

$$\sigma_{ND} = \sigma_{Tot} - (\sigma_{El} + \sigma_{SD} + \sigma_{DD} + \sigma_{CD}). \tag{2.45}$$

When generating a diffractive event PYTHIA effectively convolutes the Pomeron flux from one proton and the Pomeron-proton cross-section. This is shown in figure 2.12. Proton p_i emits a Pomeron which interacts with proton p_j. The Pomeron is assumed to be independent of its parent proton and is modelled using the Ingelman-Schlein approach i.e. as a hadronic state[74]. The Pomeron PDF is obtained from H1 data[75]. The proton-Pomeron collision is then modelled using PYTHIA's perturbative framework for semi-hard interactions, and probability distribution functions

set the values of t and M_X. The cross-section is then calculated as[69]:

$$\frac{d^2\sigma_{SD}}{dtd\xi} = \frac{g_{3\mathbb{P}}}{8\pi}\beta^3_{\mathbb{P}P}\frac{1}{\xi}e^{B(\xi)t}F_{SD}(\xi). \tag{2.46}$$

The value of the triple Pomeron coupling term, $g_{3\mathbb{P}}$, is calculated from data. $\beta^3_{\mathbb{P}P}$ is the proton-Pomeron coupling and F_{SD} is a ξ-dependent 'fudge factor' to account for behaviour outside of the triple Regge limit.

The default SD model in PYTHIA8 uses the Schuler and Sjöstrand (SS) Pomeron flux factor: a simple $\frac{1}{\xi}$ dependence as shown in equation 2.46. Other models are available, one of which is the Donnachie and Landshoff (DL) flux factor, which follows the ξ dependence predicted by the triple Pomeron cross-section (equation 2.39) and so uses $\frac{1}{\xi}^{2\alpha_{\mathbb{P}}(t)-1}$ with the default value $\epsilon = 0.085$[69, 60].

2.9 Recent ATLAS results on SD at $\sqrt{s} = 8$ TeV

The analysis presented in this thesis measures the SD cross-section at $\sqrt{s} = 13$ TeV. It follows on from an analogous analysis at $\sqrt{s} = 8$ TeV. The same detector components and many of the methods presented here were used by, if not developed by, the $\sqrt{s} = 8$ TeV analysis team. Since the author was part of the analysis team and due to its relevance to the main analysis, the unfolded results from the $\sqrt{s} = 8$ TeV analysis are summarised here. The details of the analysis are not discussed; many of them overlap with what is presented later in the thesis, but they are well described in other sources[3, 50, 76]. The fiducial region of the measurement was $-4.0 < \log_{10}\xi < 1.6$ and $0.016 < |t| < 0.43$ GeV^2.

The rapidity gap distribution, defined for charged particles with $P_T > 200$ MeV is shown in figure 2.13. The expected flat plateau is visible in the central region. The excess of events at low gaps is due to 'stacking up' (see figure 4.2 for an explanation). The result in figure 2.13 is compared to the A2 and A3 tunes of PYTHIA8 and a Herwig7 sample (using the default tune in version 7.1.3)[61, 77, 78]. All MC event

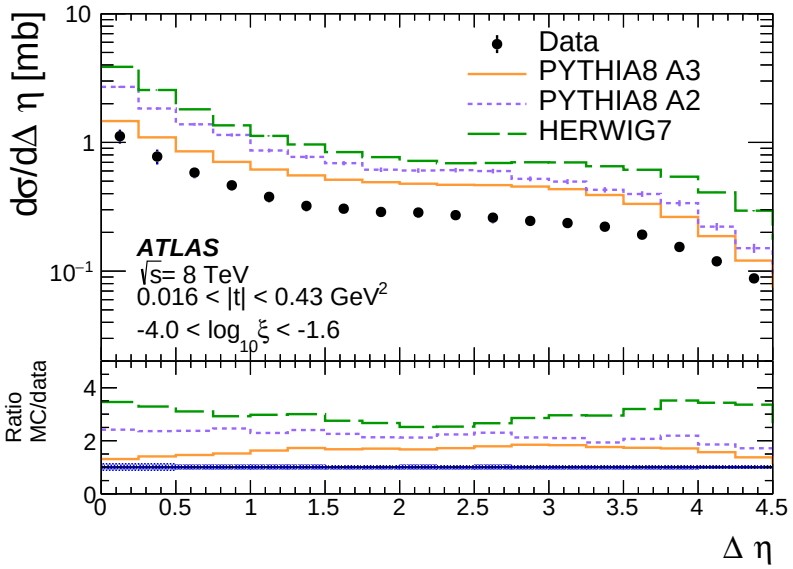

Figure 2.13: Hadron level differential cross-section as a function of $\Delta\eta$. Error bars show the statistical and systematic uncertainties added in quadrature[3].

generators show reasonable shape agreement with data but poor normalisation. The worse normalisation in Herwig7 may be due to its default modelling of diffraction which includes contributions from both SD and DD as part of its global event mix. There is no $\sqrt{s}$ dependance in the Herwig7 diffractive model, which is based on both 'A Toroidal LHC Apparatus' (ATLAS) and 'Compact Muon Solenoid' (CMS) results using rapidity-gap techniques and $\sqrt{s} = 7$ TeV data[79].

Figure 2.14 shows the $|t|$ distribution. As expressed in equation 2.41 the distribution is expected to follow a fast-falling exponential. To avoid bias in the fit from this in the binning of the data, the points are plotted at the mean $|t|$ values for each bin instead of bin centres. The fit shown in figure 2.14 is $d\sigma/dt \propto e^{Bt}$. This yields a result of $B = 7.65 \pm 0.26(\text{stat.}) \pm 0.22(\text{syst.})$ GeV^{-2}, compatible with the predictions of both the DL and SS flux factors contained in the different PYTHIA8 tunes.

Figure 2.15 shows the hadron level $\log_{10}\xi$ distribution, reconstructed from the diffractive system (see equation 2.18). The data points are consistent with a flat differential cross-section. By integrating equation 2.41 over the fiducial $|t|$ range,

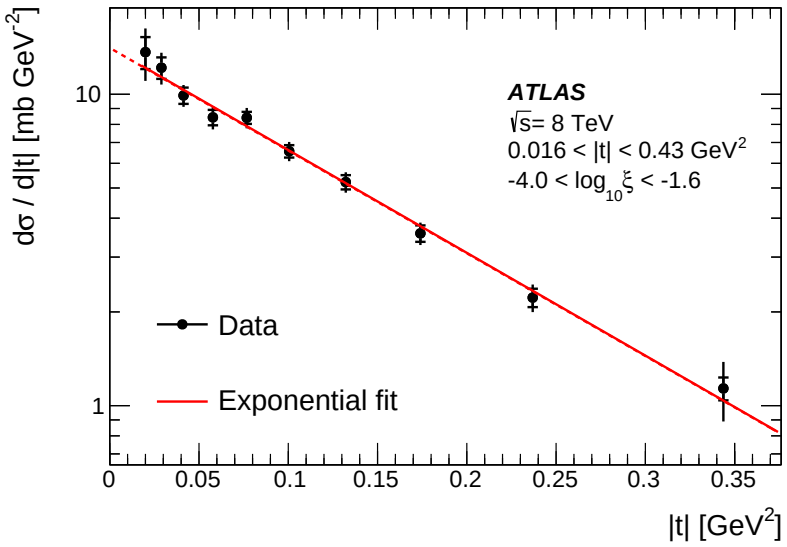

Figure 2.14: Hadron level differential cross-section in $|t|$. Statistical error bars are shown with inner errors bars. Statistical and systematic uncertainties, added in quadrature, are shown by the outer error bars[3].

one expects the differential cross-section to follow:

$$\frac{d\sigma}{d\xi} \propto \left(\frac{1}{\xi}\right)^{\alpha(0)} \times \frac{e^{Bt_{\text{high}}} - e^{Bt_{\text{low}}}}{B}. \tag{2.47}$$

This equation is fitted to the data distribution, using the measured value of B, yielding a value of $\alpha(0) = 1.07 \pm 0.02(\text{stat.}) \pm 0.06(\text{syst.}) \pm 0.06(\alpha')$. The additional uncertainty is due to the 100% error on the assumed value of $\alpha' = 0.25$ GeV^2. This result is comparable to the predictions from PYTHIA8 of 1.14 and 1.00 from the A3 and A2 tunes, respectively.

Within the fiducial range the cross-section was measured to be 1.59±0.13(stat. + syst.) mb. Having measured the B parameter, it was then extrapolated over the full t range. The cross-section is compared with the predictions from MC in table 2.1.

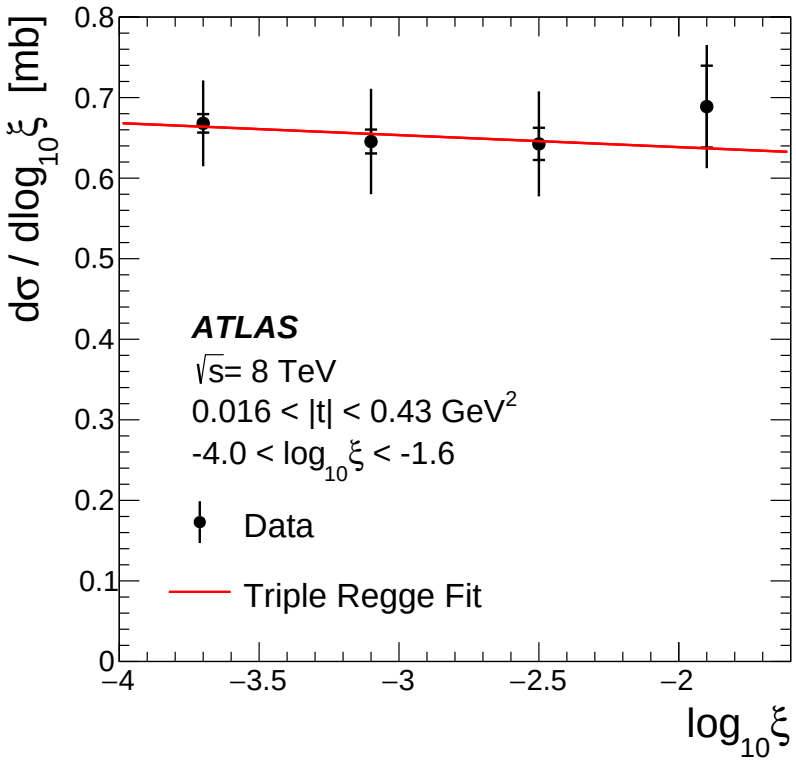

Figure 2.15: Hadron level differential cross-section in $\log_{10}\xi$. Error bars are shown as in figure 2.14[3].

Table 2.1: The measured SD cross-section compared with that predicted by MC[3].

Distribution	$\sigma_{SD}^{\text{fiducial}(\xi,t)}$ [mb]	$\sigma_{SD}^{\text{all } t,\ \text{fiducial}(\xi)}$ [mb]
Data	1.59 ± 0.13	1.88 ± 0.15
PYTHIA8 A2 SS	3.69	4.35
PYTHIA8 A3 DL	2.52	2.98
Herwig7	4.96	6.11

CHAPTER 3

ATLAS and the LHC

This chapter introduces the LHC briefly and then provides details on ATLAS. The performance of its different components will be outlined and explanations will be given on how they are used to identify the physics objects in the analysis presented in this thesis.

3.1 LHC

The 'Large Hadron Collider' (LHC) is a particle accelerator designed to accelerate protons to 7 TeV and subsequently collide them at a centre of mass energy of $\sqrt{s} =$ 14 TeV and an instantaneous luminosity of 10^{34} cm^{-2} s^{-1}. The first protons were accelerated round the LHC on 10th September 2008 but a cryogenic problem soon after required repair work and commissioning was delayed. $\sqrt{s} = 7$ TeV collisions were first achieved on 30th March 2010. Two of the LHC detectors, ATLAS[80]

and CMS[81], simultaneously announced the discovery of a particle consistent with the standard model Higgs boson at a mass of 125 GeV on the 4th July 2012[82, 83]. Since then the physics programme has continued with a second run. The LHC has not yet reached its design energy, the highest collision energy achieved for proton-proton collisions so far is $\sqrt{s} = 13$ TeV, the nominal collision energy during its second run period. Some of the successes from run2 include LHCb's observation of pentaquarks[29], ATLAS's observations of light-by-light scattering in $Pb + Pb$ collisions[84] and Higgs production in assosicaition with vector bosons in $p + p$ collisions[85]. On 3rd December 2018 this run period ended and Long Shutdown 2 (LS2) began in preparation for upgrade work. Refer to chapter 10 for more details on the LHC and ATLAS upgrades.

The collider is situated underground below the French-Swiss border in a tunnel 26.7 km in circumference, used previously by an e^+e^- collider, the 'Large Electron Positron' (LEP) collider. It forms part of the 'European Laboratory for Particle Physics' (CERN) accelerator complex as shown in figure 3.1. A chain of accelerators from this complex are used to prepare protons for injection to the LHC. The source of protons is a tank of hydrogen from which the atoms are ionised. Linear Accelerator 2 (LINAC2), which was shutdown to be replaced in November 2018, was the first accelerator in the chain and reached 50 MeV before the protons entered the Proton Synchrotron booster (PSB). In the PSB the protons reached 1.4 GeV and subsequently the Proton Synchrotron (PS) increased the energy to 26 GeV. The last accelerator before the LHC is the Super Proton Synchrotron (SPS) in which the protons reached an energy of 450 GeV before LHC injection. Many of the accelerators, as well as supplying the LHC, are used by other experiments. For example, North Area 62 (NA62) is a fixed target kaon decay experiment that uses protons from the SPS[86].

Radio-frequency (RF) cavities rapidly apply alternating electromagnetic fields to accelerate the beams of protons. The LHC uses over 50 different types of magnet to operate. 1232 dipole magnets bend the path of the beams of protons and they are focused using sets of quadrupole magnets. There are also higher order magnets

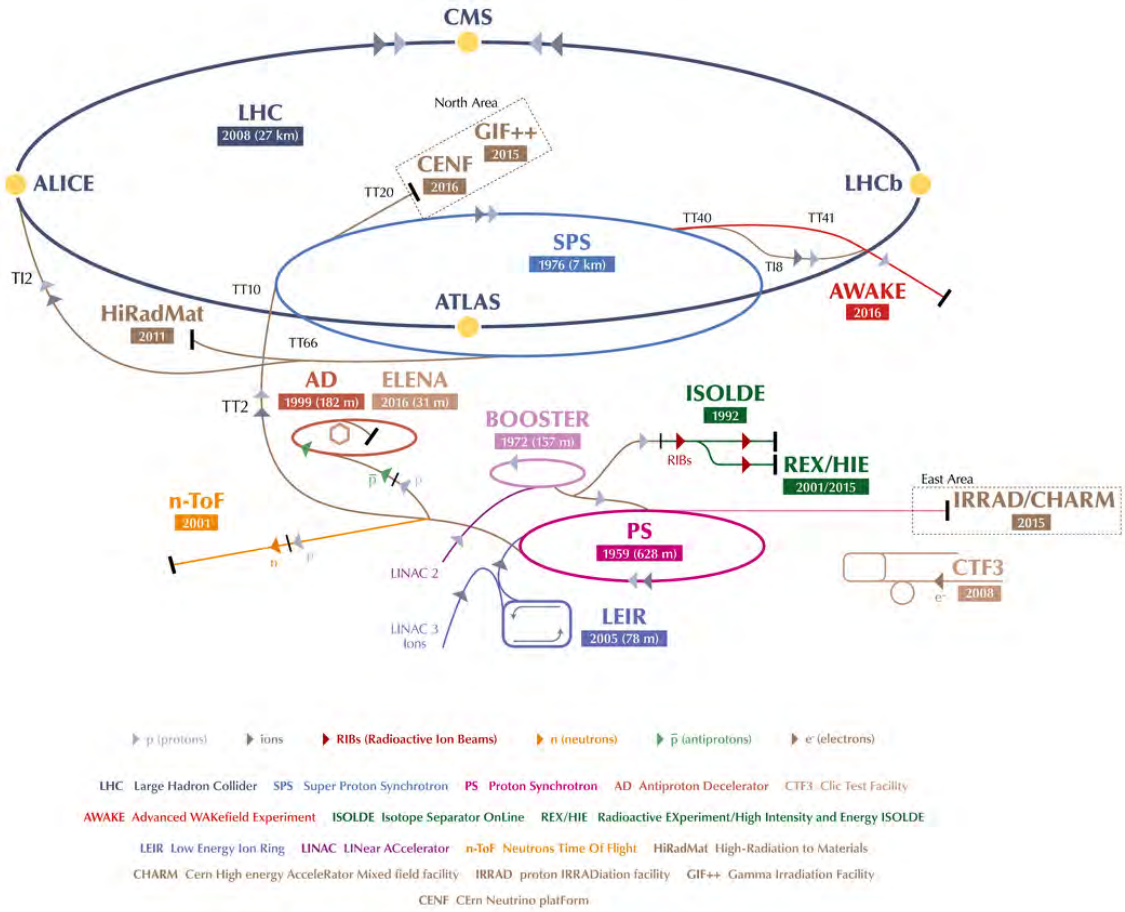

Figure 3.1: The CERN accelerator complex [87].

(sextuples, octupoles and decapoles) that make small corrections to the fields. On either side of the interaction points, sets of quadruples, known as triplet magnets, focus the beams of protons to provide a high rate of interactions. $\beta*$, the amplitude function of the beam at the interaction point, is a measure of how focussed the beam is and so depends on the configuration of the accelerator magnets[35]. A small $\beta*$ indicates highly focused beams, which is preferable for high luminosity running.

The alternating RF cavities result in bunches of protons, instead of continuous beams. Segments which could potentially contain protons are referred to as 'buckets' and not every bucket is filled. For example, empty buckets are required to dump the beam without damaging LHC infrastructure. A 'filled' bunch crossing therefore refers to two filled RF buckets passing through the Interaction Point (IP) simultaneously and can result in no, single or multiple collisions. The average number of interactions per bunch crossing is usually denoted $\langle\mu\rangle$.

There are 4 LHC IPs and consequently 4 detectors. There are two general purpose detectors at the LHC: CMS[81, 88, 89] and ATLAS, and 2 more specialised experiments that run at lower instantaneous luminosities, 'Large Hadron Collider beauty' (LHCb)[90, 91] and 'A Large Ion Collider Experiment' (ALICE)[92, 93].

3.2 ATLAS

The ATLAS detector is nearly hermetic, that is to say that it provides coverage across a solid angle of almost 4π. It consists of multiple detector systems, with the outer systems enclosing the inner ones. The detector design and performance are described in detail in [94]. Starting from the interaction point within the beam-pipe, the major detector systems and their purposes are:

- The Inner Detector (ID) tracking systems for resolving the tracks deposited by charged particles, measuring their momenta and identifying the position of vertices.

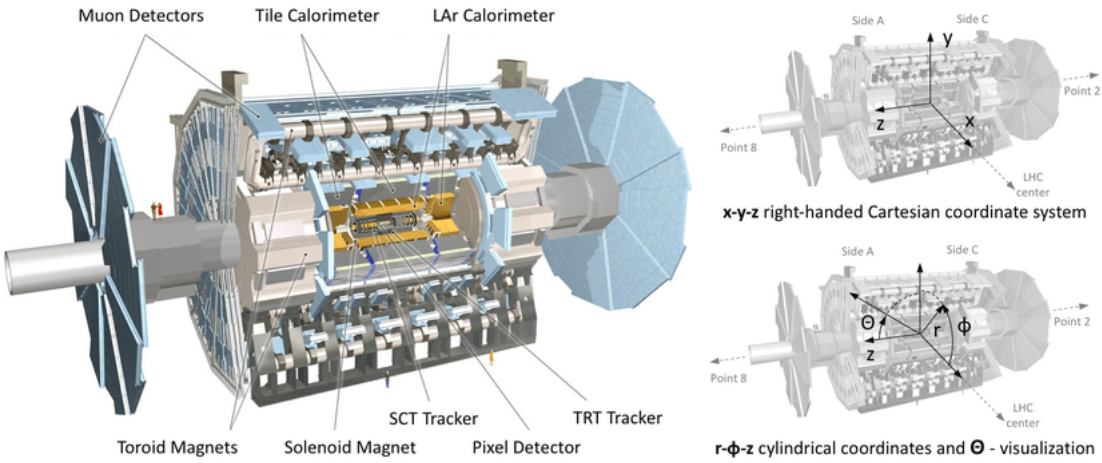

Figure 3.2: The major components of ATLAS detector and the coordinate systems used[95].

- The Electromagnetic Calorimeter (ECAL) for absorbing and measuring the energy of charged leptons, photons and early-showering hadrons.
- The Hadronic Calorimeter (HCAL) for absorbing and measuring the energy of hadronic jets.
- The muon spectrometers and toroid magnets for resolving the tracks of muons and measuring their momenta.

The arrangement of these systems is shown in figure 3.2. A cross-section of the detector and the typical response to some particles is shown in figure 3.3. The major detector components, in addition to more minor ones relevant to the analysis presented in this thesis, are described in more detail below.

3.2.1 Coordinate system

The coordinate system used to describe the ATLAS detector uses the nominal IP as the origin. In an x, y and z coordinate system, the z axis is in line with the beam-line. The positive and negative values are defined as the 'A' and 'C' side of the detector respectively. The x axis is then defined as the horizontal line perpendicular to the z axis with the positive values being towards the centre of the LHC ring. The

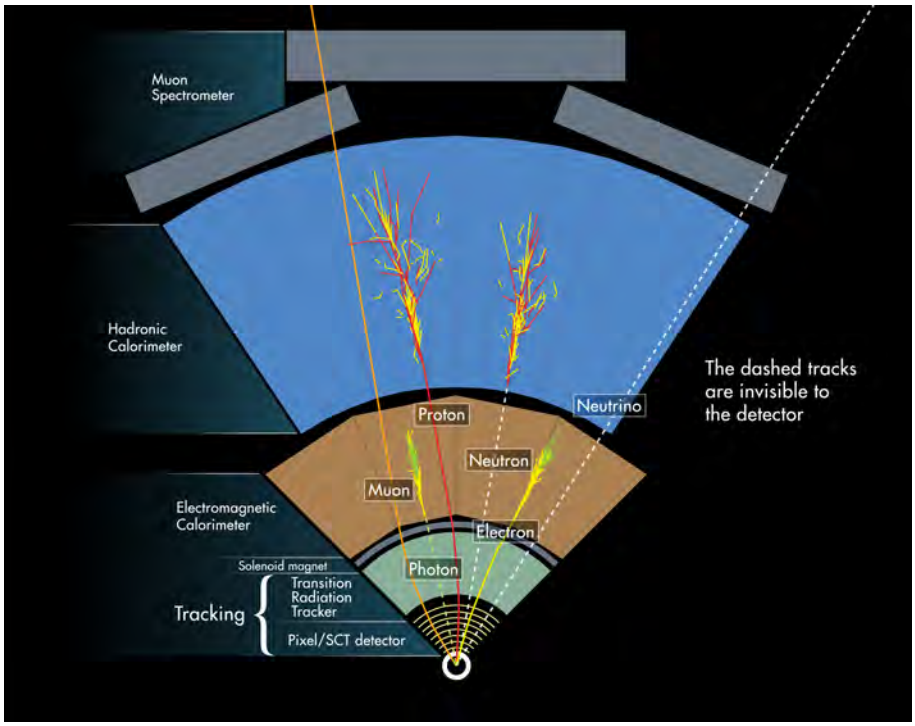

Figure 3.3: The ATLAS detector and its interaction with different types of particles. Neutrinos are identified from missing transverse momentum[96].

y axis is the vertical line going through the IP. Figure 3.2 shows a diagram of the ATLAS detector with the axes superimposed.

A polar coordinate system (r, θ, ϕ) is also used. The coordinate r is defined as $r = \sqrt{x^2 + y^2}$. The polar angle θ is then defined on the $r - z$ plane with respect to the positive z axis. The azimuthal angle ϕ is defined on the $x - y$ plane with respect to the positive x axis. Due to the usefulness of pseudorapidity, defined in section 2.2, (η, ϕ) coordinates are often used to describe positions within ATLAS.

3.2.2 Inner detector and solenoid magnet

To enable the reconstruction of ionising tracks deposited by charged particles, ATLAS uses a series of tracking detectors enclosed in a solenoid magnet. The reconstructed tracks are of interest themselves and are also used in the reconstruction of primary vertices, from the initial pp interaction. Secondary vertices, originating from the decay of very short-lived particles produced in the pp interaction, can also be re-

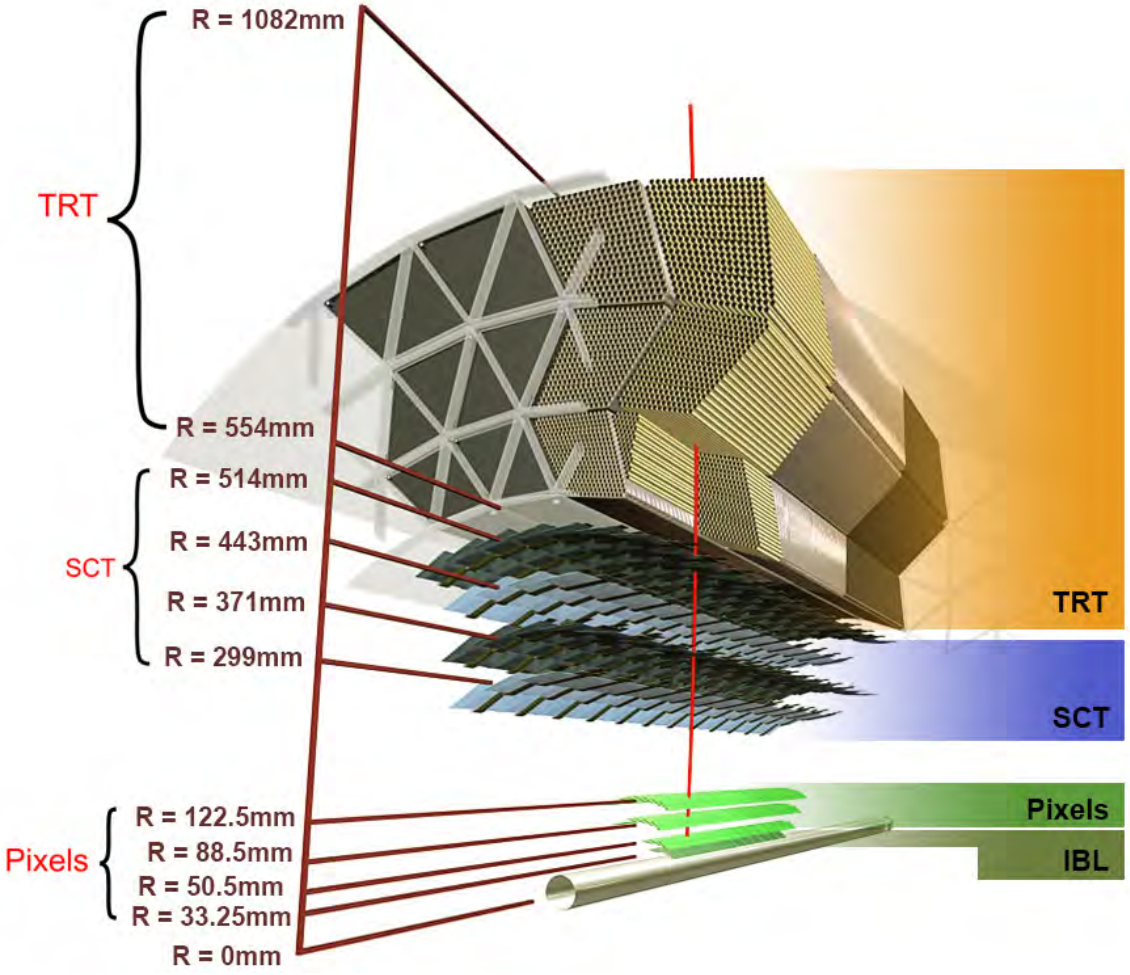

Figure 3.4: The ATLAS Inner Detector (ID)[99].

constructed. The inner-most components offer the highest granularity - the pixel detector and the Semi-Conductor Tracker (SCT). Further from the beam-pipe the Transition Radiation Tracker (TRT) provides additional tracking points using straw tubes. Collectively these components are known as the Inner Detector (ID) and provide coverage for ionizing tracks up to $\eta = 2.5$[97, 98]. A diagram of the inner detector is shown in figure 3.4 and the separate components are further detailed below.

The pixel detector consists of 4 cylindrical layers and 3 End Cap (EC) disks constructed from semiconductor pixel technology, labelled in green in figure 3.4. In Long Shut-down 1 (LS1) a smaller beam-pipe and the Insertable B-Layer (IBL) were installed, introducing the fourth layer of pixels closer to the beam-line with the pur-

pose of making the ID more robust to ageing and pile-up effects. The fine resolution and proximity of the inner layer to the beam-line also improves the discrimination of secondary vertices and the identification of short-lived particles, including the bottom quark, hence the name of Insertable B-Layer[98]. The 80 million pixels that comprise the pixel detector are constructed from silicon and segmented in $R\phi$ and z to provide a 3D space-point from each hit[98]. The outer 3 cylindrical layers have a position resolution of $\sigma_{R\phi} = 12\mu$m and $\sigma_z = 66\mu$m. The resolution for the end-caps is $\sigma_R = 66\mu$m and identical resolution in $R\phi$ to the end-caps[97].

The SCT, the blue component in figure 3.4, consists of 4 layers of silicon micro-strips and 9 EC disks on either side. The strips provide a measure of $R\phi$ and z due to the small angle stereo arrangement. The resolution for the barrel layers is $\sigma_z = 580\mu$m and for the ECs is $\sigma_R = 580\mu$m. The resolution of $\sigma_{R\phi} = 16\mu$m is identical for both[97].

The TRT, the orange component in figure 3.4, is constructed from layers of straw tube trackers arranged in such a way that each charged particle should traverse 36 straws. The large number of straws counteract the poor resolution per point ($\sigma = 170\mu$m) and in total are equivalent to a single point with resolution of $\sigma \leq 50\mu$m[97].

A solenoid magnet encloses the inner detector with the Tile Calorimeter (TileCal) also acting as a return yoke. The 2T magnetic field deflects charged particles to enable the calculation of their momenta. The bare solenoid is 44 mm thick (equivalent to $0.63X_0$[1] at $\eta = 0$) and is designed to be as thin as possible to maintain the resolution of calorimeter measurements[100][101].

3.2.3 ECAL

The ATLAS calorimeters consist of 2 distinct systems designed for the measurement of different types of particles. The Electromagnetic Calorimeter (ECAL) is designed to stop and measure the P_T of electrons and photons. It consists of the barrel, inner

[1]See section 10.1 for an explanation on radiation legnths (X_0) and interactions lengths (λ).

end-cap, outer end-cap and a Forward Calorimeter (FCAL).

The barrel calorimeter provides coverage in the central region $|\eta| < 1.475$. It is constructed from lead absorber and uses Liquid Argon (LAr) as a sampler. The electrodes are accordion shaped, as shown in figure 3.5. This figure also shows the 4 different sampling layers. The pre-sampler is a thin layer of LAr sampler used to correct for energy losses due to dead material in the ID and solenoid magnet. There are then 3 longitudinal layers. The first sampling is $6X_0$ thick[2] with its granularity[3] (0.003×0.1) finely split in the η direction. The second sampling is the thickest ($16X_0$) with square shaped cells (0.025×0.025). The third sampling is thinnest ($3X_0$) and has the coarsest granularity (0.05×0.025). The purpose of the granularity and longitudinal segmentation design is to improve π_0 rejection[101].

The inner and outer end-caps provide ECAL coverage in the region $1.375 < \eta < 2.5$ and $2.5 < \eta < 3.2$ respectively. Both end-caps also use lead-LAr sampling technology with an accordion structure. The inner end cap samplings provide a granularity similar to that in the barrel with a pre-sampler within $|\eta| < 1.8$. The outer end cap provides 2 longitudinal samplings both with reduced granularity (0.1×0.1).

FCAL1 provides coverage in the region $3.0 < \eta < 4.9$ and uses copper rods, parallel to the beam axis, with LAr sampling. It is integrated into the end-cap cryostat and positioned 4.7m away from IP. The irradiation doses are a lot worse at higher rapidities. The predicted radiation dose the FCAL receives is 5×10^6 Gy per year and a neutron flux of 10^9 cm^{-2}s^{-1}[101]. The cylindrical shape of the copper electrodes mean it does have worse spatial resolution of approximately 0.2×0.2[102].

The fractional resolution of energy measurements varies throughout the ECAL. The best resolution is in the barrel which is designed to be $\frac{\sigma_E}{E} = \frac{10\%}{\sqrt{E}} \oplus 0.7\%$[103]. The FCAL has the worst resolution. Test beam data showed measured its resolution to be $\frac{\sigma_E}{E} = \frac{0.285}{\sqrt{E}} \oplus 0.035$[101].

[2]Radiation lengths here are quoted for $\eta = 0$.
[3]Using $(\eta \times \phi)$ coordinates

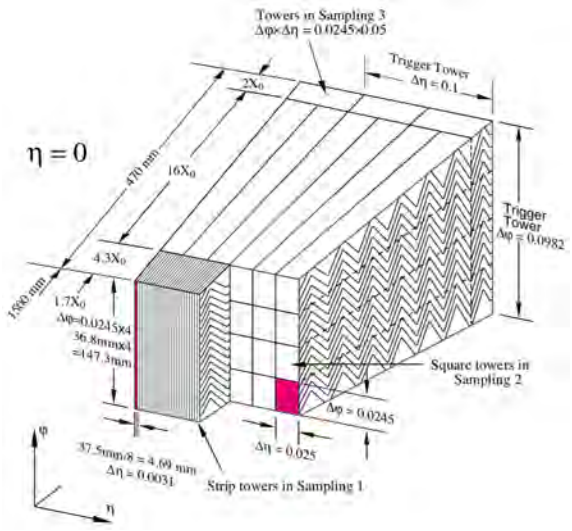

Figure 3.5: Barrel ECAL structure[101].

3.2.4 HCAL

The HCAL is designed to detect neutral and charged hadrons. It consists of the barrel and extended barrel of the Tile Calorimeter, the Hadronic End-Cap and 2 FCALs.

The TileCal provides detector coverage within $|\eta| < 1.6$. It is a non-compensating calorimeter, using steel and scintillating tiles as the absorber and active material respectively. It is split into three longitudinal layers. The first two are 1.4λ and 3.9λ thick and both have a granularity of (0.1×0.1). The third layer is 1.8λ thick with a reduced granularity of (0.2×0.1). At $|\eta| = 1$ the TileCal is split into the barrel and extended barrels with a 60 cm gap allowing for electronic services needed for the ID and ECAL. The steel also acts as a return yoke for the solenoid magnet[104].

The Hadronic End-Cap (HEC) provides coverage in the region $1.5 < \eta < 3.2$ and uses the same LAr sampling technology as the ECAL barrel and ECs. It has two sampling layers with copper plates used as the absorber material. In the central region the granularity matches that of the first 2 TileCal layers, reducing to (0.2×0.2) beyond $|\eta| = 2.5$[101].

FCAL2 and 3 are similar to the ECAL FCAL1 using LAr sampling and rods parallel

to the beam-line. The absorber rods however are constructed from tungsten. The coverage begins at $\eta = 3.1$ and 3.2 and continues to $\eta = 4.9$. The total depth of the two FCAL modules is 9.5λ[104].

The HCAL is designed to have a resolution for energy measurements of jets to be better than $\frac{\sigma_E}{E} = \frac{50\%}{\sqrt{E}} \oplus 3\%$ within $|\eta| < 3$[104].

3.2.5 Muon spectrometer and toroid magnets

The outermost component of ATLAS is a spectrometer to detect and measure the momenta of muons up to $|\eta| = 2.7$. It is designed to do this with a resolution of up to 10% for muons with $P_T \approx 1$ TeV. Magnetic fields are provided by 8 air-core superconducting toroidal magnets in the barrel region ($|\eta| < 1$) and smaller end-cap magnets in the outer region ($1.4 < |\eta| < 2.7$). 3 layers of Monitored Drift Tubes (MDTs) are able to make up to 24 measurements of the η position of tracks. Up to $|\eta| = 1$, the ϕ measurements are made by the Resistive Plate Chambers (RPCs) which also provide trigger signals. Outside the coverage of the RPCs the Thin Gap Chambers (TGCs) provide the same capabilities up to $|\eta| = 2.4$. Due to high background rates, above $|\eta| = 2$ Cathode Strip Chambers (CSCs) are used for η measurements of tracks. The resolution for single hits varies across the different systems within $60 - 80\mu$ m[105].

3.2.6 MBTS

The Minimum Bias Trigger Scintillator (MBTS) was designed to be used for triggering during early low luminosity fills in run1. After the first three to four months it was expected the scintillator performance would degrade and the MBTS would be of no more use[106]. However, its performance remained sufficient much longer than expected and it proved useful throughout run1 for minimum bias triggering, secondary luminosity measurements[107] and highly efficient triggering during special

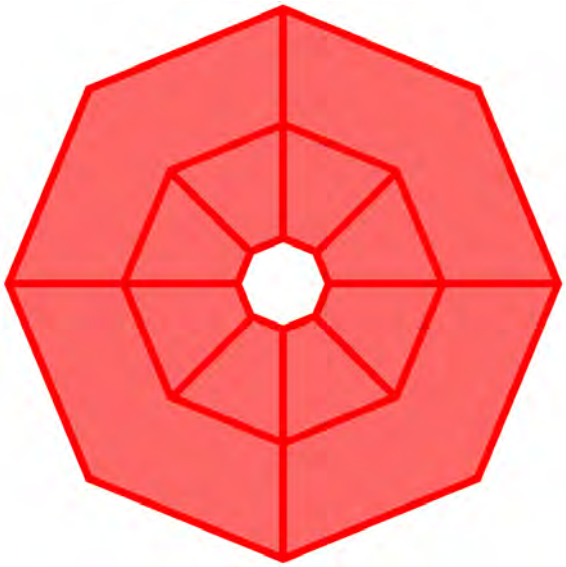

Figure 3.6: A diagram of the run2 version of the MBTS. The outer ring consists of 4 scintillator tiles and the inner ring consists of 8.

runs[108]. It was upgraded during LS1, prior to run2, and was again used during the first, low luminosity, fills at $\sqrt{s} = 13$ TeV and other special runs. The run2 MBTS consists of 2 cm thick scintillators positioned ~ 3.6 m away from the IP. The MBTS acceptance is within the range $2.08 \leq |\eta| \leq 3.86$. It is comprised of an inner ring of 8 tiles while the outer ring consists of 4 tiles[109]. A diagram of the MBTS is shown in figure 3.6.

3.2.7 ATLAS forward detectors

The ATLAS experiment uses a number of forward detectors for reconstructing particles at very high pseudorapidities that would otherwise fall outside the coverage of the components already discussed[110]. These are:

- LUminosity Cherenkov Integrating Detector (LUCID), situated ± 17 m away from the IP and providing detector coverage at $5.6 \leq \eta \leq 5.9$. LUCID is constructed from quartz photo-multipliers and intended for measuring both the integrated and per-bunch instantaneous luminosity[111]. During run2, LUCID provided the main online and offline luminosity measurements for ATLAS[112].

- Zero Degree Calorimeter (ZDC), when installed in position, is situated ±140 m away from the IP, providing detector coverage for neutral particles at $\eta \geq 8.3$. Its installation position is past the point where the LHC beam pipes are split into 2 after being merged for collisions. Neutral particles are not affected by the LHC magnets, continuing straight, and the ZDC is positioned in this region[113]. The ZDC is only used during heavy-ion runs of the LHC and is not installed permanently due to the very high radiation levels it would experience during standard high-luminosity running[114].

- ATLAS Forward Protons (AFP), the newest of the forward detectors positioned in Roman Pots (RPs) (see section 3.2.8 for an explanation on RPs) at ±206 m and ±214 m. It is designed for the tagging and measurement of forward protons in both standard run conditions as well as special LHC runs. 4 planes of silicon detectors in each detector provide resolutions of $\sigma_x = 10$ μm and $\sigma_y = 30$ μm. The same 3D silicon pixel technology is used as was developed for the IBL. In the stations closest to the IP, quartz Cerenkov detectors have also been installed with the aim of providing time of flight measurements[115].

- Absolute Luminosity For ATLAS (ALFA), the most forward detector and the one used in this analysis. It is therefore given a more thorough description in section 3.2.8 below.

3.2.8 ALFA

In chapter 2 the optical theorem was introduced to explain the relationship between the elastic and total cross-sections. The ALFA detector was originally designed to use this relationship to provide an absolute measurement of the luminosity by measuring intact protons scattered at small angles (~ 10 μrad)[116].

ALFA consists of 8 detectors, each housed in a Roman Pot (RP), a special movable housing constructed from thin stainless steel and positioned within the primary LHC

vacuum. The RPs remain in a retracted position, away from the beam pipe, until stable beams have been established. Following this they can be inserted in steps of 5 μm allowing the sensitive systems to get as close to the beam line as possible and ensuring the maximum coverage possible. The movement of the RPs is shown in figure 3.7a. The edges of the RPs that the beam is expected to cross are designed to be as thin as possible to reduce proton showering. The closest edge to the beam-line is also designed to be extremely thin to allow it to move the detector as close to the beam as possible, typically as close as 10σ of the beam transverse extent, where σ is the width of the beam envelope. Due to the thin walls, a secondary vacuum is maintained on the inside of each RP.

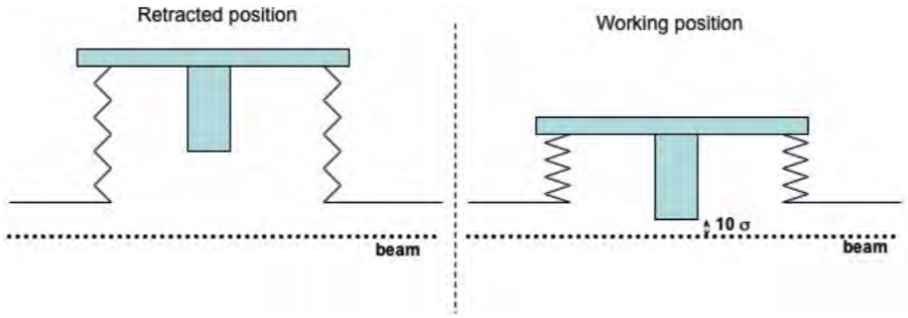

(a) The mechanical movement of a Roman Pot (RP). The RP itself is blue[116].

(b) A side-on view of both the upper and lower RPs in a single ALFA station[116].

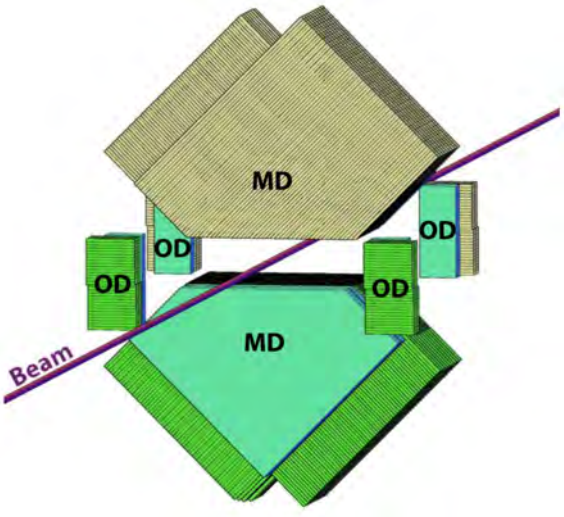

(c) A view of the scintillating fibres of both the upper and lower RPs in a single ALFA station. The main detectors (MD) and overlap detectors (OD) are labelled[117].

Figure 3.7: The layout of ALFA.

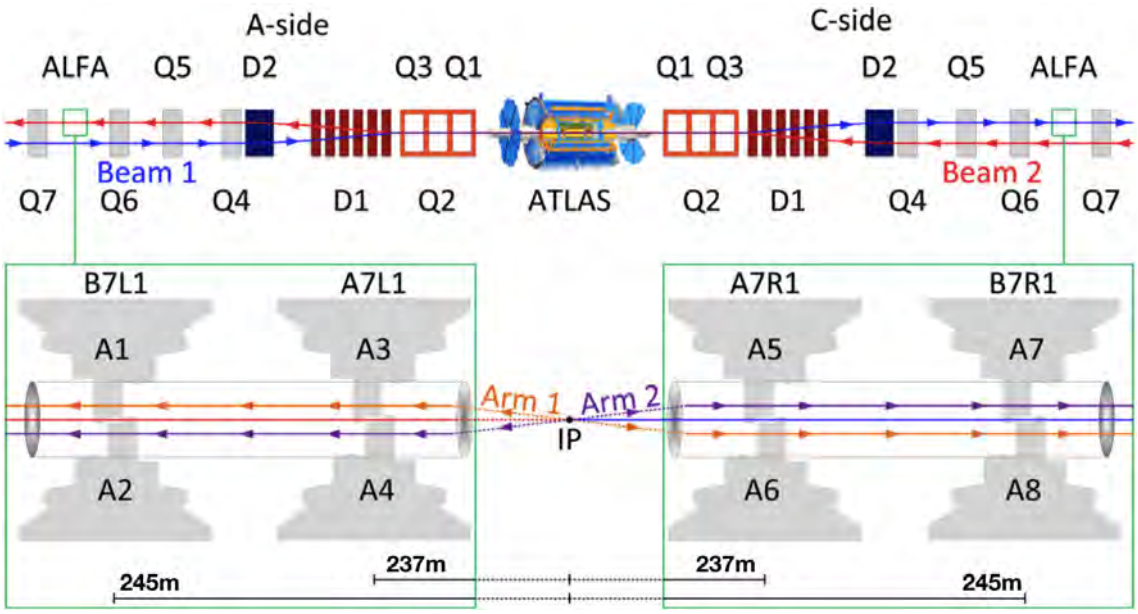

Figure 3.8: A diagram of the position of ALFA stations relative to the main ATLAS detector. Updated and adapted from [117].

Within each RP there is a main detector, 2 overlap detectors and trigger counters. This arrangement is shown in figure 3.7c.

The main detector in each RP consists of 10 titanium plates separated by 70μm. Each plate has a layer of 64 scintillating fibres mounted on either side. The 2 sets of fibres on a single plate are angled 90° to each other and 45° to the horizontal plane. They are referred to as u and v fibre and can be seen in figure 3.7c. Each scintillating fibre is 50μm wide and to minimise cross-talk across fibres each is given a thin aluminium coating. Test data have shown the position resolution of a reconstructed proton track to be 30μm for each RP. The high resolution is partially due to the staggering of subsequent fibres to reduce the overlap between gap regions[76]. The efficiency for a single layer to detect a proton was found to be 93%[116].

The overlap detectors are mechanically fixed to the main detectors positioned as shown in figure 3.7c. They are constructed in a similar manner to the main detectors with fewer plates per detector and fewer fibres per plate. Test data have shown them to have a position resolution of 50μm, slightly worse than the main detectors.

Triggering capabilities are provided by 3mm thick scintillator plates positioned on

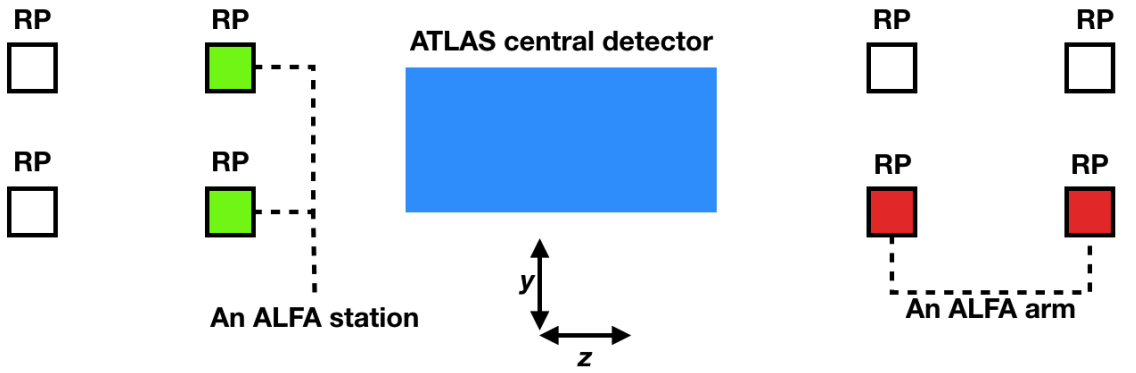

Figure 3.9: Each Roman Pot is labelled. A pair of RPs that share a common z coordinate are referred to as a station. A pair of RPs that share a y coordinate and are on the same side of the IP are referred to as an arm. Any individual RP can be described by a 3 letter acronym (i.e. AUF) indicating whether it's on the A or C of ATLAS, the Upper or Lower RP and at the Near or Far station. An arm can be described by a 2 letter acronym following the same convention.

a single side of the main and overlap detectors.

The 8 RPs are arranged in pairs above and below the beam-line at the same z coordinate, referred to as a station. There are 2 stations on either side of ATLAS. For run2 the near stations were positioned at $\pm$237m away from the IP and the far ones at $\pm$245m. This is shown in figure 3.8. If a particle is detected by ALFA it should leave tracks in two RPs; both the near and far RPs on a single side of ATLAS either above or below a beam-line. This is referred to as an arm. Figure 3.9 demonstrates these naming conventions, which will be used throughout the rest of this thesis.

Due to the movement of the RPs the positions of the sensitive detectors are not consistent between LHC fills. When the RPs are lowered into position both overlap detectors of the upper and lower RPs can detect the same protons allowing the calculation of their relative alignment. The alignment of RPs relative to the IP is calculated using elastically scattered protons, which are expected to have tracks back-to-back to each other[118].

3.2.9 Data taking and reconstruction

3.2.9.1 TDAQ

The recording of data is carried about by the 'Triggering and Data Acquisition' (TDAQ) system.

The nominal bunch crossing rate of the LHC is $\sim$ 40 MHz with the exact rate dependent on the filling scheme in use. ATLAS data can neither be read from the detector or recorded to disk at this rate. Therefore a trigger system is needed to reduce the data transfer rate to reasonable levels. During run2 (2015-18) ATLAS used a two-level trigger system. The Level-1 Calorimeter Trigger (L1CALO) is the first level of trigger, running on a hardware based system using low-granularity calorimeter data. The RPCs and TGCs of the muon spectrometer systems also provide data for level-1 triggering. The latency limit and maximum output rate of L1CALO are $\sim$ 2.5 μs and $\sim$ 100 kHz respectively. L1CALO is discussed in more detail in chapter 10.

When L1CALO accepts an event, Region of Interests (RoIs) are passed to the High Level Trigger (HLT). Here, latency limits are increased (to $\sim$ 200 ms) allowing more sophisticated algorithms to be run, making further selections. The maximum HLT output rate is $\sim$ 1 kHz[119]. A schematic diagram of the run2 trigger system is shown in figure 3.10.

To decrease trigger rates and ensure they fall below acceptable limits, E_T thresholds can be raised. If this increase would lead to a loss of physics performance the trigger can alternatively be prescaled to decrease the rate. This can be applied at either of the trigger levels and means only accepting a random subset of events that pass the trigger algorithm: for a prescale value of p only $\frac{1}{p}$ of events are accepted that pass the selection. Prescales can also be adjusted throughout a single run, for example as the instantaneous luminosity decreases trigger rates should also decrease. Therefore prescales can be decreased to maximise the acceptance of potentially interesting

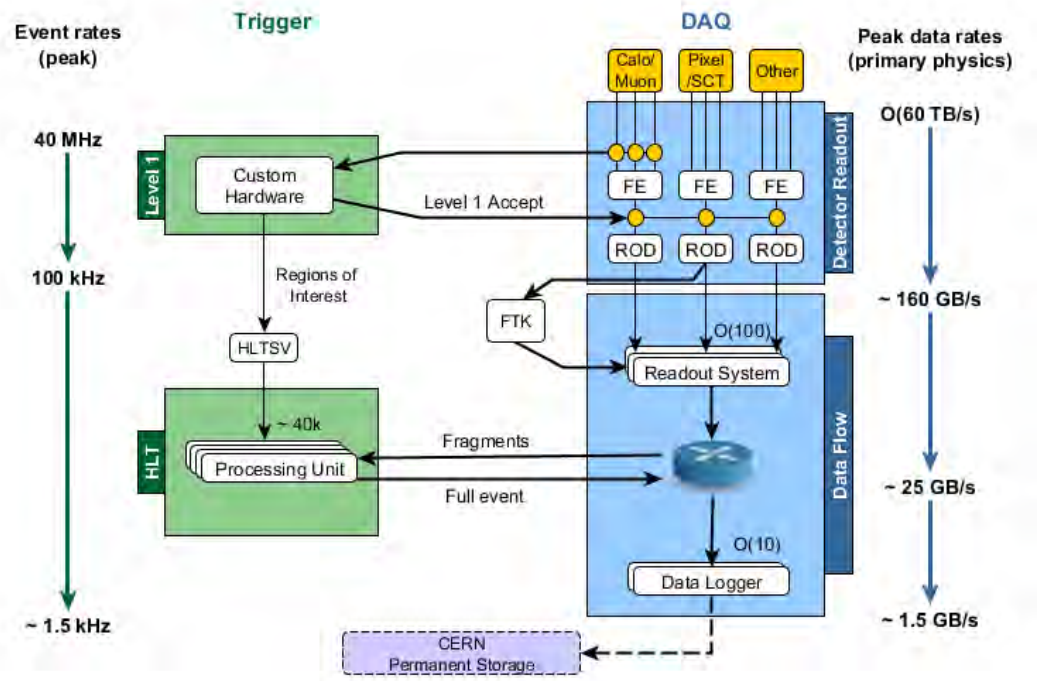

Figure 3.10: The schematic layout of the ATLAS run2 trigger system[120].

events.

Both levels of the trigger system have settings, referred to as a trigger menu. Most of the time the menu is kept consistent to reduce complications to physics analyses. They can be customised to accept different events, however. For the special run analysed in this thesis, standard physics triggers were switched off and a special diffractive menu was used. This is necessary due to ALFA not being in use during standard running. The distance between the ALFA detectors from the ATLAS cavern mean that latency settings also need adjusting from standard running ones.

3.2.9.2 Off-line reconstruction

Once an event has been accepted by the HLT the raw event data is read off and stored on tape at CERN. Events are then reconstructed using software on PC farms to identify what physics objects were present and measure their properties. Identical

reconstruction algorithms are also run on HITS files produced from the simulation step in MC production. Some of the algorithms used for the data studied in this analysis are outlined here.

Inner Detector tracks Tracks are reconstructed using an inside-out approach beginning with silicon hits in the ID. Clusters of hits in the silicon pixels and strips are converted into space points and those originating from pixel hits are used to seed the tracks. The space points arising from strips are then also considered and can be assigned to multiple tracks. Every track is giving a rating in the 'track scoring' step which is based on characteristics including χ^2 values. Following this step any ambiguous points are assigned to the tracks with higher scores and removed from the competing track. The track scores are then recalculated and tracks are vetoed if they do not reach a minimum value. The remaining tracks are then considered individually with all of the hits found in the TRT to form a complete track.

Full details of the standard algorithm are given in [121, 122]. However this analysis uses a looser algorithm, adapted for soft interactions. Tracks have lower transverse momenta than those originating from hard interactions and so less stringent requirements are used in reconstruction. For example the minimum P_T is lowered to 100 MeV compared to the standard minimum of $\sim$ 400 MeV. The full list of requirements is the same as that used in [123].

The P_T resolution is dependent on the particle's P_T and η. In 2018 data the resolution of the standard algorithm was unfolded from measurements in data. For low P_T, central tracks ($P_T < 1$ GeV and $0.2 < \eta < 0.4$) the transverse and longitudinal impact parameter resolution were measured as $\sigma_{d_0} = 95\mu$m and $\sigma_{z_0} = 167\mu$m respectively. The resolution improves for higher P_T tracks[124].

Primary vertices Primary vertices (PV) are reconstructed by iterative fitting using the ID tracks. Incompatible tracks are down-weighted between iterations and removed from the fit once it has converged. Excluded tracks are then used for the

reconstruction of additional vertices. This is repeated until it is not possible to find any more vertices with the remaining tracks[125]. The resolution of vertex reconstruction has been studied in $t\bar{t}$ MC without pile-up or beam-spot constraints. The resolution was $\sigma_x = \sigma_y = 11\mu$m and $\sigma_z = 24\mu$m[98].

ATLAS low-p_T vertex reconstruction requires 2 ID tracks with at least 100 MeV to form a PV. Like with the reconstruction of ID tracks this is a looser requirement compared to the standard algorithm.[123].

Topological clusters Topological clusters are 3D clusters reconstructed from calorimeter cells and designed to suppress the effects of pile-up and electronic noise. The significance of a cell is dependent on the energy (E^{EM}_{cell}) and the average expected noise ($\sigma^{EM}_{noise,cell}$) of the cell using the EM energy scale. It is calculated as:

$$\varsigma^{EM}_{cell} = \frac{E^{EM}_{cell}}{\sigma^{EM}_{noise,cell}}. \tag{3.1}$$

The clustering then proceeds as follows:

- Seeding - Potential seed cells are identified as cells with significance above the primary seed threshold ($|\varsigma^{EM}_{cell}| > 4$). These cells are the start of the proto-clusters.
- Growth - Cells are considered neighbours if they are directly adjacent and from the same calorimeter layer or have partial overlap and are from different calorimeter layers. Neighbour cells are added into the proto-cluster if they have significance above the threshold for growth control ($|\varsigma^{EM}_{cell}| > 2$). If this cell is part of another proto-cluster already the proto-clusters are merged. The growth step is repeated until there are no neighbouring cells that satisfy the condition. A final growth step is carried out a single time adding all neighbouring cells to the proto-cluster.
- Splitting - The clustering algorithm then identifies local maxima. These are cells with an E_T sampling which is a local maximum, has an EM contribution

that fulfils $E_{cell}^{EM} > 500$ MeV and at least four neighbour cells. If there is more than one local maximum in a single proto-cluster it will be split. Individual cells can be shared but only between 2 proto-clusters. The fraction of signal shared by a cell is decided by the cluster energy and the distance from the cell to the cluster centre.

Once a topological cluster has been formed it is interpreted as a massless pseudo-particle. Kinematic properties are calculated based on the energy of the cluster and its η and ϕ coordinates. The (η, ϕ) barycentre of the cluster is determined by an E_T weighting of all the cells.

Topological clusters can be seeded on, or include, cells with large negative E_T values. This should on average, and at a global level, cancel the effect of positive E_T clusters arising from positive fluctuations in calorimeter noise arising from out-of-time pile-up (collisions from previous bunch crossings)[126].

ALFA reconstruction The reconstruction of protons in ALFA is carried out in two distinct steps. The initial step is the reconstruction of track coordinates in the RPs. The latter step is the reconstruction of proton kinematics using the measured PV position and the track positions in RPs.

The design of ALFA and its track reconstruction method relies on the assumption that protons will be travelling perpendicular to the scintillating fibres. To reach any of the RPs the proton must be travelling at a negligible angle relative to the beam and therefore this is a reasonable assumption to make. For a track to be reconstructed there must be at least 3 fibres hit in each plane of an RP. The local detector (u and v) coordinates of the track will then be reconstructed independently of each other. The algorithm looks for the coordinates with the highest overlap between fibres as shown in figure 3.11. A small number of fibres will show signal due to beam-related backgrounds, cross-talk between fibres and electronic noise. It is possible for the algorithm to reconstruct several tracks. The efficiency for the reconstruction algorithm is estimated using a data driven method, presented in

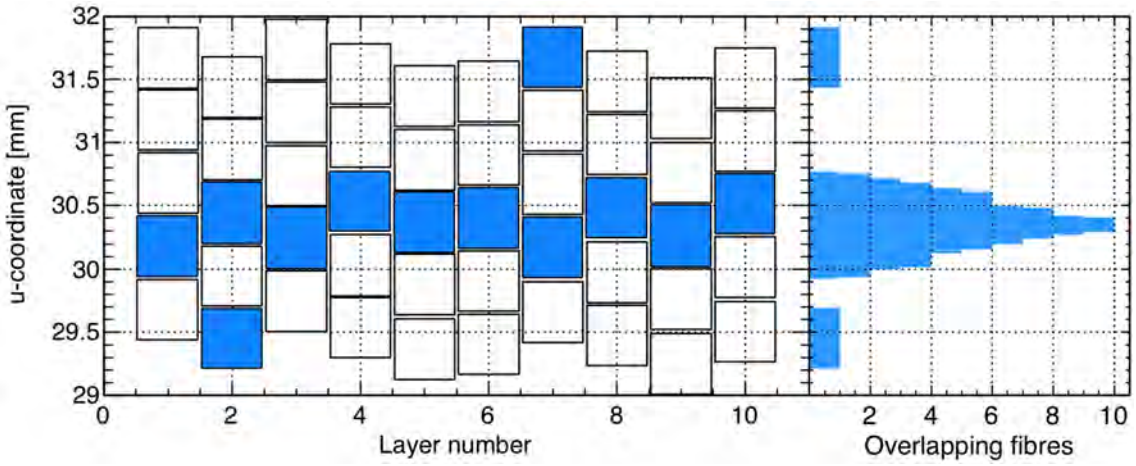

Figure 3.11: An example of the hit pattern of fibres for a single coordinate. If other requirement are also a met, a proton track is reconstructed with the u-coordinate matching the position of maximum overlap shown[117].

section 5.4.

The track coordinates are first converted between two local set of coordinates from (u and v) to (x and y). There are then converted to an ATLAS coordinate system (x, y and z) using the matrix equation shown in equation 3.2. θ_z, x_{Off}, y_{Edge}, D and y_{Off} are all constants calculated in the alignment procedure.

$$\begin{bmatrix} x_{beam} \\ y_{beam} \end{bmatrix} = \begin{bmatrix} cos\theta_z & -sin\theta_z \\ sin\theta_z & cos\theta_z \end{bmatrix} \begin{bmatrix} x_{Det} - x_{Off} \\ y_{Det} + y_{Edge} \end{bmatrix} + \begin{bmatrix} 0 \\ \frac{D}{2} + y_{Off} \end{bmatrix}. \tag{3.2}$$

The proton kinematics $(E, \vec{p})$ can then be reconstructed using the corrected ALFA track coordinates. The reconstruction package first needs to be tuned due to its dependance on the beam optics. This is done using MC techniques. MC simulated protons are transported to ALFA station positions using MAD-X software. This then shows where protons of different momenta should be measured by ALFA. Using this tuning, one can then reconstruct the proton energy and momenta for a set of ALFA tracks[28, 127].

3.2.9.3 Data storage

As already mentioned a copy of the original readout data from the detector is stored on tape at CERN. The fully reconstructed events with all of the physics objects are stored as Analysis Object Data (AOD) files. This data format is too large to be particularly useful for data analysis at different sites. More light-weight formats, called Derived Analysis Object Datas (DAODs) are produced, designed for different analysis needs. Data that is of no use to analyses are not copied across to the DAOD format. For example this analysis uses ALFA tracks but not reconstructed muons so the derivation used reflects that by including ALFA data and excluding muon data.

CHAPTER 4

Analysis strategy, data samples and selection

At the start of this chapter the analysis strategy is summarised in section 4.1. In section 4.2 the data samples available are listed. The full event selection is then outlined in section 4.3 and the fiducial range is defined in section 4.4. The experimental resolutions on the variables studied are calculated, used to apply a calibration and decide the bin widths, in sections 4.5 and 4.6, respectively.

4.1 Analysis strategy

The aim of this analysis is to measure the differential cross-section of single diffraction as a function of the fractional energy loss of the proton (ξ), the observed rapidity gap ($\Delta\eta$) and the squared four-momentum transferred (Mandelstam $|t|$). See chapter 2 for an introduction to these variables and an explanation as to their importance in single diffraction.

In brief - the analysis uses ATLAS data from a special LHC run for diffractive physics and ALFA is used to tag and reconstruct the intact proton. The MBTS and ID are used to trigger the event and to reconstruct the primary vertex and the mass of the dissociative system.

4.1.1 Fractional energy loss ξ

Different methods are available for calculating ξ. The energy of the intact proton can be measured by tagging and reconstructing the forward proton directly to evaluate:

$$\xi_P = 1 - \frac{E'_P}{E_P}. \tag{4.1}$$

The dissociative system can also be reconstructed using energy, E_i, and z-component of the momentum $p_{z,i}$, of its constituent particles in the 'E_{Pz}' method:

$$\xi_{EPz} \approx \frac{\sum_i E_i \pm p_{z,i}}{\sqrt{s}}. \tag{4.2}$$

The $\pm$ coefficient of the $p_{z,i}$ term is decided by which side the proton is tagged on. Section 2.3.1 demonstrates the viability of the E_{Pz} approximation. Due to its small size in the region of the measurements, the base-10 logarithm of ξ is quoted.

The analysis presented here is able to make use of data from the ATLAS calorimeters, ID or ALFA. A ξ_{EPz} measurement can then be made from either the ID tracks ($\log_{10}\xi_{\mathrm{ID}}$) or calorimeter clusters ($\log_{10}\xi_{\mathrm{Calo}}$). The detector systems can not be combined to form a single measurement due to the possibility of counting charged particles twice. No additional P_T thresholds was applied to either the calorimeter clusters or ID tracks to calculate ξ. As discussed in chapter 3 calorimeter clusters require a $|\varsigma_{cell}^{EM}| > 4$ and the ID tracks have a minimum requirement of $P_T > 100$ MeV.

The response matrices of the different methods are shown in figure 4.1. These plots indicate that ξ_{Calo} should be a better measurement method than ξ_{ID}. This is

understood to be due to the wider η coverage and the sensitivity to neutral particles. However a large discrepancy was found between the calorimeter response in MC, compared to that in data. This was realised late in the analysis and so there was insufficient time to find the cause of, or correct for, the discrepancy. Possible causes are pile-up effects (or lack there-of in MC) or an inadequate simulation of noise in the calorimeters.

ID tracks did not demonstrate such a discrepancy and so $\log_{10}\xi_{\mathrm{ID}}$ was chosen as the method for reconstructing ξ. The response matrix (figure 4.1b) suggests good resolution should be achievable. It indicates a decrease in performance at higher ξ values, due to the lack of sensitivity to neutral particles or limited η coverage. In comparison, $\log_{10}\xi_{\mathrm{ALFA}}$ (figure 4.1a) showed good resolution at very high values of $\log_{10}\xi$ but poor resolution at lower values.

The 'raw,' uncalibrated value $\log_{10}\xi_{\mathrm{ID}}^{\mathrm{Raw}}$ is used in this chapter until a calibration is introduced to improve the response in section 4.5.

4.1.2 Mandelstam t

The magnitude of Mandelstam t is reconstructed using the primary vertex and the tracks of intact protons in ALFA relying on the relation shown in section 2.3.2:

$$t \approx -p_T'^2. \tag{4.3}$$

Despite showing poor resolution for ξ, the ALFA reconstruction is a good measure of $|t|$ (as can be seen looking at figure 7.1). The ALFA reconstruction code is provided by collaborators at the University of Copenhagen[127] with an updated tuning of parameters for $\sqrt{s} = 13$ TeV LHC optics[28]. Like ξ, a calibration is also applied to $|t|$ in section 4.5.

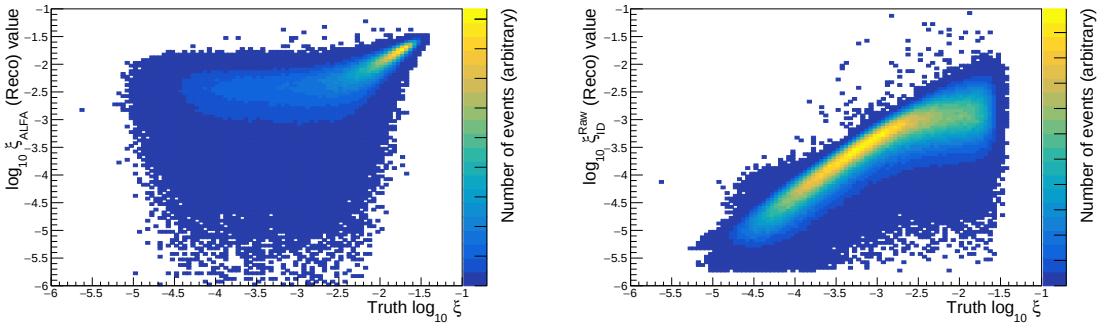

(a) Using ALFA

(b) Using ID tracks (uncalibrated)

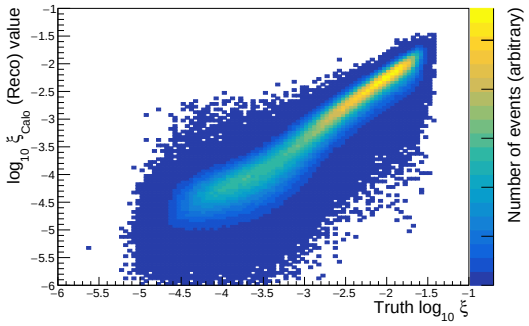

(c) Using calorimeter clusters

Figure 4.1: The response matrices for the different methods of reconstructing $\log_{10}\xi$ generated using SD MC following the event selection presented in this chapter.

4.1.3 Rapidity gap

The observed rapidity gap ($\Delta\eta$) is measured relative to the side of the ATLAS detector with the tagged proton, between the edge of the detector-sensitive region and the closest ID track. The ATLAS rapidity gap cross-section analysis showed that to maintain sensitivity to diffractive physics one must use a reasonable p_T cut for the ID tracks considered[128]. Therefore a cut of $p_T > 200$ MeV was applied to ID tracks used to calculate $\Delta\eta$.

An effect observed in previous ATLAS SD and minimum bias rapidity gap cross-section analyses is referred to as the 'stacking up' of events[128, 3]. This is demonstrated in figure 4.2, which compares the $\Delta\eta$ measurements of two high ξ events with large multiplicities of ID tracks. For one event (fig 4.2a) the particle closest to

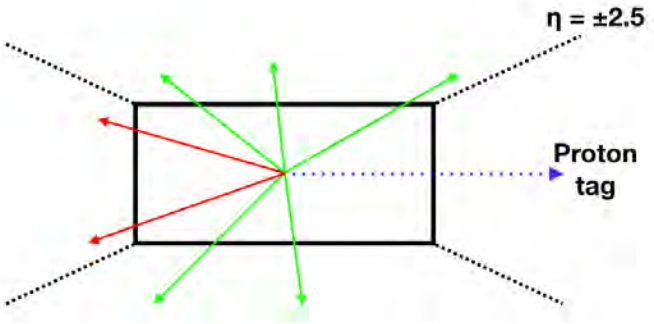

(a)

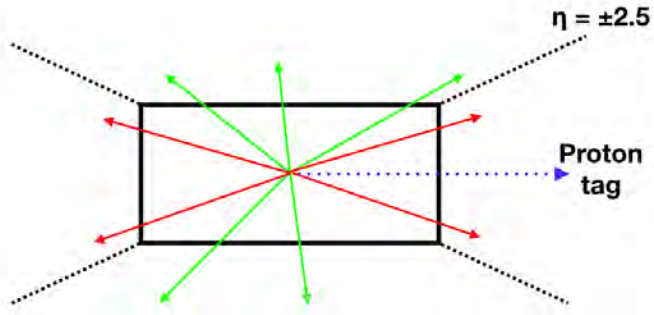

(b)

Figure 4.2: 'Stacking up' of events at low values of $\Delta\eta$: Both diagrams show high ξ events with $\Delta\eta$ reconstructed as ~ 0. The proton tag is on the right side of the detector (dotted blue lines) and $\Delta\eta$ is measured from the edge of the detector on that side (dashed black lines marked as $\eta = \pm 2.5$). Measured final state particles are shown in green and ones that fall out of the detector coverage are shown in red. The event shown in (a) does not contain any tracks outside the sensitive region of the detector on the side of tag. The event shown in (b) does. Both events are reconstructed as $\Delta\eta \sim 0$.

the intact proton is at $\eta = 2.5$ and therefore $\Delta\eta \sim 0$. For the other event (fig 4.2b) there are particles at higher values than $\eta = 2.5$. These are beyond the coverage of the detector but particles are still present at $\eta \lesssim 2.5$. Therefore both of these events are reconstructed as $\Delta\eta \sim 0$, resulting in an excess of events in the first few bins compared to the flat diffractive plateau initially expected from diffractive events.

4.2 Samples

4.2.1 Data samples

This analysis uses data from a single ATLAS run, number 282420 from LHC fill 4509. 201.5 nb^{-1} of collisions were recorded. This was the highest integrated luminosity ATLAS run from the special 90m β^* runs[129] of the LHC for diffractive and elastic physics analyses in 2015. The run conditions are summarised in table 4.1 and are also shown alongside typical values for 'normal' high pile-up running at the ATLAS IP during 2015[130].

Table 4.1: Run conditions for the LHC fill studied in this analysis (4509) and typical values for standard high luminosity running during 2015[130].

Property	Fill 4509	Typical value for 2015
Centre of mass energy $\sqrt{s}$ (TeV)	13	13
Maximum instantaneous luminosity $\mathscr{L}$ (cm^{-2} s^{-1})	9.5×10^{29}	5×10^{33}
Average Interactions per bunch crossing $\langle\mu\rangle$	0.099	13.7
β^* (m)	90	0.3

4.2.2 MC samples

Tunes of the PYTHIA event generator have been performed by the ATLAS collaboration to give a good description of the measured distributions of charged particles and the measured inelastic cross-section. The A2 tune[78] of PYTHIA8 was tuned using run1 $\sqrt{s} = 7$ TeV data and the Schuler and Sjöstrand (SS) model of the Pomeron flux factor[72, 73]. The A3 tune[77] is newer and uses run1 $\sqrt{s} = 900$ GeV and early run2 $\sqrt{s} = 13$ TeV data in addition to that used in the A2 tuning. Compared to the A2 tune, it provides better modelling of the inelastic cross-section with similar levels of agreement in other distributions. This improvement is due

to its use of the Donnachie and Landshoff (DL), rather than the SS, Pomeron flux factor[48].

The A3 SD sample used in this analysis had the tuning parameter ϵ[1] set to 0.074, similar to the result of $\epsilon = 0.07 \pm 0.09$ found by the ATLAS $\sqrt{s} = 8$ TeV SD cross-section analysis[3]. α' was kept at 0.25 GeV^{-1}, the default value for PYTHIA for the DL model[47]. Section 2.8.3 provides further details on modelling of SD in PYTHIA.

The MC samples available for this analysis are summarised in table 4.2. They were generated using PYTHIA version 8.212[60] and the LHAPDF[131] set NNPDF23-lo-as-0130-qed[132]. For all of the samples, with the exception of the A2 SD sample, the full response of the ATLAS central detector was simulated and reconstructed. Unless specified otherwise, the A3 SD sample is being referred to when 'SD MC' is used.

Table 4.2: The MC samples used in this analysis. All are generated by PYTHIA and the luminosities shown are calculated using the default fully integrated PYTHIA8 cross-sections indicated.

Process	Number of events	Integrated luminosity (nb^{-1})	Cross-section (mb)
A3 Single Diffraction (SD)	$\sim 8 \times 10^6$	6.16×10^{-1}	12.83
A3 Non-Diffractive (ND)	$\sim 5 \times 10^5$	8.56×10^{-3}	56.79
A3 Central Diffraction (CD)	$\sim 5 \times 10^5$	3.89×10^{-1}	1.279
A3 Double Diffraction (DD)	$\sim 5 \times 10^5$	5.65×10^{-2}	8.798
A3 Elastic (EL)	$\sim 5 \times 10^5$	2.28×10^{-2}	21.89
A2 Single Diffraction (SD) (Truth level only)	$\sim 5 \times 10^6$	3.85×10^{-1}	12.83

Pile-up effects were not included in the MC samples, section 5.1 discusses a correction for this. Also, for technical reasons, it was not possible to simulate the detailed

[1] $\alpha_{\mathbb{P}}(0) = 1 + \epsilon$. See section 2.6 for further details on the importance of these parameters.

response of ALFA or reconstruct its tracks. Instead, final state truth protons were transported through the optics of the LHC as part of the analysis. If the proton reached the position of ALFA (at $z = \pm 237.398$m and $z = \pm 245.656$m) the x and y coordinates of the proton were smeared, using best estimates of the detector response, and used as the coordinates for tracks. The smearing applied was Gaussian and used the known resolution of the detector (30 μm)[116]. This process is to as the 'forward transport method.'

To check the reliability of the forward transport method, the smeared coordinates of transported protons were used as input to ALFA reconstruction code as was done in the main analysis. The truth and reconstructed values of the p_x and p_y of the final state protons were plotted as shown in figures 4.3a and 4.3b. Figures 4.7a and 4.7d compare the distributions of the ALFA tracks following the application of selection cuts in x and y. The plots show reasonable agreement indicating this method worked adequately.

The ALFA scintillating fibres are known to be highly efficient and so no efficiency correction was applied for the detection of protons by the fibres. An efficiency correction, presented in section 5.4, was applied due to the potential failures of the track reconstruction algorithm in data.

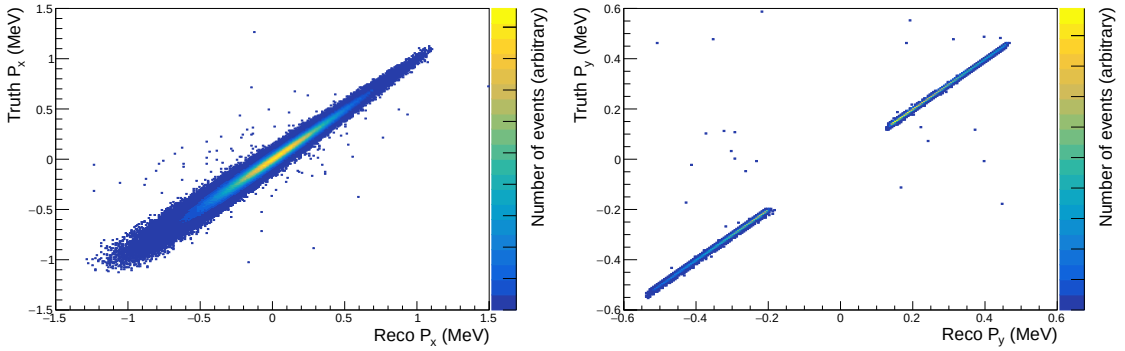

(a) (b)

Figure 4.3: Comparison of truth and reconstructed values for the diffracted proton p_x and p_y. The gap in the p_y distribution is due to the position of the ALFA detectors and the limited accepted in y due to the beam pipe.

4.3 Event selection

As discussed in the analysis strategy (section 4.1) the analysis selects events using the characteristics of SD. This selection is applied in two stages: 'online' using the trigger system and 'offline' using more elaborate selection cuts. The purpose of both is to maintain high acceptance for SD events while removing as many background sources as possible.

4.3.1 Online selection

As explained in section 3.2.9.1, ATLAS uses a trigger system to identify which events to read-out. The first level of trigger used in this analysis consisted of the 'AND' of several signals:

- A filled bunch crossing
- A signal in at least one MBTS segment
- A signal in the trigger counters of both near and far RPs of an ALFA arm, on the opposing side of ATLAS to the MBTS trigger

In ATLAS terminology this forms the '`L1_MBTS_1_A_ALFA_C`' and '`L1_MBTS_1_C_ALFA_A`' trigger items. The MBTS requirement was to ensure that the trigger rates were reasonable while having minimal impact on the acceptance for SD events. The HLT did not apply any further trigger algorithms other than a prescale of 190.

The two components of the triggers used were also enabled separately, albeit with higher prescales, as the '`L1_MBTS_1`' and '`L1_ALFA_SDIFF`' trigger items. The total prescales for these items were 24000 and 9998.34, respectively. As with the main signal trigger, the HLT did not apply any further algorithms to either trigger item other than prescaling. These triggers allowed for the trigger efficiency studies that are described in section 5.2.

The studies of the noise in the MBTS use the only trigger for empty bunch crossings that was enabled ('L1_ALFA_ANY_EMPTY'). This trigger accepts any event with an ALFA trigger signal from two empty RF buckets at the IP, with a safety margin of 5 crossings away from a paired crossing[133].

4.3.2 Offline selection

The offline selection consists of a series of selection cuts, described below, grouped by the detector system used.

4.3.2.1 Luminosity Blocks

While running and collecting data, ATLAS groups periods of approximately one minute with similar run conditions into Luminosity Blocks (LBs). Approximately 10% of LBs in the run analysed contained events with faulty detector components and so were vetoed. The main fault was a value of 0pC consistently recorded as the charge read from some MBTS tiles, suspected to be due to a problem with the read-out for the TileCal. A summary of the LBs vetoed is shown in the appendices in table A.1. The integrated luminosity of the data unaffected by any fault was 169.9 nb^{-1}. This was sufficient data to make the measurement without large statistical uncertainties limiting the result. Therefore it was decided to veto the LBs with faults as this was simpler than including them and accounting for the issues otherwise.

4.3.2.2 MBTS

The MBTS was used in the online trigger selection to maintain reasonable trigger rates. To ensure the trigger efficiency was well understood an offline requirement was placed on the charge measured in each of its tiles. The offline measurements of charge did not correlate well with the trigger signal and so the offline threshold needed to be tuned, taking into account the noise from electronics.

It was known from previous analyses that the MBTS noise distribution in MC was different from that in data[50]. To investigate the electronic noise, different selections were placed on the two samples.

Empty bunch crossings were used to study the electronic noise in data. These were events passing the '`L1_ALFA_ANY_EMPTY`' trigger - the only trigger available for empty bunch crossings. The ALFA component of this trigger was superfluous to the study, since the majority of the signals are caused by beam effects with no correlation with ATLAS activity, it should not affect the measured MBTS distributions. This sample should therefore only contain data from when ATLAS was empty, with a small amount of contamination from out-of-time pile-up. No other selection was placed on this sample.

The elastic MC sample was used with no event selection applied. Elastic ($pp \to pp$) events with no pile-up effects should have no other activity apart from the two intact protons which, in the vast majority of cases, continue out of the detector very close to the beam-line. Therefore the MBTS charge distribution in this MC sample should only consist of the simulated electronic noise.

From these samples, distributions of the charge collected in each MBTS tile were obtained. The inner and outer tiles exhibited different Gaussian distributions and so were plotted separately. A Gaussian function was fitted to each of the distributions. The normalised distributions and fitted functions are shown in figure 4.4. The fits to the MC distributions show very good agreement with the Gaussian assumption. The fits in the data distributions also show good agreement with a small amount of contamination from pile-up or other effects. The offline threshold was chosen to be $\mu + 5\sigma$ using the fit parameters for each group of tiles. The full set of fit parameters and offline thresholds is listed in the appendix in table A.2.

To ensure the thresholds were not too high, a non-diffractive sample was used. ND events are typically high multiplicity with many final state particles across a wide-range in η. Therefore the majority of ND events should contain at least one

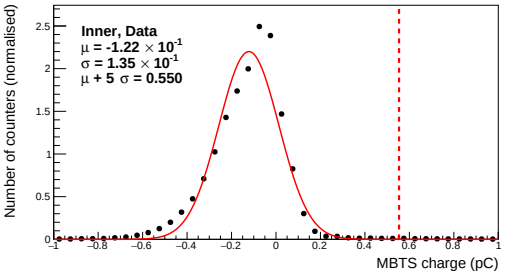

(a) Inner tiles in data

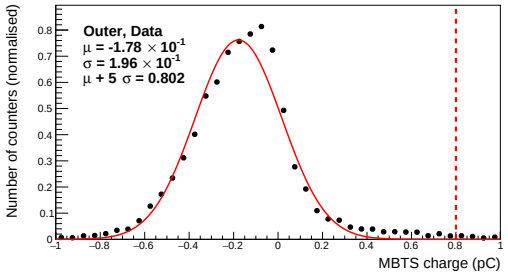

(b) Outer tiles in data

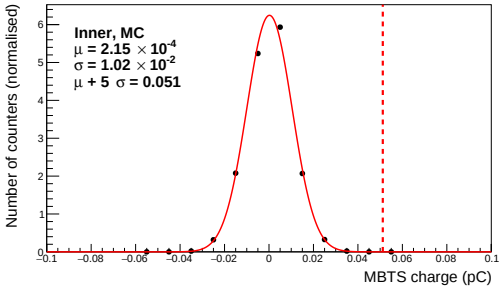

(c) Inner tiles in MC

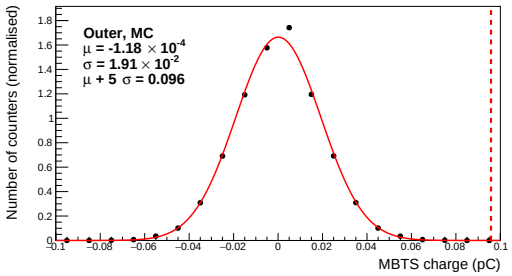

(d) Outer tiles in MC

Figure 4.4: The noise distributions in the MBTS response normalised to the number of counters. The black points mark the data or MC response. The solid red line indicates the Gaussian fit and the dotted red line indicates the offline threshold calculated from the fit.

MBTS counter passing the off-line threshold, if the thresholds have been correctly tuned. For data a random trigger was used with the additional requirements of a reconstructed primary vertex and a small (< 0.5) rapidity gap on both sides of the detector to ensure the event contained ND activity. For MC, the ND sample was used without any further selection. The distributions of all MBTS counters are shown in figure 4.5. More than 99.7% of events in both samples contained at least one MBTS counter above its threshold and more than 99.5% of events in both samples contained at least two MBTS counter above their thresholds.

The first study ensured that the MBTS offline thresholds were high enough to avoid the noise distributions. The second study showed that they were not too high as to miss genuine signal. Together they showed the thresholds were correctly tuned for separating signal from noise distributions.

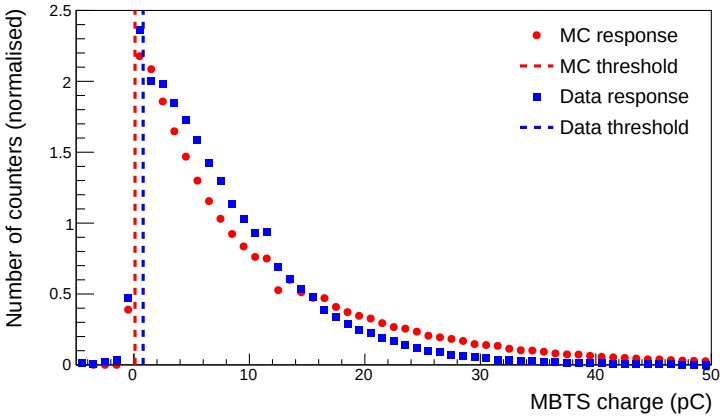

Figure 4.5: The distributions from all MBTS tiles in a ND MC and ND enriched data sample. The offline threshold for the outer tiles for each sample is shown for reference. Statistical errors are shown but obscured by the markers.

The trigger efficiency studies, fully discussed in section 5.2, showed very poor efficiency for events with fewer than 2 MBTS counters passing the offline threshold. Therefore the offline event selection required at least 2 MBTS counters, on the opposing side to the ALFA tag, to pass their relevant thresholds.

4.3.2.3 Vertex and ID requirements

The requirement of a primary vertex reduced the acceptance for low ξ events. However the position of the primary vertex was required to enable the reconstruction of $|t|$. Therefore a single well-reconstructed vertex was required using the ATLAS low-p_T vertexing algorithm, which requires at least two ID detector tracks with $P_T > 100$ MeV. The vertex selection procedure is described in more detail in [134]. For use in the analysis, ID tracks were required to have $P_T > 100$ MeV and at least five SCT hits.

To reduce the effects of pile-up, events with additional primary vertices, reconstructed from at least three ID tracks, are vetoed.

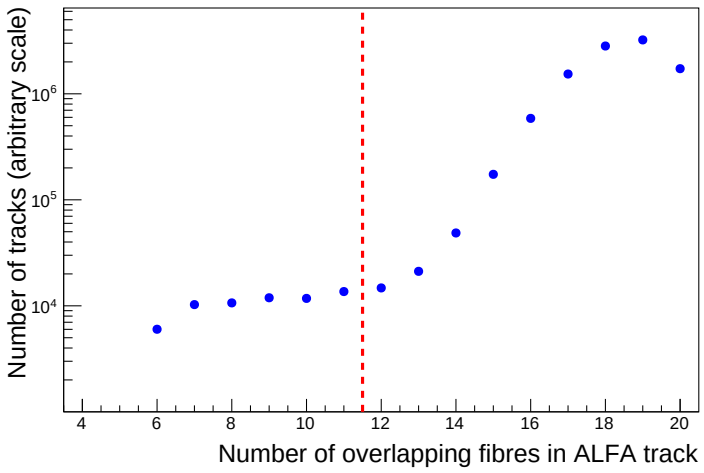

Figure 4.6: The number of overlapping fibres used to reconstruct tracks. The offline threshold of requiring a track to be formed of at least 12 fibres is indicated with a red line. Statistical errors are shown but obscured by the markers.

4.3.2.4 ALFA selection

Proton tagging allows discrimination between different diffractive processes and indicates in which direction any intact protons leave the detector. This allows for the reconstruction of $|t|$ and, to some extent, ξ. Therefore the basic requirement was a single reconstructed track in both the near and far RPs of an ALFA arm that matches the trigger signal. Single diffraction should only result in a single intact proton and high pseudo-rapidities. Therefore a veto was placed on activity in any other RP.

The majority of tracks were reconstructed from a large number of overlapping fibres. Figure 4.6 shows the number of fibres used to reconstruct tracks with the reconstruction algorithm's minimum requirement of six overlapping fibres visible. To ensure the tracks were well reconstructed, tracks with fewer than twelve planes of scintillating fibres (six from each of the u and v planes) were vetoed as indicated by a red dashed line in the plot. The efficiency correction of the track reconstruction algorithm is discussed in section 5.4. The distributions of the tracks in an ALFA RP following this basic selection is shown in figure 4.7a.

The beam-screen is a part of the LHC infrastructure for shielding and protecting the quadrupole magnets. Parts of the sensitive regions of ALFA are obscured by the beam-screen. These areas should be vetoed as protons are unlikely to pass through the beam-screen and the ones that do are very likely to shower, which heavily impacts the performance of the reconstruction algorithm. To calculate the position of the beam-screen, the distribution of the y coordinates of ALFA tracks for each RP was plotted. An example of the distribution is shown in figure 4.7b. Two sharp edges are visible: the edge of the detector on the side closest to the beam ($y = 0$) and the start of the beam-screen shadow. The edges were identified by finding the bins with the biggest difference with respect to their neighbours. ALFA tracks were only used if they were ≥ 0.2 mm away from the edge of the detector on the beam side and ≥ 2 mm away from the edge of the beam-screen. A larger tolerance was used on the beam-screen side due to the possibility of showering. These tolerances are approximately double those used by previous analyses which had the detector edges calculated by dedicated elastic measurements using a more detailed method[50, 76, 118].

Th x coordinate of tracks was restricted in data due to the shape of the sensitive material of the ALFA RPs, as can be seen in figure 4.7c. Therefore in MC a veto on tracks with $|x| \geq 20$ mm was used. If this had been the only selection placed on tracks this would have resulted in a minor difference in acceptance between MC and data. This difference is visible in the upper right corner of the accepted regions in figures 4.7a and 4.7d. However the elliptical selection, discussed below, applied further vetoes to the tracks based on the x coordinate and so this difference does not impact the analysis.

To remove pile-up and beam-induced background effects, a veto was placed on events with a trigger signal or reconstructed track in any other RP. To further reduce contamination, a selection was placed on the correlation between quantities calculated from both the near and far stations of a single ALFA arm: the average x coordinate ($\bar{x} = \frac{x_{\text{near}} + x_{\text{far}}}{2}$) and the local angle ($\theta = \frac{\Delta x}{\Delta z}$). In figure 4.8 plots of these variables for data and the different MC samples are shown for an example arm. In the data plot

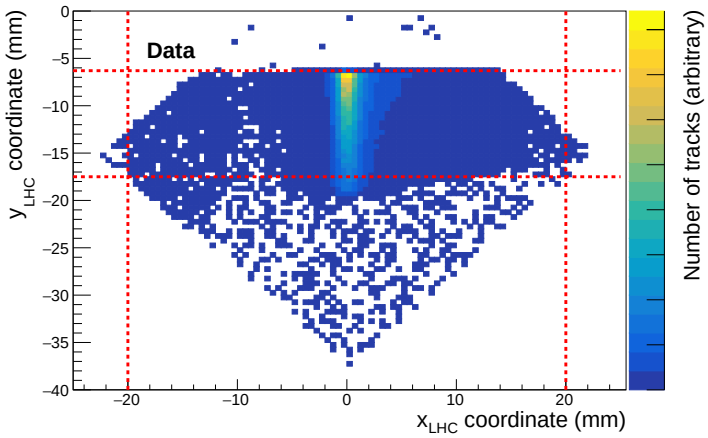

(a)

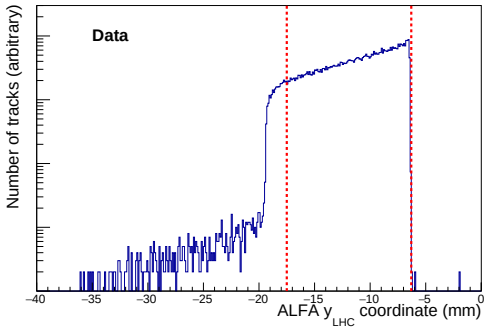

(b)

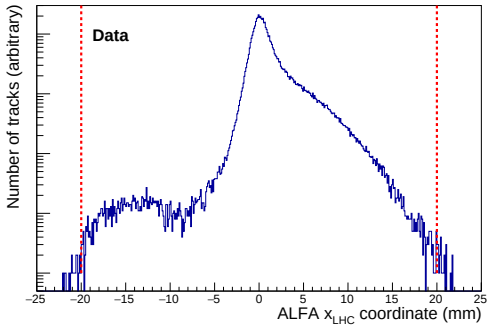

(c)

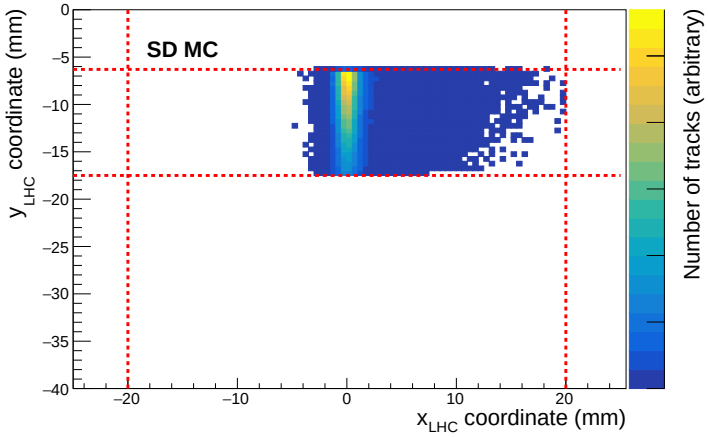

(d)

Figure 4.7: Figure (a) shows an example distribution of tracks in ALFA without any additional selection for the ALF RP. The edges of the distributions, indicated by red dashed lines, are identified using x and y projections of this plot. Examples are shown in (b) and (c). The full list of edges is presented in the appendix in table A.3. Figure (d) shows the equivalent distribution for SD MC following the application of the edge selection to tracks. The uneven distribution in x shown in (d) is due the energy loss of the intact protons resulting in them falling inwards towards the centre of the LHC.

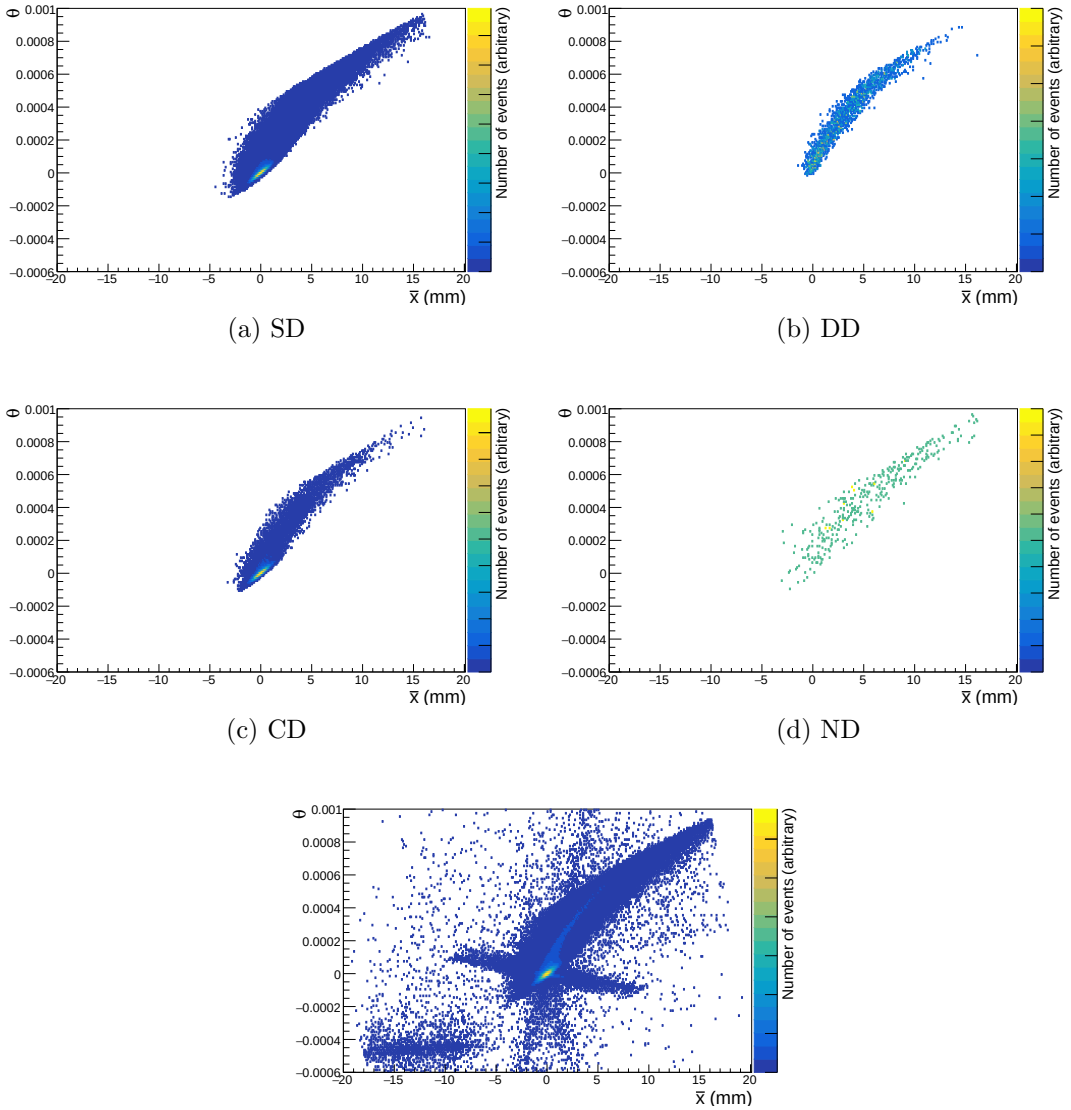

(a) SD

(b) DD

(c) CD

(d) ND

(e) Data

Figure 4.8: Correlations between $\bar{x}$ and θ for the AU arm for the different MC samples and data.

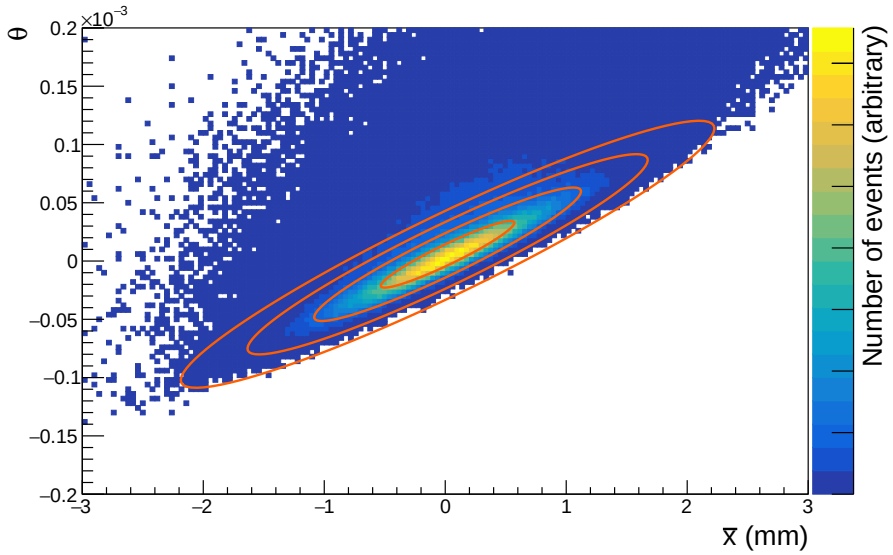

Figure 4.9: Distributions of $\bar{x}$ and θ for the AU arm for the SD MC. The red curves shows the elliptical fits with 1σ, 2σ, 3σ and 4σ.

(figure 4.8e) additional distributions from background processes, including beam halo, are visible as well as a population that is compatible with SD and CD MC.

Figure 4.9 shows the same distribution for SD MC protons, scaled to focus on the peak of the bivariate Gaussian distribution. A fit was performed on each arm separately, resulting in an elliptical equation applied to each arm i:

$$\frac{(\bar{x}_i - x_c)^2}{\sigma_{\bar{x}}^2} - \frac{2\rho(\bar{x}_i - x_c)(\theta_i - \theta_c)}{\sigma_{\bar{x}}\sigma_\theta} + \frac{(\theta_i - \theta_c)^2}{\sigma_\theta^2} = 1 - \rho^2. \tag{4.4}$$

The variables obtained from the fit are: x_c and θ_c, the centre of the ellipse, $\sigma_{\bar{x}}$ and σ_θ, the standard deviations, and ρ, the correlation coefficient. The fit parameters for each arm are shown in table A.4 in the appendix.

The elliptical distribution provides a way of vetoing background events. Figure 4.10a shows the acceptance of the SD MC following the event selection explained thus far, with a veto placed on the $\bar{x}$ and θ. The cut is defined by the number of standard deviations of the elliptical fit (n_σ) used. If an event falls outside the elliptical selection, it is vetoed. The plot shows that using a cut of $n_\sigma < 4$ has minimal impact on the acceptance below $\log_{10}\xi$ (Truth) $= -2$, the expected upper

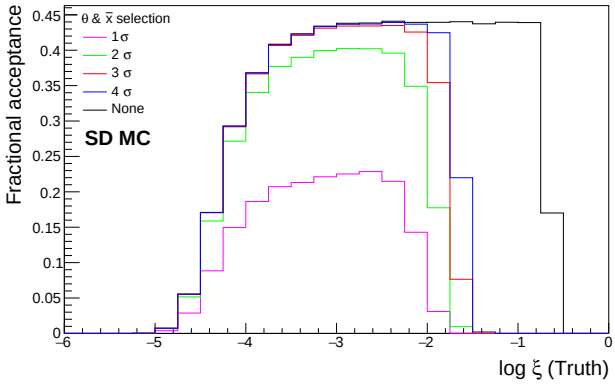

(a)

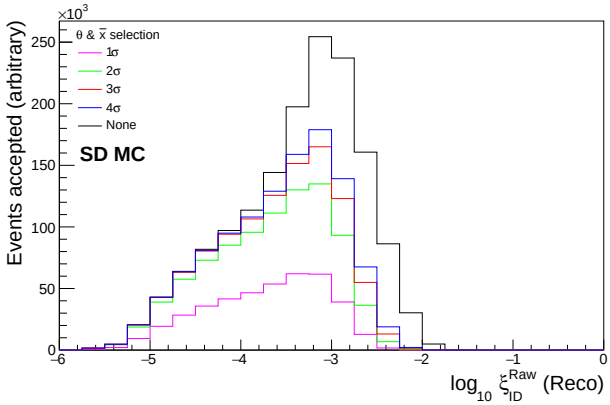

(b)

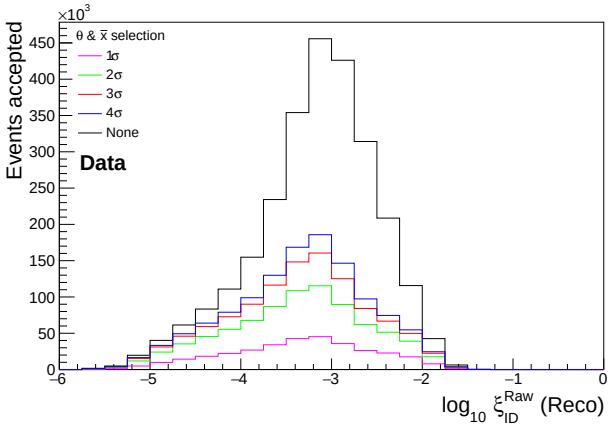

(c)

Figure 4.10: Acceptance for different elliptical $\bar{x}$ and θ cuts, shown as a function of $\log_{10}\xi$ (Truth) for SD MC in (a) and as a function of $\log_{10}\xi_{\mathrm{ID}}^{\mathrm{Raw}}$ for unscaled SD MC in (b) and data in (c).

limit on the fiducial range of ξ.

Figures 4.10b and 4.10c show the effect of the same veto on the reconstructed value of $\log_{10}\xi_{\mathrm{ID}}^{\mathrm{Raw}}$ in SD MC and data, respectively. The requirement of $n_\sigma < 4$ cuts out a large number of data events and a comparatively small number of SD events. Further tightening of the cut removes similar proportions of events in both the SD MC and data, suggesting signal events are being vetoed. Most of the data events being vetoed with the $n_\sigma < 4$ cut are therefore attributed to background. A tighter requirement would start to impact the acceptance.

4.4 Fiducial region

The fiducial region of this analysis is defined entirely in terms of $|t|$ and $\log_{10}\xi$. The limit on acceptance is mostly determined by the physical coverage and position of the ALFA detector. The requirement of a reconstructed vertex also impacts the lower limit of the ξ range.

To decide the fiducial range of the measurement, the acceptance (as defined in equation 4.5) of the SD MC sample was calculated as a function of the truth level $|t|$ and $\log_{10}\xi$, using the event selection detailed in this chapter. This is shown in figure 4.11 in comparison with the generator level distributions without any selection cuts applied.

$$\text{Acceptance} = \frac{\text{Number of events accepted}}{\text{Number of events generated}}. \tag{4.5}$$

The acceptance in $\log_{10}\xi$ (figure 4.11b) shows a plateau region of reasonably constant acceptance with a steep fall either side. As discussed in the previous section, high backgrounds were expected in the region $-2 \lesssim \log_{10}\xi$ and so this was used as the upper limit. The lower limit was chosen to be above the sharp fall in acceptance at $\log_{10}\xi \approx -4$ as this could complicate unfolding. Therefore the fiducial range was

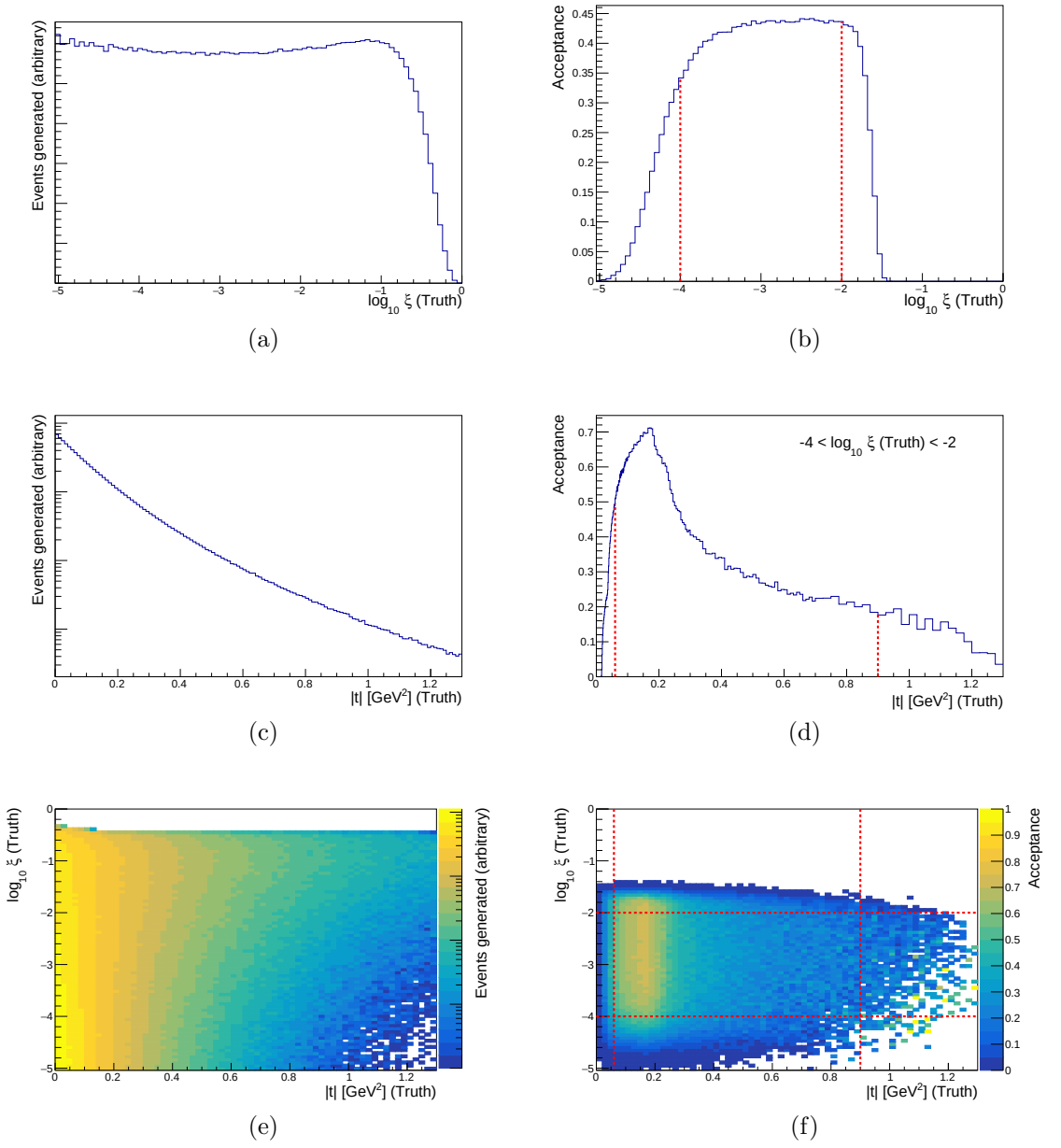

Figure 4.11: Truth level distributions of: (a) $\log_{10}\xi$; (c) $|t|$ and (e) $|t|$ against $\log_{10}\xi$. The acceptance is shown as a function of: (b) truth $\log_{10}\xi$; (d) truth $|t|$ with the additional requirement of $-4 < \log_{10}\xi(\text{Truth}) < -2$; and (f) truth $\log_{10}\xi$ against $|t|$. The limits on the fiducial range are indicated with red lines.

chosen to be $-4 < \log_{10}\xi < -2$.

Figure 4.11d shows the acceptance in truth $|t|$ following the event selection with the additional requirement of $-4 < \log_{10}\xi(\text{Truth}) < -2$. This shows a sharp fall in acceptance at one end of the distribution and then a slowly falling tail on the other.

The fiducial region was chosen to avoid the majority of the sharp fall at the lower end of $|t|$. Due to the exponential dependence on $|t|$ the tail at high $|t|$ suffered from statistical fluctuations. The upper limit was chosen to avoid issues from these fluctuations. Therefore the range was chosen to be $0.06\ \text{GeV}^2 < |t| < 0.9\ \text{GeV}^2$.

4.5 Calibration

Events should only be accepted if they fall within the fiducial region based on the reconstructed values. To optimise the selection near the edge of the fiducial region it is important to ensure the reconstructed variables have the best resolution possible and minimum bias. The resolution was calculated by plotting, for each SD MC event, the quantity:

$$\text{Residual} = \text{Truth value} - \text{Reconstructed value}. \tag{4.6}$$

The bias, and resolution, was then defined as the mean value, and the standard deviation, of the residual in each reconstructed bin, respectively. The bias of the raw, uncalibrated values of both $\log_{10}\xi_{\text{ID}}$ and $|t|$ are shown in figure 4.12. For both variables the bias varied substantially and so functions were fitted to the distributions, shown in red on the plots. These functions were used to correct the raw values to calibrated ones.

For $\log_{10}\xi_{\text{ID}}$, a third degree polynomial was fitted to the bias distribution. Therefore the calibrated variable is:

$$\begin{aligned}\log_{10}\xi_{\text{ID}} = & \\ & -6.67 \times (\log_{10}\xi_{\text{ID}}^{\text{Raw}})^3 - 6.38 \times (\log_{10}\xi_{\text{ID}}^{\text{Raw}})^2 \\ & -0.8 \times \log_{10}\xi_{\text{ID}}^{\text{Raw}} - 0.16.\end{aligned} \tag{4.7}$$

For $|t|$, a second degree polynomial was sufficient to fit to the bias distribution.

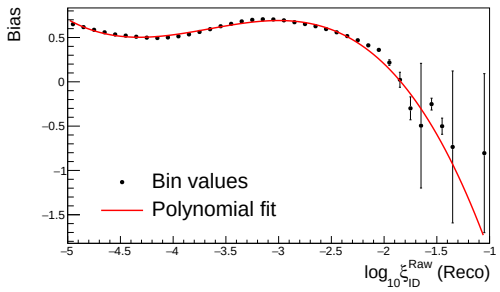

(a)

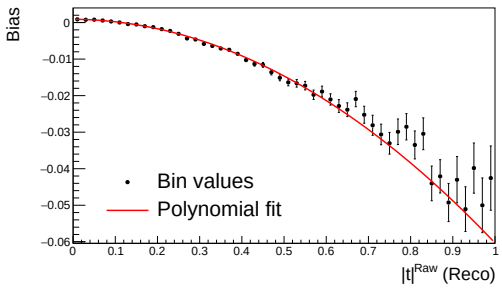

(b)

Figure 4.12: The bias plotted as a function of the reconstructed variable. The raw, uncalibrated values are shown as black points and the fitted polynomials are shown as red curves.

Therefore the calibrated variable is:

$$|t| = 0.001 \times (|t^{\mathrm{Raw}}|)^2 + 1.002 \times |t^{\mathrm{Raw}}| - 0.08. \tag{4.8}$$

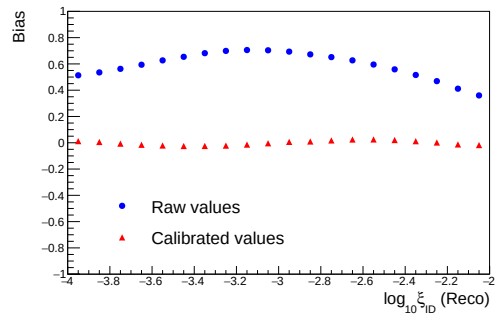

(a)

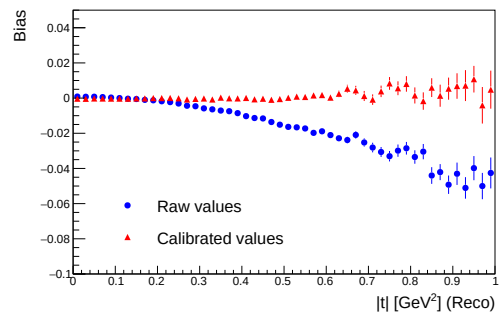

(b)

Figure 4.13: The bias plotted as a function of the reconstructed variable. The raw, uncalibrated values are shown as blue points and calibrated values as red points.

Within the fiducial region this step improves the bin purities and makes the response matrices more diagonal. However this effect does not change the final results as the unfolding is capable of doing the same in accounting for migrations. The resolution of the raw and calibrated variables are plotted in figure 4.13. These plots show the improvement that the calibration step provides by bringing the bias closer to 0.

Henceforth the reconstructed values of $\log_{10}\xi$ and $|t|$ refer to the calibrated variables defined in equations 4.7 and 4.8.

4.6 Bin widths and resolution

The bias and resolution were calculated as a function of each of the analysis variables as described in section 4.5. These quantities are shown for all three analysis variables in figure 4.14. The calibration step ensures the bias was small for $\log_{10}\xi$ and $|t|$. No calibration was necessary for $\Delta\eta$, as can be seen in figure 4.14f.

The resolutions, as shown in figure 4.14, were used to decide the bin widths of the analysis variables. To ensure reasonable purity the binning was chosen to ensure the width of each bin was at least the resolution in that region. The bin widths for the final $\Delta\eta$ bins were chosen to ensure enough statistics were available for the efficiency studies presented in the next chapter.

The bin edges chosen were:

- For $\log_{10}\xi$: $-4.$, -3.7, -3.3, -2.85, -2.4 and -2.
- For $|t|$ (in units of GeV^2): 0.06, 0.09, 0.12, 0.16, 0.21, 0.28, 0.37, 0.49, 0.66 and 0.9.
- For $\Delta\eta$: 0., 0.25, 0.5, 0.75, 1., 1.25, 1.5, 1.75, 2., 2.25, 2.5, 2.75, 3., 3.25, 3.5, 3.75, 4., 4.5, and 5.

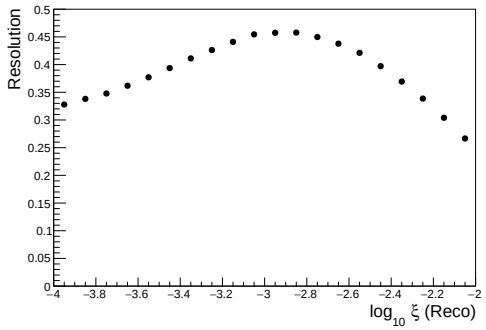

(a)

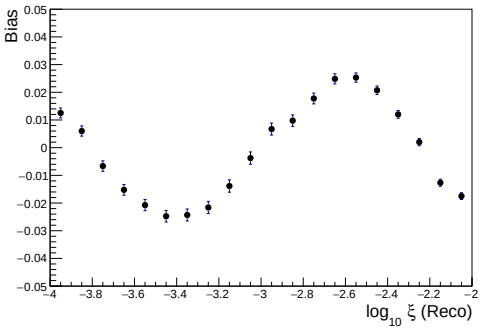

(b)

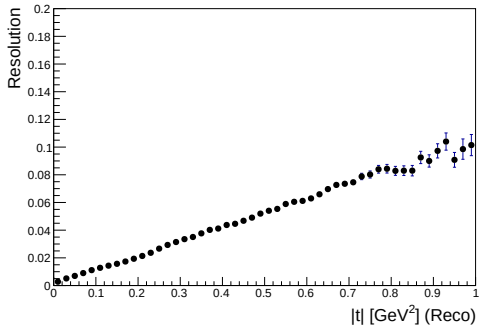

(c)

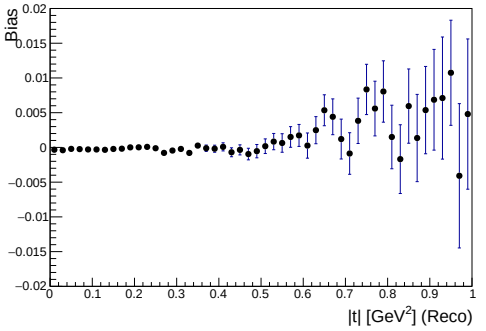

(d)

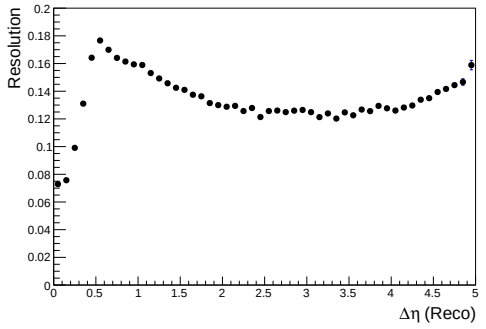

(e)

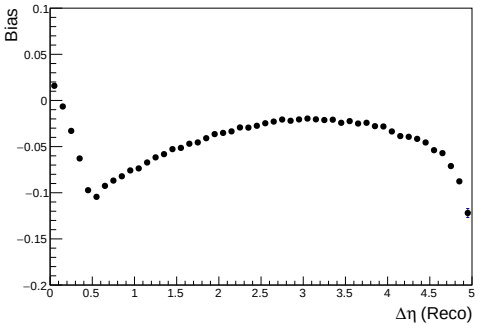

(f)

Figure 4.14: The bias and resolution as a function each reconstructed variable. For $|t|$ and $\log_{10}\xi$ this is shown following the calibration.

CHAPTER 5

Efficiency Corrections

This chapter explains the efficiency corrections applied to MC. Neither pile-up, the trigger nor the response of ALFA to protons were simulated in the MC samples. In sections 5.1 and 5.2 the corrections needed due to pile-up collisions and the finite trigger efficiency are calculated. Section 5.3 calculates the vertex reconstruction efficiency in both data and MC. Low ξ and high $\Delta\eta$ events, characteristic of SD, should be measured with similar detection efficiency regardless of whether the event is modelled in MC as an SD event or a statistically unlikely ND event. Therefore no attempt is made to subtract background contributions prior to the efficiency studies. The ALFA track reconstruction efficiency is calculated using a data-driven technique as described in section 5.4. This study includes a correction for background contributions to the efficiency calculation process. To conclude this chapter, section 5.5 explains how the corrections are implemented in the measurement.

5.1 Pile-up

Pile-up and its effects were not simulated in the MC samples used. During the data run the average number of collisions per bunch crossing ($\langle\mu\rangle$) was 0.099. There was some minor variance in this value throughout the run as shown in figure 5.1. This variance was small so $\langle\mu\rangle$ was assumed to be constant.

Data events with reconstructed pile-up vertices were vetoed. To account for this the MC samples were scaled down by a small factor to compensate this difference with data. Pile-up interactions were assumed to occur at a constant average rate over time and therefore Poisson statistics were applicable. Using this assumption, it was calculated that there was a 4.6×10^{-3} chance of at least 2 interactions occurring per bunch crossing.

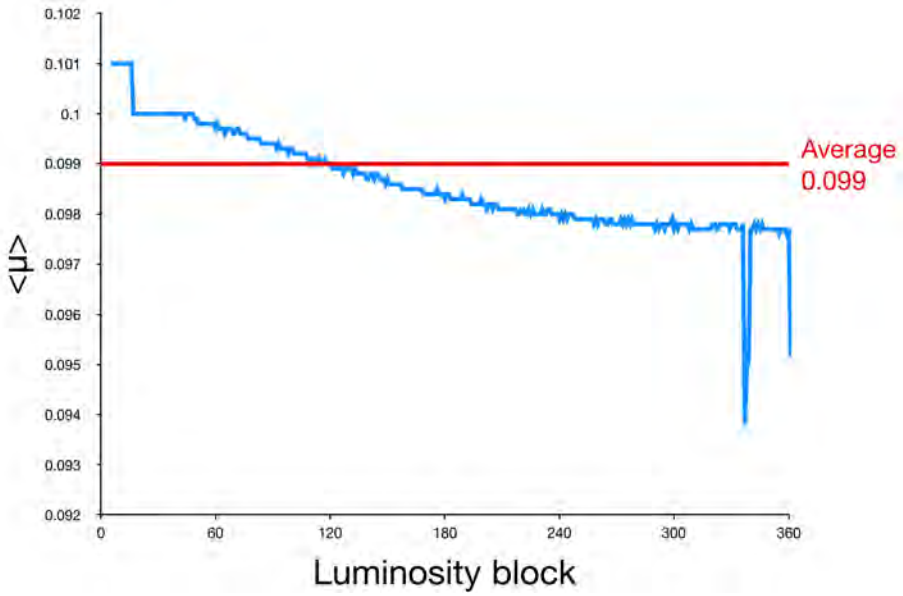

Figure 5.1: Average number of collisions per bunch crossing as a function of the LB. Data obtained from [135].

5.2 Trigger

The signal trigger, '`L1_MBTS_1_A_ALFA_C OR L1_MBTS_1_C_ALFA_A`' (explained in section 4.3.1), used to select data events had finite efficiency. Therefore this efficiency needed to be measured and corrected for.

The '`L1_MBTS_1`' and '`L1_ALFA_SDIFF`' triggers were used as reference triggers to evaluate the ALFA and MBTS components of the signal trigger, respectively. Events were selected using the reference triggers and the event selection was applied. The efficiency of the trigger component was then measured as the proportion of events in these references samples that passed the signal trigger before the prescale was applied. This is shown in the equation below, with the colours corresponding to those used in the Venn diagram shown in figure 5.2:

$$\epsilon = \frac{\text{Events passing (Reference trigger} \cap \text{Offline event selection} \cap \text{Signal trigger)}}{\text{Events passing (Reference trigger} \cap \text{Offline event selection)}} \tag{5.1}$$

$$= \frac{\textbf{Number of events}}{\textbf{Number of events}}.$$

Using this method, without applying the offline MBTS requirement, the efficiency of the MBTS trigger component was measured as a function of the number of MBTS tiles that were above their offline threshold on the side opposing the ALFA tag. This is shown in figure 5.3 and motivates the requirement of 2 MBTS tiles to ensure a reasonable trigger efficiency.

With the MBTS requirement being applied the ALFA component of the trigger was measured to have an overall efficiency of 0.939 ± 0.003. The trigger efficiencies for both the MBTS and ALFA components were calculated as a function of each of the reconstructed analysis variables. These efficiency measurements are shown figure 5.4. All analysis variables demonstrate good trigger efficiency across the whole range

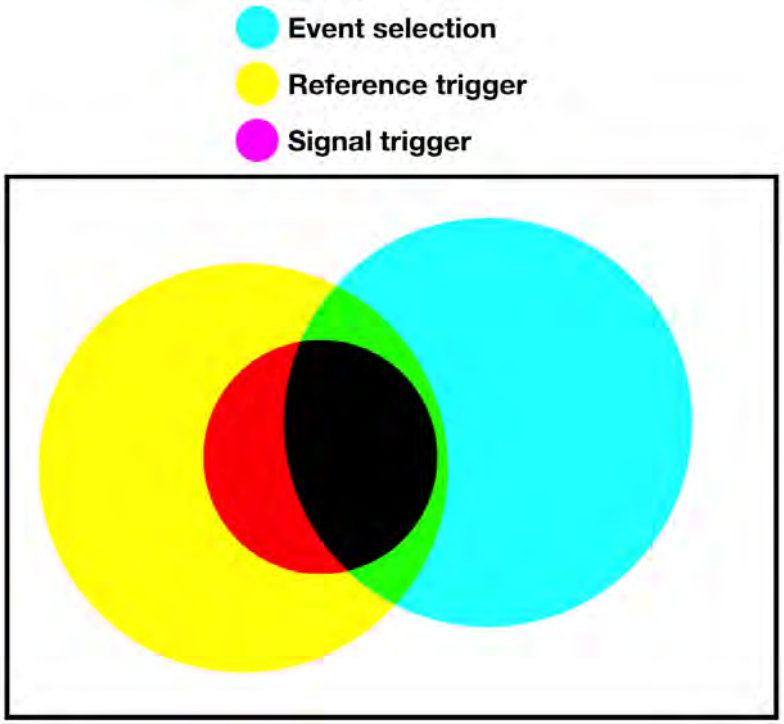

Figure 5.2: The selections used to estimated the trigger efficiency. The signal trigger is a subset of the reference trigger and so a magenta-only contribution is not seen.

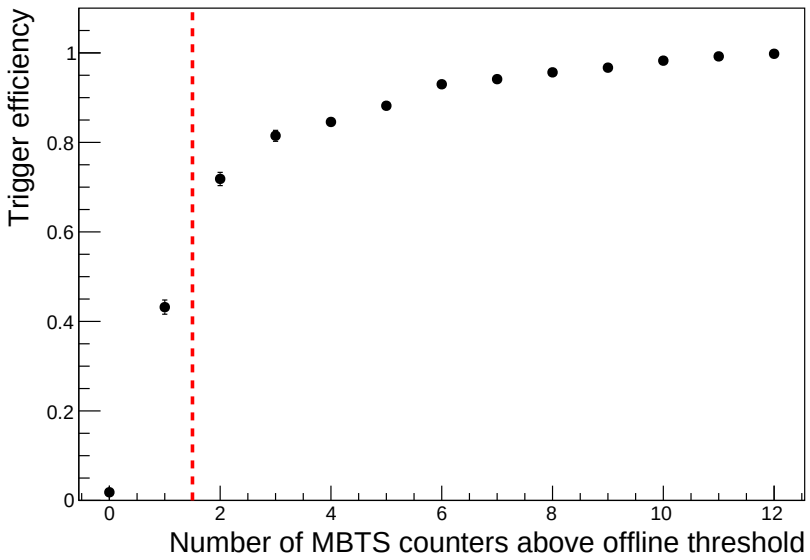

Figure 5.3: The efficiency as a function of the number of MBTS tiles above the relevant offline threshold. The selection requirement of at least 2 tiles above threshold is indicated by a red dashed line.

examined. There is a dependence of the trigger efficiency on the analysis variables, however it is small. Therefore a bin-by-bin correction is appropriate to correct for

the trigger efficiency.

5.3 Vertex reconstruction

The ATLAS low-P_T vertexing algorithm is less well studied than the standard one, therefore its performance was ascertained in both data and SD MC. It was possible that the simulated performance didn't match the real algorithm well and this would need correcting.

To measure the vertexing performance a similar method was followed as was used to measure the trigger efficiency in section 5.2. Events were selected with the full event selection with the exception of the vertex. A vertex is required by the ALFA proton reconstruction code so $|t|$ could not be reconstructed for the reference sample and the fiducial $|t|$ requirement was therefore not applied in this study. This should not bias the study as the vertexing algorithm uses ID tracks whose distributions are expected to have little dependence on $|t|$. The vertex reconstruction efficiency was then measured as the proportion of events in the sample that had a reconstructed vertex.

The efficiency was measured in both data and SD MC as a function of the number of ID tracks and the reconstructed values of $\Delta\eta$ and $\log_{10}\xi$. This is shown in figure 5.5. The plots show reasonable agreement between data and MC across the whole range of $\log_{10}\xi$ and $\Delta\eta$. To correct for the difference in efficiency a bin-by-bin correction is applied to MC as $\epsilon_{\text{Data}}/\epsilon_{\text{SD}}$.

There is a small discrepancy when there are few tracks passing the offline requirement being reconstructed with at least 5 SCT hits, possibly due to modelling imperfections or non-SD contributions in data. At least two ID tracks are required to reconstruct a PV but there is no requirement on the number of SCT hits for these tracks. Therefore it is possible to reconstruct a vertex and then very few ID tracks pass the offline selection. It is dealt with as a systematic uncertainty in section 8.7.

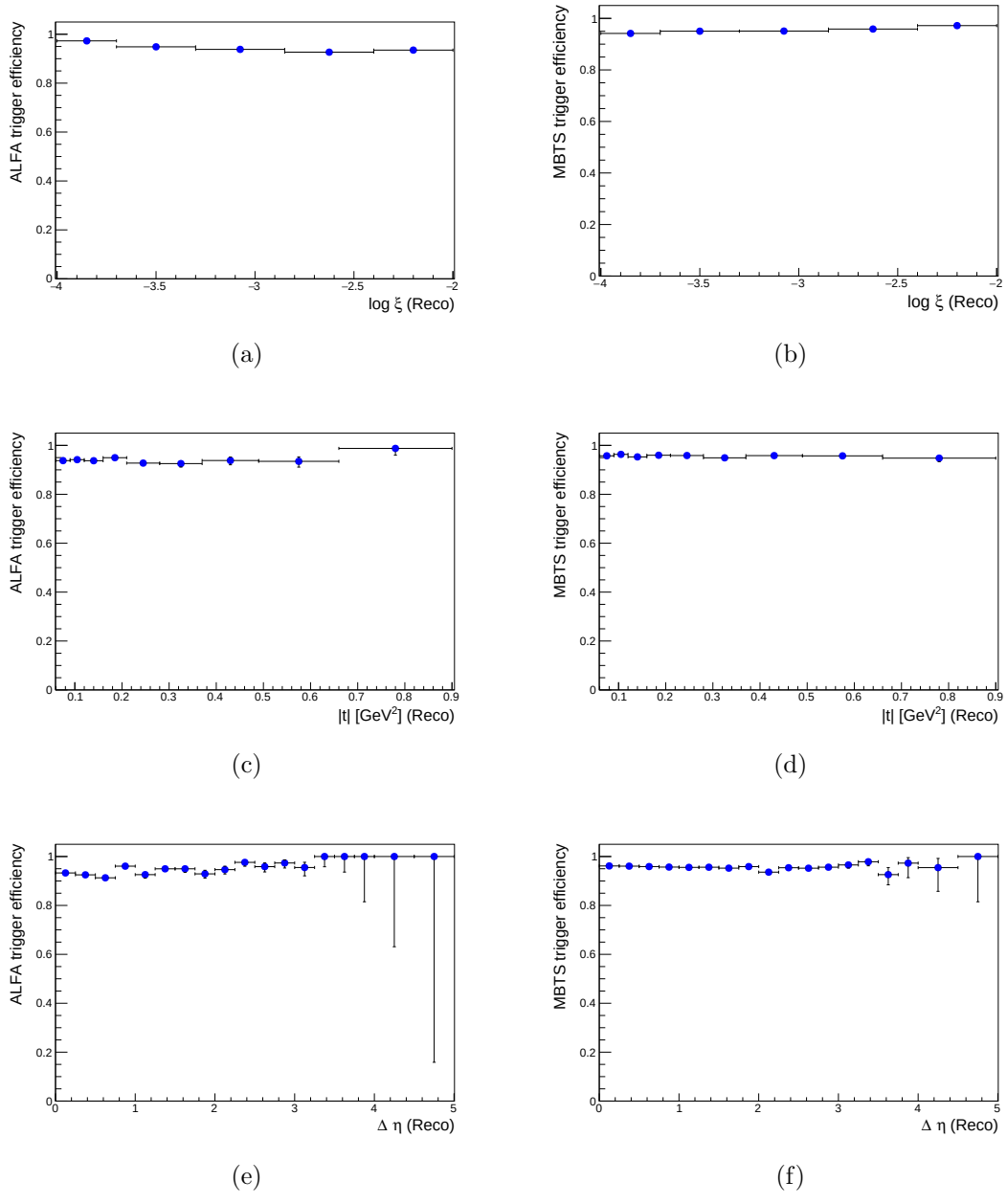

Figure 5.4: The calculated trigger efficiency as a function of each of the analysis variables. The efficiency is calculated separately for the ALFA and MBTS components of the trigger.

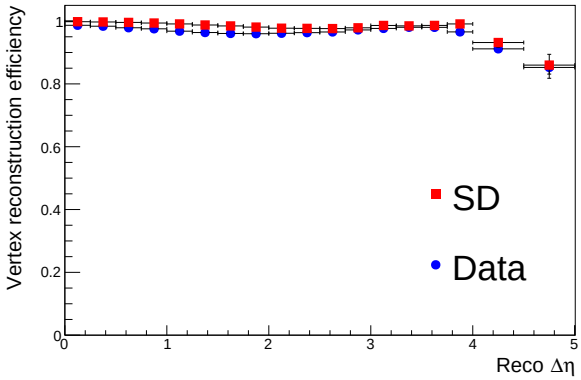

(a)

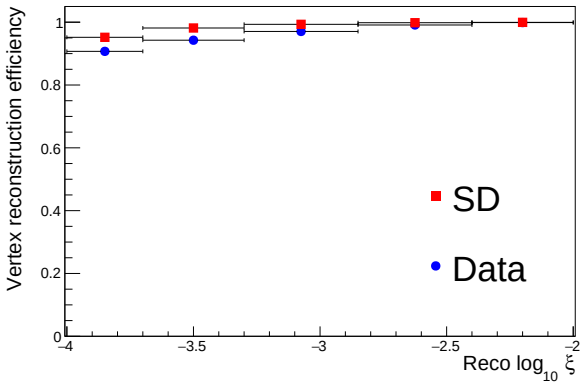

(b)

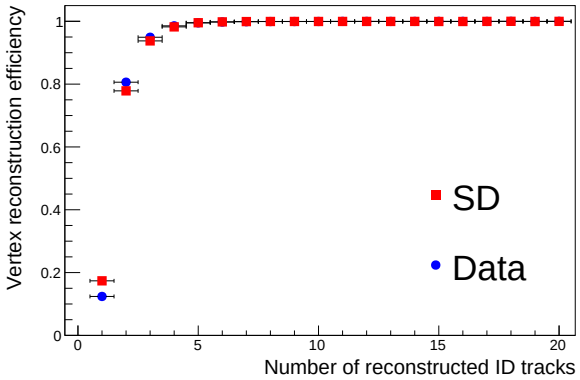

(c)

Figure 5.5: Vertex reconstruction efficiency as calculated for data and SD MC.

Figure 5.6: The tag and probe method. The solid green lines indicate the tag arm, which is required to contain a track passing the offline selection. The diagonally opposite arm is then probed for a corresponding proton, assuming elastic scattering, as indicated by the dashed blue line.

5.4 ALFA track reconstruction

The algorithm used by ALFA to reconstruct tracks, explained in section 3.2.9.2, is known to not be perfectly efficient. When there is a high multiplicity of fibres hit, the algorithm can incorrectly reconstruct the track position or fail to reconstruct a track at all. This can be caused by the showering of particles, pile-up collisions and other background processes. As noted already, the efficiency of the ALFA scintillating fibres is known to be approximately 100%[118] and so the dominant inefficiency in ALFA is the failure of the reconstruction algorithm.

The ALFA elastic cross-section analyses developed a data-driven tag-and-probe method for estimating the efficiency of the reconstruction algorithm[117, 118] which was adapted by the $\sqrt{s} = 8$ TeV SD cross-section analysis for measurements only requiring a single ALFA arm to be filled[3, 50]. The adapted method still uses elastic proton-proton collisions as they result in protons leaving the collision point in a back to back configuration and so, if detected by one arm of ALFA, should also be detected by the diagonally opposite arm. One arm, the tag, is required to contain a reconstructed track and the diagonally opposite arm, the probe, is tested for the presence of another reconstructed track. This configuration is shown in figure 5.6.

To select events, the elastic triggers (‘`L1_ALFA_ELAST11`’ and ‘`L1_ALFA_ELAST12`’) are used. These triggers are the result of a boolean ‘AND’ applied to the signals from

the four ALFA RPs in each elastic configuration.

It is possible for the elastic triggers to be fired by non-elastic events, in particular if two or more non-elastic events happen in coincidence. Non-elastic events should contain activity in the ATLAS central detector and therefore be detected by either the MBTS, LUCID or calorimeter systems. To remove these events from the sample studied, trigger items based on these systems ('`L1_MBTS_1`', '`L1_LUCID_1`' and '`L1_TE20`') are used as a veto. Section 5.4.1 describes how the residual background after theses vetoes is dealt with.

The ALFA arms that provide the trigger signals are only used as a 'tag' if they contain a track passing the full offline track selection: a single track in each RP containing at least 6 fibres from each plane, passing the x and y coordinate cuts and the elliptical selection in $\bar{x}$ and θ.

The probe arm is then the diagonally opposite arm, indicated by the dashed blue line in figure 5.6. To ensure that a proton has indeed passed through each RP of the probe arm and therefore there is a reasonable expectation for a track to have been reconstructed, the trigger counter must have fired (due to the requirement of the elastic trigger) and at least 12 different layers of scintillating fibres must have registered hits. If the probe arm does not satisfy these conditions it is discounted from the sample.

The track selection is then applied to the probe arm. If the arm passes the track selection it is recorded as $\mathrm{N_{Pass}}$. If it fails due to the θ and $\bar{x}$ selection only it is recorded as $\mathrm{N}_{\theta/\bar{x}}$, as explained in the following paragraph. Otherwise it is recorded as $\mathrm{N_{Fail}}$.

If the probe arm only fails the selection due to the θ and $\bar{x}$ requirement, it is recorded separately and not as a pass or fail event. The algorithm has not failed and so it would be wrong to classify it as a failure. The aim of this study is to understand the efficiency of the algorithm within the selection used by the analysis so it would also be wrong to classify it as a pass. Therefore tracks that fall outside of the θ

and $\bar{x}$ selection are recorded as $N_{\theta/\bar{x}}$ and are not used in the efficiency calculation directly. This occurrence could be due to a proton interacting with the near RP while passing through it and its path being altered as a consequence. The recorded number of failures, N_{Fail}, includes a contribution from the failure of the algorithm to form tracks that would have been outside the θ and $\bar{x}$ selection. This contribution can be estimated by assuming a reconstruction efficiency of 95%, the approximate efficiency measured when such a background is ignored. This assumption is tested as a systematic uncertainty in section 5.4.2. For every 20 protons outside of the θ and $\bar{x}$ selection, there should be 19 tracks reconstructed and 1 failure. The number of successful reconstructions is recorded ($N_{\theta/\bar{x}}$) and so the contribution to N_{Fail} from failures of the algorithm outside of the θ and $\bar{x}$ selection should be $\frac{1}{19}N_{\theta/\bar{x}}$.

Neglecting backgrounds, which are corrected for in the following section, the ALFA reconstruction efficiency is then calculated as:

$$\epsilon = \frac{N_{Pass}}{N_{Fail} + N_{Pass} - \frac{1}{19}N_{\theta/\bar{x}}}. \tag{5.2}$$

The values measured for each of these is shown in the appendix in table B.1.

5.4.1 Background

The calculation in equation 5.2 contains small contributions from uncorrelated background processes that should be removed to improve the accuracy of the measured efficiency. These background processes contribute to both the number of passes and failures.

To quantify this contribution, the elastic configuration where both arms pass the track selection criteria (i.e. the case corresponding to N_{Pass}) is investigated further. Due to the ATLAS central detector vetoes, the most probable cause of activity in the other RPs is from an additional elastic collision. To remove the contribution from two elastic collisions in coincidence, one of the non-elastic arms is required to have less than 12 plates with any fibres registering a hit. This is marked as the

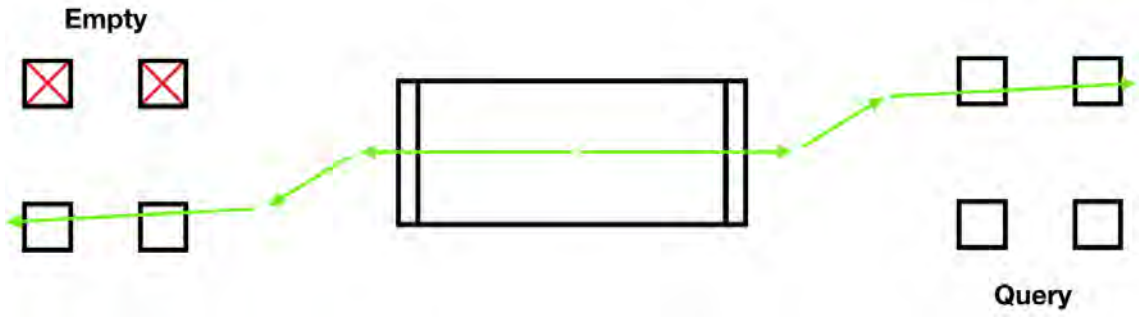

Figure 5.7: Measuring the background rate to the tag and probe method. The track selection is applied to elastic protons, indicated by the solid green lines. One of the other arms is required to be empty with less than 12 plates registering a fibre hit, indicated by the red crossed out boxes. The remaining arm is then queried to find the background rate of tracks.

empty arm in figure 5.7. The remaining arm, referred to as the query arm, is then used for estimating the background for each arm. Any activity within it is expected to be from backgrounds, uncorrelated with the elastic event. The rate of activity in the query arm can then be used to correct for background processes in the efficiency calculation.

The number of events in this configuration, depicted in figure 5.7, is recorded as $n_{Queries}$. The 'fail background' events are the cases where the query arm does not contain a track passing the track selection but does have at least 12 plates registering a hit fibre in each RP. The probability per bunch crossing at which this happens is then taken to be:

$$P_{Fail}^{Background} = \frac{n_{Fail}^{Background}}{n_{Queries}}. \tag{5.3}$$

The 'pass background' category is the cases where the query arm passes the track selection. The probability is similarly calculated as:

$$P_{Pass}^{Background} = \frac{n_{Pass}^{Background}}{n_{Queries}}. \tag{5.4}$$

The probabilities can then be combined and scaled by the number of bunch crossings

in the sample ($n_{\text{Bunch crossings}}$) and the trigger prescale (PS) to find the expected number of successes and failures of the track reconstruction due to the uncorrelated background. The contributions from the background processes are calculated as below, using the A-side upper (AU) arm as an example:

$$N_{\text{Pass}}^{\text{Background}}(\text{AU}) = \frac{P_{\text{Pass}}^{\text{Background}}(\text{AU}) \times P_{\text{Pass}}^{\text{Background}}(\text{CL}) \times n_{\text{Bunch crossings}}}{\text{PS}}. \tag{5.5}$$

$$N_{\text{Fail}}^{\text{Background}}(\text{AU}) = \frac{P_{\text{Fail}}^{\text{Background}}(\text{AU}) \times P_{\text{Pass}}^{\text{Background}}(\text{CL}) \times n_{\text{Bunch crossings}}}{\text{PS}}. \tag{5.6}$$

The corrected efficiency calculation for each pot is then extended from equation 5.2 and calculated as:

$$\epsilon = \frac{N_{\text{Pass}} - N_{\text{Pass}}^{\text{Background}}}{N_{\text{Fail}} - N_{\text{Fail}}^{\text{Background}} + N_{\text{Pass}} - N_{\text{Pass}}^{\text{Background}} - \frac{1}{19}N_{\theta/\bar{x}}}. \tag{5.7}$$

The ALFA track reconstruction efficiency as calculated by equation 5.7 is shown in table 5.1 with statistical errors. The measured value of each parameter of equation 5.7 is shown in the appendix in table B.1.

Table 5.1: Efficiency values for ALFA track reconstruction. Errors are statistical, obtained using the binomial distribution[136, 137].

Arm	Efficiency ϵ
A Upper	0.9733 $\pm$0.0001
A Lower	0.9872 $\pm$0.0001
C Upper	0.9769 $\pm$0.0001
C Lower	0.9863 $\pm$0.0001

5.4.2 Systematic uncertainty

To estimate the systematic uncertainty on the ALFA track reconstruction efficiency, the selection criteria are varied as described below. The difference in the resulting efficiency is then taken to be the systematic uncertainty from that source, with a separate 'up' and 'down' variation for each criterion varied. From each criterion, the largest of each of the up and down uncertainties is summed in quadrature to find the total systematic uncertainty. This conservative approach is taken as the correlations between criteria are not explored.

The criteria varied are:

- **Elliptical selection.** The selection accepts tracks within 4σ of the centre of the $\bar{x}/\theta$ elliptical distribution. This was varied in both directions by 1σ away from the nominal value to 3σ, the optimal cut value used by the $\sqrt{s} = 8$ TeV analysis, and 5σ[50].

- **Assumed efficiency outside the ellipse.** The tag-and-probe method assumes a 95% reconstruction efficiency for ALFA tracks outside the $\bar{x}/\theta$ selection and corrects for the 5% of cases that failed. The assumed efficiency was varied to 100% and 90%.

- **Background process contribution.** The tag-and-probe method estimates the number of tracks which are formed (and not formed) due to background processes as $\mathrm{N}_{\mathrm{Pass}}^{\mathrm{Background}}$ (and $\mathrm{N}_{\mathrm{Fail}}^{\mathrm{Background}}$). The efficiency was calculated without any of these tracks and double the number.

- **The number of bunch crossings.** The number of tracks from background processes is dependent on the number of bunch crossings in the data sample analysed. The total number of bunch crossings in the sample was known but the number in the vetoed LBs was not. This number was assumed to be the total number of bunch crossings in the run, scaled by the fraction of the integrated luminosity analysed following the LB veto outlined in section

4.3.2.1. The number of bunch crossings was varied by scaling the nominal number by 0.95 and 1.05.

- **Minimum number of fibres.** The nominal selection requires at least 12 fibres in total to form a track, with at least 6 u and 6 v fibres. The tag-and-probe method also requires or vetoes RPs if they have at least 12 fibres hits. The minimum number of fibres was varied between 10 and 14.

- **Y coordinate selection.** As explained in section 4.3.2.4, ALFA tracks are only accepted if they fall within a range of y coordinates, the edges of which are fixed by the beam-side edge of ALFA and the LHC beam-screen on the outer edge. The region within which tracks are accepted is varied by ± 0.2 mm on the beam-side and ± 0.1 mm on the beam-screen side.

The individual systematic uncertainties are presented in the appendix in table B.2. The total uncertainties are shown for each arm in table 5.2.

Table 5.2: Calculated track reconstruction efficiency for each ALFA arm. The uncertainty shown is the sum, in quadrature, of the statistical and systematic uncertainties.

Arm	Efficiency	Total uncertainty
AU	0.97	± 0.04
AL	0.99	± 0.02
CU	0.98	± 0.02
CL	0.99	± 0.02

5.5 Correction method

Sources of differences in efficiencies between the data and MC have been studied and quantified in the previous sections. To correct for the differences the MC was given different weighting factors due to:

- **Pile-up**: A constant factor of 0.9954.
- **Trigger prescale**: A constant factor of 190.
- **Trigger efficiency**: A bin-by-bin correction for the analysis variables, using the efficiency values shown in figure 5.4. For the supporting plots of the ID track or MBTS multiplicity, the correction is based on the number of MBTS counters above their threshold on the opposite side to the ALFA tag, using the efficiency values shown in figure 5.3.
- **Vertex reconstruction efficiency**: For $\Delta\eta$ and $\log_{10}\xi$, a bin-by-bin correction using the efficiency values shown in figure 5.5. For the remaining distributions a correction based on the number of ID tracks. The correction factor, $\epsilon_{\text{Data}}/\epsilon_{\text{MC}}$ takes into account the measured efficiency in both data and MC. For events with more than 10 ID tracks the vertex reconstruction is assumed to be 100% efficient in both data and MC so no weighting is applied.
- **ALFA track reconstruction efficiency**: A per track correction based on the arm a proton would have been detected in, using the probabilities shown in table 5.2.

No weights were applied to data.

CHAPTER 6

Background determination

The event selection, explained fully in chapter 4, was optimised for selecting SD events and removing background contributions. There was, however, still some contamination present which needed to be understood in order to be subtracted. This chapter describes how the backgrounds were modelled, prior to subtraction from the data distributions and unfolding. Section 6.1 discusses the contributions to the background from individual processes. Section 6.2 explains how an additional source of background, which is due to the coincidence of separate activity in ATLAS and ALFA, is modelled. Section 6.3 then presents reconstructed distributions of data and MC, including the background sources explained here.

6.1 Simulated backgrounds

MC samples were used to assess the background contributions from non-SD, non-elastic physics processes. Despite its relatively small cross-section, the largest contribution was from CD, due to the presence of a central diffractive system and intact protons. If one of the two intact CD protons is detected by ALFA, a CD event should appear similar to an SD event (as can be seen by comparing figures 6.1a and 6.1b). The background contribution from CD is assessed as a systematic uncertainty using a dedicated control region, this is described in section 8.9.

Background contributions can arise from ND and DD due to the formation of protons at high pseudorapidities in hadronic showers. However this is found to be statistically unlikely and so these contributions are very small when assessed using MC.

6.2 Overlay backgrounds

An additional, more significant, source of background is due to the coincidence of two unrelated background processes in ATLAS and ALFA. Individually the processes would not meet the selection criteria but when occurring in coincidence they result in the dominant background in this analysis. ND events make the largest contribution to the ATLAS central detector process. Possible sources of background in ALFA include beam halo events[1] or elastic scattering. In a scenario such as simultaneous ND and beam halo events, ATLAS would contain a vertex and MBTS activity and ALFA would contain a proton track and therefore the event selection could be satisfied. Figure 6.1c demonstrates how this produces a similar signal to SD events. The contribution of this type of background to the analysis, referred to as the 'overlay background', is estimated using an adapted method first devised for the $\sqrt{s} = 8$ TeV SD analysis[50].

[1]Beam halo events are due to protons, usually far from the centre of bunches, interacting with detector or collider infrastructure resulting in a shower of particles[138].

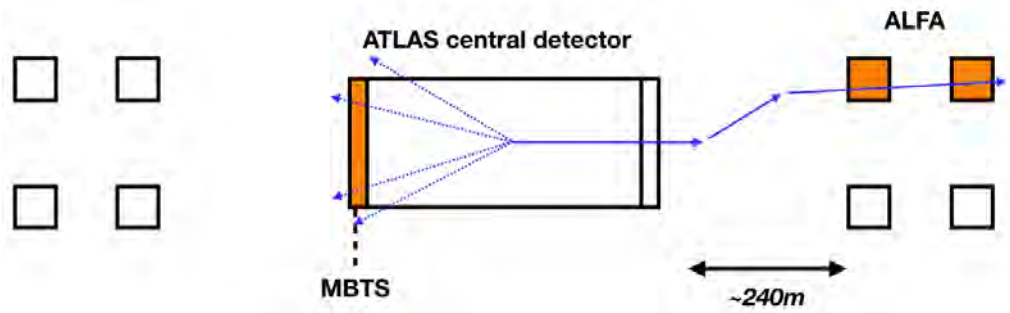

(a) A signal SD event. The intact proton is detected by ALFA and the dissociative system is detected by the MBTS.

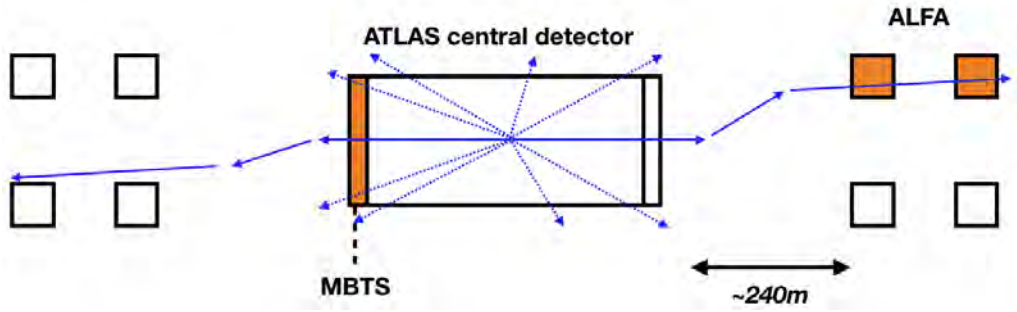

(b) A background CD event. There are two intact protons in the final state but in this case only one is detected by ALFA. The central diffractive system is detected by the ID and MBTS.

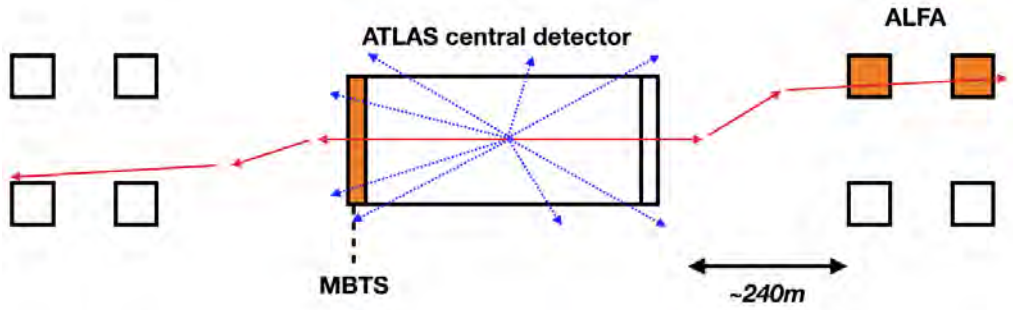

(c) An overlay background event. A high ξ pile-up event (blue) triggers the MBTS, fulfils the vertex requirement and is measured by the ATLAS central detector. Simultaneously ALFA detects a single proton (red). This could be due to an elastic collision, as shown in the diagram, or from beam backgrounds.

Figure 6.1: SD and the two major background sources that produce similar detector responses. Solid lines indicate intact protons and dashed lines indicate particles measured by the central ATLAS detector.

An event selection, referred to here as the 'ND selection,' is applied to data to obtain a ND enriched sample. The sample is selected using the '`L1_MBTS_1`' trigger with the offline requirement of a reconstructed vertex, all counters of the MBTS passing their offline thresholds and only a small (≤ 0.5) rapidity gap on both sides of the detector. According to MC, more than99.5% of this data selection consists of ND events.

As the vast majority of the events in this sample should be ND there should be a minimal number of intact protons at high rapidities. MC predicts that less than 5×10^{-6} of ND events passing the selection should produce activity in ALFA. Therefore to very good approximation, any protons that are reconstructed in ALFA should not be from the event seen in the ATLAS central detector and instead be from the background sources that contribute to the overlay background. The number of protons detected in ALFA that pass the selection cuts, including the fiducial $|t|$ selection, are recorded from this sample.

It is possible, but unlikely, that some of the protons observed in ALFA in this sample are due to single-source diffractive processes that pass the ND selection. To correct for this, the same event selection is applied to the MC samples and for each sample, the number of protons seen in ALFA is subtracted from the number measured in data as a function of $|t|$. This results in an approximately 10% correction as more than 1500 data events and approximately 150 MC events[2] contained any ALFA protons.

It is assumed that the remaining protons observed in the ND selection in data are due to background processes unrelated to the events observed by the central ATLAS detector. No further effort is made to understand the cause of the overlay protons, or the processes that lead to them. It is assumed that the overlay protons occur at a constant rate and probability, regardless of the event occurring in ATLAS.

The probabilities of overlay protons occurring are shown in table 6.1. The event

[2]Calculated by scaling the MC samples to the luminosity of the data, taking into account the prescale of the trigger used here.

selection and weighting of MC samples is adjusted to account for these probabilities.

Table 6.1: Probabilities of overlay ALFA protons, calculated as described in section 6.2.

Number of ALFA protons	Probability
0	0.9892
1	0.0064
2	0.0044
3	$\leq 2 \times 10^{-5}$
4	$\leq 2 \times 10^{-5}$

MC events that pass the nominal event selection are given a weight of 0.9892 to account for the probability of an overlay proton causing the event to fail the selection.

MC events that pass the nominal event selection with the exception of the ALFA proton requirement are considered as part of the overlay background and are used to quantify the subtraction necessary from the raw data as explained below[3]. The overlay probabilities do not include directional information about which arm of ALFA any overlay protons occur in and so the weighting must reflect that:

- If a particular MC event only exceeds the MBTS requirement on one side of the detector, it is given a weight of $0.0032 (= 0.0064 \times 0.5)$. The 0.0064 factor corresponds to the probability of one overlay proton, as shown in table 6.1. The additional factor of 0.5 is to account for the fact that, in half of all cases, an overlay proton would not be on the side opposing the MBTS tiles and so the event would still fail the event selection. This can be seen by comparing figures 6.2a and 6.2b. Similar considerations must be made for the $\log_{10}\xi$ measurement due to the sign of the $p_{z,i}$ term depending on the direction of the proton tag (see equation 4.2).

[3]It is worth noting the method for calculating the overlay probabilities already takes into account the ALFA track reconstruction efficiency and so overlay protons do not need this weighting applied.

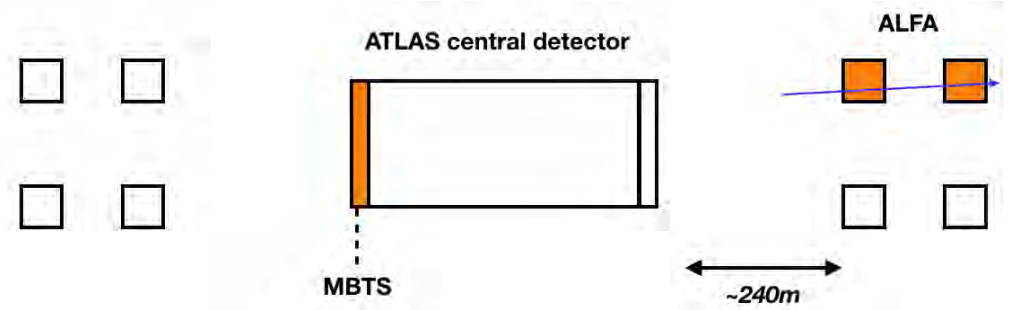

(a) Contributes to the overlay background (with additional weight of 0.5).

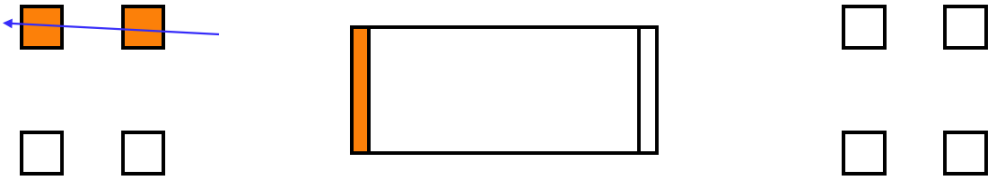

(b) Does not contribute to the overlay background.

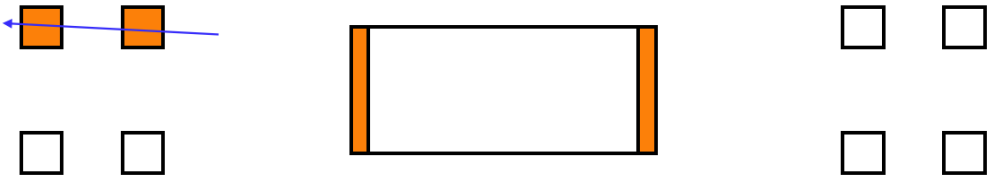

(c) Contributes to the overlay background.

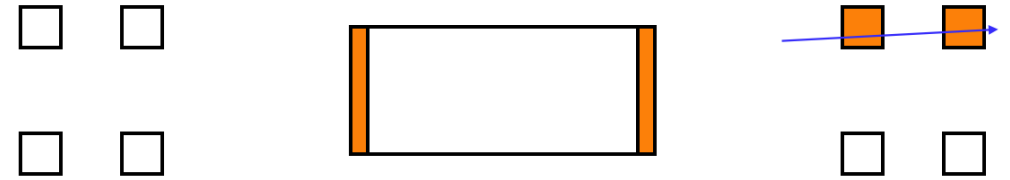

(d) Contributes to the overlay background.

Figure 6.2: Possible arrangements of an overlay background event, with overlay protons shown as blue arrows. In the case of a single side of the detector passing the MBTS requirement, an additional weighting of 0.5 is applied to account for the probability of the overlay proton being on either side of the detector and consequently passing or failing, as in (a) and (b). In the case of both sides of the detector passing the MBTS requirement, two values of $\Delta\eta$ and $\log_{10}\xi$ are reconstructed and given an additional weighting of 0.5 to account for the probability of the proton being on either side of the detector, as in (c) and (d).

- In the cases where both sides of the detector pass the MBTS and $\log_{10}\xi$ requirements, as shown by figures 6.2c and 6.2d, two values are reconstructed for $\Delta\eta$ and $\log_{10}\xi$. The rapidity gap on either side of the detector is used for $\Delta\eta$ and $\log_{10}\xi$ is reconstructed using both signs of $p_{z,i}$. Each of the variables are then assigned a weight of 0.0032, accounting for the fact that the overlay proton could be on either side of the detector.

To model the $|t|$ distribution from the overlay background, a template is formed based on the distribution measured in the ND-enriched data sample. The $|t|$ distributions predicted from the MC samples passing the ND event selection are subtracted. The template is then normalised (to the number of protons contributing to it), scaled down according to the measured trigger efficiencies and then scaled up according to the weighting of events forming the overlay background, following the considerations above.

To assess the accuracy of this method in modelling data, a two proton control region is defined. This is identical to the nominal event selection except for the requirement of a second proton passing the ALFA selection. No explicit requirement is placed on the direction of the second proton, although the dominant case is protons leaving the detector in opposing directions as expected in elastic scattering. For overlay protons, the second proton is therefore assumed to be going in the opposite direction to the 'real' proton.

In data, this control sample is seeded by the '`L1_MBTS_1`' trigger and so the ALFA trigger efficiency is not applied to MC. All reconstructed plots are scaled using the same weighting to account for the trigger and vertex reconstruction efficiencies. The trigger efficiency is calculated as a function of the number of MBTS counters above their offline threshold on each side of the detector using the efficiency shown in figure 5.3. The efficiency shown is for a single side of the detector, whereas for the control sample, either side may provide the trigger signal. Therefore the efficiency ($\epsilon_{\text{A or C}}$)

is calculated using the trigger efficiency from each side of the detector (ϵ_{A} or ϵ_{C}) as:

$$\epsilon_{\mathrm{A\ or\ C}} = \epsilon_{\mathrm{A}} + \epsilon_{\mathrm{C}} - \epsilon_{\mathrm{A}}\epsilon_{\mathrm{C}}. \tag{6.1}$$

The vertex reconstruction efficiency is calculated as a function of the number of ID tracks.

The two proton control region is dominated by the overlay background, with a small contribution from CD. The overlay background distributions in this control region are formed from MC events with 2 overlay protons added, with a nominal weight of 0.0044, and events with 1 ALFA proton and 1 overlay proton, with a nominal weight of 0.0064 (see table 6.1).

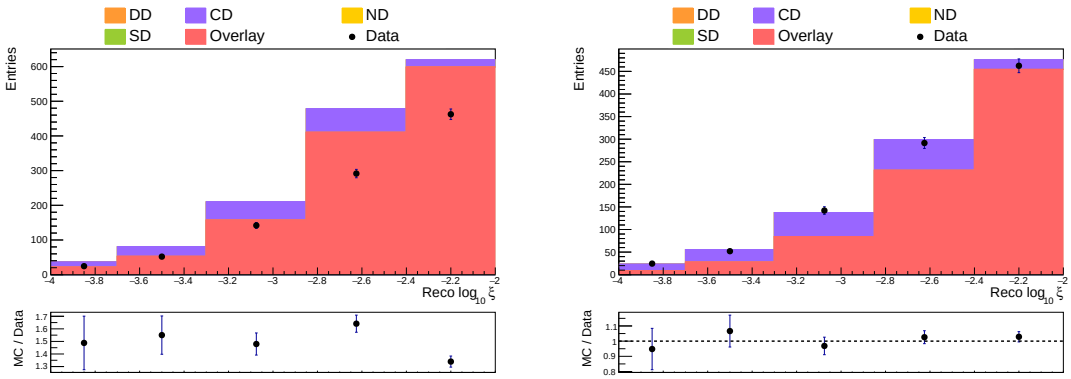

(a) (b)

Figure 6.3: Reconstructed distributions of $\log_{10}\xi$ in the two proton control region, before (a) and after (b) re-weighting using equation 6.2.

The two proton control region showed that the data-driven model over-predicted the contribution from the overlay background, as shown by figure 6.3a. The excess exhibits a $\log_{10}\xi$ dependence, without depending significantly on other variables. Therefore to correct this, a third-degree polynomial was used to re-weight the overlay background to better match data:

$$\text{Weighting} = 11.16 \times (\log_{10}\xi^3) - 10.53 \times (\log_{10}\xi^2) - 3.46 \times (\log_{10}\xi) - 0.38. \tag{6.2}$$

Figure 6.3b shows the reconstructed $\log_{10}\xi$ distribution after the re-weighting was

applied in the two proton control region.

6.3 Reconstructed distributions

Reconstructed plots are shown, using the two proton control region and with the re-weighting applied, in figure 6.4. These plots show the analysis variables: $\log_{10}\xi$, $\Delta\eta$ and $|t|$. They also show the number of MBTS counters above their offline threshold and the number of ID tracks. All of the distributions demonstrate reasonable agreement between data and the model, with the exception of the high $\Delta\eta$ region (where statistics are limited) and for the number of MBTS counters above threshold (which is due to simulation discrepancies). This is not a concern as this region is excluded from the analysis due to non-closure of the unfolding procedure, (see section 7.3 for details). CD dominates in low MBTS multiplicity events, as is visible in figure 6.4d. This region is therefore used to define an additional control region for assessing the systematic uncertainty arising from the CD contribution to the background, as explained in section 8.9.

The equivalent set of reconstructed plots is shown for the nominal event selection in figure 6.5. All of the plots show the model based on the MC samples and overlay background over-predicts the data distribution. This is as expected as the $\sqrt{s} = 8$ TeV analysis showed the over-prediction of the SD cross-section, as demonstrated by figure 2.13, so one can expect similar effects at $\sqrt{s} = 13$ TeV. Shape disagreement in the multiplicity plots of MBTS counters and ID tracks (figures 6.5d and 6.5e) has been observed by other analyses, so is not unexpected[50, 52].

The over-prediction of MC, is also observed in the unfolded distributions from this analysis, as shown in figure 9.1. By comparing the measured cross-sections, with those predicted by MC, a normalisation difference of approximately $\frac{5}{3}$ is observed (see table 9.1). This factor is applied to the SD contributions in the reconstructed distributions in figure 6.6. This figure shows better agreement and demonstrates how the normalisation is the main source of the disagreement in figure 6.5. The

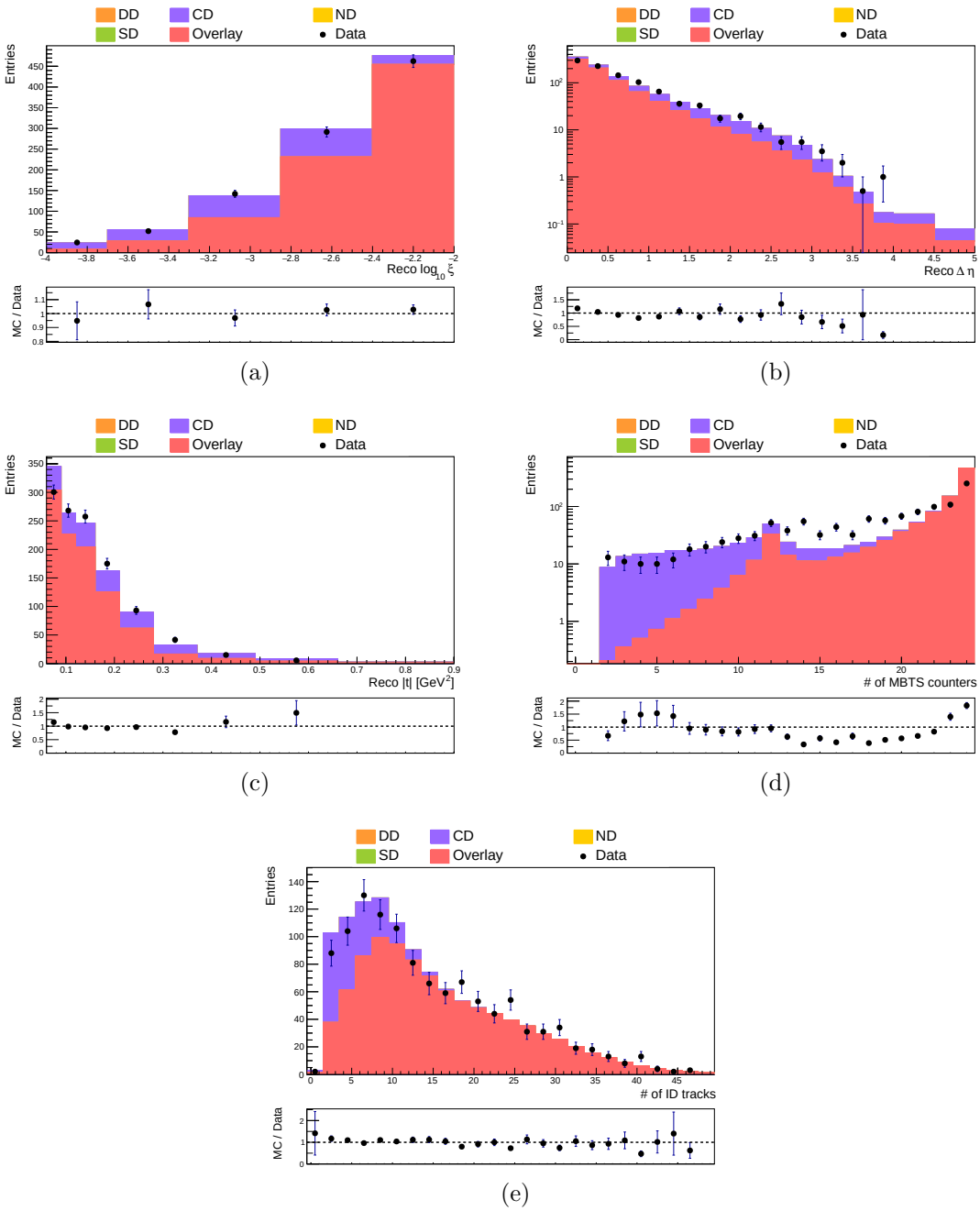

Figure 6.4: Reconstructed distributions using the two proton event selection.

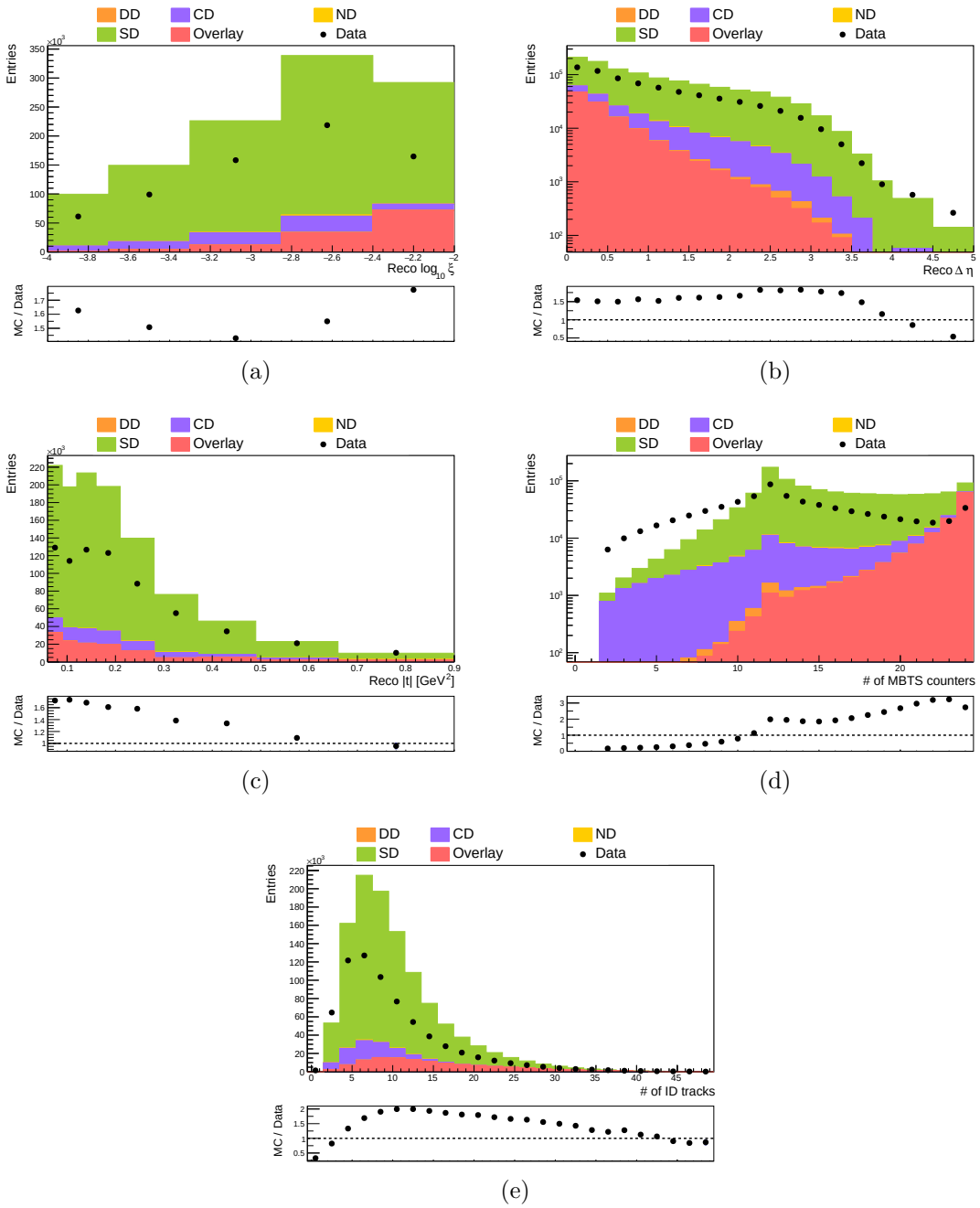

Figure 6.5: Reconstructed distributions using the nominal event selection.

distribution of $\Delta\eta$, shown in figure 6.6b, demonstrates good agreement below $\Delta\eta = 3.5$. The distribution of $\log_{10}\xi$, shown in figure 6.6a, shows good agreement with the exception of the last bin where the overlay background dominates. The overlay background contribution is varied as a systematic uncertainty in section 8.8, in part to account for such discrepancies. Figure 6.6c, the $|t|$ distribution, still demonstrates some shape disagreement, made more obvious in the ratio plot. This corresponds to the discrepancy in the measured slope parameter with that used by the SD MC, see chapter 9 for more details.

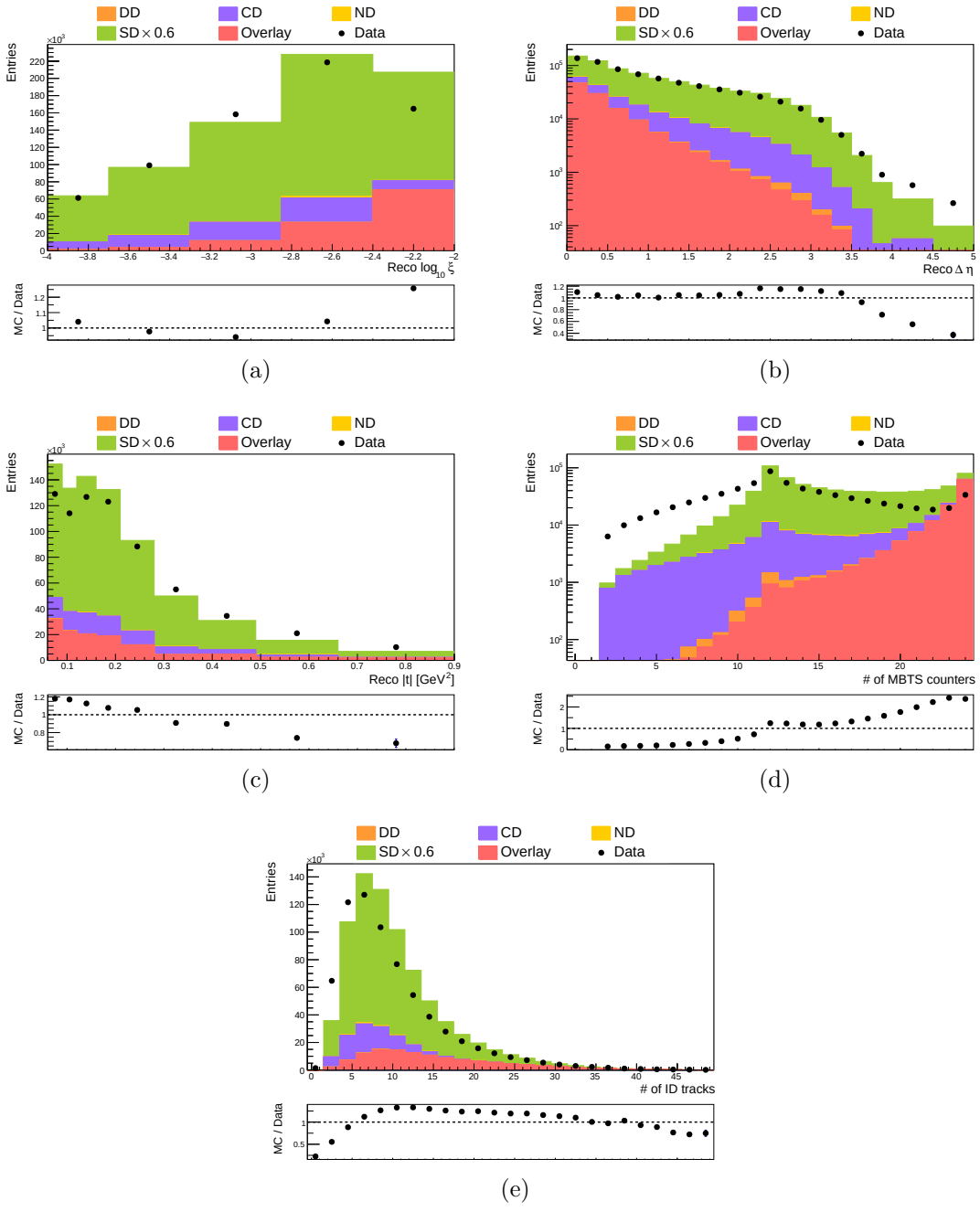

Figure 6.6: Reconstructed distributions using the nominal event selection, with the SD contribution scaled down by a constant factor of 0.6.

CHAPTER 7

Unfolding

The reconstructed data distributions, after efficiency corrections and background subtraction, are 'unfolded' to find the hadron level distributions. Unfolding is explained in section 7.1. Section 7.2 presents plots that support the validity of unfolding the unfolding method. Section 7.3 explains how the unfolding procedure was optimised, including a treatment of the systematic uncertainties arising from it.

7.1 The Concept of Unfolding

Like many particle physics analyses, this analysis measures continuous distributions in discretely binned histograms. The resulting histograms include statistical fluctuations as well as instrumentation effects arising from the finite detector resolution, acceptance and efficiency. The measured distributions are therefore distorted compared to their hadron level counterparts. To compare data to a single theoretical

prediction, one could apply the detector smearing effects to an MC model and compare the resulting distributions. Removing the detector effects from data instead, known as unfolding, allows one to make direct comparisons between the measured distributions and theoretical predictions and other experimental results[136, 139]. An unfolded result is more easily interpreted by theorists or other experimentalists, as one does not need to understand the performance of the detector in question. The measured distribution, $\vec{m}$, is considered the result of a hadron level (or truth) distribution, $\vec{t}$, smeared by a response matrix $\mathbf{R}$:

$$\mathbf{R}\vec{t} = \vec{m} \tag{7.1}$$

One wants to know which hadron level distribution ($\vec{t}$) results in the measured data ($\vec{m}$). This is not a simple problem as the response matrix ($\mathbf{R}$) does not necessarily have an inverse.

There are several methods for unfolding available. For example, rudimentary bin-by-bin unfolding estimates the measurement efficiency in the diagonal bins of the response matrix and corrects for the relative differences between MC and data. It does not generally account for migrations between bins and so a minimal amount of migration, or high purity (defined below in equation 7.3) is required to ensure reasonable results[136, 139]. Iterative Bayesian unfolding has several advantages, two of which are that it can take into account any kind of smearing or migration and can be written as a fast program[140, 141]. This is the procedure chosen to unfold the data in this analysis.

In practice (for a single, one-dimensional distribution) an MC sample is used to produce a response matrix by plotting each reconstructed bin against the corresponding hadron level bin. In addition to a distribution of all truth values and a distribution of all reconstructed values in the MC sample, all the information required to unfold a measured data distribution is obtained. Using these distributions, the `RooUnfold` implementation of iterative Bayesian unfolding takes into account events that fail

the event selection or migrate into other reconstructed bins[139].

The number of iterations used to unfold each distribution should be carefully chosen. In the case of a high number of iterations, statistical fluctuations blow up due to positive feedback across each iteration[141]. Too few iterations will not fully account for the detector effects present in the measured data distribution. There are different methods for deducing the optimal number of iterations. The method used here is explained in section 7.3.

To calculate a differential cross-section from a histogram of reconstructed values, one uses the equation:

$$\frac{d\sigma}{dX_i} = \frac{1}{\mathscr{L} \times \Delta X_i} \sum_j \mathbf{R}_{ij}^{-1} \left(N_j^{\text{Obs}} - N_j^{\text{Back}} \right) \tag{7.2}$$

The background subtracted data distribution, $N_j^{\text{Obs}} - N_j^{\text{Back}}$, is unfolded using the inverted response matrix $\mathbf{R}_{ij}^{-1}$. This should also account for missing signal events or signal events migrating from outside the fiducial range. Each bin in the unfolded histogram is then divided by the bin width ΔX_i and the luminosity $\mathscr{L}$, taking into account the trigger prescale.

7.2 Validation

While able to account for bin migrations, iterative Bayesian unfolding is more reliable when applied to diagonal response matrices. The response matrices for this analysis are normalised to unity in each truth bin and can be seen in figures 7.1a, 7.1c and 7.1e. All of the response matrices are reasonably diagonal, with the exception of the upper end of the $\Delta\eta$ plot (7.1e) which is possibly due to poor statistics in this region.

Purity is defined as the fraction of events in a reconstructed bin that fall into the

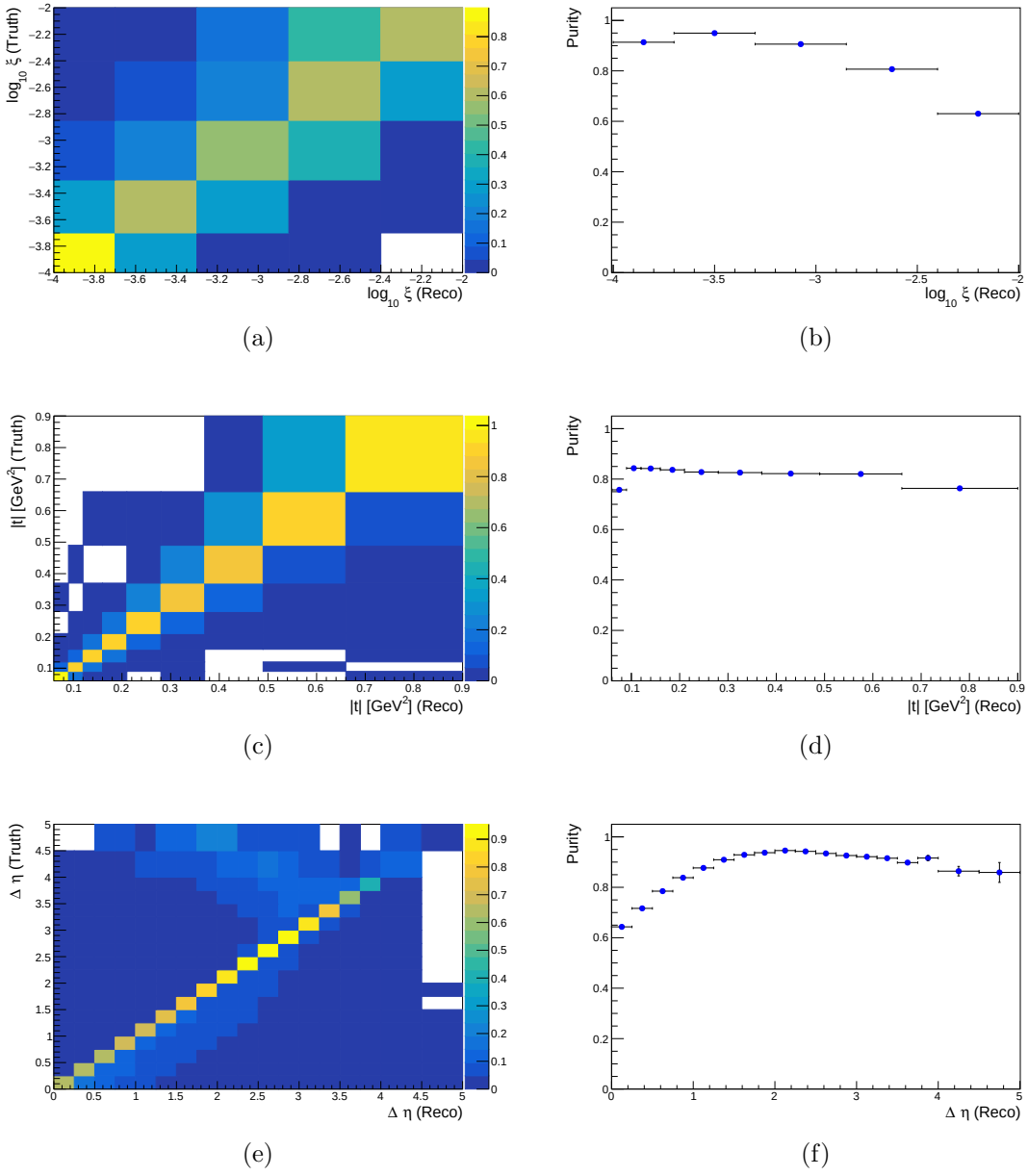

Figure 7.1: The normalised response matrices (left) and purity distributions (right). Purity is defined in equation 7.3.

corresponding truth bin:

$$\text{Purity} = \frac{\text{N}^{\text{Reco and Truth}}}{\text{N}^{\text{Reco}}}. \tag{7.3}$$

Plots of purity are shown in figures 7.1b, 7.1d and 7.1f. All of the distributions show reasonable purity, with the higher bins in $\log_{10}\xi$ showing the worst, but still satisfactory (> 0.5), purity.

Iterative Bayesian unfolding accounts for events reconstructed in the incorrect bin. The fake factor of a reconstructed bin is the proportion of events that correspond to another truth bin:

$$\text{Fake factor} = \frac{\text{N}^{\text{Reco}} - \text{N}^{\text{Reco and truth}}}{\text{N}^{\text{Reco}}} = 1 - \text{Purity}. \tag{7.4}$$

The miss factor, the proportion of events of a truth bin that fall into another reconstructed bin, is also accounted for:

$$\text{Miss factor} = \frac{\text{N}^{\text{Truth}} - \text{N}^{\text{Reco and truth}}}{\text{N}^{\text{Truth}}}. \tag{7.5}$$

Figure 7.2 shows the fake and miss factors for the analysis variables on the left and right, respectively. All of the variables exhibit a consistently low (< 0.4) fake factor. $\Delta\eta$ demonstrates a very high miss factor in the highest bins, which has already been observed in the response matrix (figure 7.1e). The miss factors may appear high, but take into account the acceptance of the measurement which has already been shown, for example, to be less than 45% at its maximum for $\log_{10}\xi$ in figure 4.11. This is dominated by the ALFA acceptance which is well understood and so should be accounted for in the unfolding procedure.

To test the unfolding tools were correctly set up, the reconstructed MC distributions were used in place of the data distributions and unfolded using a single iteration. The unfolded reconstructed distributions should match the truth level distributions, removing all of the detector effects arising from the event selection and reconstruction. Figure 7.3 shows the output of this (simple) closure test. The unfolded and truth distributions match, indicating that the unfolding was functioning correctly.

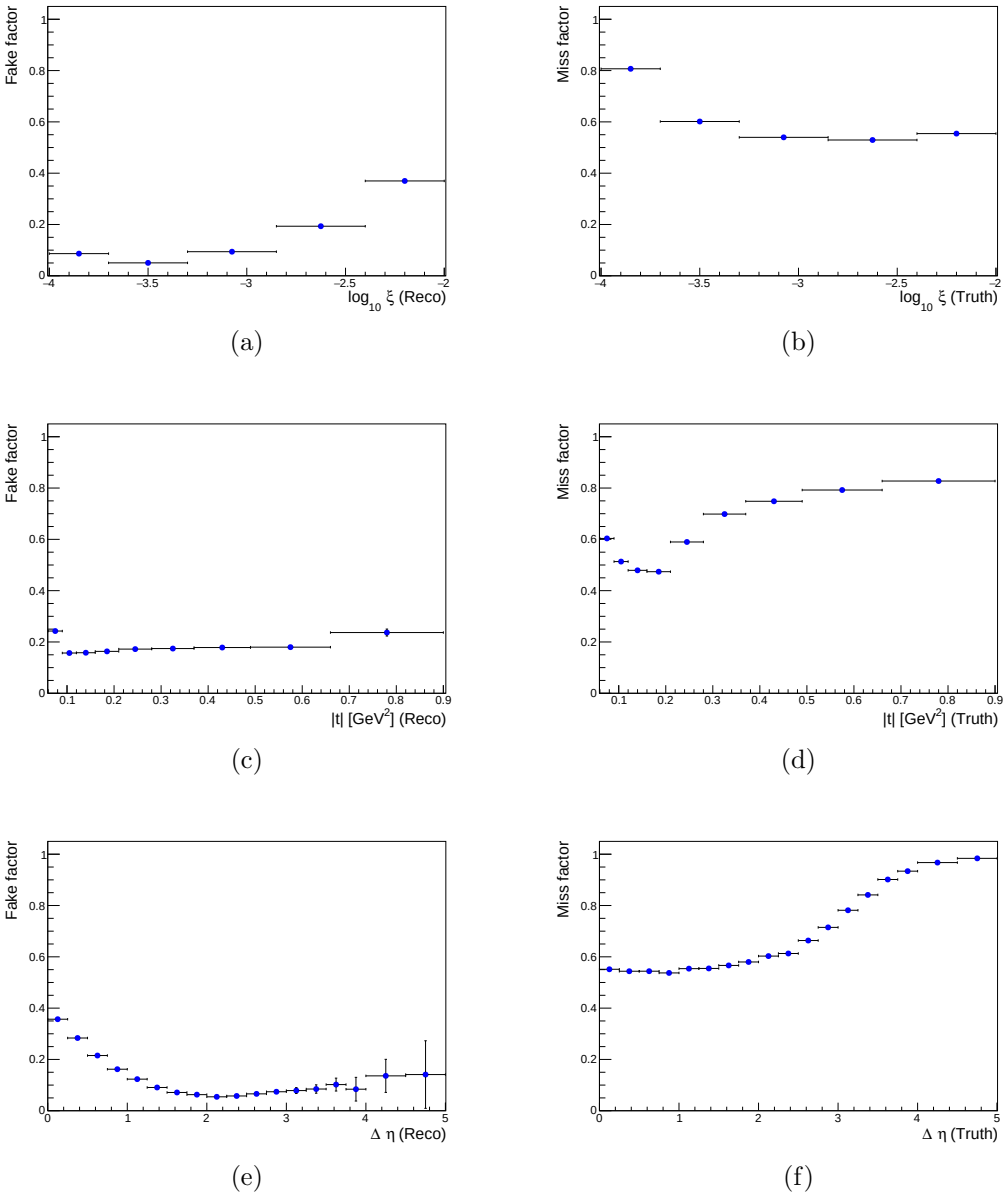

Figure 7.2: The fake and miss factors, defined in equations 7.4 and 7.5, respectively.

7.3 Optimisation

As mentioned already, one needs to choose how many iterations of unfolding should be used to correct the data distributions. The ATLAS standard model recommendation is followed here[142].

The MC is re-weighted using a polynomial function of each seperate truth level variable. The reconstructed MC background distributions are subtracted from the reconstructed data distribution, prior to division by the reconstructed (signal) SD distribution. The function is fitted to the resulting distribution and used to reweight the MC to make it more 'data-like'.

The systematic uncertainty is calculated for each iteration by assessing the ability of the unfolding procedure applied to the data-like distribution. The reconstructed MC is re-weighted using the polynomial function and then unfolded. The truth distribution is re-weighted by the same function. The systematic uncertainty is then taken as the difference between the unfolded, re-weighted, reconstructed distribution and the truth, re-weighted distribution. The number of iterations is chosen to either minimise the average uncertainty per bin (when no fit is performed on the unfolded distribution as is the case for $\Delta\eta$) or to minimise the uncertainty on the fit to the unfolded data (when a fit is performed on the unfolded distribution as is the case for $\log_{10}\xi$ and $|t|$ in sections 9.4 and 9.3, respectively).

The functions used to re-weight each distribution were:

$$\begin{aligned}
\text{Weight}(\log_{10}\xi) &= -0.052 \times \log_{10}\xi^3 - 0.704 \times \log_{10}\xi^2 - 2.900 \times \log_{10}\xi - 3.134. \\
\text{Weight}(|t|) &= -0.220 \times |t|^3 + 0.553 \times |t|^2 + 0.545 \times |t| + 0.415. \\
\text{Weight}(\Delta\eta) &= 0.009 \times \Delta\eta^4 - 0.025 \times \Delta\eta^3 - 0.053 \times \Delta\eta^2 + 0.165 \times \Delta\eta + 0.490.
\end{aligned} \tag{7.6}$$

The reconstructed distributions of data, MC and re-weighted MC are shown in figures 7.4a, 7.4c and 7.4e. The unfolded, re-weighted MC is shown in figures 7.4b,

7.4d and 7.4f with the truth level, re-weighted MC. The number of iterations of unfolding used in these plots is the same as those chosen for unfolding the data, shown in table 7.1. The $\Delta\eta$ distribution shows significant non-closure above $\Delta\eta = 3.5$ and therefore this region was excluded from further use. The deviation in $\log_{10}\xi$ shows that the unfolding procedure is not working as well as for the other distributions. This non-closure is accounted for in the unfolding systematic uncertainty.

The fractional uncertainty in each bin for several different iterations can be seen in figures 7.5a, 7.5b and 7.5c. The non-closure of $\Delta\eta$ above $\Delta\eta = 3.5$ appears as a large uncertainty in this region.

Using the method outlined above, the average fractional uncertainty (across all the bins) for each variable is shown in figures 7.6a, 7.6c and 7.6e. The bins above $\Delta\eta = 3.5$ were excluded from the average calculation to avoid biasing it. Figure 7.6e indicates that 5 iterations of unfolding is optimal for $\Delta\eta$.

The unfolded distributions were fitted, with and without the unfolding systematic uncertainties, following the procedure explained in chapter 9 to calculate the fit uncertainty for each iteration of unfolding. Figures 7.6b and 7.6d shows this as a function of the number of iterations of unfolding. Both plots indicate one iteration is optimal for unfolding $\log_{10}\xi$ and $|t|$.

With the considerations outlined above, the number of iterations of unfolding applied to each result was decided and is summarised in table 7.1.

Table 7.1: The number of iterations of unfolding applied to each analysis variable.

Variable	Number of iterations
$\log_{10}\xi$	1
$\|t\|$	1
$\Delta\eta$	4

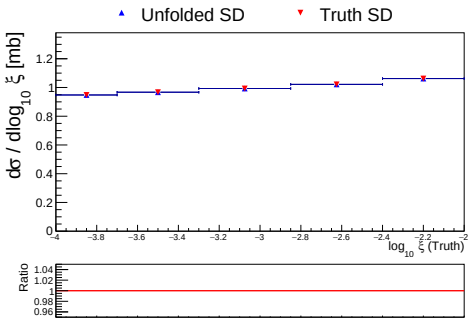

(a)

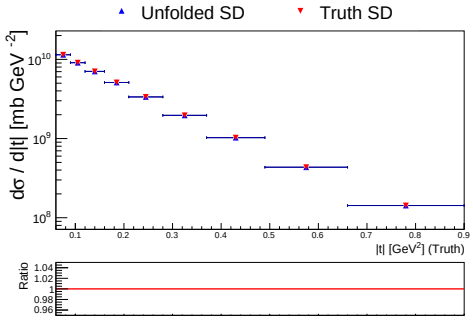

(b)

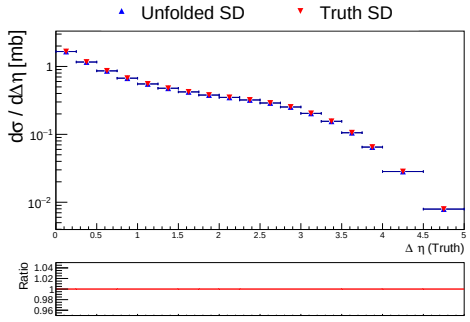

(c)

Figure 7.3: A simple closure test. The unfolded MC distribution matching the truth distribution demonstrates the unfolding package was being implemented properly and working correctly. The ratio indicated is the truth distribution divided by the unfolded distribution.

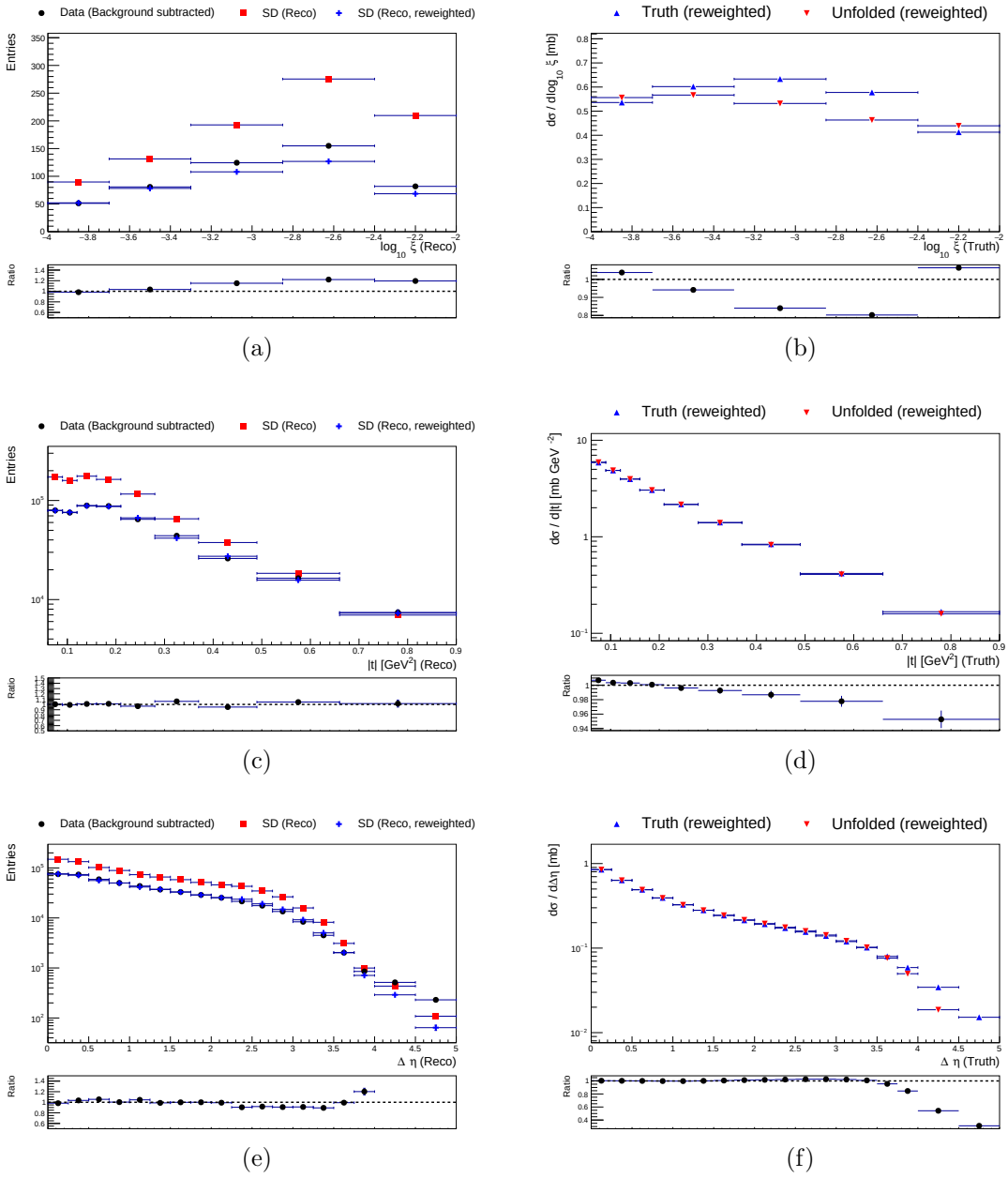

Figure 7.4: The MC is re-weighted with a smooth function to match the reconstructed data distribution (left). The ratio indicated in these plots is the background-subtracted data divided by the re-weighted MC distribution and is used to fit the re-weighting function. Closure is assessed by unfolding the re-weighted MC and comparing it to the re-weighted truth distribution (right). The ratio in these plots is the truth re-weighted distribution divided by the unfolded re-weighted distribution and is used to assess the systematic uncertainty arising from the unfolding process.

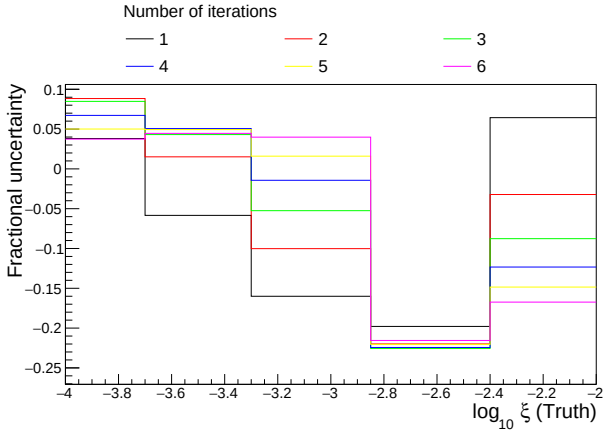

(a)

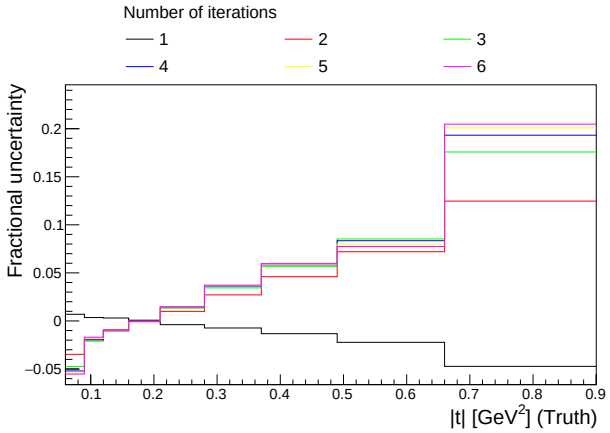

(b)

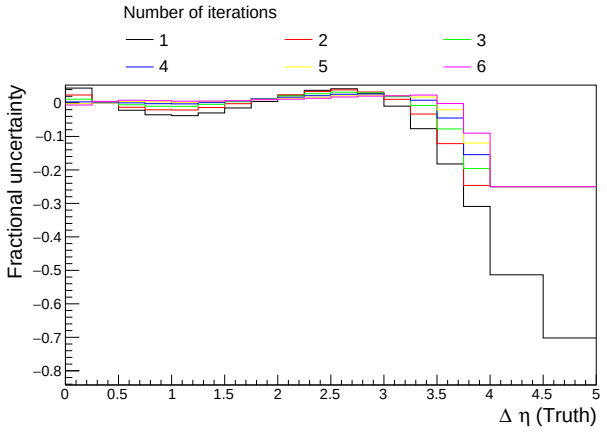

(c)

Figure 7.5: The systematic uncertainty arising from unfolding for each bin, for between one and six iterations of unfolding.

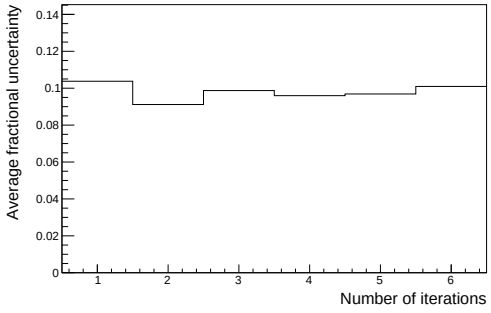

(a) Average uncertainty per bin for $\log_{10}\xi$

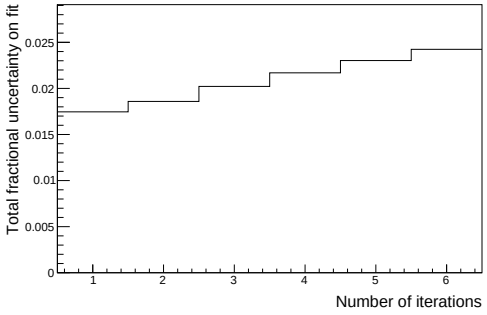

(b) Fit uncertainty for $\log_{10}\xi$

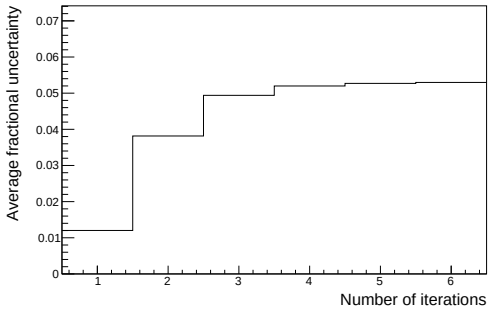

(c) Average uncertainty per bin for $|t|$

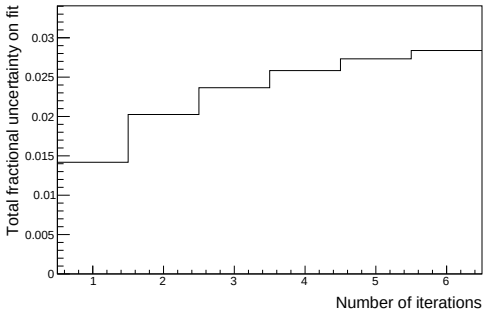

(d) Fit uncertainty for $|t|$

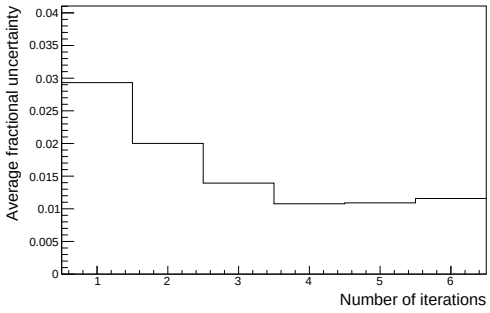

(e) Average uncertainty per bin for $\Delta\eta$

Figure 7.6: The average uncertainty per bin (figures (a), (c) and (e)) and the uncertainty on the final fits (figures (b) and (d)), both plotted as a function of the number of iterations of unfolding. The average uncertainty plotted in figure (e) excludes bins above $\Delta\eta = 3.5$. The fit procedure is explained in section 9.3 and 9.4.

CHAPTER 8

Systematic uncertainties

This chapter presents the methods by which different sources of systematic uncertainties were assessed. For each source, the analysis was repeated twice with the parameter in question varied away from the nominal value in both directions. The difference between the nominal and the varied results provided an estimation of the uncertainty arising from that source. Sections 8.1 to 8.9 below explain how each of the sources of uncertainty were investigated and quantifies their effect on the results. Section 8.10 details further sources of uncertainty not evaluated here. For each source of uncertainty, the upward and downward deviations were approximately symmetric with deviations from symmetry compatible with statistical fluctuations. Therefore, to provide a conservative estimate, the total systematic uncertainty was calculated as the sum in quadrature of the larger of the two deviations from each source in each bin. To conclude the chapter, section 8.11 summarises the major sources of uncertainty and presents the total uncertainty.

8.1 Number of MBTS tiles

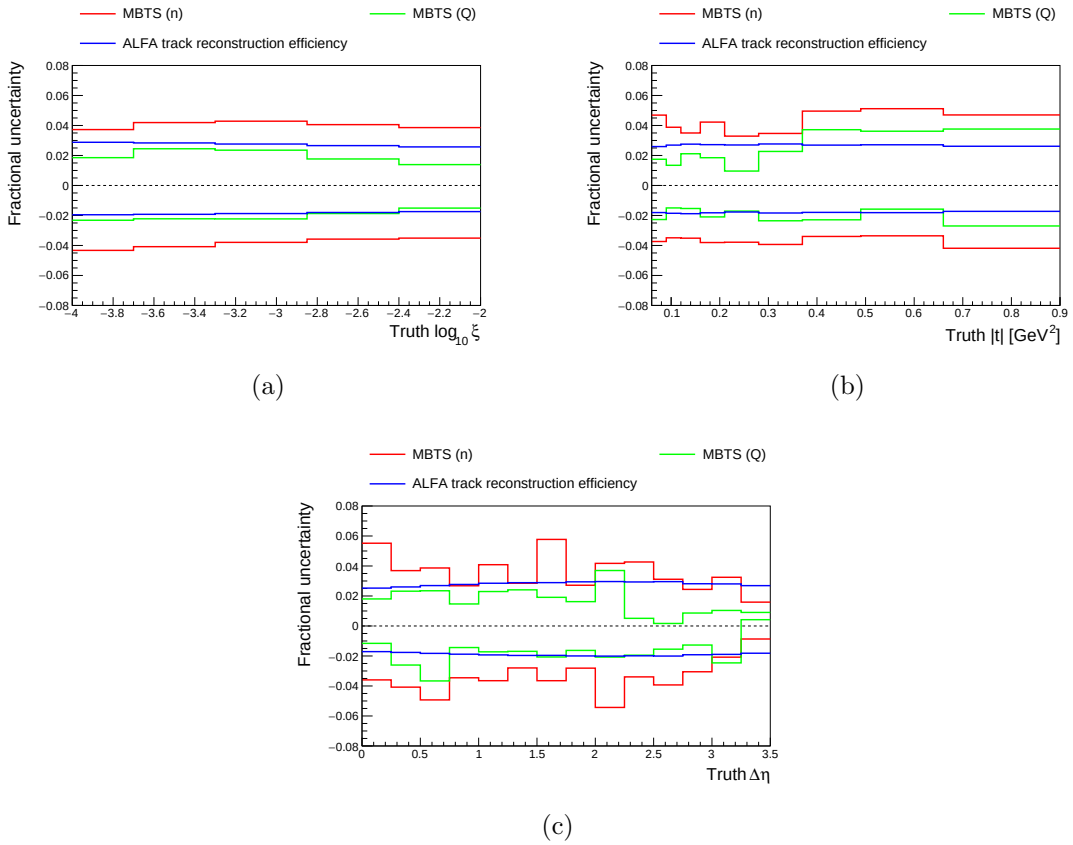

(a) (b)

(c)

Figure 8.1: The systematic uncertainty arising from the ALFA track reconstruction efficiency and the MBTS selection.

The minimum number of MBTS counters required in the analysis to be above their offline threshold on the opposite side of the detector to the ALFA tag was 2, as motivated by the discussion on the trigger efficiency in section 5.2. This requirement was varied up and down by 1 counter, resulting in an uncertainty of ∼4–5% across all bins. The uncertainty is indicated in red in figure 8.1.

8.2 Charge of MBTS tiles

The offline threshold applied to the MBTS was tuned separately to data and MC, as explained in section 4.3.2.2, assuming a Gaussian distribution. The offline threshold

was varied up and down by one standard deviation of the fit to $\mu + 4\sigma$ and $\mu + 6\sigma$, resulting in an uncertainty of ∼2–4% across all bins. The uncertainty is indicated in green in figure 8.1.

8.3 ALFA reconstruction efficiency

Section 5.4 explains how the ALFA track reconstruction efficiency is measured and includes an estimation of the systematic uncertainty on the calculated efficiencies, shown in table 5.2. The uncertainty is assessed by repeating the analysis with the efficiency varied in both directions by the uncertainty values presented. Due to the way the total uncertainty on the efficiency was calculated, the upward shift could be above 100% and so was restricted to unity. This results in an uncertainty of $\sim 3\%$ across all bins, indicated in blue in figure 8.1.

8.4 $\bar{x}/\theta$ selection

As explained in section 4.3.2.4, the analysis vetoes ALFA tags based on the average x coordinate ($\bar{x}$) and the local angle between stations (θ). The cut values are tuned to 4σ of the centroid of an ellipse fitted to $\bar{x}$ and θ (figure 4.9). The analysis was repeated with the cut values changed to be consistent with 3σ and 5σ of the elliptical fit. This varied the cut by 1σ and meant the lower value matched the cut identified as optimal by the $\sqrt{s} = 8$ TeV analysis. This produced a relatively large uncertainty in the results, typically of 5%–10%, rising to almost 20% at points. It is shown in blue in figure 8.2.

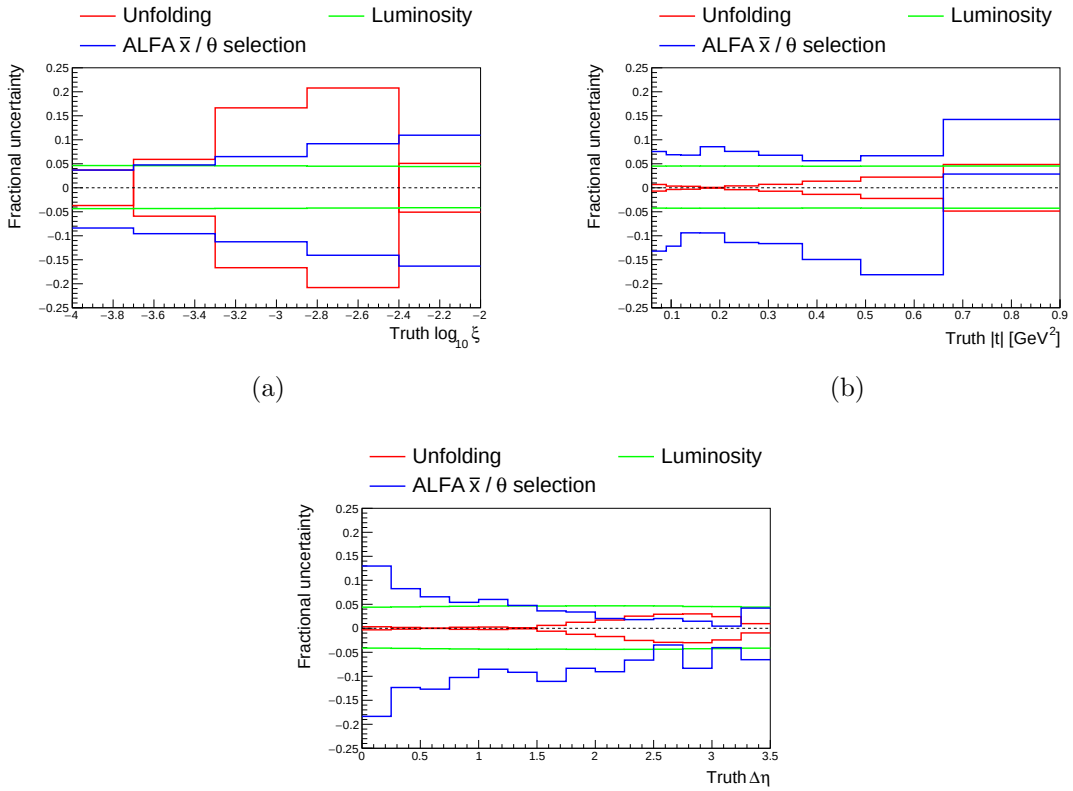

Figure 8.2: The systematic uncertainty arising from the $\bar{x}/\theta$ selection, unfolding and the luminosity.

8.5 Unfolding

The method of estimating the systematic uncertainty arising from the unfolding procedure is explained in section 7.3. It results in a consistently small uncertainty ($\leq 3\%$) in $|t|$ and $\Delta\eta$. The uncertainty in $\log_{10}\xi$ is greater, reaching $\sim 20\%$ at its maximum. It is shown in red in figure 8.2.

8.6 Luminosity

The luminosity of the data sample was calculated using the ATLAS `LumiCalc` tool to be 169.9 nb^{-1}[107]. The global luminosity uncertainty for all of ATLAS 2015 data was 2.1% and this is assumed to reflect the uncertainty for this single run[143].

A dedicated luminosity study of the run in question may improve the uncertainty but that is not attempted here. This results in an almost constant normalisation uncertainty of $\sim 5\%$ as shown in green in figure 8.2.

8.7 Vertex reconstruction efficiency

The vertex reconstruction efficiency was measured in both data and MC with a correction applied to MC for the small discrepancy observed. This process is described in more detail in section 5.3. To assess the uncertainty arising from the vertex reconstruction efficiency, the analysis was repeated assuming the same efficiency for both data and MC. The resulting uncertainty was symmetrised and is shown in red in figure 8.3. This produces a negligible uncertainty in $|t|$. The uncertainty in $\log_{10}\xi$ and $\Delta\eta$ is greater, but still reasonable, at a level of $\sim 5\%$.

8.8 Overlay background

In the nominal analysis, the overlay background distributions were re-weighted by a function of $\log_{10}\xi$, equation 6.2. A comparison of the $\log_{10}\xi$ distribution before and after the re-weighting is shown figure 6.3 and a full set of reconstructed distributions, after the re-weighting, is shown in figure 6.5. To account for the uncertainty in the overlay background, the measurement was repeated without the re-weighting, and the square of the weighting, applied. Assessing the uncertainty in this way accounts for differences in both the shape and normalisation in the distributions. This is shown in green in figure 8.3. The uncertainty was largest where the overlay background is largest, at high $\log_{10}\xi$ and low $\Delta\eta$.

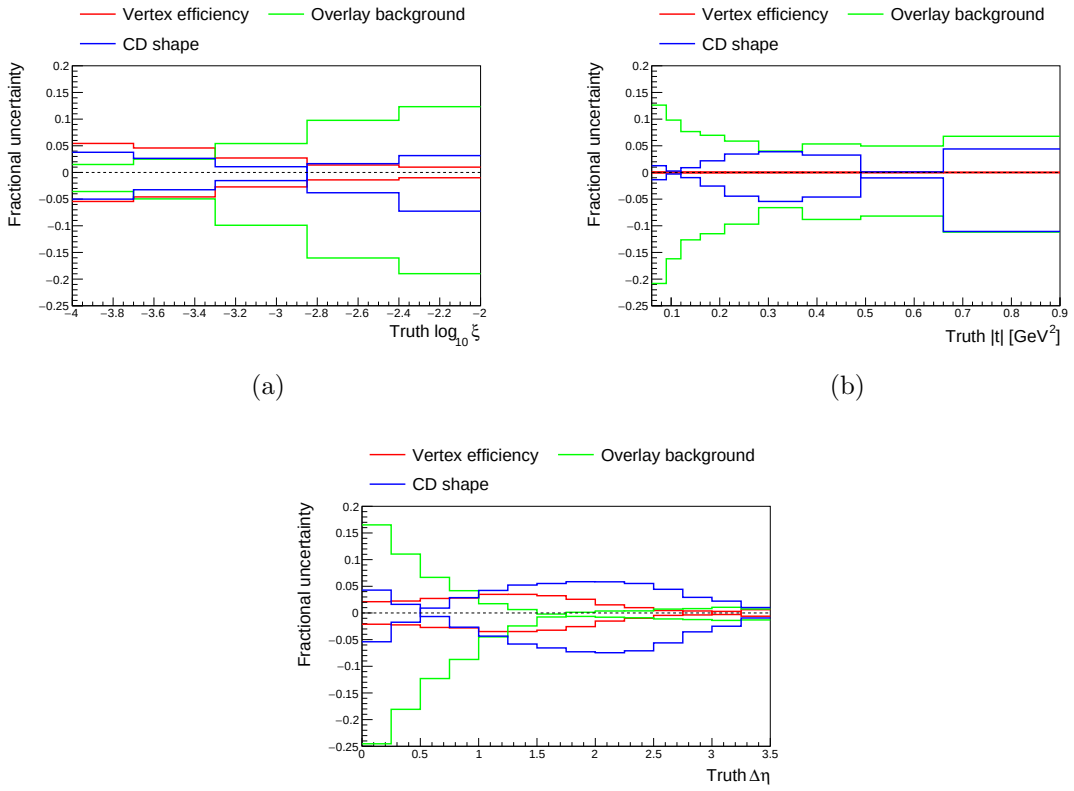

Figure 8.3: The systematic uncertainty arising from the vertex reconstruction efficiency, overlay background and the CD background.

8.9 CD background uncertainty

To assess the uncertainty in the CD distributions an additional control region was defined. This was the same as the nominal selection except for the requirement of an additional proton and a requirement for the number of MBTS counters passing their offline thresholds to fulfil $2 \leq n_{\text{MBTS}} \leq 10$. It is therefore a subset of the two proton control region. The MBTS requirement is chosen to minimise the contribution from the overlay background while maintaining sufficient statistics. The reconstructed distributions for this control region are show in figure 8.4. The distributions are dominated by CD. They show approximate agreement, but poor statistics mean the agreement is hard to assess.

To account for differences in the shape and normalisation of the CD distributions

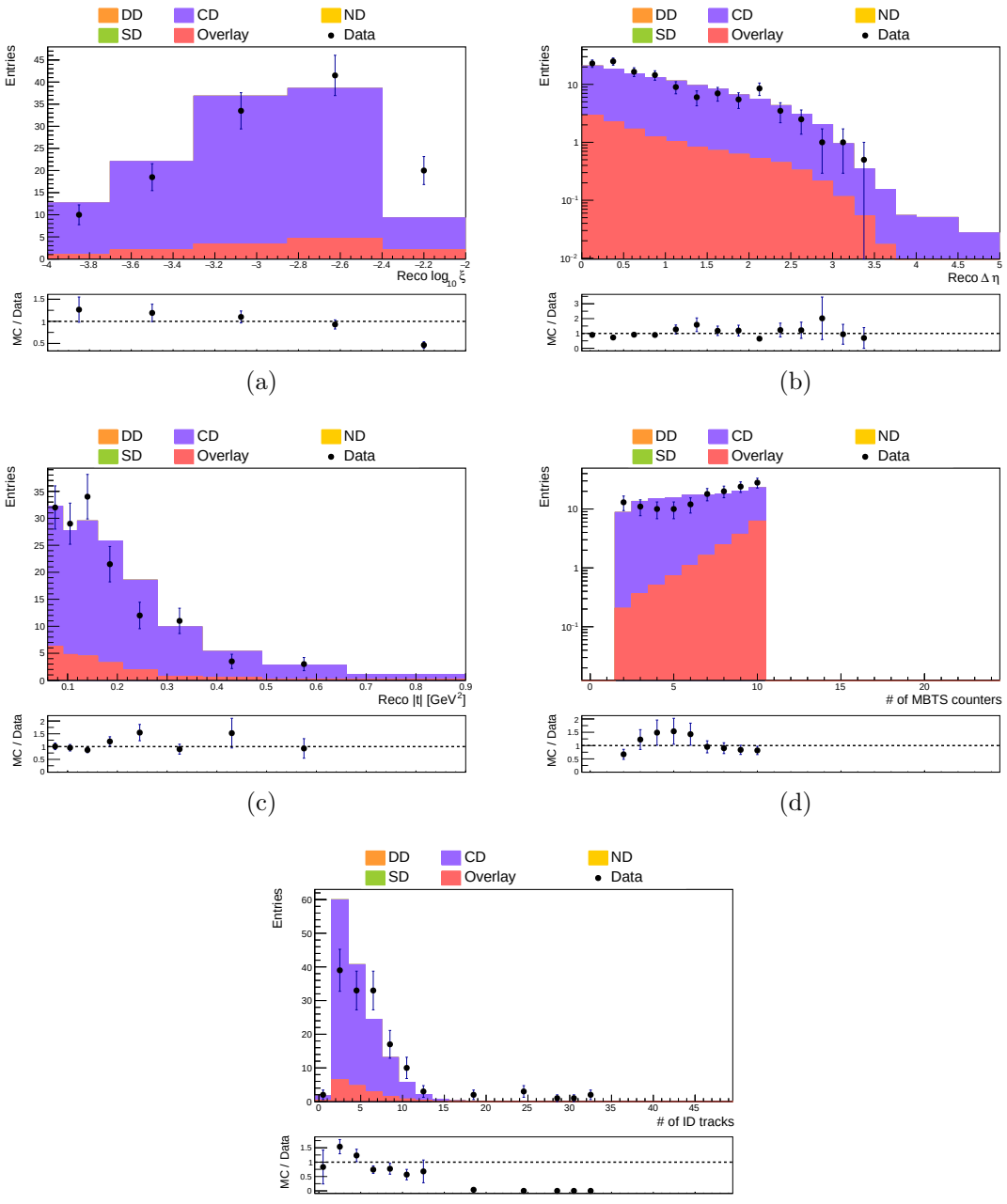

Figure 8.4: Reconstructed distributions using the CD event selection.

a third degree polynomial function was fitted to the ratio between the background-subtracted data and the CD MC in the $\log_{10}\xi$ distribution. This function was used to assess the uncertainty in the CD distributions by re-weighting the sample according to this function. A 'downward' shift was provided by re-weighting the sample according to the inverse of the value of the function. This uses a similar approach to that used to assess the overlay background, with the difference being that the CD sample is not re-weighted in the nominal analysis. Compared to a bin-by-bin re-weighting, this approach provides the advantage that it minimises the effect of statistical fluctuations in the CD control region. This method accounts for differences in the shape and normalisation of the distributions. Compatible results were obtained when each distribution was fitted and re-weighted separately. The uncertainty arising from the CD contribution is shown in blue in figure 8.3.

8.10 Other sources of uncertainty

There were some other potential sources of systematic uncertainty that were not evaluated. These were:

- **The ID track reconstruction efficiency.** The $\sqrt{s} = 8$ TeV analysis demonstrated that this produced only a minor systematic uncertainty of, typically, 2%[50]. As there is still the possibility of using calorimeter information to publish a $\sqrt{s} = 13$ TeV measurement if the differences between MC and data can be understood, there was little benefit in assessing this uncertainty.

- **The trigger efficiency.** There was no additional trigger stream available that provided a high number of appropriate events. The $\sqrt{s} = 8$ TeV analysis assessed the trigger efficiency using a random, track-seeded trigger and assessed the uncertainty using the LUCID trigger. The uncertainty was shown to be small, typically $\leq 1\%$[50]. In the run analysed here, the random trigger was very highly prescaled and did not provide enough events to evaluate the efficiency. The track requirement present in it would have also biased the result as

there was no such requirement in the main analysis. The independent, LUCID trigger was disabled. Therefore this uncertainty was not assessed here and is not expected to be large compared with the overall systematic uncertainty.

- **Hadronization.** Herwig7 uses a cluster model for hadronization whereas PYTHIA8 uses a Lund string approach[65, 60]. The $\sqrt{s} = 8$ TeV analysis assessed the effect of different hadronization models using a Herwig7 sample of SD and found the uncertainty to be $\sim 5\%$[3]. A reliable Herwig7 sample could not be generated at $\sqrt{s} = 13$ TeV within the ATLAS simulation framework in time for this thesis. This should be addressed for the publication of this measurement.

- **ALFA RP alignment.** The $\sqrt{s} = 8$ TeV analysis demonstrated that this produced only a minor systematic uncertainty of, typically, 1%[50]. Due to time constraints this uncertainty was therefore ignored.

- **DD and ND cross-sections.** The contributions of ND and DD to the analysis were negligible. The main contributions were through the overlay background and the uncertainty on this was assessed separately. The uncertainties on the cross-sections of ND and DD were therefore ignored.

8.11 Total systematic uncertainty

The uncertainty in the overlay background and the ALFA $\bar{x}/\theta$ selection were the dominant systematic uncertainties in all three of the distributions. The unfolding procedure and the CD background were additional major systematics for the $\log_{10}\xi$ and $\Delta\eta$ distributions, respectively. The largest (upwards or downwards) shifts in each bin from each systematic source were added in quadrature to obtain the total systematic uncertainty. This results in a typical systematic uncertainty of 25% and is shown in figure 8.5 with the major contributions for each distribution.

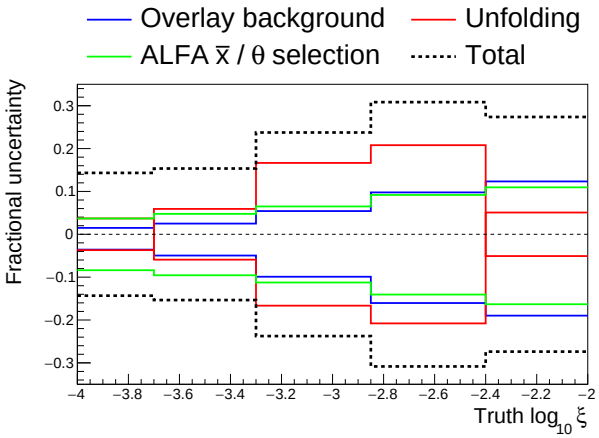

(a)

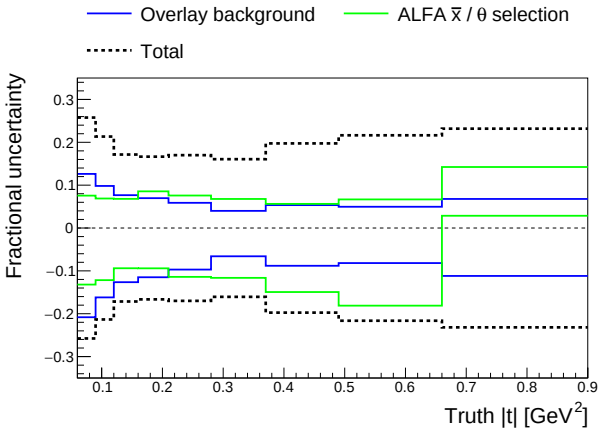

(b)

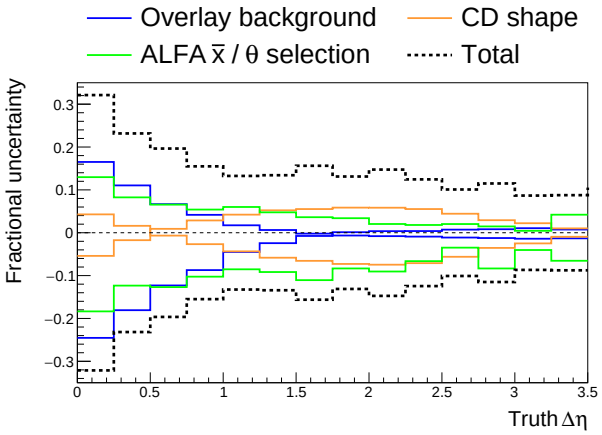

(c)

Figure 8.5: The total and dominant systematic uncertainties in each distribution. The colour scheme is not consistent with other figures in this chapter but is consistent between the sub-figures. The total systematic uncertainty is the sum in quadrature of the largest of the two (upward or downward) shifts from each source in each bin.

CHAPTER 9

Results and summary for diffraction

In this chapter unfolded results are presented for the fiducial region ($0.06\ \text{GeV}^2 < |t| < 0.9\ \text{GeV}^2$, $-4 < \log_{10}\xi < -2$). Section 9.1 presents the integrated cross-section. Section 9.2 presents the differential cross-sections for each of the analysis variables. The slope parameter, B, and Pomeron intercept[1], $\alpha(0)$, are extracted from the $|t|$ and $\log_{10}\xi$ distributions in sections 9.3 and 9.4, respectively. The fits are performed in a framework beginning from the double differential cross-section of SD from chapter 2, in particular, equations 2.41 and 2.42, repeated below for convenience:

$$\frac{d^2\sigma_{SD}}{dtd\xi} \propto \left(\frac{1}{\xi}\right)^{\alpha(0)} e^{Bt}, \tag{9.1}$$

with B, the slope parameter:

$$B = B_0 - 2\alpha' \ln\xi. \tag{9.2}$$

[1]The subscript $\mathbb{P}$, used to distinguish the Pomeron intercept ($\alpha_{\mathbb{P}}(0)$) from the Reggeon intercept ($\alpha_{\mathbb{R}}(0)$) earlier in this thesis, is omitted in this chapter.

Table 9.1: The integrated cross-section within the fiducial range. The uncertainties on the MC parameters are statistical only, whereas the data uncertainty is the sum in quadrature of the statistical and systematic uncertainties, listed in detail in table 9.2.

Sample	$\sigma_{SD}^{\xi,t}$ [mb]
PYTHIA8 A2	2.17±0.01
PYTHIA8 A3	2.01±0.01
Data	1.1±0.2

A summary of the measurement is provided in section 9.5.

9.1 Integrated cross-section

The integrated cross-section within the fiducial region is calculated from data and MC samples and shown in table 9.1. The cross-section is over-predicted by MC by a factor of approximately $\frac{5}{3}$, as expected from previous analyses[3]. The systematic uncertainty is calculated for data by integrating the cross-section in each systematic sample and summing in quadrature the larger of the upward and downward shifts. The overlay background produces the largest systematic uncertainty.

9.2 Differential cross-sections

Unfolded distributions for $\Delta\eta$, $|t|$ and $\log_{10}\xi$ are shown in figure 9.1. Each data point's total uncertainty is calculated as the sum in quadrature of the statistical and systematic uncertainties, with the systematic uncertainty calculated as described in section 8.11 and the statistical uncertainties generally being negligible. The total

Table 9.2: The nominal values and statistical and systematic uncertainties for the integrated cross-section (section 9.1) and each fit performed (sections 9.3 and 9.4). The total systematic uncertainty is the sum in quadrature of the largest of each shift, either up or down. Some additional sources of uncertainty were only applied to the fit to the $\log_{10}\xi$ distribution and so have no values indicated for $\sigma_{SD}^{\xi,t}$, A or B.

Source	$\sigma_{SD}^{\xi,t}$ [mb]	A	B [GeV^{-2}]	C [mb]	D	$\alpha(0)$
Nominal	1.122	2.131	5.476	1.589	-0.146	1.146
Stat	0.019	0.011	0.044	0.012	0.001	0.001
Unfolding (Up)	-0.004	0.014	-0.072	-0.062	0.005	-0.005
Unfolding (Down)	0.004	-0.012	0.066	0.038	-0.006	0.006
ALFA ϵ (Up)	-0.020	-0.019	0.001	-0.024	0.001	-0.001
ALFA ϵ (Down)	0.030	0.026	0.002	0.033	-0.001	0.001
n_{MBTS} (Up)	-0.041	-0.037	-0.002	-0.034	0.002	-0.002
n_{MBTS} (Down)	0.046	0.035	0.014	0.051	-0.001	0.001
MBTS Q (Up)	-0.022	-0.016	-0.015	-0.001	0.002	-0.002
MBTS Q (Down)	0.023	0.009	0.048	-0.017	-0.003	0.003
Overlay (Up)	0.085	0.101	-0.149	0.553	0.029	-0.029
Overlay (Down)	-0.140	-0.180	0.254	-0.650	-0.050	0.050
$\mathscr{L}$ (Up)	-0.048	-0.043	-0.000	-0.062	0.001	-0.001
$\mathscr{L}$ (Down)	0.051	0.044	0.000	0.066	-0.001	0.001
CD (Up)	0.010	-0.003	0.068	-0.157	-0.011	0.011
CD (Down)	-0.019	-0.113	0.406	-0.072	0.010	-0.010
$\bar{x}/\theta$ (Up)	0.083	0.067	0.017	0.320	0.017	-0.017
$\bar{x}/\theta$ (Down)	-0.129	-0.086	-0.160	-0.326	-0.020	0.020
Vertex ϵ (Up)	-0.001	-0.001	0.001	-0.075	-0.011	0.011
Vertex ϵ (Down)	0.001	0.001	-0.001	0.093	0.012	-0.012
α' (Up)	-	-	-	-0.900	-0.119	0.119
α' (Down)	-	-	-	1.984	0.117	-0.117
$\langle\log_{10}\xi\rangle$ (Up)	-	-	-	-0.030	-0.001	0.001
$\langle\log_{10}\xi\rangle$ (Down)	-	-	-	0.030	0.001	-0.001
B (Up)	-	-	-	0.278	0.006	-0.006
B (Down)	-	-	-	-0.253	-0.007	0.007
Total Sys	0.207	0.239	0.512	2.142	0.132	0.132
Total Uncertainty	0.208	0.239	0.514	2.142	0.132	0.132

uncertainty on each data point in this chapter is shown as a vertical error bar. Horizontal error bars are used to indicate bin edges in the displayed plots to the reader and are not used in the fitting procedure. Truth level distributions are also shown from the A2 and A3 tunes of PYTHIA8 which use the SS and DL Pomeron fluxes, respectively (see sections 2.8.3 and 4.2 for further details of the PYTHIA8 implementation and tuning of these models).

The unfolded distribution of $\Delta\eta$ is shown in figure 9.1a. The definition of $\Delta\eta$ is the distance between $\eta = |2.5|$ (the edge of the ID acceptance) on the side of the proton tag and the nearest charged particle with $P_T > 200$ MeV and $|\eta| < 2.5$. The upper limit on the distribution is imposed due to the large systematic uncertainty arising from the unfolding procedure above $\Delta\eta = 3.5$. The plot shows that both tunes of PYTHIA8 consistently over-predict the cross-section, which is in agreement with the previous ATLAS measurements of SD at $\sqrt{s} = 7$ TeV and $\sqrt{s} = 8$ TeV[128, 3]. The shapes of the two tunes are similar, with the A3 tune providing slightly better normalisation agreement with data. Data and both tunes of PYTHIA8 show a large number of events at low values of $\Delta\eta$. This is understood as 'stacking-up' of events as explained in section 4.1, in particular figure 4.2, which is expected and has been observed by the earlier ATLAS measurements. The cross-section falls with increasing $\Delta\eta$ in a similar way in data and both MC distributions and does not exhibit a flat diffractive plateau as naively expected, due to the kinematic restrictions.

The unfolded distribution of $|t|$ is shown in figure 9.1b. The data points for this distribution are plotted at the 'centre of gravity' of each bin to avoid biasing the fit performed in section 9.3. The A3 tune is used as a prior to calculate the average $|t|$ value per bin. Table C.1 in the appendix presents the adjusted centres. All three data and MC distributions are consistent with an exponentially falling cross-section, with the data showing a less steep fall than the MC. Below $|t| = 0.49$ GeV^2 both PYTHIA8 tunes over-predict the cross-section.

The unfolded distribution of $\log_{10}\xi$ is shown in figure 9.1c. An approximately flat

distribution is observed, as expected upon inspection of equation 9.1 with $\alpha(0) \sim 1$. PYTHIA8 again over-predicts the measured cross-section and exhibits a slight rise with increasing ξ. A fit is performed to extract the Pomeron intercept in section 9.4.

9.3 Extraction of slope parameter

To extract the slope parameter from equation 9.1, one can neglect the $\log_{10}\xi$ dependence and fit to a differential cross-section in $|t|$. Therefore a fit of the form

$$\frac{d\sigma}{d|t|} = e^{A+Bt} \tag{9.3}$$

was performed. The fitted parameter A contains the normalisation of the distribution, while the fitted parameter B corresponds to the slope parameter. Figure 9.2 shows the data distribution with the result of the fit overlaid. The fit parameters for data are shown and compared with those obtained from separate fits to the MC distributions in table 9.3. The nominal fit values are obtained by fitting to the nominal data points with statistical errors only, with the resulting uncertainty on the fit parameters taken as the statistical uncertainty. The nominal fit has a $\chi^2/\text{n.d.f.} = 48.3/7$, this relatively high value suggests a systematic effect could be changing the shape of the distribution. To obtain the systematic uncertainties, listed in table 9.2, the fit was repeated using each of the systematically shifted distributions. The total systematic uncertainty is the sum in quadrature of the largest ('up' or 'down') shifts from each of the systematic sources. The largest sources of uncertainty on the slope parameter are the overlay background and the $\bar{x}/\theta$ selection.

The extracted slope parameter corresponds to a $\langle\log_{10}\xi\rangle = -2.98 \pm 0.05$, where the nominal value is obtained from the A3 tune and the uncertainty is the difference between the values obtained from the A3 and A2 tunes. The measured value of the slope parameter $B = 5.5 \pm 0.5$ GeV^{-2} is compatible with the prediction of the A3 tune of PYTHIA8 within 2.3σ. The result is less compatible with the A2 tune,

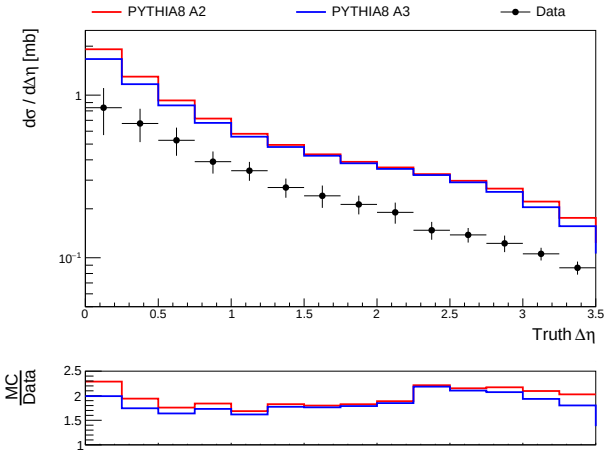

(a)

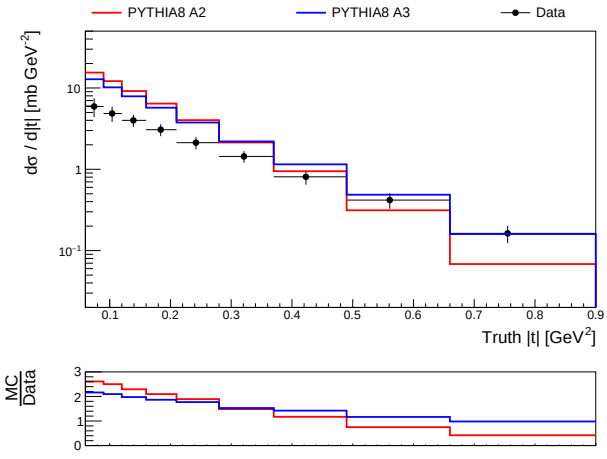

(b)

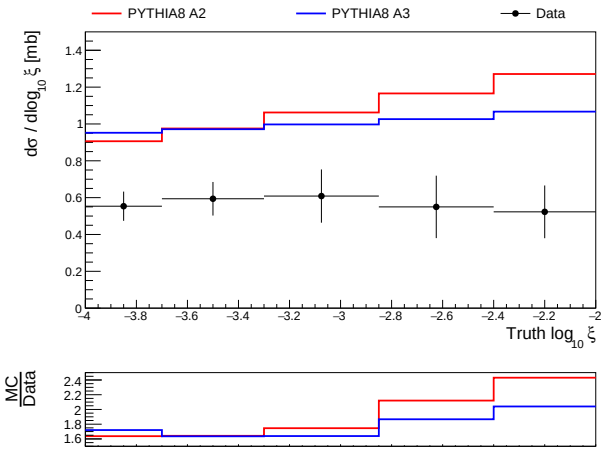

(c)

Figure 9.1: Unfolded differential cross-sections.Truth level PYTHIA8 MC is shown for comparison.

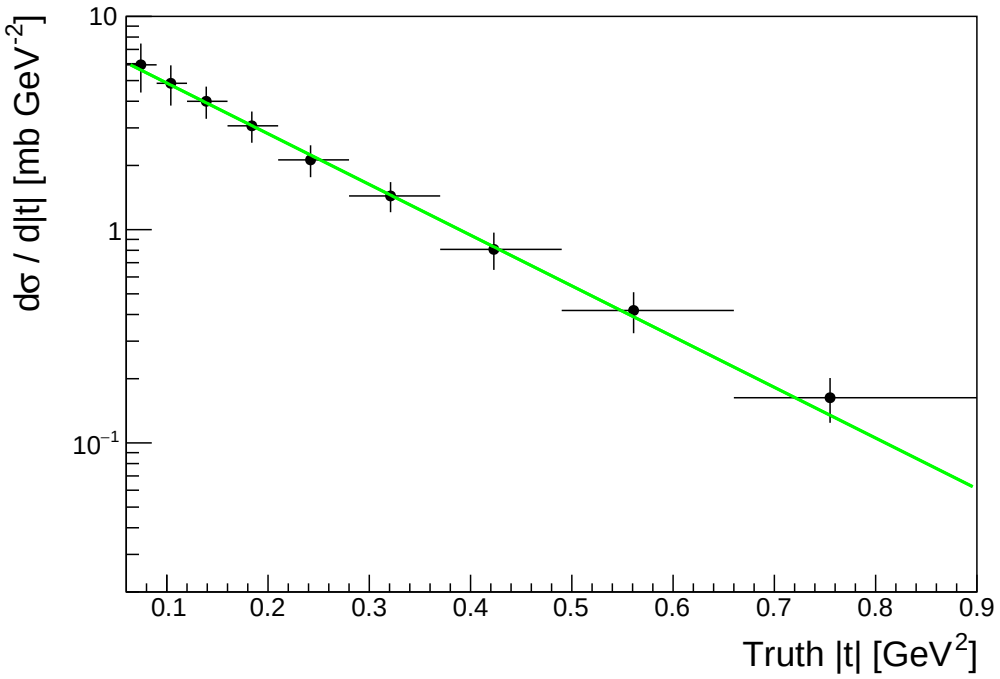

Figure 9.2: The unfolded $|t|$ differential cross-section. Data points are plotted at the centre of gravity for each bin with vertical error bars indicating the total uncertainty and horizontal error bars indicating the bin edges. The nominal fit is performed on the nominal data points with statistical uncertainties only and is overlaid in green.

being $\sim 5\sigma$ from the prediction.

9.4 Extraction of Pomeron intercept

To extract the Pomeron intercept, $\alpha(0)$, from the $\log_{10}\xi$ distribution, equation 9.1 is again used as a starting point. One needs to integrate over $|t|$ to get:

$$\frac{d\sigma}{d\xi} \propto \left(\frac{1}{\xi}\right)^{\alpha(0)} \frac{1}{B(\xi)} \left(e^{B(\xi)t_{\text{high}}} - e^{B(\xi)t_{\text{low}}}\right), \tag{9.4}$$

where t_{high} and t_{low} are the upper and lower limits to the t fiducial range, respectively. t is negative. As a reminder, the ξ dependence of B is indicated explicitly. To fit

Table 9.3: The fitted A and B parameters following the fit to the $|t|$ differential cross-section using equation 9.3. The uncertainties on the MC parameters are statistical only, whereas the data uncertainties are the sum in quadrature of the statistical and systematic uncertainties, listed in detail in table 9.2.

Sample	A	B [GeV^{-2}]
PYTHIA8 A2	3.340±0.002	8.07±0.01
PYTHIA8 A3	2.970±0.002	6.64±0.01
Data	2.1±0.2	5.5±0.5

to the distributions measured in this analysis, one then needs to convert the ξ dependence to a $\log_{10}\xi$ dependence:

$$\begin{aligned}\frac{d\sigma}{d\log_{10}\xi} &\propto \left(\frac{1}{\xi}\right)^{\alpha(0)-1}\frac{1}{B(\xi)}\left(e^{B(\xi)t_{\text{high}}}-e^{B(\xi)t_{\text{low}}}\right)\\ &\propto 10^{-\epsilon\log_{10}\xi}\frac{1}{B(\log_{10}\xi)}\left(e^{B(\log_{10}\xi)t_{\text{high}}}-e^{B(\log_{10}\xi)t_{\text{low}}}\right),\end{aligned} \tag{9.5}$$

where $\alpha(0) = 1+\epsilon$. Therefore to extract the value of ϵ, and subsequently the Pomeron intercept $\alpha(0)$, a fit is performed of the form

$$\frac{d\sigma}{d\log_{10}\xi} = C10^{D\log_{10}\xi}\frac{1}{B(\log_{10}\xi)}\left(e^{B(\log_{10}\xi)t_{\text{high}}}-e^{B(\log_{10}\xi)t_{\text{low}}}\right). \tag{9.6}$$

The parameter C contains the overall normalisation and is not of primary interest. The extracted Pomeron intercept is $\alpha(0) = 1-D$. The value of B_0 (equation 9.2) is fixed to 2.04 using the measured slope parameter B, the $\langle\log_{10}\xi\rangle$ value from MC and the assumed value of the Pomeron slope, $\alpha' = 0.25$ GeV^{-2}, the default value used in PYTHIA8[60].

For each systematic uncertainty, the extracted value of the slope parameter B is used in the $\log_{10}\xi$ fit. In addition to the systematic uncertainties discussed in chapter 8, the fixed parameters of the fit are varied as additional systematic uncertainties propagated through equation 9.6. The total uncertainty on the measured slope parameter B and $\langle\log_{10}\xi\rangle$ calculated in the previous section are used. A conservative 100% uncertainty is assigned for the Pomeron slope, α', due to the measurement being from a much-lower, non-LHC centre of mass energy[144, 145]. The fit was

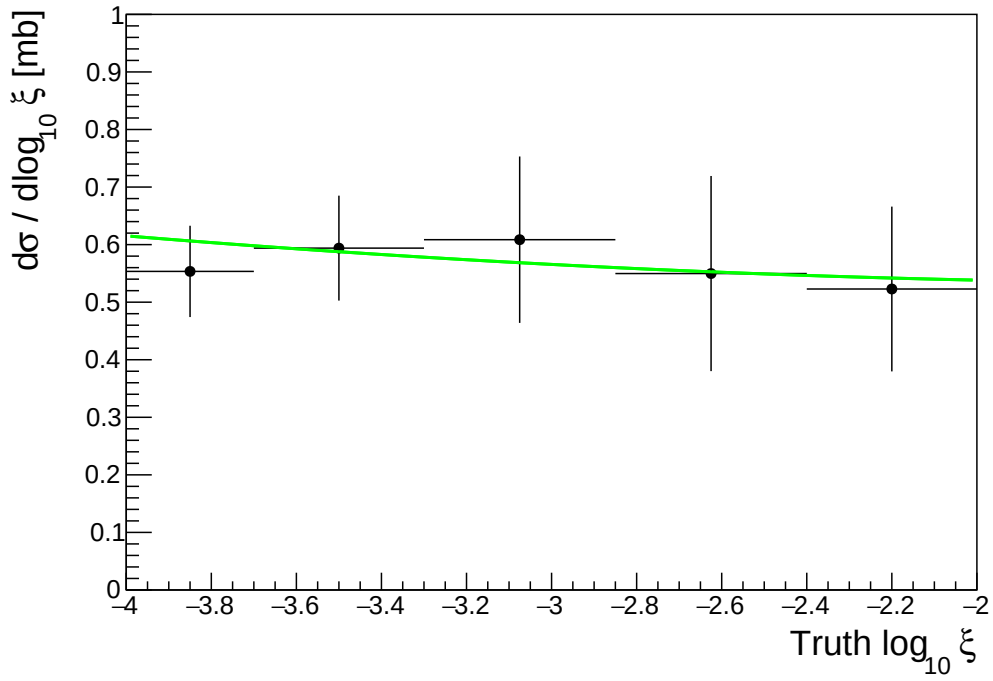

Figure 9.3: The unfolded $\log_{10}\xi$ differential cross-section. The nominal fit is overlaid in green.

repeated separately, using the nominal data points, for each systematic shift in each of the fit parameters. The resulting uncertainties are shown as additional rows in table 9.2, with no entries for the error on the slope parameter or integrated cross-section.

The data points, with the fit overlaid, are shown in figure 9.3. The fit parameters and extracted Pomeron intercept are shown in table 9.4. The measured Pomeron intercept is compatible with both the A2 and A3 tunes of PYTHIA8 within 1σ. As can be seen in table 9.2, the largest uncertainty on the measured Pomeron intercept arises from the Pomeron slope whilst the largest experimental source is the overlay background. Separating the theoretical contributions to the uncertainty which includes α', the result can be written as is $\alpha(0) = 1.15 \pm 0.01(\text{statistical}) \pm 0.06(\text{experimental systematics}) \pm 0.12(\text{theoretical systematics})$.

Table 9.4: The fitted C and D parameters and the calculated Pomeron intercept following the fit to the differential $\log_{10}\xi$ cross-section using equation 9.6. The uncertainties on the MC parameters are statistical only, whereas the data uncertainties are the sum in quadrature of the statistical and systematic uncertainties, listed in detail in table 9.2.

Sample	C [mb$\times 10^3$]	D	$\alpha(0)$
PYTHIA8 A2	14.0 ± 0.1	-0.003 ± 0.001	1.003 ± 0.001
PYTHIA8 A3	5.98 ± 0.03	-0.074 ± 0.001	1.074 ± 0.001
Data	1.6 ± 2..1	-0.15 ± 0.13	1.15 ± 0.13

9.5 Summary and discussion of results

The measurement presented here is the first measurement of SD at $\sqrt{s} = 13$ TeV. No other measurements, preliminary or otherwise, can be found on SD at this centre of mass energy.

The analysis closely follows methods developed for the equivalent measurement at $\sqrt{s} = 8$ TeV which had a similar fiducial range and is outlined in section 2.9[50, 3]. The dominant uncertainties on both measurements of the Pomeron intercept, $\alpha(0)$, were due to the value of the Pomeron slope, α', used in the fit. Performing either of the analyses double differentially in ξ and t would allow the simultaneous measurement of the Pomeron slope and intercept and would therefore help reduce the uncertainty in the measured Pomeron intercept. Both analyses were made at fixed $\sqrt{s}$ but could also be combined with a global fit to explore the centre of mass energy dependence of the Pomeron intercept and integrated cross-section.

Like the $\sqrt{s} = 8$ TeV analysis, a large over-prediction by PYTHIA8 of around $\frac{5}{3}$ is observed in the cross-section at $\sqrt{s} = 13$ TeV. The measured values of the slope parameter and the Pomeron intercept in the $\sqrt{s} = 8$ TeV analysis were both in good agreement with those predicted by the A2 and A3 tunes of PYTHIA8. Table 9.5 compares the extracted parameters from both analyses.

Table 9.5: A comparison of the fiducial range, integrated cross-section and extracted parameters from both SD measurements[3].

$\sqrt{s}$ [GeV]	Fiducial range	$\sigma_{SD}^{(\xi,t)}$ [mb]	B [GeV^{-2}]	$\alpha(0)$
8	$-4.0 \leq \log_{10}\xi \leq 1.6$, $0.016 \leq \lvert t\rvert \leq 0.43$ GeV^2	1.6 ± 0.1	7.65 ± 0.34	1.07 ± 0.09
13	$-4 \leq \log_{10}\xi \leq -2$ $0.06 \leq \lvert t\rvert \leq 0.9$ GeV^2	1.1 ± 0.2	5.5 ± 0.5	1.15 ± 0.13

The availability of calorimeter information in this measurement would allow a more precise measurement of ξ and a wider range of $\Delta\eta$ to be studied. The discrepancy between the MC and data in calorimeter data should therefore be understood. Other measurements using the same data as analysed here are ongoing, and would also benefit from this knowledge. With or without the third method of measuring ξ using calorimeter data, the existing methods (using the ID as done here, or using ALFA) could be combined in a multivariate analysis to exploit the advantages each method provides.

The $\sqrt{s} = 8$ TeV analysis is nearly ready for publication, having gone through the ATLAS approval procedures and been submitted to JHEP. This analysis will continue to be developed before following a similar pathway.

CHAPTER 10

Upgrade of L1CALO

"And now for something completely different."[146]

During LS2, the LHC and its detectors are undergoing upgrades. Following its upgrade, ATLAS's L1CALO will be able to compute more complicated algorithms using finer granularity data. Of particular interest to UK L1CALO institutes are the components used for identifying electrons and photons in the e/γ algorithm. Preliminary studies on the new e/γ algorithm have previously been published by ATLAS[147]. To motivate choices in firmware design, more thorough studies were needed that handled clustering logic more robustly. This chapter presents the studies on this topic completed by the author.

Section 10.1 explain the physics of EM showers and is followed by section 10.2 which

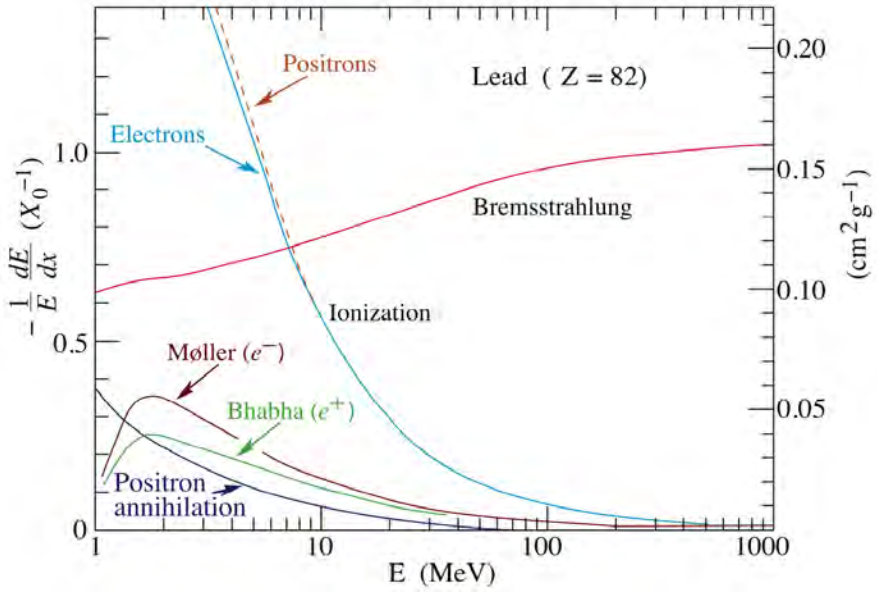

Figure 10.1: Fractional energy loss per radiation length in lead as a function of electron or positron energy[35].

discusses the run2 e/γ algorithm. Section 10.3 discusses the relevant upgrades of the LHC and ATLAS. The decisions made are then presented in chronological order in section 10.4. The expected performance of the resultant algorithm during run3 is then shown in section 10.5 within the summary.

10.1 Electron showers and detection

When travelling through matter, there are several processes through which an electron can lose energy. Figure 10.1 shows the contribution to energy loss from the different processes using lead as an example material. At low energies the dominant process is ionization. At higher energies Bremsstrahlung is dominant and is therefore more important for detection of high P_T electrons.

Energy loss due to ionization is characterised by the Bethe formula[148, 35]. Figure 10.2 shows the expected energy loss for different materials based on this formula. In all materials the energy loss reaches a minimum at $\beta\gamma \approx 3$ and is followed by a slow rise, increasing proportional to $\ln E$ where E is the energy of the incident particle.

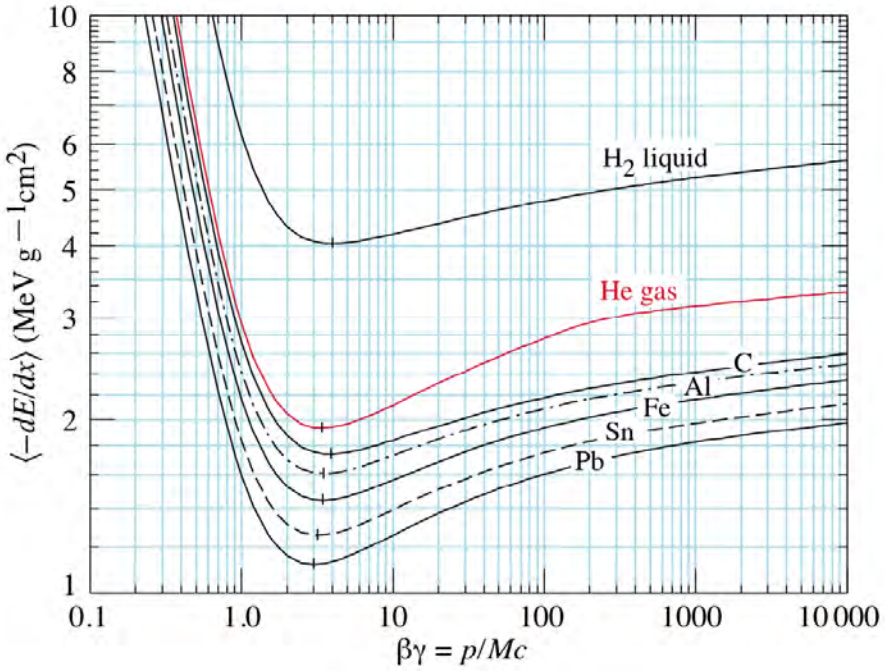

Figure 10.2: Mean energy loss rate in various materials shown as a function of $\beta\gamma$[35].

Bremsstrahlung, "braking radiation," is photon emission from a charged particle due to its deceleration in the presence of another charged particle. The right hand side of figure 10.3 shows a Feynman diagram representing the interaction in the case of an electron in the presence of a nucleus. An incident electron is decelerated via an EM interaction with a nucleus and a photon is subsequently emitted ensuring conservation of momentum. Energy loss (per distance travelled) due to bremsstrahlung is approximately proportional to the energy of the electron. A useful quantity is the radiation length, X_0, which is defined using the differential energy loss[35, 149]:

$$-\frac{dE}{dX} = \frac{E}{X_0} = \frac{E_0 e^{\frac{-X}{X_0}}}{X_0}. \tag{10.1}$$

Using this definition the radiation length is the distance over which an electron is expected to lose $^1/_e$ of its energy through bremsstrahlung. The value of the radiation length depends on the absorber material and can be approximately calculated as[35]:

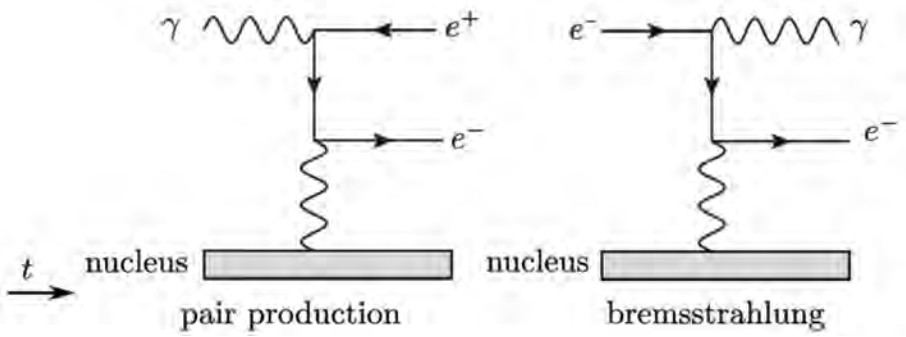

Figure 10.3: Feynman diagram of pair production (left) and bremsstrahlung (right), adapted from [150]. Both processes are key to an EM shower.

$$X_0 = \frac{180A}{Z^2} \text{g cm}^{-2}, \tag{10.2}$$

for the absorber material atomic number Z.

When a high energy electron is detected in a calorimeter it is due to the formation and detection of an electromagnetic shower. The initial electron emits a bremsstrahlung photon and this starts a chain reaction. The photon produces an electron-position pair in the vicinity of a nucleus, as shown on the left hand side of figure 10.3. Then the initial electron and new e^-e^+ pair undergo further bremsstrahlung and emit more photons. This will continue to the point where the energy of photons is below the pair production threshold for electrons ($2 \times m_e = 1.02$ MeV)[149]. Below this point ionization provides the dominant contribution to the energy loss. The critical energy, E_C, of an electromagnetic shower is defined (using the Rossi definition) as the energy at which ionization loss per radiation length is equal to the electron energy[151]. This is approximately consistent with alternate definitions that define the critical energy as the energy at which an electron loses energy at the same rate from Bremsstrahlung and from ionisation[149]. Its value is approximately[7]:

$$E_C = \frac{800 \text{ MeV}}{Z}. \tag{10.3}$$

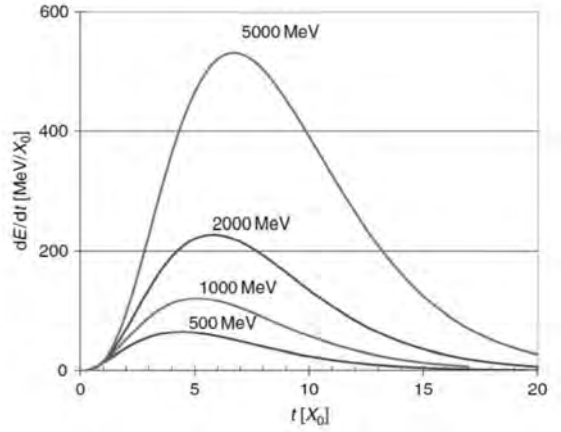

Figure 10.4: Simulation of energy deposition of electron of different energies[152].

As the dominant energy loss of an incident electron is through the emission of photons, at any point the energy loss of the electron is not the same as the energy deposited in the target material. Figure 10.4 shows the simulation of the energy deposited as a fraction of the total energy per radiation length.

Multiple scattering of electrons determines the lateral width of EM showers with the width increasing with shower depth. Typically 90% of a particle's energy will be deposited within the Moliere radius, R_M which is calculated as:

$$R_M \approx \frac{X_0 \times 21 \text{ MeV}}{E_C}. \tag{10.4}$$

In the presence of a magnetic field the EM shower will not be symmetrical, this causes EM showers to be wider in ϕ than in η in ATLAS. This is particularly so in the case of early showering starting before the calorimeter which results in two deposits of energy in the ECAL separated in ϕ.

10.2 run2 e/γ algorithm

High energy electrons and photons both form EM showers but with different initial steps. A photon will pair produce an e^+e^- pair which will subsequently undergo

bremsstrahlung, whereas an initial electron will itself bremsstrahlung. The detector signal is very similar and the two cannot be discerned using the low granularity data used by L1CALO. Therefore the L1CALO algorithm is identical for both. Electrons and photons can be discerned at the HLT or during reconstruction using ID tracks.

The main background for the e/γ algorithm is hadrons[153]. Hadron shower development depends on nuclear interaction length, rather than radiation length, and this is typically significantly larger. As a result both charged and neutral hadrons travel further through material before depositing all of their energy[7]. The longer interaction length of hadrons also means energy deposits are wider than those formed from the EM showers of electrons or photons. Hadrons are typically formed as part of jets. Therefore one of the strategies used in e/γ trigger and identification algorithms is to identify isolated E_T deposits and use measures of isolation to discriminate signal from background. This strategy is effective for reducing acceptance of neutral pions (π^0) which produce EM showers but are typically formed within jets.

Input data to L1CALO during runs 1 and 2 were trigger towers, analogue sums of E_T from either the ECAL or HCAL in areas of (0.1×0.1) up to $|\eta| < 2.5$. Upgrades made during LS1 allowed for E_T-dependent isolation thresholds and dynamic pedestal corrections, to remove bunch train effects from E_T samplings, as well as other improvements. Trigger towers and the algorithm described here will be used initially during run3 as part of the 'legacy' system to ensure commissioning of the new system proceeds with minimal impact on physics performance.

Figure 10.5 shows how the input data available to L1CALO were used in the run2 e/γ algorithm. The area considered consists of 4×4 trigger towers from both calorimeter systems. The algorithm, referred to as the 'sliding window,' was repeated across the calorimeter in steps of 0.1 in both η and ϕ directions. For an e/γ candidate to be accepted:

- The most energetic of either the vertical or horizontal sums of 2 neighbouring ECAL towers must be greater than a threshold;

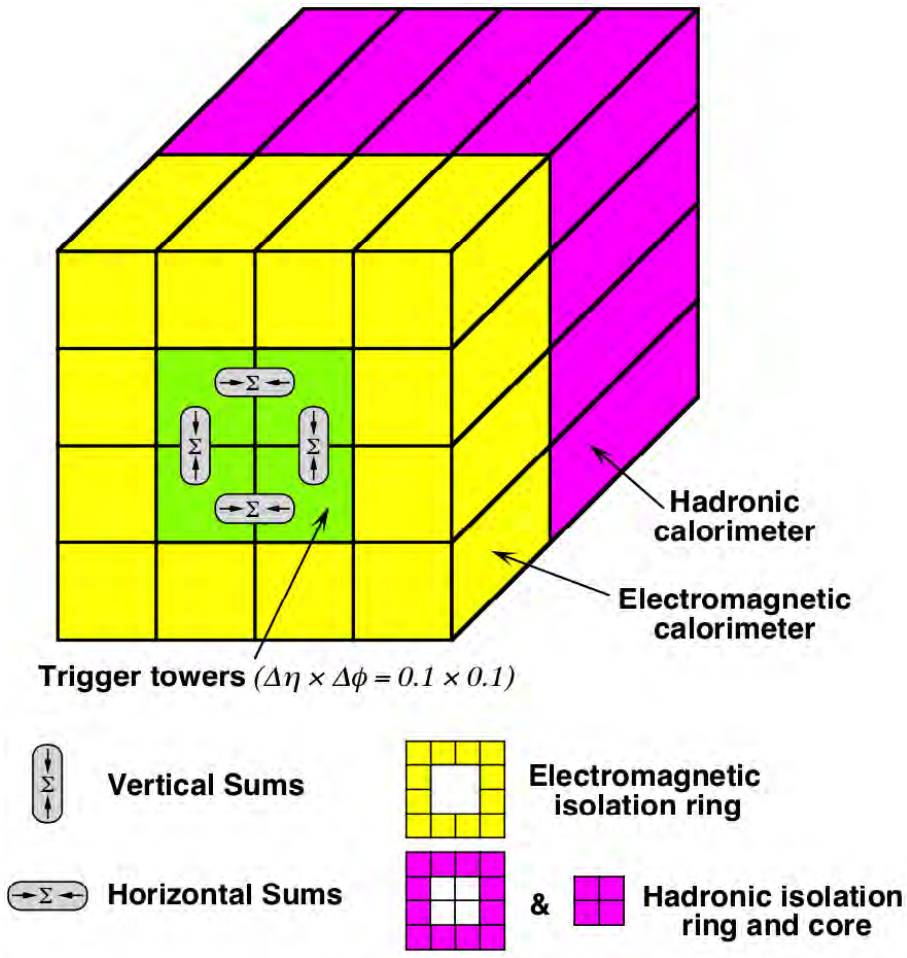

Figure 10.5: Elements of the run2 trigger algorithm[154].

- The E_T sum of the EM isolation ring (yellow) must be below a threshold;
- The E_T sum of the hadronic isolation core (behind green) must be below a threshold;
- The 'core' area (the 2×2 trigger towers in green in figure 10.5) must be a local maximum.

If a tower exceeded the E_T sampling range it was considered 'saturated,' no isolation thresholds were applied and therefore the algorithm was passed. For the case of matching digitised E_T values when comparing maxima between neighbours a convention was used (of 'greater than' or 'greater than or equal to' depending on direction). This ensured, in a deterministic way, only one candidate was accepted if neighbouring cores had the same E_T[153, 154].

10.3 LS2 upgrades

To increase its physics potential the LHC has upgrades planned for installation during long shutdowns, each of which are approximately two years long. The schedule is shown in figure 10.6. During 2019-20 the LHC will be switched off for LS2 and upgrades to the CERN accelerator complex will increase the instantaneous luminosity and centre of mass energy of collisions. The increased luminosity and pile-up will provide challenges to the detector systems so during the shut-down ATLAS will install its phase-1 upgrades. Run3 of the LHC will begin in 2021 and is expected to produce 300 fb^{-1} of data, before being shut down again at the end of 2023.

10.3.1 Upgrades of the CERN accelerator complex

In November 2018, the LHC finished the final physics collisions of run2 and was switched off for the coming 2 years.

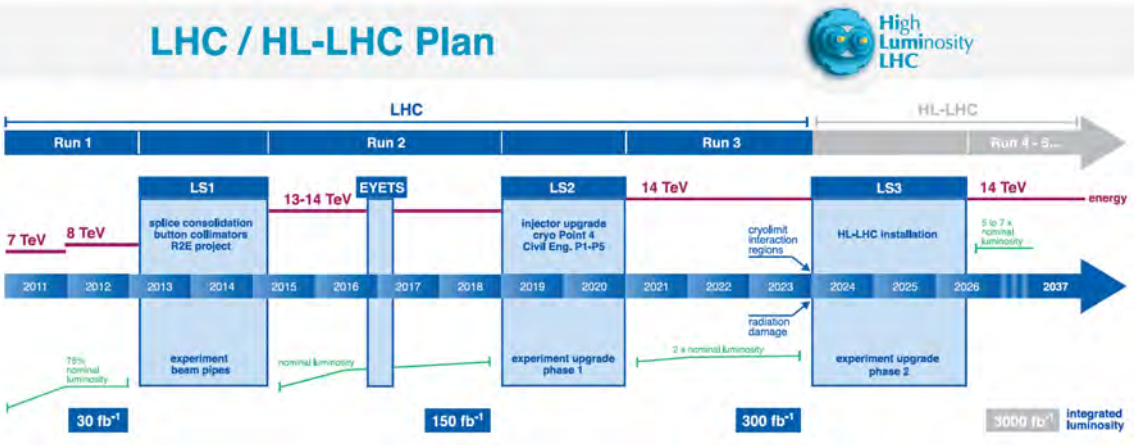

Figure 10.6: The road map to the HL-LHC [155].

During this time the accelerators used to prepare the beam for injection to the LHC will be upgraded or replaced. LINAC2, the first linear accelerator in the chain that feeds protons into the LHC, will be replaced. The replacement Linear Accelerator 4 (LINAC4) will accelerate negative hydrogen ions (H^-) to 160 MeV, rather than protons to 50 MeV, and should produce bunches with double the brightness and intensity compared to those produced previously[156]. Commissioning began in spring 2017 and the system showed good reliability during its initial stand-alone run programme[157]. It will be connected to the next accelerator in the chain, the PSB, in early 2019. Additionally the PSB will be upgraded to handle the injection of negative H^- ions, known as "charge-exchange injection," and subsequent acceleration of protons to 2 GeV[158, 157].

Within the LHC 20 dipole magnets will be replaced to ensure they conform to standards. The diodes of the remaining dipoles will have reinforced insulation to reduce trips at the high voltages needed to reach a beam of 7 TeV per proton. 4 new 11 T triplet magnets will be installed to focus the beams and reduce the β^*. A magnet training campaign, expected to require up to 110 quenches per dipole magnet, is planned to allow protons beams to reach the centre of mass energy of $\sqrt{s} = 14$ TeV[159]. Early studies from the start of LS2 suggest the length of time required for this campaign is longer than originally planned so discussions are ongoing as to what energy protons will collide in run3.

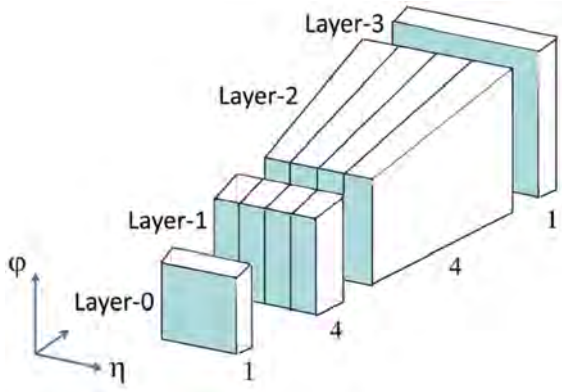

Figure 10.7: 1-4-4-1 super-cell layout of the upgraded LAr calorimeters in a (0.1×0.1) region[162].

10.3.2 Phase-I upgrade of ATLAS

To cope with the higher luminosity provided by the LHC in run3 ATLAS has prepared its phase-1 upgrade program. The aim of the program is to maintain acceptable rates from the first level of trigger without an increase of E_T thresholds or loss of efficiency[160]. The systems with major upgrades planned are the LAr calorimeters, TDAQ and the muon spectrometers[161]. The end caps of the muons spectrometers were to be replaced with the New Small Wheel (NSW), providing angular precision of 1 mrad for the level-1 trigger. However technical issues have lead to delays and it is not clear if the upgraded system will be installed on both sides. The muon spectrometer upgrades are not relevant to work presented here and are not discussed any further.

The LAr calorimeter systems will be upgraded to provide improved data to L1CALO with better granularity in η, better E_T resolution and longitudinal information. This is done by using 'super-cells,' sums of at least 4 calorimeter cells with E_T digitised by the LAr electronics, instead of trigger towers for level-1 trigger data. Using super-cells 10 E_T samplings will be made per 0.1×0.1 area in a 1-4-4-1 scheme as illustrated in figure 10.7. Figure 10.8 compares the trigger data provided by legacy and upgraded systems for an electron.

In the legacy system, analogue data were sent to the pre-processor of L1CALO to

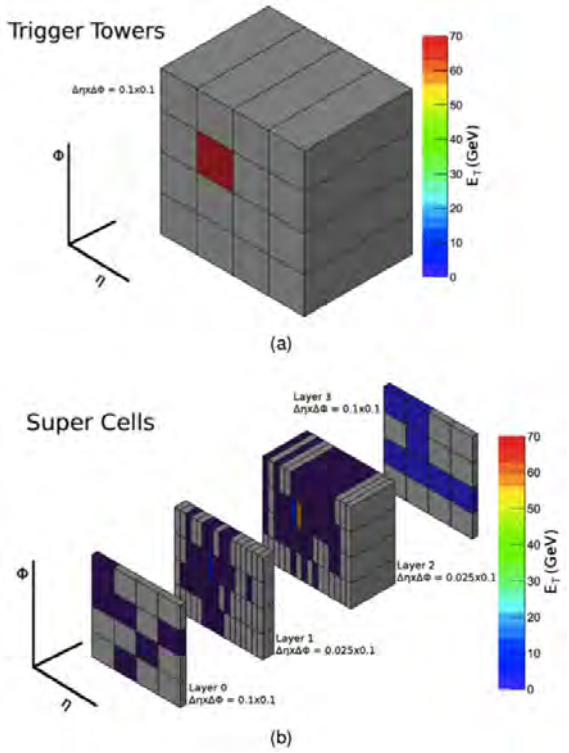

Figure 10.8: Simulation of a $E_T = 70$ GeV electron. The simulation of the run2 system is shown above and the run3 system shown below[160].

digitise it, assign it to a bunch crossing and scale it to an E_T value. The upgraded LAr systems will digitise the E_T samplings and send digitised data to L1CALO. It is expected that the new digitization scheme will improve the E_T resolution by at least a factor of 4 compared to the previous scheme. As discussed in section 3.2.3 the LAr system is used for the entirety of the ECAL and part of the HCAL. The TileCal, the other major component of the HCAL, is not being upgraded and the legacy L1CALO pre-processor will digitise the analogue signals received from it.

L1CALO will be upgraded to take advantage of the higher granularity of the LAr samplings. The improvement in the granularity of data should mean that isolation vetoes can be improved to help reject pile-up. Figure 10.9 shows an overview of the upgraded L1CALO. In this system digital data are provided from the LAr calorimeters and received at the new optical plant. Analogue TileCal data is received by the pre-processor. Here it is assigned to a bunch crossing and scaled to an E_T value before being transferred to the optical plant via the Jet Energy Processor

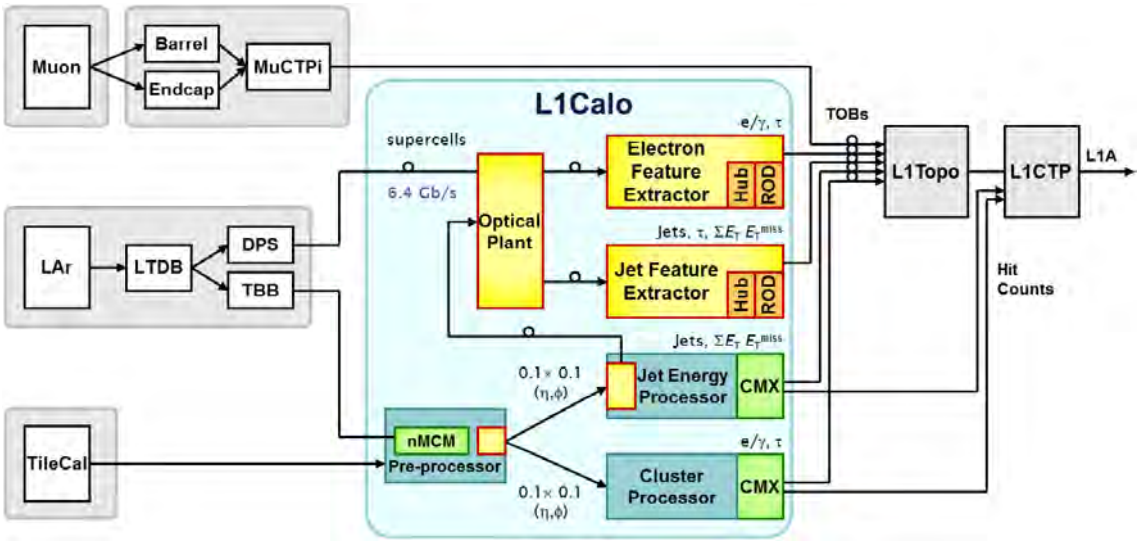

Figure 10.9: Overview of the L1CALO system in run 3. Phase-1 components are shown in yellow[147].

(JEP). The optical plant then transfers the data to the new feature extraction modules which calculate new algorithms not previously possible at level-1.

The new feature extraction modules are the Jet feature extraction module (jFEX), Global feature extraction module (gFEX) and Electromagnetic feature extraction module (eFEX). The jFEX is responsible for identifying energetic jets using finer-granularity data over a larger area compared to the legacy system. The gFEX is responsible for identifying global event features, such as E_T^{MISS}, and very large area jets. The eFEX, discussed in more detail in section 10.3.2.1, is responsible for identifying isolated E_T deposits in the ECAL to trigger on e/γ and τ particles.

The outputs from the feature extraction modules are Trigger Objects (TOBs) which describe trigger candidates based on location, E_T value and isolation values. A list of TOBs is optically transmitted from each module to L1TOPO, where topological algorithms are performed. The results are then transmitted to the Central Trigger Processor (CTP). The CTP will be upgraded to be more flexible in its handling of trigger menu items and also handle double the number of inputs.

Until the system is fully commissioned the legacy system will remain in place. This includes the analogue ECAL data systems shown in figure 10.9. The front-end elec-

tronics of the detector are not being upgraded until phase-II upgrades and therefore the latency and acceptance rate limits remain unchanged ($\sim 2.2\ \mu s$ and ~ 100 kHz respectively).

10.3.2.1 eFEX

The Electromagnetic feature extraction module (eFEX) is the new module of L1CALO responsible for identifying isolated E_T deposits characteristic of e/γ particles. It is designed to use the full granularity of the calorimeter data available to L1CALO and so, for each (0.1×0.1) region, it will handle 10 ECAL samplings (in the form of super-cells) and 1 HCAL sampling. Using this data it will be able to run more sophisticated algorithms than were possible with the legacy hardware and more similar to the algorithms run in offline software. The eFEX provides coverage within $|\eta| \leq 2.5$. It will be able to calculate up to three different isolation calculations with several possible values used to veto on each. As the eFEX is designed to identify the small, isolated showers it should also be useful for triggering τ particles.

The eFEX can produce no more than one TOB for each (0.1×0.1) region. While computing an instance of an algorithm, data are provided from a maximum area of (0.3×0.3), referred to as an environment area. In terms of hardware there are 24 eFEX modules in total. Each module has identical hardware and firmware, with any modifications for incomplete environment areas made with programmable parameters.

10.3.3 Summary for first level electron trigger

The upgraded LHC will provide a better physics reach for the experiments but also a more difficult environment for identifying e/γ. The increased number of pile-up interactions in particular will reduce the effectiveness of isolation vetoes. Upgrades to ATLAS will provide L1CALO with the ability to perform more sophisticated algorithms through the use of the eFEX. The data provided to it will be of finer

granularity in η and will contain longitudinal information. The algorithms it will perform have not yet been finalised.

10.4 Algorithm decisions considered

This work was completed as part of an ATLAS authorship task - work assigned to a new collaboration member that must be carried out before being added to the author list. The purpose was to perform simulation studies and explore different choices of the eFEX algorithm. Previous studies are presented elsewhere but details, such as the clustering and digitisation of super-cells, were not dealt with correctly[147]. The outcomes from the studies presented here have been used to motivate choices in the design of the eFEX firmware.

10.4.1 Methods and samples

When considering the performance of a trigger, there are two major factors one must consider: the efficiency and the rejection power. A trigger that accepted every event would be 100% efficient. However it would have no rejection and be entirely impracticable for ATLAS. Conversely the better rejection a trigger has the more likely its efficiency will decrease due cutting into signal. A good trigger maintains a high efficiency with good rejection for background processes.

The efficiency of a trigger is typically dependent on the E_T of the candidate particle so is often shown as a function of it on a turn-on curve. An optimal trigger would have a turn-on curve with: very low efficiency below its threshold (demonstrating good background rejection); a sharp upwards curve demonstrating it quickly reaching a high efficiency above the threshold; and a flat plateau at $\sim$ 100% efficiency making trigger efficiency corrections for subsequent analyses simpler. These features can be seen in the example curve from ATLAS data, shown in figure 10.10.

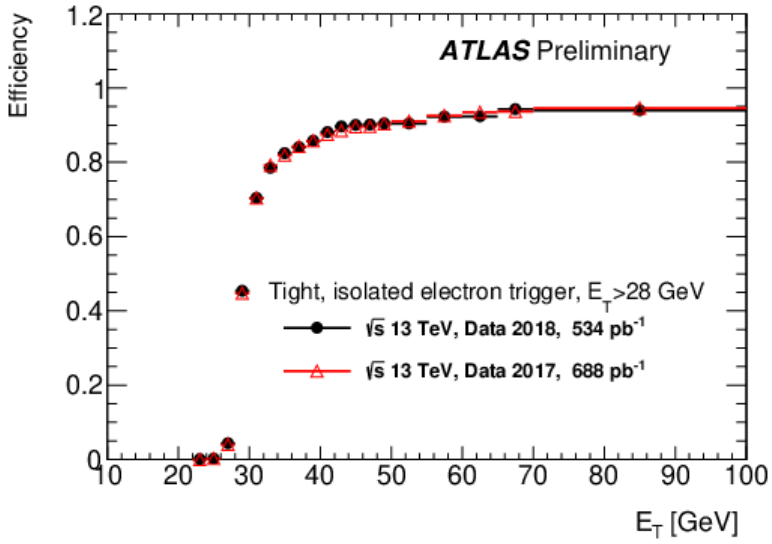

Figure 10.10: Efficiency of the tight, isolated electron trigger using ATLAS data. The x-axis shows the transverse energy of the electron candidates as calculated by offline algorithms. The efficiency was calculated through the tag-and-probe method[163].

In these studies, minimum bias MC samples were used to estimate the acceptance rate. The dataset consisted of 10^5 events for collisions with $\sqrt{s} = 13$ TeV and 60 collisions per bunch crossing on average. These conditions represent the minimum level of pile-up expected for run3. An event was considered accepted if it had at least one cluster passing the algorithm. To produce an approximate rate the maximum filled bunch crossing rate was taken to be 30 MHz (assuming 3 of every 4 possible bunches are filled). While this may not be entirely accurate, the purpose is to compare the relative acceptance rates, and this assumption only changes the scale. The acceptance rate was calculated as shown in equation 10.5:

$$\text{Acceptance rate} = \frac{30 \text{ MHz} \times \text{Number of events accepted}}{\text{Total number of events}}. \tag{10.5}$$

For some studies the 'RoI acceptance factor' is used rather than an acceptance rate. This was primarily used to compare isolation vetoes - if a particular event had more than one cluster then it makes more sense to compare the effect of the veto on each cluster.

MC samples of $Z \rightarrow e^+e^-$ events were used to calculate the efficiency. There were 5×10^4 events available. The use of MC meant it was possible to access the truth information in event records and subsequently turn-on curves are shown with respect to the truth E_T of electrons (rather than the reconstructed E_T as shown in figure 10.10). An electron was considered as successfully triggered if there was a cluster passing the algorithm within $dR < 0.3$ of it. This was to ensure that the trigger result obtained was only due to the algorithm being applied in the region of the electron and not due to background processes in other parts of the detector. The efficiency was then defined as shown in equation 10.6:

$$\epsilon = \frac{\text{Number of successful triggered electrons}}{\text{Total number of electrons}}. \tag{10.6}$$

The errors on both the acceptance rate and efficiency are estimated as binomial errors as shown in equation 10.7 for a total of N events with k passes[137, 136]:

$$\sigma = \frac{1}{N}\sqrt{k\left(1 - \frac{k}{N}\right)}. \tag{10.7}$$

For simplicity only one electron per event was considered. This was chosen to be the most energetic electron within the coverage of the eFEX ($|\eta| < 2.5$). Due to the loss of performance of the detector in its overlap region ATLAS analyses typically veto physics objects in ($1.37 < |\eta| < 1.52$). Therefore it was decided to not consider this region when optimising the trigger. Electrons in this region were vetoed for this study, with the exception of the plots shown in section 10.4.4.

To compare the performance of triggers, two types of plots are used: same-rate turn on curves or Receiver Operating Characteristic (ROC) curves. The former will show the efficiency as a function of the object's E_T for a fixed acceptance rate. The latter will show the average efficiency, over an E_T range, as a function of the acceptance rate.

It is also worth noting that the cumulative effect of many consecutive filled bunches in a bunch train leads to an upwards baseline shift in the calorimeter response. During run2 L1CALO used a dynamic pedestal correction to help remove this effect from its algorithms[164]. The simulation of the dynamic pedestal subtraction had not been implemented in the reconstruction of the MC samples. To correct for this a veto was placed on all Bunch Crossing IDentification (BCID) numbers that were less than 20 from the front of their train. It is expected that the dynamic pedestal subtraction will be in place for data-taking and should correct for these effects.

10.4.2 Cluster size and shape

The algorithm is seeded by layer 2 of the ECAL. The thickness of this layer is $16X_0$ and therefore this is where electrons are expected to deposit most of their energy. The first step in the algorithm is requiring a super-cell from this layer which is a local maximum compared to its neighbours. The requirement of a local maximum helps reduce the formation of overlapping clusters around the same E_T deposits. Clusters are then built starting with the seed cell.

The first algorithm choice to be investigated was the size and shape of the cluster, defining which super-cells are used to calculate the E_T total. The two shapes, compared in figure 10.11, considered are:

- Narrow clusters that only included the central η super-cells from each of the pre-sampler and layer 3 (where appropriate).
- Wider clusters including super-cells from all layers that overlap with the second layer.

For each shape of cluster different sizes were also investigated. The cluster size is quoted using the number of super-cells in the second layer of the calorimeter. The size was varied in the η direction from three super-cells at a minimum up to seven

super-cells maximum. The size in ϕ was varied between two and three super-cells wide in ϕ. For clusters two super-cells wide in ϕ, the direction was chosen to include the most energetic neighbour of the seed cells neighbours in the direction ϕ.

To compare the performance same-rate turn-on curves were produced. The E_T cut was varied to ensure each cluster size and shape produced approximately the same rate. Figure 10.12 shows a set of turn on curves comparing the optimum cluster shape, a 3×2 narrow cluster, with other similar options. The turn on curves were produced with an acceptance rate of $\sim$ 20 kHz, the approximate rate allowable in the final algorithm. A 44 GeV E_T threshold was required to reach the target rate with the narrow 3×2 cluster. The isolation vetoes, still to be determined at this point, were expected to reduce the acceptance rate with a minimal loss in efficiency. Therefore the turn on curves were reproduced with a more relaxed target rate of $\sim$ 100 kHz. This shows the same cluster shape, a narrow 3×2 cluster, is better with this rate. To produce this target rate, a 26 GeV E_T threshold was required.

10.4.3 Isolation vetoes

As discussed in section 10.3.2.1 the upgraded trigger system will be able to apply up to 3 vetoes using more complicated calculations than previously possible. The following sections explain how the isolation vetoes were determined and tuned.

10.4.3.1 Definition of variables

Off-line electron identification variables were used as a starting point[165]. As the eFEX can only use data from calorimeter systems, variables that rely on data from other systems were not considered. The definitions of the remaining variables were adjusted to use super-cell granularity rather than the full calorimeter granularity used off-line. The most effective variables are summarised in table 10.1.

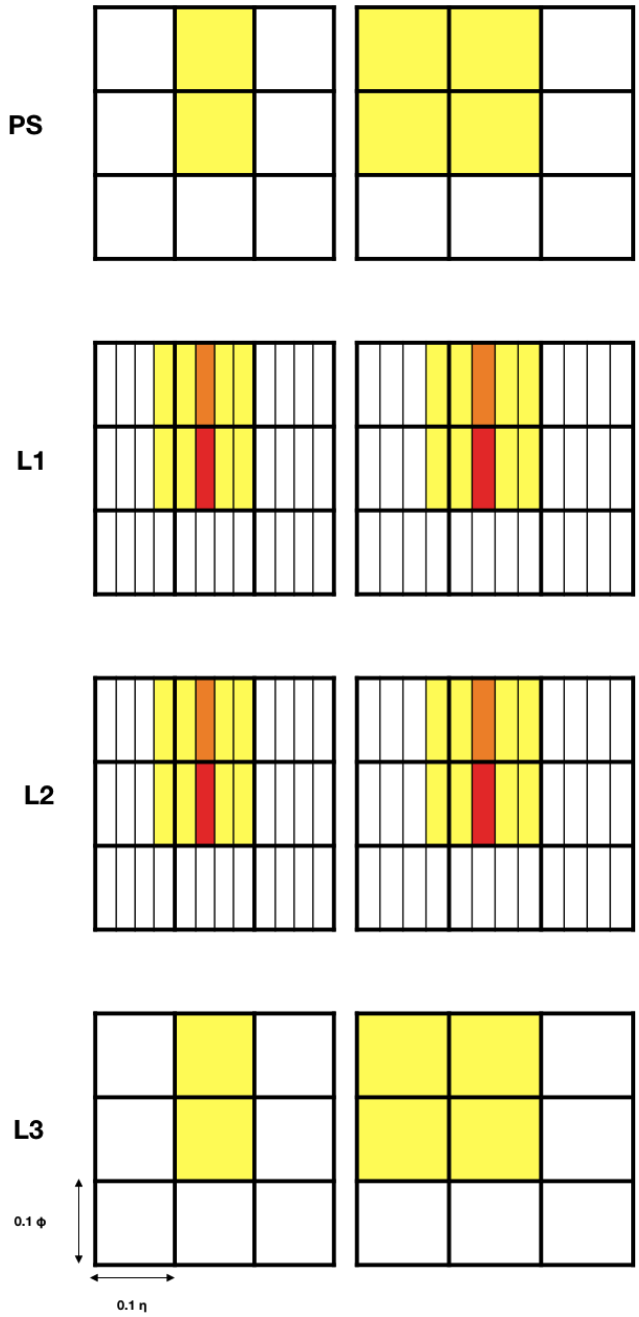

Figure 10.11: A diagram comparing the inclusion of super-cells in a 5×2 cluster. Seed cells are shown in red, the most energetic ϕ neighbour in orange and the other super-cells included in the cluster are shown in yellow. A narrow cluster is shown on the left and a wide cluster on the right. Both clusters include the 5×2 super-cells in layers 1 and 2. The narrow cluster only includes two super-cells in the pre-sampler and layer 3 - the ones that overlap with the seed and its ϕ neighbour. The wider cluster includes all super-cells in the pre-sampler and layer 3 that overlap with the 5×2 super-cells in layer 2.

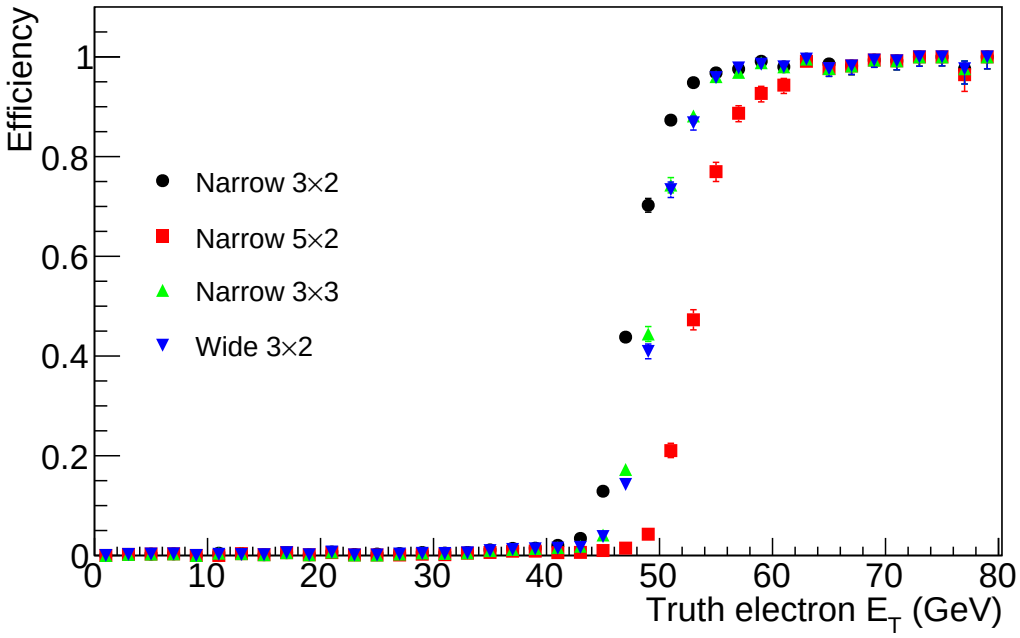

(a) Target rate of ∼20 kHz

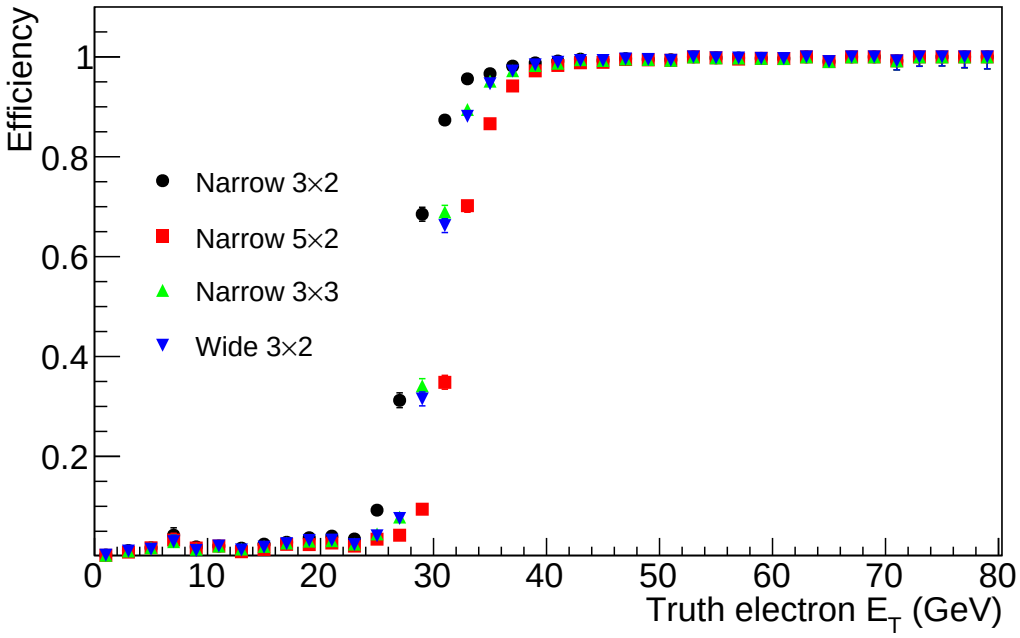

(b) Target rate of ∼100 kHz

Figure 10.12: Same-rate turn on curves comparing the eFEX efficiency as a function of truth electron E_T. Each plot shows the turn-on curves for different cluster sizes or shape with the E_T cut tuned to give a similar rate.

Table 10.1: An explanation of the isolation vetoes discussed in this chapter. It is a slimmed down list of those presented in [165], excluding those less effective or using data from other systems.

Variable	Description	Calculation	Chosen size
R_η	Measurement of shower width in L2 of the ECAL comparing the E_T in a smaller region to a wider region, shown pictorial in figure 10.13.	$1 - \frac{E_T \text{ (smaller window)}}{E_T \text{ (larger window)}}$	$3 \times 2 : 7 \times 3$
R_{Had}	Measurement of shower depth comparing the E_T in the ECAL and the HCAL trigger towers or super-cells behind it	$\frac{E_T\text{Had}}{E_T\text{Had} + \text{ECAL}}$	3×3
f_3	Measurement of shower depth comparing the E_T in the third layer of the ECAL to total in a region	$\frac{E_T(layer3)}{E_T(ECAL)}$	3×2
w_{stot}	Measurement of shower width in the layer 1 of the ECAL	$\sqrt{\frac{\Sigma E_i (i - i_{max})^2}{\Sigma E_i}}$	5×3
$w_{\eta 2}$	Measurement of shower width in the layer 2 of the ECAL	$\sqrt{\frac{\Sigma E_i \eta_i^2}{\Sigma E_i} - \left(\frac{\Sigma E_i \eta_i}{\Sigma E_i}\right)^2}$	5×3

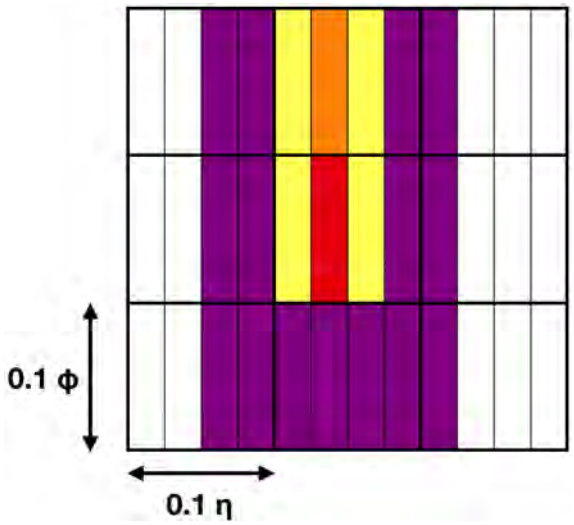

Figure 10.13: A diagram showing layer 2 of the ECAL demonstrating how R_η is calculated. The inner window (yellow) is centred on, and includes, the seed cell (red) and its most energetic neighbour (orange). The outer window is shown in purple.

For each isolation veto the optimum window size was found by comparing ROC curves. Each isolation veto was applied to narrow 3×2 clusters passing a 26 GeV E_T threshold. The ROC curves show the predicted acceptance rate and efficiency for electrons with $30 <$ truth $E_T < 50$ GeV. The lower limit on the E_T range was chosen as the cluster and E_T threshold by themselves reached ≈100% efficiency for 30 GeV (as shown by figure 10.12b). The upper limit was chosen to remove any bias from high E_T electrons which are typically very isolated.

An example of the comparisons of ROC curves is shown for some window sizes for R_η in figure 10.14a. For most variables the performance differences between window sizes were minor however the best definition of each variable was always chosen by comparison of the ROC curves of the different window sizes. Table 10.1 shows the optimum definition of each variable.

This step was repeated for each isolation veto being considered. The resulting ROC curves comparing the best definition of each variable are shown in figure 10.14b. This shows that the two most effective individual vetos are R_η and $w_{\eta 2}$, both measures of isolation in the second layer of the calorimeter. As they both measure the same characteristic it was assumed that applying them together would give little, if any, reduction in rate. The next best variable is R_{Had}.

10.4.3.2 Combination of 2 vetoes

Two combinations of two isolation variables were considered: R_η with R_{Had} and $w_{\eta 2}$ with R_{Had}. To do this, 2D plots were produced showing the efficiency and acceptance rate as a function of the threshold applied to each isolation veto. The same efficiency definition was used as for the ROC curves. These plots, shown in figure 10.15, were then used to find the set of thresholds that would produce the lowest acceptance rate while maintaining 90% efficiency. These thresholds were then used to produce turn-on curves to examine the efficiency across a wider E_T range.

The turn on curves in figure 10.16a show almost identical efficiency between the

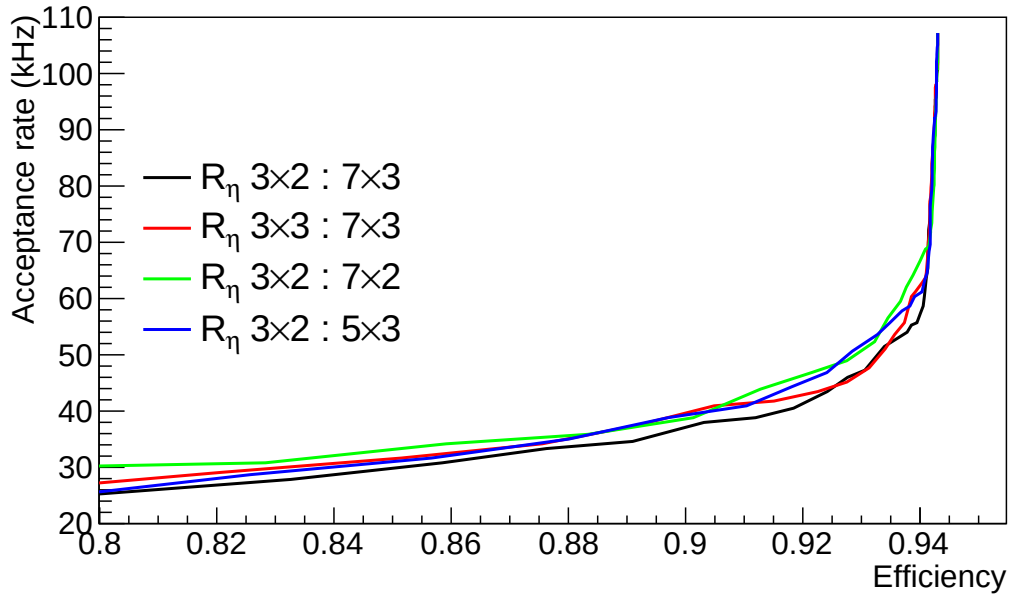

(a) Comparisons of different R_η window sizes

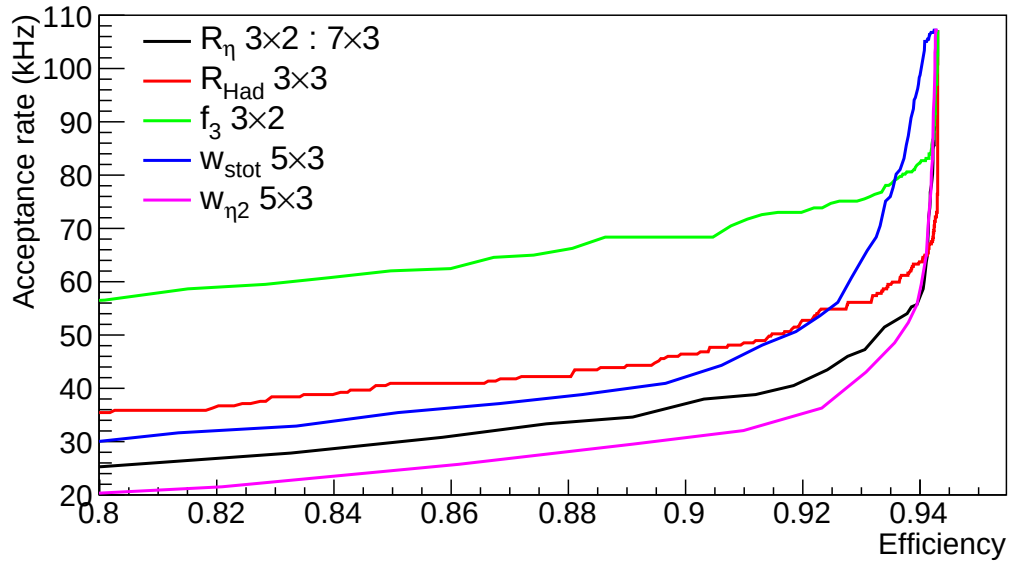

(b) Comparisons of different vetoes

Figure 10.14: ROC curves comparing performance of different variables in combination with a narrow 3×2 cluster and an E_T threshold of 26 GeV. The efficiency is calculated for electrons with 30 GeV $\leq$ truth $E_T \leq$ 50 GeV. The upper limit on the efficiency and acceptance rate is due to the cluster and E_T threshold.

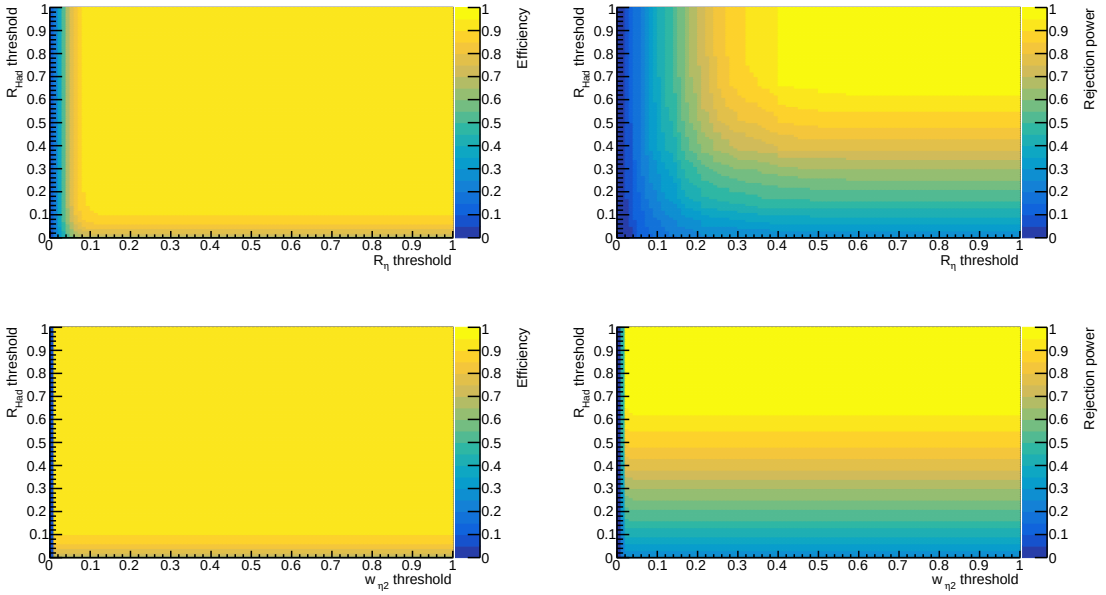

Figure 10.15: The predicted efficiency and acceptance rate as a function of two isolation thresholds.

two combination considered. The predicted acceptance rates for R_η and R_{Had} are slightly lower and therefore this combination was favoured.

10.4.3.3 Combination of 3 vetoes

To choose the third veto to be used in the algorithm the remaining vetoes were considered in addition to the two already chosen. Therefore algorithms using R_η and R_{Had} and either f_3 or w_{stot} were compared. To tune the threshold to be applied to each variable, the method used in the previous step was repeated using 3D plots rather than 2D plots. The plots, analogous to those in figure 10.15, allowed the value of each variable to be plotted for the signal and background samples. From these plots the combination of thresholds were found that produced the lowest acceptance rate while maintaining 90% efficiency. These thresholds were then used to produce turn-on curves, shown in figure 10.16b.

These turn-on curves show almost identical efficiency across the E_T range studied. The algorithm using w_{stot} as the third veto (blue markers in figure 10.16b)

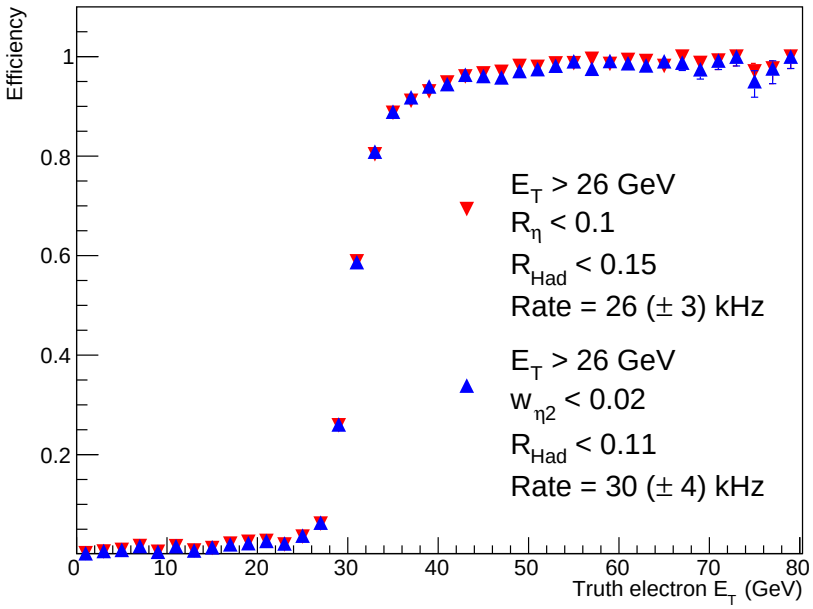

(a) Using two isolation vetoes.

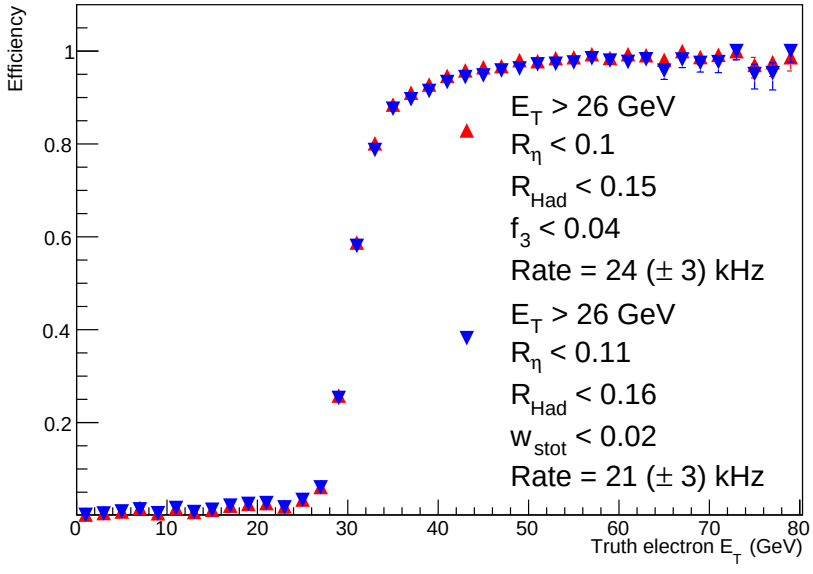

(b) Using three isolation vetoes.

Figure 10.16: The efficiency of the prototype eFEX algorithm.

demonstrated a slight lower acceptance rate 21 ± 3 kHz, compared to the alternative algorithm's rate of 24 ± 3 kHz. Compared to using two isolation thresholds this was a decrease in rate of $\sim 20\%$ while maintaining similar efficiency.

10.4.4 Efficiency as a function of η

The efficiency was examined as a function of pseudorapidity. An ideal trigger is uniformly efficient in its plateau region without any dependence on other variables (i.e. coordinates) as this can bring complications and biases into subsequent analyses. Therefore the efficiency was calculated as function of the η coordinate of the candidate electron. To prevent bias from energetic electrons this was calculated for 2 E_T ranges: 30 GeV$< E_T <$ 35 GeV and 35 GeV$< E_T <$ 50 GeV.

The resulting plot is shown in figure 10.17a. The drop in efficiency is expected in the region $1.37 < |\eta| < 1.52$ due to the overlap region of the detector. For this reason electrons in this region are vetoed in every other part of this study.

Also visible in figure 10.17a is a drop in efficiency at high pseudorapidities ($|\eta| > 2.3$) for both E_T ranges studied. This was caused by the reduction in granularity in the ECAL end-caps. This drop in granularity in particular effects layer 1, the sampling layer used to calculate w_{stot}. Therefore this isolation veto was not applied above $|\eta| = 2.3$ and the resulting efficiency is shown in figure 10.17b. There was no measurable change in the acceptance rate.

The efficiency in figure 10.17b is still not uniform in η. This is due to the varying amounts of material in the detector at different η coordinates. During run2 this was compensated for by making the isolation threshold η dependent. No such correction was attempted here.

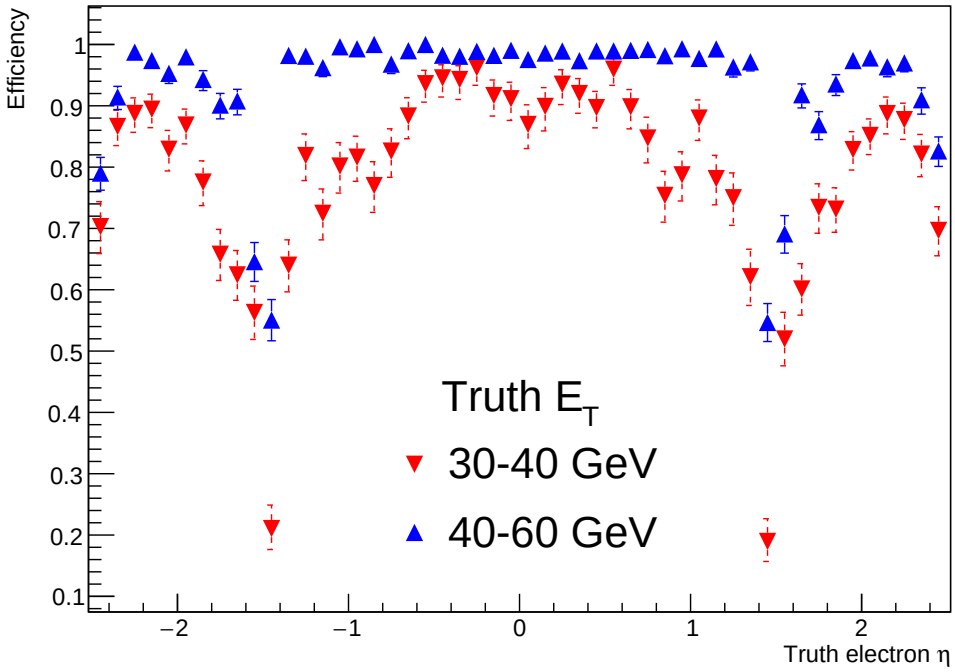

(a) Prototype algorithm using R_η, R_{Had} and w_{stot}.

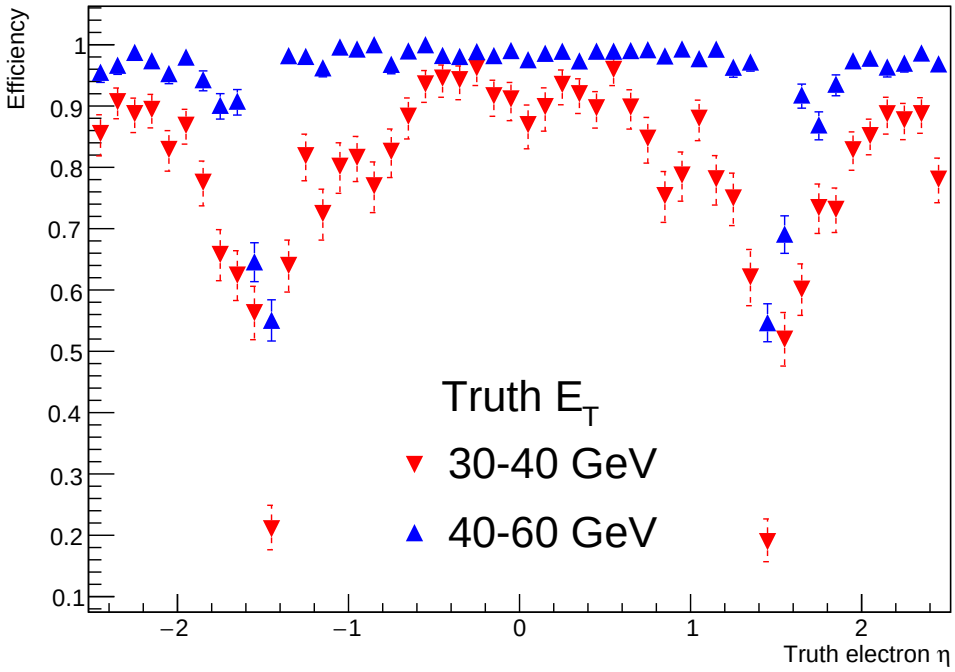

(b) Prototype algorithm using R_η, R_{Had} and in the region $|\eta| < 2.3$, w_{stot}.

Figure 10.17: The efficiency as a function of η for the prototype algorithm.

10.4.5 Digitisation

A digitization scheme had not been implemented in the reconstruction of the MC samples although the eFEX will use one. Therefore up until this point a scheme using a noise cut of 125 MeV and digitisation scale of 62.5 MeV was implemented in the analysis code. The digitisation was then briefly investigated to find if changes would cause a large difference in the rates or efficiencies. Two values were varied: the noise cut i.e. the minimum E_T value needed to be considered as non-zero in E_T samplings and the digitisation scale i.e. the steps of E_T that could then be considered. For example, if using a noise cut of 100 MeV and digitisation scale of 25 MeV the possible values E_T samplings would be 0 MeV, 100 MeV, 125 MeV, 150 MeV and so on.

The algorithm developed thus far was then run with different choices of digitisation and noise cut. The different schemes considered are summarised in table 10.2 with the predicted acceptance rate and minimum E_T required to reach 95% efficiency. This study suggested similar performance was possible with different combinations of digitisation and noise cut: the lower noise cuts (-750, 0 and 50 MeV) with the largest digitisation scale (50 MeV) produced the same efficiency and rate as high noise cuts (100 and 150 MeV) with most of the digitisation scales (10, 25 and 50 MeV).

10.4.6 Isolation vetoes for high E_T electrons

The thresholds were tuned to give high efficiency for particular E_T ranges. Therefore it was decided to not apply the thresholds for high E_T clusters ($E_T > 50$ GeV) similar to what is done in the current trigger. This led to an increase of 50%; further tuning could reduce this rate increase.

Table 10.2: The noise cut and digitisation schemes investigated shown with the predicted acceptance rate and the minimum truth E_T of electrons required to reach 95% efficiency.

Noise cut (MeV)	Digitisation scale (MeV)	95% efficiency point (GeV) (±0.5 GeV)	Acceptance rate (kHz) (±3 kHz)
−750	0	49	20
	10	45	20
	25	44	21
	50	43	21
0	0	49	20
	10	45	20
	25	44	21
	50	43	21
50	0	49	20
	10	45	20
	25	44	21
	50	43	21
100	0	49	20
	10	43	21
	25	43	21
	50	43	21
150	0	49	20
	10	43	21
	25	43	21
	50	43	22

10.5 Summary and projected performance of electron trigger

The shape of the eFEX cluster outlined in previous studies remains the best option, producing the best efficiency for a given rate. The possible isolation vetoes that could be used by the eFEX have been explored. The best combination found is to use R_η and R_{Had} through the coverage of the eFEX and w_{stot} within $|\eta| \leq 2.3$. The cluster E_T requirement and isolation vetoes are expected to achieve a reasonable acceptance rate although this could potentially be lowered with further studies. These studies, including the definition of isolation calculations, has helped feed into the firmware decisions for the eFEX.

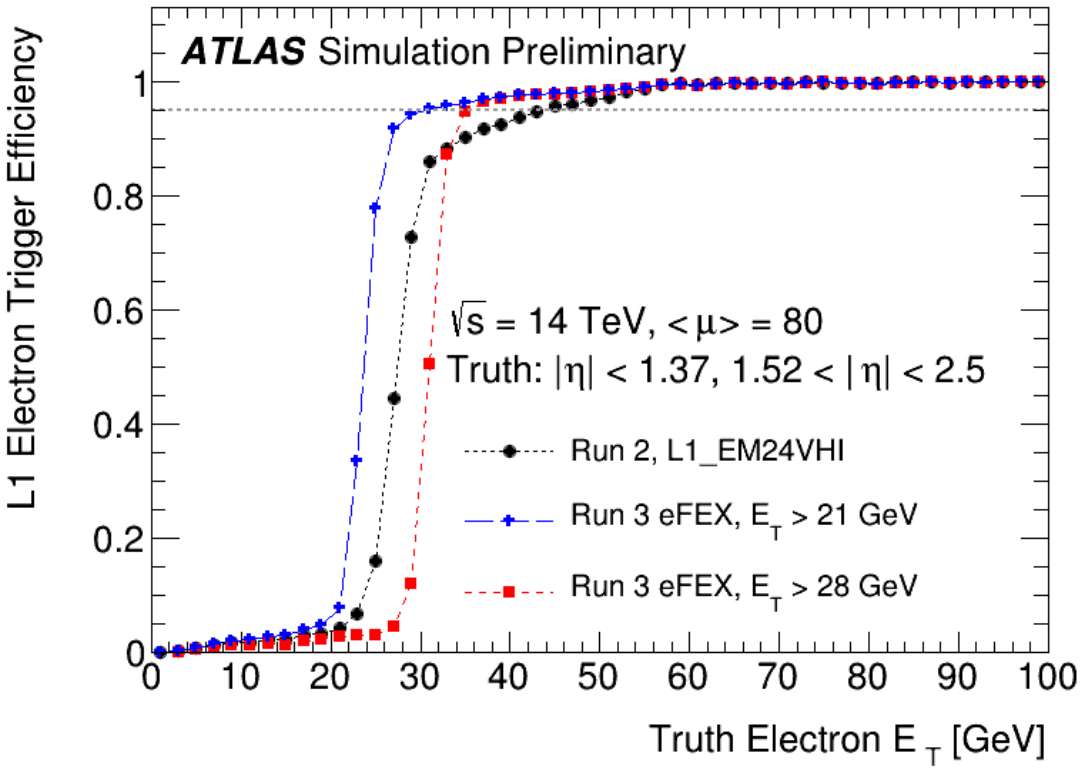

Figure 10.18: Expected performance of the trigger during run3. Black and blue points are approximately same rate while red are approximately half rate

The expected performance of the eFEX is summarised in the turn-on curve shown in figure 10.18. These curves are produced using the same algorithm presented in this chapter with slightly different thresholds applied. The run2 trigger algorithm simulation (black points) are shown. The eFEX algorithm is shown with an E_T cut of 21 GeV (blue points) resulting in a similar acceptance rate to the run2 algorithm. This demonstrates the improvement in performance the new system provides, reaching 95% efficiency $\sim$ 15 GeV sooner than the legacy hardware. The eFEX algorithm with a higher E_T cut of 28 GeV (red points) produces approximately half the acceptance rate of the legacy system. In comparison it still results in a sharper turn-on curve reaching its plateau region sooner.

There are still areas of the algorithm which could be improved. For example the E_T resolution of the eFEX clusters was not optimised. This could be done based on the η position of the cluster or the contributions of super-cells from different

layers could be scaled. Either of these treatments of E_T resolution could lead to a further improvement in the algorithm performance. Another option for further improvements in performance is by implementing E_T-dependent isolation vetoes, similar to what is done in the current system.

The tools developed for the studies presented here have been shared with colleagues and have provided the starting point for equivalent performance studies for the τ algorithm.

REFERENCES

[1] R. Feynman *et al.*, *The Feynman Lectures on Physics; Vol. I*, vol. 33. 1965.

[2] The LHCb collaboration, "Measurement of the $b_s^0 \to \mu^+\mu^-$ branching fraction and effective lifetime and search for $b^0 \to \mu^+\mu^-$ decays," *Phys. Rev. Lett.*, vol. 118, p. 191801, 2017.

[3] ATLAS collaboration, "Measurement of Differential Cross Sections for Single Diffractive Dissociation in $\sqrt{s} = 8$ TeV pp collisions using the ATLAS ALFA Spectrometer." Submitted to JHEP, prepint: arXiv:1911.00453, 2019.

[4] S. Weinberg, "A model of leptons," *Phys. Rev. Lett.*, vol. 19, pp. 1264–1266, Nov 1967.

[5] C. N. Yang and R. L. Mills, "Conservation of isotopic spin and isotopic gauge invariance," *Phys. Rev.*, vol. 96, pp. 191–195, Oct 1954.

[6] J. Greensite, ed., *An Introduction to the Confinement Problem*, vol. 821 of *Lecture Notes in Physics*, 2011.

[7] M. Thomson, *Modern Particle Physics*. Cambridge University Press.

[8] UA1, "Experimental Observation of Isolated Large Transverse Energy Electrons with Associated Missing Energy at $\sqrt{s} = 540$ GeV," *Phys. Lett.*, vol. B122, pp. 103–116, 1983.

[9] M. Banner *et al.*, "Observation of Single Isolated Electrons of High Transverse Momentum in Events with Missing Transverse Energy at the CERN $\bar{p}p$ Collider," *Phys. Lett.*, vol. B122, pp. 476–485, 1983.

[10] F. J. Hasert *et al.*, "Search for elastic muon neutrino electron scattering," *Phys. Lett. B*, vol. 46, pp. 121–124, 1973.

[11] D. P. Barber *et al.*, "Discovery of Three Jet Events and a Test of Quantum Chromodynamics at PETRA Energies," *Phys. Rev. Lett.*, vol. 43, p. 830, 1979.

[12] W. Pauli, "Über den zusammenhang des abschlusses der elektronengruppen im atom mit der komplexstruktur der spektren," *Zeitschrift für Physik*, vol. 31, no. 1, pp. 765–783, 1925.

[13] P. Dirac, "The Quantum Theory of the Electron," *Proceedings of the Royal Society of London Series A*, vol. 117, pp. 610–624, 1928.

[14] O. W. Greenberg, "Spin and unitary-spin independence in a paraquark model of baryons and mesons," *Phys. Rev. Lett.*, vol. 13, pp. 598–602, 1964.

[15] P. W. Higgs, "Broken Symmetries and the Masses of Gauge Bosons," *Physical Review Letters*, vol. 13, pp. 508–509, 1964.

[16] F. Englert and R. Brout, "Broken Symmetry and the Mass of Gauge Vector Mesons," *Physical Review Letters*, vol. 13, pp. 321–323, 1964.

[17] Fukuda *et al.*, "Evidence for Oscillation of Atmospheric Neutrinos," *Physical Review Letters*, vol. 81, pp. 1562–1567, 1998.

[18] R. Davis *et al.*, "Search for Neutrinos from the Sun," *Physical Review Letters*, vol. 20, pp. 1205–1209, 1968.

[19] G. R. Farrar and M. E. Shaposhnikov, "Baryon asymmetry of the universe in the minimal standard model," *Physical Review Letters*, vol. 70, pp. 2833–2836, 1993.

[20] J. Ellis, "Dark matter and dark energy: Summary and future directions." Royal Society Discussion Meeting on Dark Matter and Dark Energy, January 2003.

[21] S. Mandelstam, "Determination of the Pion-Nucleon Scattering Amplitude from Dispersion Relations and Unitarity. General Theory," *Physical Review*, vol. 112, pp. 1344–1360, 1958.

[22] J. D. Bjorken, S. J. Brodsky, and H. J. Lu, "Rapidity-gap events in e^+e^- annihilation," *Physics Letters B*, vol. 286, no. 1, pp. 153 – 159, 1992.

[23] H. S. Bansil, *Diffractive Dijet Production in* $\sqrt{s} = 7$ *TeV pp collisions at the ATLAS Experiment*. PhD thesis, 2013.

[24] J. D. Bjorken, "Rapidity gaps in deep inelastic scattering," 1996.

[25] E. L. Berger, G. C. Fox, and A. Krzywicki, "Quantitative measure of cluster formation in multiparticle production," *Phys. Lett. B*, vol. 43, no. CERN-TH-1593. 2, pp. 132–6, 1973.

[26] H. Fritzsch, M. Gell-Mann, and H. Leutwyler, "Advantages of the color octet gluon picture," *Physics Letters B*, vol. 47, pp. 365–368, 1973.

[27] M. Gell-Mann, "Symmetries of baryons and mesons," *Phys. Rev.*, vol. 125, pp. 1067–1084, 1962.

[28] A. Lind, *A Study of Diffractive Scattering with the ATLAS and ALFA Experiment*. PhD thesis, 2017.

[29] LHCb collaboration, "Observation of J/ψ resonances consistent with pentaquark states in Λ_b^0 to $J/\psi\, K^- p$ decays," *Phys. Rev. Lett.*, vol. 115, p. 072001, 2015.

[30] B. Andersson, G. Gustafson, and B. Söderberg, "A general model for jet fragmentation," *Zeitschrift für Physik C Particles and Fields*, vol. 20, no. 4, pp. 317–329, 1983.

[31] K. Geiger, "Particle production in high-energy nuclear collisions: Parton cascade-cluster hadronization model," *Phys. Rev. D*, vol. 47, pp. 133–159, 1993.

[32] P. Skands, "Introduction to QCD." Lecture notes from a course given at TASI `arXiv:1207.2389`, 2012.

[33] C. N. Yang and R. L. Mills, "Conservation of Isotopic Spin and Isotopic Gauge Invariance," *Physical Review*, vol. 96, pp. 191–195, 1954.

[34] S. Bethke, "Determination of the QCD Coupling α_S," *Journal of Physics G*, vol. 26, no. 7, pp. R27–R66, 2000.

[35] M. Tanabashi *et al.*, "Review of particle physics," *Phys. Rev. D*, vol. 98, p. 030001, 2018.

[36] D. J. Gross and F. Wilczek, "Ultraviolet Behavior of Non-Abelian Gauge Theories," *Physical Review Letters*, vol. 30, pp. 1343–1346, 1973.

[37] H. D. Politzer, "Reliable Perturbative Results for Strong Interactions?," *Physical Review Letters*, vol. 30, pp. 1346–1349, 1973.

[38] Andy Buckley *et al.*, "General-purpose event generators for LHC physics," *Physics Reports*, vol. 504, no. 5, pp. 145 – 233, 2011.

[39] C. T. Davies et al, "High-Precision Lattice QCD Confronts Experiment," *Physical Review Letters*, vol. 92, no. 2, p. 022001, 2004.

[40] H. Yukawa, "On the Interaction of Elementary Particles I," *Proc. Phys. Math. Soc. Jap.*, vol. 17, pp. 48–57, 1935.

[41] T. Regge, "Introduction to complex orbital momenta," *Il Nuovo Cimento*, vol. 14, no. 5, pp. 951–976, 1959.

[42] P. Newman, *A study of the Dynamics of Diffractive Photoproduction at HERA*. PhD thesis, 1996.

[43] A. V. Barnes *et al.*, "Pion charge-exchange scattering at high energies," *Phys. Rev. Lett.*, vol. 37, pp. 76–79, 1976.

[44] The TOTEM Collaboration, "First measurement of elastic, inelastic and total cross-section at $\sqrt{s} = 13$ TeV by TOTEM and overview of cross-section data at LHC energies," *The European Physical Journal C*, vol. 79, no. 2, p. 103, 2019.

[45] I. I. Pomeranchuk, "Equality of the nucleon and antinucleon total interaction cross section at high energies," *Zh. Eksp. Teor. Fiz.*, vol. 34, no. 3, pp. 725–728, 1958.

[46] R608 Collaboration, "Evidence for pomeron single-quark interactions in proton diffraction at the ISR," *Phys. Lett. B*, vol. 163, no. CERN-EP-85-129, pp. 267–272. 9 p, 1985.

[47] A. Donnachie and P. V. Landshoff, "Elastic Scattering and Diffraction Dissociation," *Nucl. Phys.*, vol. B244, p. 322, 1984.

[48] A. Donnachie and P. V. Landshoff, "Total cross sections," *Phys.Lett.*, no. B296, pp. 227–232, 1992.

[49] M. Froissart, "Asymptotic behavior and subtractions in the Mandelstam representation," *Phys. Rev.*, vol. 123, pp. 1053–1057, 1961.

[50] A. Foster, *Single Dissociative Diffraction of protons in* $\sqrt{s} = 8$ *TeV collisions with the ATLAS experiment*. PhD thesis, 2018.

[51] The TOTEM Collaboration, "Measurement of Elastic pp Scattering at $\sqrt{s} =$ 8 TeV in the Coulomb-Nuclear Interference Region – Determination of the ρ Parameter and the Total Cross-Section," *Eur. Phys. J. C*, vol. 76, no. 12, p. 661, 2015.

[52] ATLAS collaboration, "Measurement of the Inelastic Proton-Proton Cross Section at $\sqrt{s} = 13$ TeV with the ATLAS Detector at the LHC," *Phys. Rev. Lett.*, vol. 117, no. CERN-EP-2016-140, 2016.

[53] S. Giani *et al.*, "Diffraction at TOTEM," in *Elastic and Diffractive Scattering. Proceedings, 13th International Conference, Blois Workshop, CERN, Geneva, Switzerland, June 29-July 3, 2009*, pp. 249–256, 2010.

[54] J. D. Bjorken, "Hard diffraction," in *Spin structure in high-energy processes: Proceedings, 21st SLAC Summer Institute on Particle Physics, 26 Jul - 6 Aug 1993, Stanford, CA*, pp. 581–589, 1994.

[55] A. H. Mueller, "O(2,1) Analysis of Single Particle Spectra at High-energy," *Phys. Rev.*, vol. D2, pp. 2963–2968, 1970.

[56] T. Martin, *Diffractive dissociation of protons in* 7 *TeV collisions at the ATLAS detector*. PhD thesis, 2012.

[57] A. B. Kaidalov, "Diffractive Production Mechanisms," *Phys. Rept.*, vol. 50, pp. 157–226, 1979.

[58] O. V. Kancheli, "Inelastic Differential Cross Sections at High energies and Duality," *ZhETF Pisma Redaktsiiu*, vol. 11, p. 397, 1970.

[59] CHLM collaboratioin, "Inelastic diffractive scattering at the CERN ISR," *Nucl. Phys. B*, vol. 108, no. 1, pp. 1–29, 1976.

[60] T. Sjöstrand *et al.*, "An Introduction to PYTHIA 8.2," *Computer Physics Communications*, vol. 191, pp. 159 – 177, 2015.

[61] J. Bellm *et al.*, "Herwig 7.0 / herwig++ 3.0 release note," *The European Physical Journal C*, vol. 76, p. 196, Apr 2015.

[62] S. Agostinelli *et al.*, "GEANT4—a simulation toolkit," *Nuclear Instruments and Methods in Physics Research Section A: Accelerators, Spectrometers, Detectors and Associated Equipment*, vol. 506, no. 3, pp. 250 – 303, 2003.

[63] T. Gleisberg *et al.*, "Event generation with SHERPA 1.1," *Journal of High Energy Physics*, vol. 2009, p. 007–007, Feb 2009.

[64] S. Gieseke, F. Loshaj, and P. Kirchgaeßer, "Soft and diffractive scattering with the cluster model in herwig," *The European Physical Journal C*, vol. 77, p. 156, Mar 2017.

[65] M. Bahr *et al.*, "Herwig++ physics and manual," *The European Physical Journal C*, vol. 58, p. 639–707, Nov 2008.

[66] T. Affolder *et al.*, "Charged Jet Evolution and the Underlying Event in $p\bar{p}$ Collisions at 1.8 TeV," *Phys. Rev.*, vol. D65, p. 092002, 2002.

[67] ATLAS collaboration, "The ATLAS Simulation Infrastructure," *The European Physical Journal C*, vol. 70, pp. 823–874, Dec 2010.

[68] T. Novak, "New Techniques for Pile-up Simulation in ATLAS." ATL-SOFT-SLIDE-2018-453, 2018.

[69] S. Navin, "Diffraction in PYTHIA," no. LUTP-09-23, MCNET-10-09, 2010.

[70] C. O. Rasmussen, "Hard Diffraction in PYTHIA8." XLV International Symposium on Multiparticle Dynamics, 2015.

[71] C. O. Rasmussen and T. Sjöstrand, "Models for total, elastic and diffractive cross sections," *Eur. Phys. J.*, vol. C78, no. 6, p. 461, 2018.

[72] G. A. Schuler and T. Sjöstrand, "Towards a complete description of high-energy photoproduction," *Nucl. Phys. B*, vol. 407, no. CERN-TH-6796-93, pp. 539–605. 66 p, 1993.

[73] G. A. Schuler and T. Sjöstrand, "Hadronic diffractive cross sections and the rise of the total cross section," *Phys. Rev. D*, vol. 49, pp. 2257–2267, 1994.

[74] G. Ingelman and P. E. Schlein, "Jet structure in high mass diffractive scattering," *Phys. Lett. B*, vol. 152, no. CERN-TH-4062, pp. 256–260. 13 p, 1984.

[75] H1 Collaboration, "Measurement and QCD Analysis of the Diffractive Deep-Inelastic Scattering Cross Section at HERA," *Eur. Phys. J .C*, vol. 48, pp. 715–748, 2006.

[76] ATLAS collaboration, "Measurement of the inclusive single diffractive dissociation cross section in pp collisions at $\sqrt{s} = 8$ TeV with the ATLAS detector using the ALFA forward detetctor." Internal note ATL-COM-PHYS-2018-031.

[77] ATLAS Collaboration, "A study of the Pythia 8 description of ATLAS minimum bias measurements with the Donnachie-Landshoff diffractive model." ATL-PHYS-PUB-2016-017, 2016.

[78] ATLAS Collaboration, "Further ATLAS tunes of PYTHIA6 and PYTHIA8." ATL-PHYS-PUB-2011-014, 2011.

[79] S. Gieseke, F. Loshaj, and P. Kirchgaeßer, "Soft and diffractive scattering with the cluster model in Herwig," *Eur. Phys. J.*, vol. C77, no. 3, p. 156, 2017.

[80] ATLAS collaboration, "The ATLAS Experiment at the CERN Large Hadron Collider," *JINST*, vol. 3, p. S08003, 2008.

[81] The CMS collaboration, "The CMS Experiment at the CERN LHC," *JINST*, vol. 3, p. S08004, 2008.

[82] ATLAS collaboration, "Observation of a new particle in the search for the Standard Model Higgs boson with the ATLAS detector at the LHC," *Physics Letters B*, vol. 716, pp. 1–29, 2012.

[83] The CMS collaboration, "Observation of a new boson at a mass of 125 GeV with the CMS experiment at the LHC," *Physics Letters B*, vol. 716, pp. 30–61, 2012.

[84] ATLAS collaboration, "Observation of light-by-light scattering in ultraperipheral Pb+Pb collisions with the ATLAS detector." ATLAS-CONF-2019-002, 2019.

[85] ATLAS collaboration, "Observation of $H \to b\bar{b}$ decays and VH production with the ATLAS detector," *Phys. Lett. B*, vol. 786, 2018.

[86] F. Hahn *et al.*, "NA62: Technical Design Document." NA62-10-07, 2010.

[87] E. Mobs, "The CERN accelerator complex." OPEN-PHO-ACCEL-2016-009, 2016.

[88] The CMS collaboration, "CMS Physics: TDR Volume 1: Detector Performance and Software." CERN-LHCC-2006-001, 2006.

[89] The CMS collaboration, "CMS Physics: TDR Volume 2: Physics Performance." CERN-LHCC-2006-021, 2007.

[90] The LHCb collaboration, "The LHCb Detector at the LHC," *JINST*, vol. 3, no. LHCb-DP-2008-001. CERN-LHCb-DP-2008-001, p. S08005, 2008. Also published by CERN Geneva in 2010.

[91] LHCb Collaboration, "LHCb reoptimized detector design and performance: TDR." CERN-LHCC-2003-030, 2003.

[92] K. Aamodt *et al.*, "The ALICE experiment at the CERN LHC," *JINST*, vol. 3, p. S08002, 2008.

[93] ALICE Collaboration, "ALICE: Physics Performance Report. ALICE physics performance : TDR." CERN-LHCC-2005-030, 2005.

[94] ATLAS collaboration, "ATLAS detector and physics performance: Technical Design Report." CERN-LHCC-99-014, 1999.

[95] F. Kuger *et al.*, *Signal Formation Processes in Micromegas Detectors and Quality Control for large size Detector Construction for the ATLAS New Small Wheel*. PhD thesis, 2017.

[96] J. Pequenao and P. Schaffner, "A computer generated image representing how ATLAS detects particles." CERN-EX-1301009, 2013.

[97] ATLAS collaboration, "ATLAS Inner Detector: TDR, 1." CERN-LHCC-97-016, 1997.

[98] ATLAS collaboration, "ATLAS Insertable B-Layer TDR." CERN-LHCC-2010-013, 2010.

[99] K. Potamianos, "The upgraded Pixel detector and the commissioning of the Inner Detector tracking of the ATLAS experiment for Run-2 at the Large Hadron Collider," *PoS*, vol. EPS-HEP2015, no. ATL-PHYS-PROC-2016-104, p. 261, 2015.

[100] ATLAS collaboration, "ATLAS central solenoid: TDR." CERN-LHCC-97-021, 1997.

[101] ATLAS collaboration, "ATLAS liquid-argon calorimeter: TDR." CERN-LHCC-96-041, 1996.

[102] ATLAS collaboration, "ATLAS calorimeter performance: TDR." CERN-LHCC-96-040, 1996.

[103] Z. Meng, "Performance of the ATLAS liquid argon calorimeter," in *Physics at the LHC2010. Proceedings, 5th Conference, PLHC2010, Hamburg, Germany, June 7-12, 2010*, pp. 406–408, 2010.

[104] ATLAS collaboration, "ATLAS tile calorimeter: TDR." CERN-LHCC-96-042, 1996.

[105] ATLAS collaboration, "ATLAS muon spectrometer: TDR." CERN-LHCC-97-22, 1997.

[106] ATLAS collaboration, "MBTS detector webpages." `https://twiki.cern.ch/twiki/bin/view/Atlas/MBTS_RunI`. Accessed August 2019 (Internal).

[107] S. Maettig, "The Online Luminosity Calculator of ATLAS," in *Conference on Computing in High Energy and Nuclear Physics 2010*, 2011.

[108] ATLAS collaboration, "Performance of the Minimum Bias Trigger in p-p Collisions at $\sqrt{s} = 7$ TeV," Tech. Rep. ATLAS-CONF-2010-068, CERN, Geneva, 2010.

[109] ATLAS collaboration, "Minimum Bias Trigger Scintillators in ATLAS Run II." ATL-DAQ-PROC-2014-010, 2014.

[110] P. Ruzicka, "Forward physics at the ATLAS experiment." Proceedings of the 25th Advanced Studies Institute on Symmetries and Spin, ATL-LUM-PROC-2010-001, 2010.

[111] O. Viazlo and the ATLAS LUCID Collaboration, "ATLAS LUCID detector upgrade for LHC Run 2," Tech. Rep. ATL-FWD-PROC-2015-004, CERN, Geneva, Oct 2015.

[112] G. Avoni *et al.*, "The new LUCID-2 detector for luminosity measurement and monitoring in ATLAS," *JINST*, vol. 13, no. 07, p. P07017, 2018.

[113] ATLAS collaboration, "Zero Degree Calorimeters for ATLAS." CERN-LHCC-2007-001, 2007.

[114] M. W. Phipps, "A New ATLAS ZDC for the High Radiation Environment at the LHC," 2018. ATL-FWD-SLIDE-2018-288.

[115] ATLAS collaboration, "TDR for the ATLAS Forward Proton Detector." CERN-LHCC-2015-009, 2015.

[116] ATLAS collaboration, "ATLAS Forward Detectors for Measurement of Elastic Scattering and Luminosity TDR." CERN-LHCC-2008-004, 2008.

[117] ATLAS collaboration, "Measurement of the total cross section from elastic scattering in pp collisions at $\sqrt{s} = 7$ TeV with the ATLAS detector," *Nucl. Phys.*, vol. B889, pp. 486–548, 2014.

[118] ATLAS collaboration, "Measurement of the total cross section from elastic scattering in pp collisions at $\sqrt{s} = 8$ TeV with the ATLAS detector," *Physics Letters B*, vol. 761, p. 158–178, Oct 2016.

[119] A. R. Martínez, "The run-2 ATLAS trigger system," in *Journal of Physics: Conference Series*, vol. 762, p. 012003, IOP Publishing, 2016.

[120] ATLAS collaboration, "ATLAS public results - ApprovedPlotsDAQ." `https://twiki.cern.ch/twiki/bin/view/AtlasPublic/ApprovedPlotsDAQ`. Accessed December 2018.

[121] T. Cornelissen *et al.*, "Concepts, Design and Implementation of the ATLAS New Tracking (NEWT)." ATL-SOFT-PUB-2007-007, 2007.

[122] T. Cornelissen *et al.*, "The new ATLAS track reconstruction (NEWT)," in *Journal of Physics: Conference Series*, vol. 119, p. 032014, 2008.

[123] ATLAS collaboration, "Charged-particle distributions at low transverse momentum in $\sqrt{s} = 13$ TeV pp interactions measured with the ATLAS detector at the LHC," *Eur. Phys. J.*, vol. C76, no. 9, p. 502, 2016.

[124] ATLAS collaboration, "Track Reconstruction Performance of the ATLAS Inner Detector at $\sqrt{s} = 13$ TeV." ATL-PHYS-PUB-2015-018, 2015.

[125] F. Meloni, "Primary vertex reconstruction with the ATLAS detector," *Journal of Instrumentation*, vol. 11, p. C12060, dec 2016.

[126] ATLAS collaboration, "Topological cell clustering in the ATLAS calorimeters and its performance in LHC Run 1," *Eur. Phys. J. C*, vol. C77, p. 490, 2017.

[127] S. S. Mortensen, *Kinematic reconstruction of diffractive processes*. PhD thesis, 2013.

[128] ATLAS collaboration, "Rapidity Gap Cross Sections measured with the ATLAS Detector in pp Collisions at $\sqrt{s} = 7$ TeV," *Eur. Phys. J.*, vol. C72, p. 1926, 2012.

[129] S. Cavalier, P. Puzo, H. Burkhardt, and P. Grafstrom, "90m β^* Optics for ATLAS/ALFA." CERN-ATS-2011-134, Sep 2011.

[130] ATLAS collaboration, "ATLAS luminosity public results run 2." `https://twiki.cern.ch/twiki/bin/view/AtlasPublic/LuminosityPublicResultsRun2`. Accessed November 2018.

[131] A. Buckley *et al.*, "Lhapdf6: parton density access in the LHC precision era," *The European Physical Journal C*, vol. 75, Mar 2015.

[132] R. D. Ball *et al.*, "Parton distributions with LHC data," *Nuclear Physics B*, vol. 867, p. 244–289, Feb 2013.

[133] ATLAS collaboration, "Bunch groups definition webpages." `https://twiki.cern.ch/twiki/bin/view/Atlas/LevelOneCentralTriggerBunchGroups`. Accessed August 2019 (Internal).

[134] ATLAS collaboration, "Charged-particle distributions at low transverse momentum in $\sqrt{s} = 13$ TeV pp interactions measured with the ATLAS detector at the LHC," *Eur. Phys. J. C*, vol. 76, no. CERN-EP-2016-099. CERN-EP-2016-099, p. 502. 33 p, 2016.

[135] ATLAS collaboration, "ATLAS run query." `https://atlas-runquery.cern.ch/query.py?q=find+run+282420+%2F+show+all`. Accessed August 2019 (Internal).

[136] O Behnke *et al.*, *Data Analysis in High Energy Physics: A Practical Guide to Statistical Methods*. John Wiley & Sons, Ltd, 2013.

[137] M. Paterno, "Calculating efficiencies and their uncertainties." FERMILAB-TM-2286-CD, 2004.

[138] ATLAS collaboration, "A beam halo event of the ATLAS Experiment," ATLAS-PHO-EVENTS-2014-023.

[139] H. B. Prosper and L. Lyons, "PHYSTAT 2011 Workshop on Statistical Issues Related to Discovery Claims in Search Experiments and Unfolding." `https://cds.cern.ch/record/1306523`, 2011.

[140] G. D'Agostini, "A multidimensional unfolding method based on bayes' theorem," *Nuclear Instruments and Methods in Physics Research Section A: Accelerators, Spectrometers, Detectors and Associated Equipment*, vol. 362, no. 2, pp. 487 – 498, 1995.

[141] G. D'Agostini, "Improved iterative bayesian unfolding." `arXiv:1010.0632` Presented at the Alliance Workshop on Unfolding and Data Correction, 2010.

[142] ATLAS collaboration, "ATLAS standardmodelunfoldingnew (twiki page)." `https://twiki.cern.ch/twiki/bin/view/AtlasProtected/StandardModelUnfoldingNew`. Accessed December 2019 (Internal).

[143] "Luminosity determination in *pp* collisions at $\sqrt{s} = 13$ TeV using the ATLAS detector at the LHC." ATLAS-CONF-2019-021, Jun 2019.

[144] F. J. Llanes-Estrada and other, "QCD glueball regge trajectory and the pomeron," *Nuclear Physics A*, vol. 710, no. 1, pp. 45 – 54, 2002.

[145] A. Ballon-Bayona, R. Carcassés Quevedo, M. S. Costa, and M. Djurić, "Soft Pomeron in Holographic QCD," *Phys. Rev.*, vol. D93, p. 035005, 2016.

[146] G. Chapman, J. Cleese, *et al.*, "Monty Python's Flying Circus." BBC, 1969.

[147] ATLAS collaboration, "TDR for the Phase-I Upgrade of the ATLAS TDAQ System." CERN-LHCC-2013-018, 2013.

[148] H. Bethe, "Zur theorie des durchgangs schneller korpuskularstrahlen durch materie," *Ann. Phys. 5*, vol. 325, 1930.

[149] W. Frass and R. Walczak, "Passage of particles through matter." https://www2.physics.ox.ac.uk/sites/default/files/Passage.pdf, 2009. Oxford University lecture notes, accessed August 2019.

[150] B. Carlson, *Terrestrial gamma-ray flash production by lightning*. PhD thesis, 2009.

[151] B. Rossi and K. Greisen, "Cosmic-ray theory," *Rev. Mod. Phys.*, vol. 13, pp. 240–309, Oct 1941.

[152] S. Masciocchi, "Electromagnetic calorimeters." Lecture as part of SS2017, 2017.

[153] R. Achenbach *et al.*, "The ATLAS Level-1 Calorimeter Trigger," *Journal of Instrumentation*, vol. 3, no. 03, p. P03001, 2008.

[154] E. F. Eisenhandler *et al.*, "ATLAS Level-1 Calorimeter Trigger Algorithms." ATL-DAQ-2004-011, 2004.

[155] M. Mangano, "Weighing up the LHC's future." https://ep-news.web.cern.ch/content/weighing-lhc%E2%80%99s-future, 2018. Accessed December 2018.

[156] L. Arnaudon *et al.*, "Linac4 TDR." CERN-AB-2006-084, 2006.

[157] F. Bordry, "Summary Session of the LHC Performance Workshop 2018." https://indico.cern.ch/event/705545, 2018.

[158] K. Hanke *et al.*, "The LHC Injectors Upgrade (LIU) Project at CERN: Proton Injector Chain." CERN-ACC-2017-219, 2017.

[159] M. Schaumann, "LHC Machine Status Report at the open session of the 136th LHCC Meeting." https://indico.cern.ch/event/771106/, 2018.

[160] ATLAS collaboration, "ATLAS Liquid Argon Calorimeter Phase-I Upgrade Technical Design Report." CERN-LHCC-2013-017, 2013.

[161] ATLAS collaboration, "New Small Wheel TDR." CERN-LHCC-2013-006, 2013.

[162] "Electromagnetic Feature Extractor (eFEX) ATLAS TDAQ Phase-I Upgrade Final Design Report." ATL-COM-DAQ-2017-174, 2017. (Internal).

[163] ATLAS collaboration, "Electron and photon trigger efficiencies measured on early 2018 data for LHCC." ATL-COM-DAQ-2018-049, 2018.

[164] F. Winklmeier, "Run-2 ATLAS Trigger and Detector Performance," 2016. ATL-PHYS-SLIDE-2016-035.

[165] ATLAS collaboration, "Electron reconstruction and identification in the ATLAS experiment using the 2015 and 2016 LHC proton-proton collision data at $\sqrt{s} = 13$." ATLAS-PERF-2017-01, 2018.

APPENDIX A

Analysis selection

Table A.1: The LBs vetoed from the analysis.

LB range	Veto reason
< 5	ATLAS not ready
8	MBTS readout issue
$50 < LB < 78$	MBTS readout issue
133	MBTS readout issue
157	MBTS readout issue
182	MBTS readout issue
301	MBTS readout issue

Table A.2: Parameters from the fits to the MBTS noise.

Sample	MBTS	Mean (pC)	Sigma (pC)	Offline threshold (pC)
MC	Inner	2.15×10^{-4}	1.02×10^{-2}	0.051
	Outer	1.18×10^{-4}	1.91×10^{-2}	0.096
Data	Inner	-1.22×10^{-1}	1.35×10^{-1}	0.550
	Outer	-1.78×10^{-1}	1.96×10^{-1}	0.802

Table A.3: Calculated edges of acceptance for each RP, with the tolerances already taken into account.

RP	Lower edge (mm)	Upper edge (mm)
AUF	6.3	17.7
ALF	-17.4	-6.3
AUN	6.9	19.7
ALN	-19.5	-7.1
CUN	6.9	19.5
CLN	-19.5	-6.9
CUF	6.1	17.5
CLF	-17.3	-6.3

Table A.4: Elliptical fit parameters for each ALFA arm.

Fit parameter	AU	AL	CU	CL
x_c (mm)	0.0196	0.0227	0.0226	0.0192
$\sigma_x(mm)$	0.552	0.556	0.550	0.553
θ_c	5.80×10^{-6}	5.93×10^{-6}	-5.93×10^{-6}	-5.72×10^{-6}
σ_θ	2.86×10^{-5}	2.89×10^{-5}	2.86×10^{-5}	2.87×10^{-5}
ρ	0.943	0.947	-0.942	-0.944

APPENDIX B

Efficiency corrections

Table B.1: Measured values for each parameter used to calculate the ALFA track reconstruction efficiency, using the nominal method.

Arm	AU	AL	CU	CL
N_{Pass}	1.52052×10^6	1.46954×10^6	1.46954×10^6	1.52052×10^6
$N_{Pass}^{Background}$	148.452	142.249	142.249	148.452
N_{Fail}	44273	20356	37224	22496
$N_{Fail}^{Background}$	80.749	48.15	109.469	82.9484
$N_{\theta/\bar{x}}$	46848	23218	45523	25181

Table B.2: Efficiency values for the ALFA track reconstruction efficiency including the nominal values and the absolute variation for the systematic uncertainties.

Arm	AU	AL	CU	CL
Nominal ϵ	0.9733	0.9872	0.9769	0.9863
y edge (up)	0.0119	0.0089	0.0087	0.0011
y edge (down)	-0.0100	-0.0011	-0.0089	-0.0007
n_{fibres} (up)	0.0363	0.0179	0.0120	0.0169
n_{fibres} (down)	-0.0038	-0.0020	-0.0013	-0.0018
n_{σ} (up)	0.0002	0.0002	0.0002	0.0003
n_{σ} (down)	-0.0008	-0.0008	-0.0008	-0.0010
ϵ outside ellipse (up)	0.0015	0.0008	0.0016	0.0009
ϵ outside ellipse (down)	-0.0058	-0.0031	-0.0059	-0.0032
Background rate (up)	-0.0001	-0.0000	-0.0001	-0.0001
Background rate (down)	0.0001	0.0000	0.0001	0.0001
n_{Bunches} (up)	0.0000	0.0000	0.0000	0.0000
n_{Bunches} (down)	0.0000	0.0000	0.0000	0.0000
Total syst (up)	0.0382	0.0200	0.0149	0.0170
Total syst (down)	0.0122	0.0039	0.0107	0.0038
Total syst (largest)	0.0386	0.0203	0.0160	0.0173
Stat	0.0001	0.0001	0.0001	0.0001

APPENDIX C

Results

Table C.1: Calculated centres of gravity for the $|t|$ distribution.

Bin Edges [GeV^{-2}]	Bin Centre [GeV^{-2}]	Centre of Gravity [GeV^{-2}]
0.06-0.09	0.075	0.0744
0.09-0.12	0.105	0.104
0.12-0.16	0.14	0.139
0.16-0.21	0.185	0.184
0.21-0.28	0.245	0.242
0.28-0.37	0.325	0.321
0.37-0.49	0.43	0.423
0.49-0.66	0.575	0.561
0.66-0.9	0.78	0.755